Towards Hong-Ou-Mandel experiments to explore the anyonic statistics in the fractional Hall effect

Imen Taktak

université
PARIS-SACLAY

Towards Hong-Ou-Mandel experiments to explore the anyonic statistics in the fractional Hall effect

Thèse de doctorat de l'université Paris-Saclay

École doctorale n° 564, Physique en Ile-de-France (EDPIF)
Spécialité de doctorat: Physique
Unité de recherche : Université Paris-Saclay, CEA, CNRS, SPEC
91191, Gif-sur-Yvette, France
Référent : Faculté des sciences d'Orsay

Thèse présentée et soutenue à Paris-Saclay,
le 07 mai 2021, par

Imen TAKTAK

Composition du jury:

Adeline CREPIEUX Maitre de conférence (HDR), CPT Aix Marseille Université	Présidente
Janine SPLETTSOESSER Professeure, Applied Quantum Physics Group, MC2 (Chamers University, Suède)	Rapportrice et Examinatrice
Masaya KATAOKA Directeur de recherche, National Physical Laboratory (NPL,UK)	Rapporteur et Examinateur
Hélène BOUCHIAT Directrice de recherche, CNRS, LPS Orsay	Examinatrice
Takis KONTOS Chargé de recherche (HDR), Laboratoire Pierre Aigrain (LPA), ENS Paris	Examinateur

Direction de la thèse:

Christian GLATTLI Directeur de recherche, SPEC, CEA Saclay	Directeur de thèse

Thèse de doctorat

NNT: 2021UPASP037

Contents

List of Figures **iv**

List of Tables **x**

Abbreviations **xi**

0.1 Contexte général . . . 2
0.2 Réalisation du "HOM" électronique . . . 5
0.3 Résultats expérimentaux . . . 6
0.3.1 Résultats à $\nu = 2$ . . . 6
0.3.2 Résultats à $\nu = 2/5$ . . . 8
0.4 General context . . . 11
0.5 Implementation of the electronic "HOM" . . . 14
0.5.1 Results at $\nu = 2$ . . . 15
0.5.2 Results at $\nu = 2/5$ . . . 17

1 Introduction **20**
1.1 Semi-classical transport . . . 20
1.2 The mesoscopic scale . . . 21
1.3 Conductance quantization . . . 23
1.4 Noise in mesoscopic systems . . . 24
1.4.1 Definition of noise . . . 24
1.4.2 Thermal noise . . . 25
1.4.3 1/f noise . . . 26
1.4.4 Shot noise . . . 26
1.4.5 HOM experiment to reveal the statistics . . . 29

2 Physics in strong magnetic field **34**
2.1 The classical Hall effect . . . 34
2.2 The Integer Quantum Hall effect . . . 36
2.2.1 Landau levels . . . 38
2.2.2 The Landau gauge . . . 40
2.2.3 Conductance quantization . . . 41
2.2.4 The role of disorder . . . 42
2.2.5 The symmetric gauge . . . 44
2.2.6 Laughlin's argument . . . 46
2.3 The Fractional Quantum Hall effect . . . 48
2.3.1 Laughlin's filling factors . . . 48
2.3.1.1 Many-particle ground state . . . 48

2.3.1.2 Charged excitations . . . 50
2.4 Description of edge states . . . 51
2.4.1 Filling factors $\nu = 1/m$ . . . 51
2.4.2 Integer filling factors $\nu > 1$ . . . 54
2.4.3 Fractional filling factors $\nu = \frac{m}{2pm\pm1}$ . . . 55

3 Quantum transport in tunneling experiments 59
3.1 Perturbative approach . . . 60
3.1.1 DC transport . . . 60
3.1.2 Time-dependent transport . . . 65
3.2 The scattering approach . . . 68
3.2.1 Conductance of a mesoscopic system . . . 68
3.2.1.1 Two-terminal case . . . 68
3.2.1.2 Multi-terminal case . . . 70
3.2.2 Noise of a mesoscopic system . . . 71
3.2.3 Photo-assisted transport . . . 74
3.2.4 Photo-assisted shot noise (PASN) . . . 77

4 Experimental setup 80
4.1 Sample geometry and characteristics . . . 80
4.2 General considerations on the setup . . . 81
4.3 Power brought by the external circuit . . . 83
4.4 Noise measurements . . . 85
4.4.1 Data acquisition . . . 85
4.4.2 RLC resonator . . . 85
4.5 Noise calibration . . . 88
4.6 Amplification chain . . . 92
4.7 Measurements accuracy . . . 93
4.8 Conductance measurements . . . 96

5 Experimental results at $\nu = 2$ 99
5.1 Conductance plateaus . . . 99
5.2 Measurements at $V_{gate} = -0.2V$ . . . 101
5.2.1 Conductance . . . 101
5.2.2 DC shot noise (DCSN) . . . 101
5.2.3 Photo-assisted shot noise (PASN) . . . 104
5.2.4 HOM measurements . . . 107
5.2.4.1 Visibility optimisation . . . 108
5.2.5 HOM noise . . . 110
5.3 Measurements at $V_{gate} = -0.27V$ . . . 113
5.3.1 Conductance . . . 113
5.3.2 DCSN . . . 113
5.3.3 PASN . . . 114
5.3.4 HOM measurements . . . 115
5.4 Measurements at $V_{gate} = -0.3V$ . . . 117
5.4.1 DC measurements . . . 117
5.4.2 PASN . . . 118

5.5 Conclusion . . . 119

6 Experimental results at $\nu = \frac{2}{3}$ 121
6.1 DCSN . . . 123
6.2 PASN . . . 127
6.3 HOM measurements . . . 128

7 Experimental results at $\nu = \frac{2}{5}$ 132
7.1 DCSN . . . 133
7.1.1 Results at $\nu_B = \nu_{QPC} = 2/5$ . . . 135
7.1.2 Results at $\nu_B = 2/5$, $\nu_{QPC} = 1/3$ . . . 137
7.2 PASN . . . 139
7.3 HOM measurements . . . 141
7.3.1 Results at $\nu_B = 2/5$, $\nu_{QPC} = 1/3$ . . . 141
7.3.1.1 Visibility optimisation . . . 141
7.3.1.2 HOM measurements . . . 142
7.3.2 Results at $\nu_B = 2/5$, $\nu_{QPC} = 2/5$ . . . 145
7.4 Conclusion . . . 146

A Appendix A: Noise calibration 150
A.1 Calibration at $\nu = 2/3$ . . . 150
A.2 Calibration at $\nu = 2/5$ . . . 152
A.3 Effects of a bad thermalization . . . 153

B Sample characteristics 156
B.1 Formation of the two-dimensional electron gas (2DEG) . . . 156
B.2 QPC realization . . . 158

C Interference phenomena with RF waves 159

D DC polarisation of the sample 162

E Appendix E: Effects of the environmental noise on the PASN measurements 164

Bibliography 166

List of Figures

1 Schémas de l'échantillon utilisé. 5

2 Transmission (en vert) et réflexion (en bleu) en fonction de la tension de grille V_{gate} à $\nu = 2$. On observe bien une quantification d la conductance en unités de e^2/h. 7

3 $S^{HOM}(\tau)$ pour $V_{gate} = -0.2V$, $V_{dc} = 0V$, $f = 14.15GHz$, pour une puissance P_1 (figure de gauche) et $P_2 = 2P_1$ (figure de droite). Le fit correspond à l'expression (5.8), l'amplitude V_{ac} est un paramètre de fit. . 8

4 Transmission (en vert) et réflexion (en bleu) en fonction de la tension de grille V_{gate} à $\nu = 2/5$. Les lignes horizontales correspondent à $1/3e^2/h$ et $(2/5 - 1/3)e^2/h$. Les points (A) et (B) correspondent au régime dans lesquels des études du bruit on été menées. 9

5 $S^{HOM}(\tau)$ pour $V_{gate} = -0.42V$, $f = 14.15GHz$, une puissance P_1 (figure de gauche) et $P_2 = 2P_1$ (figure de droite). Le fit correspond à l'expression (5.8) avec e remplacé par $e^* = e/3$, l'amplitude V_{ac} est un paramètre de fit. 9

6 Scheme of the sample 14

7 Transmission (in green) and reflection (in blue) vs. gate voltage V_{gate} at $\nu = 2$. We observe a good conductance quantization in units of e^2/h. . . . 16

8 $S^{HOM}(\tau)$ for $V_{gate} = -0.2V$, $V_{dc} = 0V$, $f = 14.15GHz$, for RF power P_1 (left figure) and $P_2 = 2P_1$ (right figure). The fit corresponds to equation (4), the amplitude V_{ac} being a fitting parameter. 16

9 Transmission (green dots) and reflection (blue dots) vs gate voltage V_{gate} at $\nu = 2/5$. The horizontal lines correspond to $1/3e^2/h$ and $(2/5 - 1/3)e^2/h$. The regions (A) and (B) correspond to the regimes in which shot noise studies have been performed. 17

10 $S^{HOM}(\tau)$ for $V_{gate} = -0.42V$, $f = 14.15GHz$, a power P_1 (left figure) et $P_2 = 2P_1$ (right figure). Le fit corresponds to expression (5.8) with e replaced by $e^* = e/3$, the amplitudeV_{ac} is a fitting parameter. 18

1.1 On the top: diffusive regime, the electrons scatter many times on impurities. On the bottom: quasi-ballistic regime, only few scattering events. This image is a very simplified scheme as electrons do not have a well defined trajectory. However, as far as they can be described by time-evolving wave functions (which is the case in both situations), we are in the mesoscopic regime. 22

1.2 2-terminal conductor across which we apply a voltage $V = V_{dc}$. The number of modes is given by $N = W/\lambda_F$ and each mode carries a current $\frac{2e^2}{h}V_{dc}$ 23

1.3 2-terminal conductor on which we apply a bias V_{dc}. This generates a periodic charge injection from Left to Right. For an electron at energy E, the probability of being transmitted (resp. reflected) by the barrier is $D(E)$ (resp. $1 - D(E)$). The result is that a part I_t of the incoming current I_L is transmitted by the barrier, and the other part I_r is reflected. 26
1.4 2-particles collider with scattering amplitudes t and ir for particles x and y. The two possible initial situation are illustrated with an amplitude probability $a(x, y)$ and $a(y, x)$. 30

2.1 Classical Hall bar : we impose a current J flowing in the x direction. In the presence of a magnetic field, an electric field perpendicular to J is created: it is responsible for the Hall voltage. 35
2.2 transverse and longitudinal resistivities 36
2.3 Integer quantum Hall effect ([1]) 36
2.4 Trajectory of an electron under an electromagnetic field: the center of the orbit drifts along equipotential lines 37
2.5 The localisation of states due to disorder. The drawn lines correspond to equipotentials. 43
2.6 Energy spectrum without disorder (left-figure) and with disorder (right-figure) 43
2.7 The Corbino disc ([2]). An emf V_H is induced by slowly introducing a quantum of flux. 47
2.8 Integer and Fractional Quantum Hall effect conductance plateaus from [3] 48
2.9 Edge of a quantum hole droplet. Excitations are described by the propagation of a deformation $h(x, t)$ of the droplet with a drift velocity $v_D = v = E/B$. 51

3.1 Schematic view of charge transfer in the case of a strong barrier (upper figure) and a weak barrier from [4]. In the first situation only electrons can tunnel as the regime of FQHE is destroyed in the QPC region. In the second situation, the FQHE fluid is weakly perturbed and fractional charge transfer may occur via the FQHE fluid. 60
3.2 Schematic view of charge transfer in the case of weak tunneling through the QPC region. The left figure correspond to a stable QPC filling factor ν_{QPC}, such that no tunneling occurs between the two opposite edges of the sample. The right figure correspond to a non-stable filling factor ν'_{QPC}, allowing charge transport through the QPC region. 64
3.3 Example of two-terminal scattering problem for the case of one transverse channel. 69
3.4 4-contacts geometry. We apply a voltage on the reservoir 0 and we are interested in the current flowing in contacts 1 and 2 as well as their auto and cross correlation functions. 72

4.1 Left: PCB co-planar wave-guides, on which coaxial cables are connected to bring DC and RF signals. Right: SEM (scanning electron microscope) image of the sample. The blue part represents the 2DEG, the yellow part corresponds to the ohmic contacts. 81
4.2 Global scheme of the experimental setup. 83

4.3 Scheme of the RLC resonator. r_c is the inner conductance of the Coil, that competes with the value of R to define the height of the impedance resonance peak. . . . 86
4.4 Absolute value of the RLC impedance for the two lines (in Ω). Because of the mismatch between the C_l values (that are found to be $219pF$ for line B and $231pF$ for line B), resonance frequencies are not equal. The RLC parameters were found from the noise calibration of paragraph 4.5. . 87
4.5 Noise spectra for $\nu = 2/5$ and $T = 100mK$, for AutoA (left figure) AutoB (middle) and Cross correlation (right figure). . . . 88
4.6 Equivalent circuit of the sample and the RLC resonators at equilibrium ($V_{dc} = 0$). . . . 89
4.7 $\langle \Delta S_{A,A}(T - T_0) \rangle$ (left figure) and $\langle \Delta S_{B,B}(T - T_0) \rangle$ (right figure) versus mixing chamber temperature T . . . 90
4.8 $\Delta S_{A,A}(\omega, T - T_0)$ (left figure) and $\Delta S_{B,B}(\omega, T - T_0)$ (right figure) at $T = 100mK$ and fit using equation (A.2) and r_c,C_l and $G_{a/b}$ as fitting parameters. . . . 90
4.9 RLC parameters r_c,C_l and G_A found from the fit of $\Delta S_{A,A}(\omega, T - T_0)$ at different temperatures T. . . . 91
4.10 $|Z_{eq,A}|^2$, $|Z_{eq,B}|^2$ and $Re(Z^*_{eq,A} Z_{eq,B})$ for $\nu = 2$ and RLC parameters found from the fit of $\Delta S_{A,A}(\omega, T - T_0)$. . . . 91
4.11 Simplified schematic of HEMT amplifiers. V_{in} is the voltage to be amplified, thus V_A or V_B. . . . 93
4.12 Auto correlation $S_{VV}(f)$ spectra for $N = 10^5$. Left figure: Auto A, right figure: Auto B. . . . 94
4.13 $S_{VV}(N) - S_{VV}(N = 10^5)$ for N between 1000 and 15 000 (auto correlation spectra). Left figure: Auto A, right figure: Auto B. . . . 94
4.14 $\sigma_N \sqrt{N_{freq}}$ values extracted from the spectra of figure 4.13), versus number of averages N in log scale. . . . 95
4.15 Equivalent circuit at kHz frequencies for the transmitted current measurements. We could draw the same scheme for the reflected current measurements (on line B). . . . 96
4.16 y_A/V_0 and y_B/V_0 versus filling factor ν, from lockin measurements at frequency $f = 270Hz$ and output amplitude $V = 0.5V$. . . . 98

5.1 Conductance plateaux at zero DC bias. The dashed lines correspond to the gate voltages chosen to make noise measurements. . . . 100
5.2 Sample schematic at $\nu = 2$: we work in the regime where only the inner edge state is partitioned by the QPC. . . . 100
5.3 Conductance and reflected current for $V_{gate} = -0.2V$. The small non linearity visible in the conductance (left figure) is not visible anymore in the integral of it, that is the backscattered current (right figure). . . . 101
5.4 Transmitted and reflected conductance $G_A = G_T$ and $G_B = G_R$), as well as the sum of both for $V_{gate} = -0.2V$. . . . 101
5.5 Cross and auto-correlation functions versus DC bias V_{dc} at $V_{gate} = -0.2V$. 102
5.6 Real part $Re(A \times B) = \frac{Re(S_{cross})}{Re(C_{ab})}$ and imaginary part $Im(A \times B) = \frac{Im(S_{cross})}{Im(C_{ab})}$ of the current noise. As the current noise is measured at zero frequency, both quantities are supposed to be equal. But this is not confirmed by the datas. . . . 103

5.7 $\Delta S(V_{dc})$ at $V_{gate} = -0.2V$ for $f = 10GHz$, $P = 3dBm$ (top figure), $P = 6dBm$ (bottom figure) . . . 105
5.8 $S_{ON}(V_{dc}) - P_0 S_{OFF}(V_{dc})$ for $f = 10GHz$ and $P = 0, 3, 6dBm$. The blue dashed lines correspond to the minimisation interval, and he red dashed lines correspond to $\pm V_J$. . . . 107
5.9 Experimental setup used for photo-assisted current measurements, including the low-frequency (LF) and radio-frequency (RF) sources. The LF source is also used as a reference for the lockin. . . . 108
5.10 $G_R(V_{dc})$ at $V_{gate} = -0.3V$ for three consecutive sweeps in bias. . . . 109
5.11 Photo-current versus phase difference for $V_{gate} = -0.3V$ and $V_{dc} = -40\mu V$, and total RF power P=9dBm. The different curves correspond to different attenuation factors $A_1 - A_2$. . . . 110
5.12 Visibility versus difference of attenuation between the two RF lines $A_1 - A_2$ (in dBm), calculated from the points of figure 5.11 . . . 110
5.13 Simulation of the PASN $S_{ON}(V_{dc} = 0, \alpha)$ at $V_{gate} = -0.2V$, using equation (5.3) and the DC characteristic $S_{exp}(V_{dc})$. . . . 111
5.14 HOM measurements at $V_{gate} = -0.2V$ and $V_{dc} = 0V$, $f = 14.15GHz$, $P = 5dBm$ (top figure) and $P = 8dBm$ (bottom figure). From the fit we extract the V_{ac} amplitudes (as well as an offset value). . . . 112
5.15 $G_R(V_{dc})$, $G_T(V_{dc})$, and the sum $G_R(V_{dc}) + G_T(V_{dc})$ for $V_{gate} = -0.27V$. . . . 113
5.16 Cross and auto correlation functions versus DC bias V_{dc} for $V_{gate} = -0.27V$. The bottom figure focuses on the Cross correlation only. . . . 114
5.17 Excess noise $\Delta S(V_{dc})$ at $V_{gate} = -0.27V$, for $f = 10GHz$, $P = -1.5dBm$ (left figure) and $P = 1.5dBm$ (right figure). . . . 115
5.18 HOM noise measurements at $V_{gate} = -0.27V$, $f = 14.15GHz$, and powers $P = 2dBm$ (top), $P = 5dBm$ (middle) and $P = 8dBm$ (bottom figure). From the fit we extract the V_{ac} amplitude as well as an offset value. . . . 116
5.19 Reflection conductance $G_B(V_{dc}) = G_R(V_{dc})$ (left figure) as well as DCSN (right figure) verse DC bias V_{dc}. The three curves of $G_R(V_{dc})$ correspond to three successive measurements. . . . 118
5.20 PASN at $V_{gate} = -0.3V$, $f = 10GHz$, and powers $P = 0dBm$ (top), $P = 3dBm$ (middle) and $P = 6dBm$ (bottom figure). From the fit we extract the V_{ac} amplitude and an offset value. . . . 119

6.1 Model of a QPC device in the FQHE from Ref [5], similar to our experimental device. The filling factor ν_{QPC} depends on the density of the 2DEG under the QPC, that can be controlled through V_{gate}. In the incoherent regime where $l_{eq} << L_{QPC} << L_{arm}$ (where l_{eq} is the equilibration length, L_{arm} is the device length and L_{QPC} is the QPC length scale), stable conductance plateaus at recovered. . . . 122
6.2 Conductance $G_R(V_{dc})$ and $G_T(V_{dc})$ at $V_{dc} = 0V$ and $B = 7T$. The dashed line correspond to the gate voltage chosen to make noise measurements. . . . 123
6.3 "ON-OFF" cross correlation versus V_{gate} at $V_{dc} = \pm 96\mu V$ (blue and magenta curves) and $V_{dc} = \pm 48\mu V$ (red and orange curves). The green curve is a reference for $V_{dc} = 0V$. . . . 124
6.4 Conductance $G_B(V_{dc}) = G_R(V_{dc})$ (left figure) and backscattered current $I_B = I_R$ (right figure) for $V_{gate} = -0.0815V$. The non linearity visible G_R is almost not visible anymore in the integral of it, I_R. . . . 125

6.5 Cross and auto-correlation functions versus DC bias V_{dc}. (left figure) and cross-correlation only (right figure). The black continuous curve corresponds to $S_I(V_{dc})$ given by equation (6.2) (left figure) and to $0.4S_I(V_{dc})$ (right figure). 125
6.6 Comparison between the cross-correlation at $P = 1dBm$ ("ON") and the DCSN called "OFF", measured at $P = -20dBm$ (top figure), and excess cross-correlation $\Delta S(V_{dc})$ (bottom figure). The red dashed lines correspond to $\pm\frac{hf}{e^*}$ 128
6.7 Experimental setup used for "HOM" measurements. A_1 and A_2 are the attenuations of both RF lines (that may differ). The RF powers P_1 and P_2 are regulated in order to ensure equal amplitudes $V_{ac,1} = V_{ac,2}$ on contacts (0) and (3) of the sample, when $f = 14.15GHz$. 129
6.8 HOM measurements and fit using equation (6.4) for $P_1 = 12dBm$ (top), $P_1 = 9dBm$ (middle), $P_1 = 6dBm$ (bottom) and always $f = 14.15GHz$. . 130

7.1 Conductance plateau at $\nu = 2/5$. The green dots are the transmitted conductance $G_A = G_T$, and the blue dots are the reflected conductance $G_B = G_R$. The horizontal lines correspond to the values $1/3e^2/h$ and $(2/5 - 1/3)e^2/h$. The regions (A) and (B) are the regimes in which we performed precise DCSN measurements. 133
7.2 Cross and auto correlation for $V_{dc} = 400\mu V$ at various V_{gate} values. Bottom figure: zoom of the top figure. 134
7.3 Schematic of the sample at $\nu_B = 2/5$ and two co-propagating edge states. In the configuration (A) the tunneling of fractional charge occurs through a region with local filling factor $\nu_{QPC} = 2/5$, while in configuration (B) it occurs through a region with local filling factor $\nu_{QPC} = 1/3$. 135
7.4 $G_R(V_{dc})$ and $I_R(V_{dc})$ for $V_{gate} = -0.01V$ 135
7.5 Left figure: cross and auto correlation for $V_{gate} = -0.01V$. The continuous curve corresponds to $S_I(V_{dc})$ (equation (7.1)) with $e^* = e/5$. Right figure: cross correlation only. The continuous curve corresponds to $0.7S_I(V_{dc})$. 136
7.6 $G_R(V_{dc})$ and $I_R(V_{dc})$ for $V_{gate} = -0.42V$ and $V_{gate} = -0.4V$ 137
7.7 Cross correlation for $V_{gate} = -0.42V$ (left figure) and $V_{gate} = -0.4V$ (right figure). The black continuous line is the theoretical fit using equation (7.1), $R = 0.23$ and $e^* = e/3$. 138
7.8 $G_R(V_{dc})$ (left figure) and auto and cross-correlation (right figure) for $V_{gate} = -0.44V$ 138
7.9 $S_{ON}(V_{dc})$ and $S_{OFF}(V_{dc})$ (left figure) and excess cross-correlation $\Delta S(V_{dc})$ (right figure) for $V_{gate} = -0.44V$. The horizontal red lines correspond to $\pm hf/e^*$, $e^* = e/3$. 140
7.10 Left: S^{HOM} (cross-correlation) for $P_1 = 12dBm$ and P_2 between 9 dBm and 16 dBm. Right: evolution of the visibility with $V_{ac} = 10^{P_2/20}$. 141
7.11 Reflected current I_R and DC cross correlation at $V_{gate} = -0.42V$. 142
7.12 HOM measurements for $V_{gate} = -0.42V$, $P_1 = 8dBm$, $f = 14.15GHz$ . . . 143
7.13 HOM measurements for $V_{gate} = -0.42V$, $P_1 = 11dBm$, $f = 14.15GHz$ . . 143
7.14 HOM measurements for $V_{gate} = -0.42V$, $P_1 = 14dBm$, $f = 14.15GHz$ . . 144
7.15 HOM measurements for $V_{gate} = 0V$, $P_1 = 12dBm$, $f = 14.15GHz$ 145
7.16 HOM measurements for $V_{gate} = 0V$, $P_1 = 15dBm$, $f = 14.15GHz$ 146

7.17 A Lorentzian pulse carrying integer charge e is applied on a QPC in the FQHE in the regime of weak backscattering regime, where charges $e/3$ tunnel. On a second QPC, also in the FQHE, in the WBS regime of transmission, a Lorentzian pulse of integer charge is applied with a delay τ. The two leviton-like fractional charges are sent to a third QPC playing the role of a beam-splitter. Correlations between $I_1(t)$ and $I_2(t)$ are measured. 149

A.1 $\langle \Delta S_{A,A}(T - T_0) \rangle$ versus T for $\nu = 2/3$ 151
A.2 $\Delta S_{A,A}(\omega, T - T_0)$ (left figure) and $\Delta S_{B,B}(\omega, T - T_0)$ (right figure) for $\nu = 2/3$ and T between $40mK$ and $100mK$ 151
A.3 C_l and gains $G_{A/B}$ for lines A and B found from the fits of figure A.2. . . 152
A.4 $|Z_A|^2$, $|Z_B|^2$ and $Re(Z_A^* Z_B)$ versus frequency f 152
A.5 C_{aa}, C_{bb} and C_{ab} values found from noise calibration at $\nu = 2/3$. 153
A.6 $\langle \Delta S_{A,A}(T - T_0) \rangle$ versus T for $\nu = 2/5$ 153
A.7 $\Delta S_{A,A}(\omega, T - T_0)$ (left figure) and $\Delta S_{B,B}(\omega, T - T_0)$ (right figure) for $\nu = 2/5$ and T between $40mK$ and $100mK$ 154
A.8 C_l and gains $G_{A/B}$ for lines A and B found from the fits of figure A.7. . . 154
A.9 C_{aa}, C_{bb} and C_{ab} values found from noise calibration at $\nu = 2/5$. 155

B.1 a) Heterostructure scheme. Si donors are in the AlGaAs layer allowing the formation of the 2DEG. b) Band structure at the n-AlGaAs/iGaAs interface before charge equilibration. The dotted line represents the Fermi Energy in each structure, it is more important in AlGaAs than in GaAs. Solid lines are valence and conduction bands. c) Band structure after charge equilibration. The 2DEG, colored in blue, is formed at the interface of AlGaAs and GaAs while positively charged donors, in orange, accumulate at the AlGaAs side. 157
B.2 SEM image of the finished sample from Ref [6]. a) Image realized by electron microscope of the sample. The 2DEG is artificially colored in blue. The large bright circuit are golden leads connecting the ohmic contact in grey to the external circuit. The black lines are the gates. A zoom (figure b)) is realized at the center of the mesa where the gates are placed. 158

C.1 A standing wave is created by a reflection at both ends of a transmission line of length L and characteristic impedance $Z_0 = 50\Omega$. As $R_H >> Z_0$, the reflection coefficient $|r_2|^2$ is close to one. $|r_1|^2$ depends on non-perfect connector modeled by an impedance $Z' \neq Z_0$ 160
C.2 Transmission probability $|T|^2$ vs frequency for $|r_2|^2 = 0.99$, $|r_1|^2 = 0.01$, and $L = 20cm$ 161
C.3 Photo-current vs RF frequency for $\nu = 2$ (B=2.4T), $V_{gate} = -0.97V$. . . . 161

D.1 DC injection lines 163

List of Tables

4.1 Gain factors from noise calibration at different filling factors ν. 92
4.2 σ_N in V^2/Hz for some values of N, for the auto and cross-correlations. . . 95

5.1 V_{ac} and α values at $f = 10GHz$ and $V_{gate} = -0.2V$, deduced from the fits of figure 5.5. 106
5.2 AC amplitudes V_{ac} in μV and corresponding $\alpha = eV_{ac}/hf$ values extracted from the fits of figure 5.14, for $f = 14.15GHz$. 111
5.3 V_{ac} and $\alpha = eV_{ac}/hf$ values at $f = 10GHz$ and $V_{gate} = -0.27V$, deduced from the fits of figure 5.17. 115
5.4 V_{ac} in μV $(\pm 3\mu V)$ and $\alpha = eV_{ac}/hf$ from HOM measurements at $f = 14.15GHz$ and $V_{gate} = -0.27V$, deduced from the fits of figure 5.18 117

6.1 V_{ac}values in μV extracted from HOM measurements at different powers. . 129

7.1 V_{ac} range in μV and corresponding $\alpha = e^*V_{ac}/hf$ with $e^* = e/3$ and $f = 14.15GHz$ extracted from HOM measurements at various powers P_1. 144
7.2 V_{ac} range in μV extracted from HOM measurements at different powers. . 146

D.1 V_0 for an output voltage of 1V on the Yoko, for different falling factors ν. 163

Abbreviations

2DEG	2 Dimensional Electron Gas
QPC	Quantum Point Contact
I/FQHE	Integer/Fractional Quantum Hall Effect
PSD	Power Spectral Density
HEMT	High Electronic Mobility Transistor
HOM	Hong-Ou-Mandel
RF	Radio-Frequencies
DCSN	DC Shot Noise
PASN	Photo-Assisted Shot noise

À ma mamie...

Remerciements

Je remercie d'abord mon encadrant, Christian Glattli, qui m'a donné l'opportunité de vivre cette expérience scientifique et humaine au sein de son groupe. J'ai pu bénéficier de son riche enseignement en physique mésoscopique, et en particulier sur les mesures de "bruit". Malgré sa présence, de nombreuses difficultés techniques n'auraient pas été surmontables sans l'aide précieuse du groupe de cryogénie: Matthieu, Philippe, et Pépé (Patrick Pari), auxquels je suis réellement reconnaissante. Merci Pépé pour ta bonne humeur et ta passion pour la cryogénie! Je me dois également de remercier grandement Patrice Jacques pour son aide précieuse à mainte reprises, son efficacité, sa rigueur, sa modestie, et sa compagnie agréable en salle de manip! Je remercie également Preden Roulleau pour ses conseils sur les mesures de bruit.
Je tiens à remercier vivement tous les membres du jury pour avoir eu la patience de lire ma thèse, et pour leurs retours instructifs.

Bien sûr, ma thèse ne se jamais déroulée de la même façon sans mes amis du SPEC: merci Maëlle pour m'avoir formé à la manip avec patience et générosité, merci Matthieu pour tes conseils, merci Ramiro pour ta simplicité et ta bonne humeur, merci Ambroise pour nos discussions sur pleins de sujets passionnants (dont la physique), merci Paul et ensuite Gerbold d'avoir été des compagnons de bureau aussi sympathique et pour vos nombreux coup de mains, merci infiniment Zubert pour ton soutien du début jusqu'à la fin, merci Alex et Raphaëlle pour les moments agréables en votre compagnie!

Je remercie vivement Benoit Doucot, un physicien que j'admire et qui m'a régulièrement soutenu et suivi, mon parrain Cristian Urbina, et le responsable des thèse François Ladieu pour sa bienveillance. Je remercie Vincent Pasquier pour son enseignement passionnant sur l'effet Hall. Pour finir, je tiens spécialement remercier celle qui a été pour moi d'une grand soutien: j'ai la chance d'avoir une mère physicienne que j'admire, et dont l'enseignement m'a permis d'aborder mes expériences avec davantage de questionnements, d'entrain et de motivation. Merci maman, merci à ma famille, mes amis, et à tous ceux que j'aurais oublié.

Résumé en français

0.1 Contexte général

Ce travail s'inscrit dans le domaine de la physique mésoscopique, où les échelles de longueurs et les températures considérées sont telles que le transport électronique est décrit par le formalisme de la mécanique quantique. La taille du système étudié (plusieurs micromètres) est bien plus grande que l'échelle atomique, mais plus petite que la longueur de cohérence de phase des électrons. Cela signifie que les électrons peuvent être décrits en terme de fonctions d'onde, et que leur caractère ondulatoire doit être pris en compte. Celui-ci est responsable de la quantification de la résistance observée dans un bon nombre de systèmes mésoscopiques bidimensionnels [7][8]. Ces expériences ont été réalisables grâce aux progrès de la nanofabrication (permettant de fabriquer des échantillons de dimensions assez faibles) et de la cryogénie (les basses températures permettant d'obtenir des longueurs de cohérence assez grandes). En particulier, en 1988, la quantification de la conductance en paliers de $2e^2/h$ fut mise en évidence dans un conducteur quasi-unidimensionnel, où l'on peut faire varier le nombre de modes électroniques transmis : un contact ponctuel quantique (QPC). Un QPC est une grille déposée au dessus d'un gaz bidimensionnel d'électrons, formé le plus souvent à partir partir d'hétérostructures d'Arsenure de Gallium. En appliquant une tension sur le QPC, on peut contrôler localement la densité électronique (ou la taille de la constriction engendrée).

La résistance d'un système mésoscopique révèle le caractère ondulatoire des électrons, mais non leur caractère corpusculaire. Pour cela, il faut étudier non seulement la valeur moyenne du courant, mais également ses fluctuations autour de cette valeur moyenne (le "bruit"). C'est la raison pour laquelle l'intérêt s'est porté vers l'étude théorique et expérimentale du bruit dans les années 1990. Une particule incidente sur un conducteur mésoscopique balistique, modélisé par une barrière de potentiel, a une probabilité D dêtre transmise, et $R = 1 - D$ dêtre réfléchie. Le bruit de partition provient du caractère probabiliste de la mesure de la particule, qui avant la mesure se trouve dans une superposition d'états "transmis" et "réfléchi". La théorie de la diffusion ("scattering"

en anglais) [9] permet de calculer les fluctuations de courant dans de nombreuses situations, lorsque les quasi-particules responsables du transport n'intéragissent pas entre elles. Il a ainsi été démontré que, dans un conducteur balistique, le bruit en courant (plus exactement la densité spectrale de puissance du courant I) vaut:

$$S_I = 2eI(1 - D)$$

Cette formule a été vérifiée expérimentalement entre autres dans un QPC [10][11]. Cette formule a également été étendue à des régimes d'électrons fortement corrélés [12][13][14], où la charge e dans la formule précédente peut être remplacée par la charge des quasi-particules qui véhiculent le courant. En particulier, des mesures de shot noise dans l'effet Hall fractionnaire [15][16][17], ont montré que le courant peut être véhiculé par des quasi-particules de charge $e^* = e/3$ ou $e^* = e/5$.

Le régime d'effet Hall factionnaire, dont l'étude est l'une de nos principales motivations, est caractérisé par une conductance qui prend non pas des valeurs entières de e^2/h, mais factionnaires. Des plateaux de conductance situés à $\nu e^2/h$ où $\nu = p/q$ (p et q étant entiers) ont été observés en fonction du champ magnétique pour la première fois en 1982 [3]. Ce régime est atteint lorsqu'un fort champ magnétique est appliqué sur un gaz bidimensionnel (2DEG). Les efforts faits en vue d'améliorer la qualité des 2DEG, notamment leur mobilité (qui est de $3 * 10^6 V^{-1} cm^2 s^{-1}$ pour notre échantillon), ont permis d'étudier un tel régime.
Récemment, une étude du transport en présence d'une tension sinusodale (appelé transport "photo-assisté") [18] a confirmé les précédentes observations de charges fractionnaires, grâce à l'exploitation des singularités du bruit "photo-assisté" à $e^*V = hf$ (f étant la fréquence de la tension sinusoidale, de l'ordre de $10GHz$).

Dans le régime d'effet Hall factionnaire, il a été prédit [19] que les quasi-particules ont non seulement une charge fractionnaire, mais également une statistique fractionnaire (ou "anyonique"), c'est à dire intermédiaire entre la statistique fermionique et bosonique. Ainsi, l'échange entre deux quasi-particules (appelées "anyons") donne lieu à une phase statistique θ comprise entre 0 (cas des bosons) et π (cas des fermions):

$$\Psi(z_1, z_2) = e^{i\theta}\Psi(z_2, z_1)$$

Suite à de nombreuses tentatives [20],[21],[22],[23], la statistique anyonique a été révélée par des expériences basées sur un interféromètre de FabryPérot [24], ainsi que par des mesures de bruit de partition engendré par la "collision" de deux anyons sur un QPC [25]. C'est cette dernière approche, basée sur des mesures de bruit, que nous avons privilégié en vue d'explorer la statistique factionnaire. L'objectif à long terme est de

réaliser des expériences de type "Hong-Ou-Mandel" (HOM) [26] pour révéler la statistique anyonique. L'idée générale est la suivante: des anyons provenant de deux branches différentes incident sur un QPC (qui joue le rôle d'un lame semi-réfléchissante pour les électrons), avec un retard temporel variable τ. En optique quantique, le retard τ entre l'arrivée des deux photons sur le miroir est contrôlé par la longueur de la trajectoire optique. En optique quantique électronique, τ correspond au retard temporel entre deux pulses de tension appliqués sur deux réservoirs électroniques. Ces anyons peuvent par la suite soit emprunter des sorties différentes (c'est à dire être tous deux "transmis" ou tous deux "réfléchis" par le QPC), soit emprunter la même voie de sortie (l'un "transmis", l'autre "réfléchi"). En fonction de leur recouvrement temporel et de leur phase statistique, ils privilégieraient soit le "bunching" (même sortie) soit le "antibunching" (sorties différentes). De la même façon que le taux de coincidence entre deux détecteurs à photons uniques révèle leur caractère bosonique [26], la mesure de corrélations de courant croisées serait révélatrice de la statistique anyonique des quasi-particules incidentes sur le QPC.

Pour envoyer des anyons des deux côtés d'un QPC, il faut d'abord les créer grâce à deux autres QPC qui se trouvent également dans le régime de l'effet Hall fractionnaire. L'échantillon doit donc comporter trois QPC en tout (une géométrie similaire à celle de l'expérience [25]). De plus, le contrôle du retard entre les deux anyons - qui serait l'ingrédient supplémentaire par rapport á l'expérience [25] - suppose une bonne compréhension du transport en présence d'une tension dépendante du temps (AC). Cela représente un problème complexe, qui doit être appréhendé en commençant par effectuer des expériences de type "HOM" dans une géométrie à un *unique* QPC. Dans ce cas, des corrélations *fermioniques* sont attendues. Cela a été l'objectif principal de ma thèse.

Une autre partie de ma thèse, qui n'est pas présentée dans ce manuscrit, a été l'étude théorique et la fabrication d'un détecteur à électrons unique basé sur des méthodes bolométriques: l'électron est détecté en dissipant sont énergie dans le détecteur, engendrant une augmentation légère de température. Cette augmentation peut être détectée par des mesures de la conductance longitudinale, dont la variation avec la température est exponentielle. L'estimation de l'augmentation de température engendrée par un pulse électronique m'a poussé à l'étude théorique du transport d'énergie et de la dissipation dans un conducteur mésoscopique et en présence d'une tension alternative. L'échantillon réalisé pour ce projet n'a cependant pas pu être mesuré. Le lecteur intéressé peut se référer à mon rapport de stage.

0.2 Réalisation du "HOM" électronique

Dans le régime d'effet Hall, le courant est véhiculé par des canaux de bords formés à la périphérie de l'échantillon, tandis que le reste du gaz bidimensionel ("bulk") est isolant. Ces canaux sont l'équivalent des guides d'ondes en optique, et permettent de contrôler la trajectoire des électrons. Une illustration du dispositif expérimental est représentée figure 1. Une tension sinusodale $V_1(t)$ (resp. $V_2(t)$) est injectée au niveau du contact ohmique (0) (resp. (3)). Les excitations électroniques engendrées par les tensions $V_1(t)$

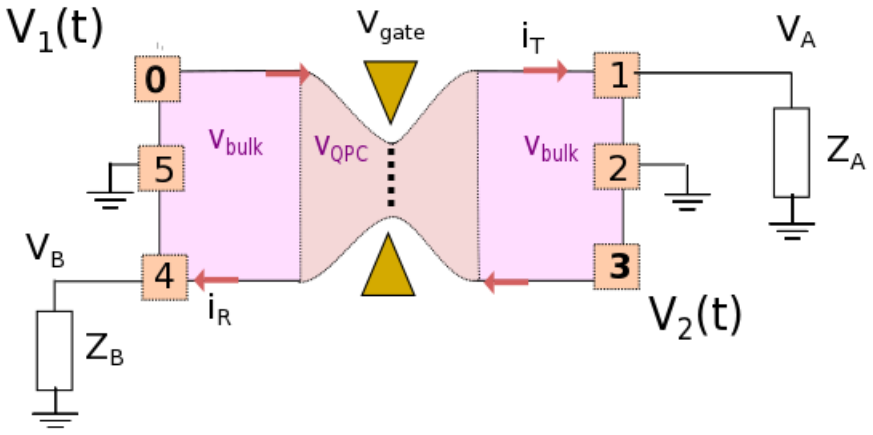

FIGURE 1: Schémas de l'échantillon utilisé.

et $V_2(t)$ se propagent de façon chirale vers le QPC. La géométrie à six contacts permet de mesurer séparément le courant transmis i_T et réfléchi i_R par le QPC. Les fluctuations de ces courants, ainsi leur fluctuations croisées, sont transformées en fluctuations de tension V_A,V_B aux bornes d'un circuit résonnant vers 2.2 MHz. Puis ces fluctuations sont amplifiées et mesurées par une carte d'acquisition qui effectue la transformée de Fourier du signal. Par ailleurs, une technique de détection synchrone permet d'effectuer des mesures de conductance (dérivées de i_T et de i_R).

Il est possible d'estimer la charge injectée Q pendant une période $T = 1/f$ de $V_1(t)$ dans chaque canal de bord supérieur par un simple calcul:

$$Q = \int_0^T I(t)dt = \frac{e^2}{h} T V_{dc}$$

où V_{dc} est la composante continue (DC) du signal. Ainsi, lorsque $eV_{dc} = hf$, $Q = e$ et on peut considérer qu'une charge e est injectée à chaque période. Pour que nos expériences soient comparables à celles de l'optique quantique, il ne suffit pas d'injecter une charge entière e à chaque période: il faut injecter un électron, ou plus précisément une excitation électronique "pure". Or généralement une tension dépendante du temps engendre des excitations électrons (au dessus de l'énergie de Fermi) et trous (en dessous de l'énergie de

Fermi). Ces excitations électrons-trous ne sont pas visibles dans le courant, mais uniquement dans le bruit de partition (qui est proportionnel à leur nombre). Il a été démontré qu'une tension de forme lorentzienne pouvait engendrer des excitations électroniques "pures" appelées "lévitons" [27]. Ces résultats on été vérifiés expérimentalement par des mesures de minimisation du bruit dans un QPC [28][29]. Dans ces travaux, des mesures de type "HOM" ont également été effectuées afin d'explorer la forme de la fonction d'onde des lévitons. En effet, les expériences de type "HOM" peuvent permettre de caractériser la fonction d'onde des quasi-particules, similairement à la "tomographie quantique" [30].

A la différence de ces dernières, nos expériences de "HOM" sont conduites dans le régime d'effet Hall (entier et fractionnaire). Elles consistent à envoyer non pas des lévitons mais une simple tension sinusoïdale des deux côtés de l'échantillon. Par simplicité, on choisis une composante DC nulle. Dans ce cas, avec une approche d'électrons indépendant, le même nombre d'excitations électrons et trous sont crées, puis partitionnées indépendemment par le QPC. Ainsi, le bruit de partition est fini. Celui-ci dépend du déphasage (ou retard τ) entre les deux sinus $V_1(t)$ et $V_2(t)$, qui peut être contrôlé soit automatiquement en utilisant deux sources radio-fréquences (RF) synchronisées, soit mécaniquement en modifiant la longueur d'une des voies RF grâce à un déphaseur mécanique. Les mesures de type "HOM" consistent à mesurer le bruit de partition (accessible en cross et auto corrélation) en fonction du retard τ. Afin d'assurer une visibilité maximale, il est nécessaire d'égaliser l'amplitude de $V_1(t)$ et $V_2(t)$, de telle sorte que $V_1(t) = V_2(t+\tau)$. Les mesures sont effectuées dans réfrigérateur à dilution permettant d'atteindre une température de 17 mK. Cependant, à cause de la puissance rayonnée par l'environnement sur l'échantillon, la température électronique de celui-ci est de l'ordre de 30 mK.

0.3 Résultats expérimentaux

Des mesures de type "HOM" ont été réalisées d'abord dans l'effet Hall entier ($\nu = 2$) puis dans l'effet Hall factionnaire ($\nu = 2/5$ et $\nu = 2/3$). La fréquence des ondes sinusodales est fixée à $f = 14.15GHz$. Le déphasage Φ est relié au retard τ: $\Phi = 2\pi f\tau$.

0.3.1 Résultats à $\nu = 2$

Les mesures à $\nu = 2$ on été effectuées pour trois tensions de grilles V_{gate} différentes (représentées par les lignes verticales figure 2), correspondant à trois valeurs différentes de la réflexion du canal interne. Pour chacune des ces valeurs de V_{gate}, des mesures

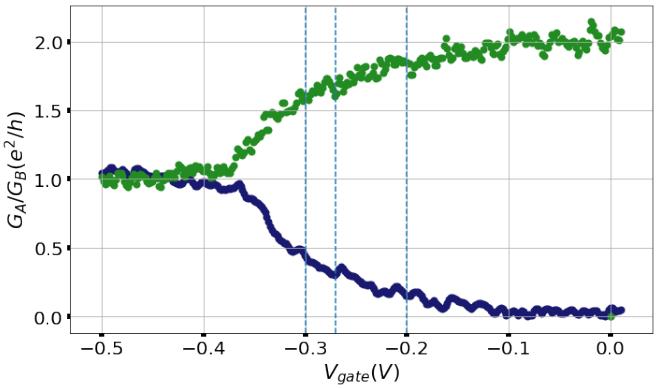

FIGURE 2: Transmission (en vert) et réflexion (en bleu) en fonction de la tension de grille V_{gate} à $\nu = 2$. On observe bien une quantification d la conductance en unités de e^2/h.

de bruit de partition en fonction de la tension V_{dc} ont été effectuées en absence et en présence d'une tension AC (appliquée sur le contact (0)). Ces mesures ont permis dans un premier temps de conforter l'image du transport "photo-assisté" [31][32], selon laquelle le bruit en présence d'une tension dépendant du temps $V(t) = V_{dc} + V_{ac}(t)$ (appelé $S^{photo}(V_{dc})$) est relié au bruit en présence de la composante continue seulement V_{dc} (appelé $S(V_{dc})$):

$$S^{photo}(V_{dc}) = \sum_l P_l(\alpha) S(V_{dc} - lhf/e) \tag{1}$$

où $\alpha = 2eV_{ac}/hf$ et $P_l(\alpha)$ est le carré de la fonction de Bessel d'ordre l. Cette relation a été dérivée dans le cas de matrice de diffusion indépendantes de l'énergie. Elle peut être généralisée à la configuration "HOM", où une tension $V_1(t) = V_{ac}sin(2\pi ft)$ (resp $V_2(t) = V_1(t+\tau)$) est appliquée sur le réservoirs (0) (resp. (3)). Dans ce cas, le bruit est théoriquement identique à celui qui serait obtenu si on appliquait une tension $V_1(t) - V_1(t+\tau)$ sur le réservoir (0). On s'attendrait alors à ce que le bruit "HOM" soit donné par:

$$S^{HOM}(\tau) = \sum_l P_l(\alpha_{eff}) S(lhf/e) \tag{2}$$

où $\alpha_{eff} = 2eV_{ac}sin(\pi f\tau)/hf$. Ce qui donne $S^{photo}(\tau = 0) = 0$, et $S^{photo}(\tau)$ maximal pour $\tau = T/2$. Bien que le facteur de réflexion soit dépendant de l'énergie (en particulier pour $V_{gate} = -0.27V$ et $V_{gate} = -0.3V$), les variations du bruit "HOM" ont pu correctement être reproduites en utilisant l'équation (2) et le bruit $S(V_{dc})$ mesuré. Les mesures du bruit "HOM" sont présentées ci-dessous pour $V_{gate} = -0.2V$ et deux différentes puissances du signal RF P_1, P_2 telles que $P_2 = 2P_1$ (soit un rapport $\sqrt{2}$ entre les amplitudes V_{ac}).

L'amplitude AC extraite des mesures à P_1 est $V_{ac} = 50\mu V$ et celle extraite à $P_2 = 2P_1$ est $V_{ac} = 72\mu V$. L'incertitude sur ces valeurs est de $3\mu V$ environ, et est surtout due

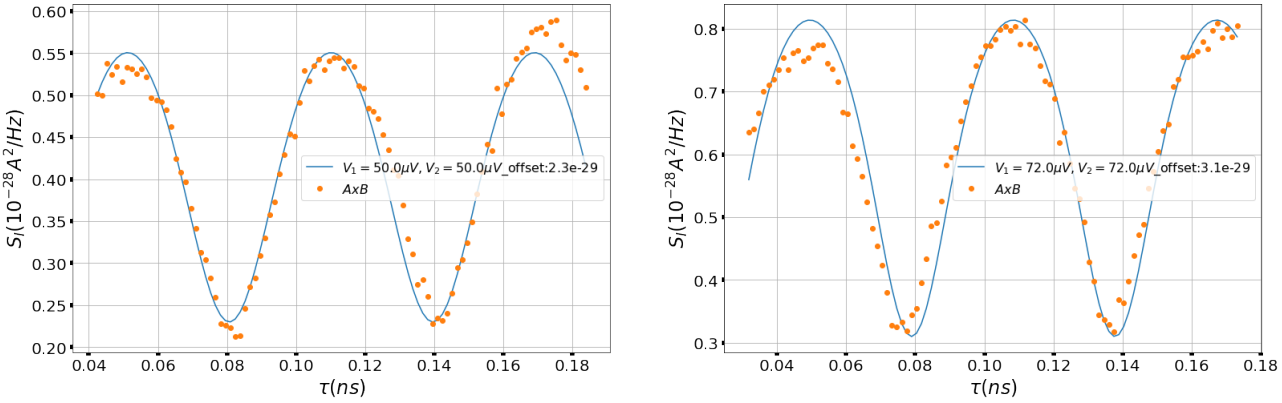

FIGURE 3: $S^{HOM}(\tau)$ pour $V_{gate} = -0.2V$, $V_{dc} = 0V$, $f = 14.15GHz$, pour une puissance P_1 (figure de gauche) et $P_2 = 2P_1$ (figure de droite). Le fit correspond à l'expression (5.8), l'amplitude V_{ac} est un paramètre de fit.

aux déviations expérimentales de la phase Φ au cours du temps. Le rapport entre ces deux valeurs de V_{ac} est très proche du facteur $\sqrt{2}$ attendu, ce qui montre un bon accord avec la théorie. Cet accord a également été observé à $V_{gate} = -0.27V$ (pour un facteur de réflexion plus important). Cependant, un aspect reste à résoudre: contrairement à ce qui est attendu, $S^{HOM}(\tau)$ ne s'annule pas à $\tau = 0$, et la visibilité demeure autour de 50%. A ce stade, nous ne pouvons pas encore trancher entre des raisons liées au montage expérimental, où à la physique de l'échantillon même.

0.3.2 Résultats à $\nu = 2/5$

A $\nu = 2/5$ (correspondant à un champ magnétique de $11.3T$), deux plateaux de conductance sont visibles lorsque l'on varie la tension de grille V_{gate} (et donc la densité électronique locale): un premier à $(2/5)e^2/h$, et un deuxième à $(1/3)e^2/h$. Ces plateaux correspondent à un facteur de remplissage local $\nu_{QPC} = 2/5$ et $\nu_{QPC} = 1/3$ sous le QPC. Nous avons étudié le bruit provenant du faible tunnel de quasi-particules dans ces deux régimes. Des mesures de bruit DC ont d'abord été menées, permettant d'obtenir la caractéristique $S(V_{dc})$ utilisée pour interpréter ensuite les mesures de $S^{HOM}(\tau)$. En effet, l'équation (2) peut être généralisée à des systèmes fortement corrélés [33] comme l'effet Hall factionnaire. Dans le régime perturbatif par rapport à l'amplitude tunnel (c'est à dire pour des courants réfléchis assez faibles), il suffit alors de remplacer e par e^* dans l'expression de $S^{HOM}(\tau)$ (2) en écrivant $\alpha_{eff} = 2e^*V_{ac}sin(\pi f\tau)/hf$.

Des mesures du bruit "HOM" sont présentées figure 5 pour une tension de grille $V_{gate} = -0.42V$, soit dans le régime de faible rétrodiffusion du canal externe. L'amplitude V_{ac} extraite de de la mesure à P_1 est $490\mu V$, et celle extraite de la mesure à $P_2 = 2P_1$ est $590\mu V$ (avec une incertitude maximale de $10\mu V$). Le rapport entre ces amplitudes est 1.2, plus faible que le ratio $\sqrt{2}$ attendu. Ainsi, la généralisation de l'équation (2)

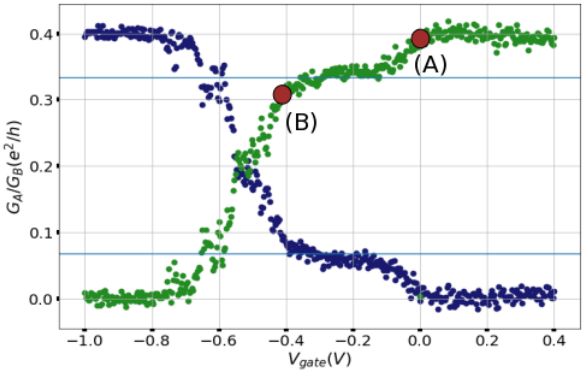

FIGURE 4: Transmission (en vert) et réflexion (en bleu) en fonction de la tension de grille V_{gate} à $\nu = 2/5$. Les lignes horizontales correspondent à $1/3e^2/h$ et $(2/5 - 1/3)e^2/h$. Les points (A) et (B) correspondent au régime dans lesquels des études du bruit on été menées.

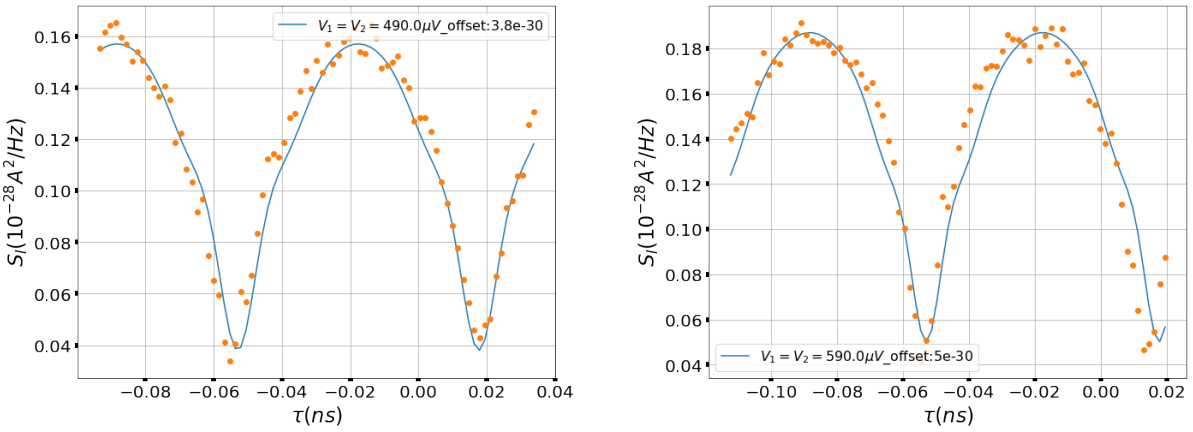

FIGURE 5: $S^{HOM}(\tau)$ pour $V_{gate} = -0.42V$, $f = 14.15GHz$, une puissance P_1 (figure de gauche) et $P_2 = 2P_1$ (figure de droite). Le fit correspond à l'expression (5.8) avec e remplacé par $e^* = e/3$, l'amplitude V_{ac} est un paramètre de fit.

au régime d'effet Hall factionnaire ne semble pas si évidente. Il est toutefois nécessaire de noter que les simulations théoriques de la figure 5 utilisent une extrapolation de la caractéristique $S(V_{dc})$ pour des tensions allant jusqu'à $900\mu V$. Cette extrapolation du bruit est nécessaire car $S(V_{dc})$ a été mesuré pour $-300\mu V < V_{dc} < 300\mu V$, mais elle peut bien sûr conduire à de fausses estimations.
Comme déjà observé à $\nu = 2$, le bruit HOM ne s'annule pas pour $\tau = 0$. La cause exacte est là aussi méconnue.

Si l'on compare les mesures HOM à $\nu = 2$ et $\nu = 2/5$, on s'aperçoit qu'il y a environ un ordre de grandeur entre les amplitudes V_{ac}. En effet, la puissance RF injectée lors des mesures à $\nu = 2/5$ est environ 9 fois plus grande qu'à $\nu = 2$: il est nécessaire d'appliquer des amplitudes plus grandes car la charge des quasi-particules est plus faible $e^* < e$ (la grandeur d'intérêt étant l'énergie e^*V_{ac}). Pour $e^* = e/3$, maintenir une énergie constante

requiert donc de multiplier l'amplitude V_{ac} par 3, et la puissance par 9. A $\nu = 2$, la comparaison de mesures HOM à différentes puissances du signal RF ont permis d'établir un bon accord avec la théorie du transport "photo-assisté".
L'étude quantitative des mesures HOM à $\nu = 2/3$ et $\nu = 2/5$ s'est avérée moins concluante, bien que celles-ci reproduisent bien la forme attendue. Elles ont été effectuées pour la première fois dans le régime d'effet Hall factionnaire. Il s'agit d'une étape importante qui a permis de mettre en lumière certaines difficultés dans la compréhension du transport en présence de signaux RF (aussi bien au niveau expérimental que théorique). L'une de ces incompréhensions est l'absence d'annulation du bruit HOM $\tau = 0$ malgré que des correlations fermioniques soient attendues. Ces difficultées doivent être résolues avant d'envisager une expérience plus complexe d'exploration de la statistique anyonique.

Summary

0.4 General context

This work is included in the mesoscopic field, where the considered length scales and the temperature are such that the electronic transport is subject to the laws of quantum physics. The length of the studied system (some μm) is much larger than the atomic length scale, but smaller than the phase coherence length of electrons. This means that electrons can be described by wave functions, and that their wave nature has to be taken into account. This wave nature is responsible for the conductance quantization in a large variety of bidimensional mesoscopic systems [7][8]. These experiments have been achievable thanks to the progress in nanofabrication (allowing to fabricate samples with low enough dimensions) and in cryogenics (low temperatures make it possible to reach large enough coherence lengths). In particular, in 1988, the conductance quantization in multiples of $2e^2/h$ was observed in a quasi one-dimension conductor, where it is possible to vary the number of transmitted electronic modes: a Quantum Point Contact (QPC). A QPC is a metallic grid deposited on top of a bidimensional electron gas (2DEG), generally fabricated in a gallium arsenite (GaAs) heterostructure. By applying a voltage on the QPC, it is possible to locally control the electronic density (or the length of the created constriction).

The conductance of a mesoscopic system reveals the wave nature of electrons, but not their particle nature. For this, it is necessary to study not only the mean value of the current, but also its fluctuations (the "noise"). This reason motivated the theoretical and experimental study of the "noise" in the nineties. A particle incident on a ballistic conductor, modelled as a potential barrier, has a probability D of being transmitted and $R = 1 - D$ of being reflected. The "shot noise" comes from the probabilistic nature of the particle measurement. Before the measurement, the particle is in a superposition of states between "transmitted" and "reflected". The scattering theory [9] enables to calculate the current fluctuations in various situations, when the quasi-particles carrying the current do not interact with each other. It was demonstrated that, in a ballistic

conductor, the current noise (or more exactly the power spectral density of the current) is given by:

$$S_I = 2eI(1 - D)$$

This formula was derived for non-interacting electrons, and has received experimental support, for example in QPC samples [10][11]. It was also extended to strongly-correlated systems [12][13][14], for which the charge e can be replaced by the charge of quasi-particles carrying the current. In particular, shot noise measurements in the fractional Hall effect [15][16][17] showed that the current can be carried by quasi-particles with fractional charge $e^* = e/3$ or $e^* = e/5$.

The fractional quantum Hall regime, that will be of particular interest during this work, is characterised by conductance plateaus located at $\nu e^2/h$, where $\nu = p/q$ (p and q integers) are non-integer fractions. These conductance plateaus have been observed while sweeping the magnetic field for the first time in 1982 [3]. The fractional Hall regime is reached when a strong magnetic field is applied perpendicularly to a 2DEG. The effort made in order to enhance the quality of the 2DEGs, particularly their mobility (that is $3 * 10^6 V^{-1} cm^2 s^{-1}$ for our sample), made it possible to study such a regime.
Recently, a study of transport in presence of a sine wave (called "photo-assisted" transport) [6] confirmed the previous fractional charge measurements by exploiting the "photo-assisted" shot noise singularities at $e^*V = hf$ (f being the frequency of the sine wave, up to 18 GHz).

In the fractional Hall regime, it was predicted [19] that quasi-particles have not only a fractional charge, but also a "fractional" statistic (also called "anyonic" statistic), intermediate between the fermionic and the bosonic statistic. This means that the exchange of two quasi-particles (called "anyons") gives rise to a statistical phase θ between 0 (case of bosons) and π (case of fermions):

$$\Psi(z_1, z_2) = e^{i\theta}\Psi(z_2, z_1)$$

After many attempts [20],[21],[22],[23], the anyonic statistic was revealed thanks to experiments based on Fabry-Perot interferometer [24], and also by shot noise measurements induced by the "collision" of two anyons on a QPC [25]. It is this last approach, based on shot noise measurements, that we decided to use as a way of exploring the anyonic statistic. The long-term objective is to implement "Hong-Ou-Mandel" [26] types of experiments to reveal the anyonic statistic. The general idea is the following: two anyons coming from two different branches impinge on a QPC (that plays the role of a semi-reflective mirror for electrons), with a variable time-delay τ. In quantum optics, τ is varied by modifying the optical length of one of the two branches. In electron quantum optics, τ is varied by controlling the phase difference between two voltage pulses applied

on electronic reservoirs. After the collision, the two anyons can either take different output branches (being both "reflected" or both "transmitted" by the QPC), either take the same output branch (one being "reflected" and the other "transmitted"). Depending on their temporal overlap and their statistical phase, they will either "bunch" (take the same output) or "antibunch" (take different outputs). In quantum optics the coincidence rate between two single photon detectors reveals their bosonic nature [26] - in electron quantum optics, the cross correlation between the transmitted and reflected currents could reveal the anyonic static of the quasi-particles impinging on the QPC.

In order to send anyons on both sides of a QPC, it is necessary to first create them thanks to two others QPC that are also in the fractional Hall regime. Thus the sample geometry consists of 3 QPCs in total: 2 QPCs are anyons sources, and the third one is the anyon collider. This geometry was used in experiment [25], where the shot noise resulting from anyons collisions (in the fractional quantum Hall regime) was compared to the one resulting from electrons collision (in the integer quantum Hall regime). The enhancement of the shot noise due to anyons collision is reminiscent from anyonic statistics. In this work, only DC voltages were used, thus there was no time-control of the anyons emission. The time delay control between the two anyons emission implies a good understanding of electronic transport in presence of time-dependent voltages. This represents a complex problem, that has to be approached by starting to make "HOM"-type experiments with a *single* QPC. In that case, *fermionic* correlations are expected, independently on the filling factor. The main objective of my PhD thesis was to make these "HOM" experiments in the integer and fractional quantum Hall regime.

Another part of my PhD work, that is not presented in this manuscript, was the theoretical study and the nanofabrication of a single-electron detector based on a bolometric method: the electron is detected after dissipation of its energy in the detector, leading to a small temperature increase ΔT. This increase could be detectable thanks to longitudinal conductance measurements, that has an exponential dependence with the temperature. The first step was to estimate ΔT through a theoretical study of energy transport and dissipation in a mesoscopic system subject to time-dependent voltages. The second step was to fabricate a single-electron detector. However, the sample fabricated for this project could not be measured. The interested reader can refer to my internship report.

0.5 Implementation of the electronic "HOM"

In the quantum Hall regime, the current is carried by chiral edge states formed at the periphery of the 2DEG, while the bulk is insulating. These edge states are the equivalent of optical wave-guides in quantum optics, as they enable to control the electrons trajectory. An illustration of the experimental setup is given in figure 6. A voltage

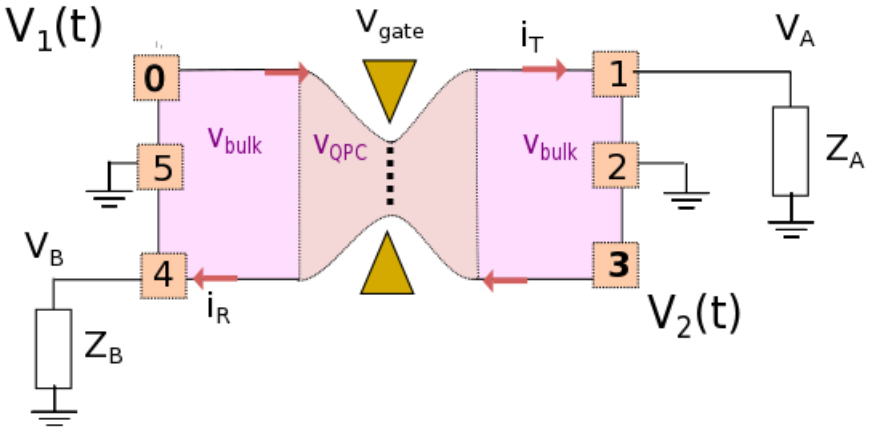

FIGURE 6: Scheme of the sample

$V_1(t) = V_{ac,1}sin(2\pi ft)$ (resp $V_2(t) = V_{ac,2}sin(2\pi ft)$) is applied on ohmic contact (0) (resp. (3)). The electronic excitations created by $V_1(t)$ and $V_2(t)$ propagate in a chiral way to the QPC. The 6-contact geometry enables to measure separately the current transmitted i_T and reflected i_R by the QPC. The fluctuations of these currents are converted into voltage V_A, V_B fluctuations across RLC circuits resonant around 2.2 MHz. Then these fluctuations are amplified and measured by an acquisition card that gives the Fourier transform of the signal. Moreover, a lockin technique is used for conductance measurements (derivative of i_T and i_R).

When the DC component V_{dc} of the signal is finite, the charge Q injected in each edge state during a period $T = 1/f$ of the signal can be estimated in a simple way:

$$Q = \int_0^T I(t)dt = \frac{e^2}{h}TV_{dc}$$

Thus when $eV_{dc} = hf$, $Q = e$ and we can consider that a charge e is injected at each period. For our experiments to be comparable to the ones of quantum optics, it is not enough to inject an integer charge e: we need to inject one electron, or more precisely one "pure" electronic excitation. But generally, a time-dependent voltage generates electronic excitations (above the Fermi sea) as well as hole excitations (under the Fermi sea). These electron-hole excitations are not visible in the current but only in the shot noise, that it proportional to their number. It was shown that a lorentzian-shaped

voltage can generate "pure" electronic excitations (with no holes) called "levitons" [27]. These predictions have received experimental support through measurement of shot noise minimization in a QPC [28][29]. In these works, "HOM" experiments have also been performed to explore the wave function shape of levitons. Indeed, these experiments can be a way to characterize the wavefunction of quasi-particles, similar to "quantum tomography" [30].

In contrast with these last experiments, our "HOM" experiments are performed in the integer and fractional Hall effect. They consist in sending sine waves instead of levitons on both sides of the sample. For simplicity, we choose a zero DC component. Generally, this leads to the same shot noise than when identical DC components are applied on both parts of the QPC. In this case, within the approach of non-interacting electrons, the same number of electrons and holes are created and partitioned by the QPC independently of each other. Thus the shot noise is finite, and it depends on the time-delay τ between the two sine waves $V_1(t)$ and $V_2(t)$. The time-delay can be controlled either automatically using two synchronized radio-frequency (RF) sources, or mechanically modifying the length of one of the RF cables that bring the signal from the source to the sample. The "HOM" measurements consist in measuring the shot noise (accessible by auto and cross-correlation measurements) while sweeping the time delay τ. To ensure a maximal visibility, it is necessary to equal amplitudes of $V_1(t)$ and $V_2(t)$, so that we have $V_1(t) = V_2(t+\tau)$. The measurements were performed in a dilution fridge that enables to cool down the sample to a temperature of $17mK$. However, because of the power radiated by the environment on the sample, its electronic temperature is of the order of 30 mK.

0.5.1 Results at $\nu = 2$

Measurements at $\nu = 2$ were performed at three different gate voltages V_{gate} (represented by the vertical dashed lines of figure 7), corresponding to three different values of the internal channel reflection. For each of these V_{gate} values, the shot noise dependence on V_{dc} was measured in absence and in presence of a RF sine wave applied on contact (0). These measurements confirmed the "photo-assisted" approach [31][32], according to which the noise in presence of a time-dependent voltage $V(t) = V_{dc} + V_{ac}(t)$ (called $S^{photo}(V_{dc})$) is linked to the noise in presence of the DC part only V_{dc} (called $S(V_{dc})$) through the relation:

$$S^{photo}(V_{dc}) = \sum_l P_l(\alpha) S(V_{dc} - lhf/e) \tag{3}$$

where $\alpha = eV_{ac}/hf$ and $P_l(\alpha)$ is the square of the l-th order Bessel function. This relation has been derived in the case of energy-independent scattering coefficients. It

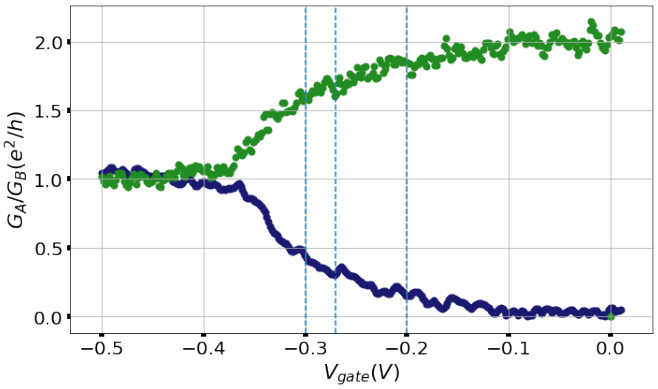

FIGURE 7: Transmission (in green) and reflection (in blue) vs. gate voltage V_{gate} at $\nu = 2$. We observe a good conductance quantization in units of e^2/h.

can be generalized to the "HOM" configuration, where voltages $V_1(t) = V_{ac}sin(2\pi ft)$ and $V_2(t) = V_1(t+\tau)$ are applied on contacts (0) and (3). In this case, the noise is identical to the noise obtained in the situation where a voltage $V_1(t) - V_1(t+\tau)$ is applied on contact (0). We then expect the "HOM" noise to be given by:

$$S^{HOM}(\tau) = \sum_l P_l(\alpha_{eff}) S(lhf/e) \tag{4}$$

where $\alpha_{eff} = 2eV_{ac}sin(\pi f\tau)/hf$. This gives $S^{photo}(\tau = 0) = 0$, and $S^{photo}(\tau)$ maximal for $\tau = T/2$. Although the reflection coefficients were not always energy-independent (in particular for $V_{gate} = -0.27V$ and $V_{gate} = -0.3V$), the variations of the "HOM" noise could be correctly reproduced using equation (4) and the measured DC shot noise $S(V_{dc})$. "HOM" noise measurements (in cross correlation) are presented below for $V_{gate} = -0.2V$ and two different powers P_1, P_2 of the RF signal such that $P_2 = 2P_1$ (meaning that the ratio between two consecutive V_{ac} values should be $\sqrt{2}$).

The AC amplitude extracted from HOM measurement at P_1 is $V_{ac} = 50\mu V$, and

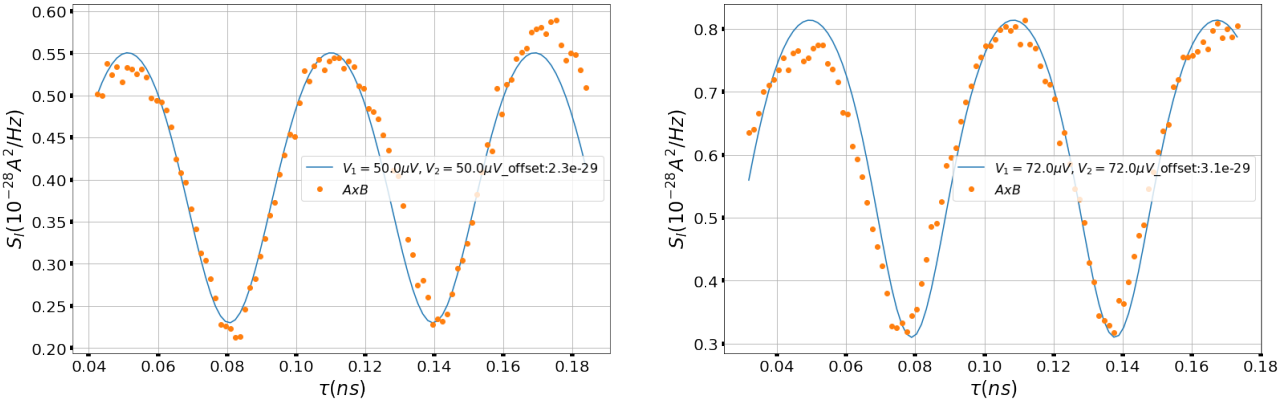

FIGURE 8: $S^{HOM}(\tau)$ for $V_{gate} = -0.2V$, $V_{dc} = 0V$, $f = 14.15GHz$, for RF power P_1 (left figure) and $P_2 = 2P_1$ (right figure). The fit corresponds to equation (4), the amplitude V_{ac} being a fitting parameter.

the one extracted from measurements at $P_2 = 2P_1$ is $V_{ac} = 72\mu V$ ($\pm 3\mu V$). The measurements accuracy is limited by experimental time drifts of the time τ (or the phase $\Phi = 2\pi f\tau$). The ratio between these two V_{ac} values is 1.44, thus very close to the $\sqrt{2}$ ratio expected. This means that our HOM data are in good agreement with the theory. A good agreement has also been established for HOM measurements at $V_{gate} = -0.27V$ (corresponding to a higher reflection coefficient). However, one aspect remains unsolved: contrary to what is expected, $S^{HOM}(\tau)$ does not cancel at $\tau = 0$, and the visibility remains around 50%. At this stage, we are not able to distinguish between reasons linked to the experimental setup and reasons linked with the sample physics.

0.5.2 Results at $\nu = 2/5$

At $\nu = 2/5$ (corresponding to a magnetic field of $11.3T$), two conductance plateaus are visible while sweeping the gate voltage V_{gate} (and thus the local electronic density): a first one located at $(2/5)e^2/h$, and a second one at $(1/3)e^2/h$. These plateaus correspond to the formation of a local filling factor $\nu_{QPC} = 2/5$ and $\nu_{QPC} = 1/3$ under the QPC as the electronic density is varied by the gate voltage. We studied the shot noise originating from the tunneling of quasi-particles in these two regimes, but for now we present measurements in the region (B) only. DC shot noise measurements were first

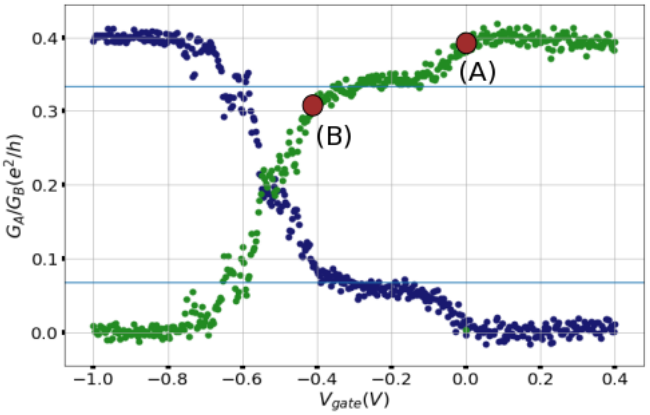

FIGURE 9: Transmission (green dots) and reflection (blue dots) vs gate voltage V_{gate} at $\nu = 2/5$. The horizontal lines correspond to $1/3e^2/h$ and $(2/5 - 1/3)e^2/h$. The regions (A) and (B) correspond to the regimes in which shot noise studies have been performed.

performed in order to get the $S(V_{dc})$ characteristic, later used in order to interpret the measurements of $S^{HOM}(\tau)$. Indeed, the relation (4) can be generalized to strongly correlated systems [33] such as the fractional Hall effect. In the perturbative regime with respect to the tunneling amplitude (that is to say for weak enough reflected current), it is enough to replace e by e^* in equation (4), writing $\alpha_{eff} = 2e^*V_{ac}sin(\pi f\tau)/hf$. As

previously for $\nu = 2$, HOM noise measurements were performed at $f = 14.15GHz$ and for two $\sqrt{2}$-spaced AC amplitudes V_{ac}. The two AC amplitudes extracted from the fits

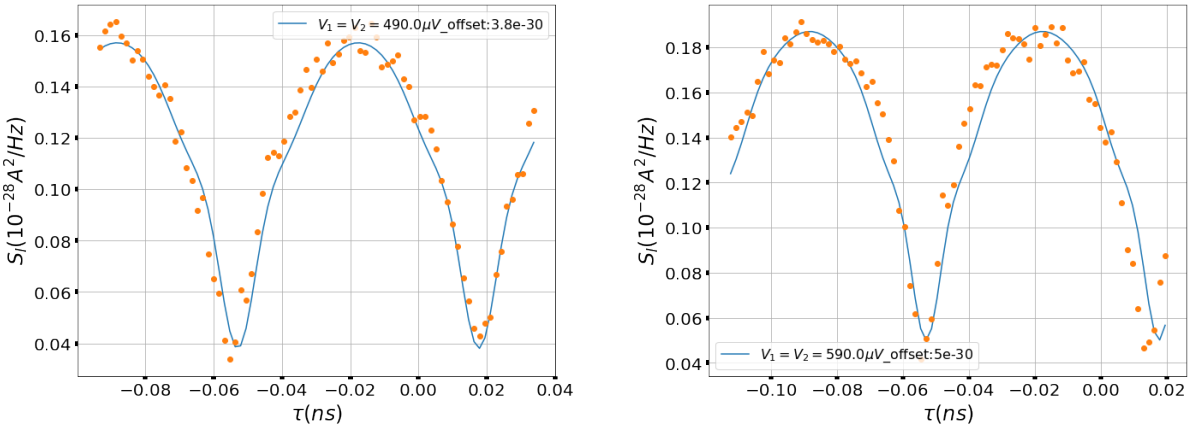

FIGURE 10: $S^{HOM}(\tau)$ for $V_{gate} = -0.42V$, $f = 14.15GHz$, a power P_1 (left figure) et $P_2 = 2P_1$ (right figure). Le fit corresponds to expression (5.8) with e replaced by $e^* = e/3$, the amplitudeV_{ac} is a fitting parameter.

of figure 10 are $490\mu V$ and $590\mu V$ ($\pm 10\mu V$). The ratio between these two values is 1.2, lower than the $\sqrt{2}$ factor expected for $P_2 = 2P_1$. Thus the generalization of equation (4) to the regime of fractional Hall effect does not seem obvious. Nevertheless, it is necessary to note that the theoretical simulations of figure 10 use an extrapolation of the DC shot noise characteristic $S(V_{dc})$ for V_{dc} up to $900\mu V$. This extrapolation is necessary because $S(V_{dc})$ was measured for $-300\mu V < V_{dc} < 300\mu V$ only - but of course it can lead to wrong estimations.
As already observed at $\nu = 2$, the HOM noise does not cancel for $\tau = 0$. Here also, the exact reason remains unknown.

If we compare HOM measurements at $\nu = 2$ and $\nu = 2/5$, we realize that there is one order of magnitude between the amplitudes V_{ac}. Indeed, the RF power injected during measurements at $\nu = 2/5$ is roughly 9 times higher than at $\nu = 2$: to reach the same energy scale e^*V_{ac}, it is necessary to apply higher AC amplitudes because the charge of quasi-particles is lower $e^* < e$. For $e^* = e/3$, keeping a constant energy scale requires that we multiply the amplitude V_{ac} by 3, and the power by 9.

At $\nu = 2$, comparisons between HOM measurements at different powers of the RF signal allowed us to establish a good agreement with the "photo-assisted" transport theory. The quantitative study of HOM measurements at $\nu = 2/5$ and $\nu = 2/3$ is less conclusive, although we recover the expected shape for the HOM noise. These are the first demonstration of HOM experiments in the fractional Hall regime. It is an important step that put into light some difficulties in the understanding of transport in presence of RF waves. One of these misunderstanding is the absence of shot noise cancellation at

$\tau = 0$ although fermionic correlations are expected. These aspects need to be resolved before considering more complex experiments with anyonic sources.

Chapter 1

Introduction

1.1 Semi-classical transport

The classical conduction of a metal can be well described by the Drude model (see Ashcroft and Mermin's book [34] for details), that treats electrons of the metal on a semi-classical level. They are accelerated by the electric field $\vec{E}$, and slowed down by scattering on impurities. We will detail in the next part the different types of collisions (or scattering events) electrons can experience. We assume that in between two collisions - spaced by a mean time τ - a conduction electron is free to move and is not submitted to any other force. Thus the scattering events redistribute the electrons velocity such as $\langle \vec{v} \rangle = 0$. Between two scattering events, electrons acquire a mean velocity : $\vec{v} = -e\tau\vec{E}/m$ and we can thus write the current vector:

$$\vec{J} = \frac{ne^2\tau}{m}\vec{E}$$

where n is the electronic density.

The classical conductivity (called Drude conductivity) of a macroscopic system is then given by :

$$\sigma_D = \frac{ne^2\tau}{m}$$

It is clear that this model needs a large number of collisions to be valid: on length scales lower than the mean free path (mean distance between two collision events), it has no meaning anymore. We will discuss below the different regimes of transport and the physical processes responsable for the finite time τ.

1.2 The mesoscopic scale

The mesoscopic scale is an intermediate scale between the macroscopic and the microscopic one. Mesoscopic sytems have dimensions lower than the coherence length l_Φ, that is the length over which electrons can be described as wave functions with a well definite phase. At this length scale, we can observe interference phenomena, similar to optic interference. On larger length scales, the electrons lose coherence because of different types of scattering events:

- the dominant one at temperatures above 1K is the electron-phonon scattering. The phonons are modes of vibration of atoms in a solid around their equilibrium position due to the finite temperature. Electrons can exchange energy with the crystalline structure of the solid, thus electron-phonon scattering is an inelastic process. We can associate to it a characteristic time (mean time between two collisions) τ_{e-ph} and a characteristic length l_{e-ph} between two successive collisions.

- At low temperatures (below 1K), the electron-phonon coupling decreases rapidly and the dominant inelastic scattering process is electron-electron collisions: it becomes the principal cause of decoherence. As $l_{e-e} \gg l_{e-ph}$, the low temperatures regime is interesting: the coherence length $l_\Phi = l_{e-e}$ is considerably increased. Electron-electron interactions play an important role as they are responsible for equilibration and thermalisation of electrons.

- Finally, we can have elastic collisions on impurities such as crystalline defects.

The time scale (and the mean collision length) of all these phenomena depend on the temperature but also the type of solids. The result is that, below 1K, the coherence length is around 200Å in a classical metal whereas it reaches some tens of micrometers in a 2D electron gas formed at the interface between two semi-conductors. By electronic lithography, the resolution obtained is of some tens of nanometers. As a consequence, thanks to the progress of cryogenic systems and nanofabrication, it is possible to fabricate circuits with dimensions lower than the coherence length, and thus to deal with quantum aspects of the transport.

As mentioned, at low temperature, the coherence length in a 2D system is principally determined by l_{e-e}. But we can also have elastic scattering events (collisions during which electrons do not lose their phase) with length scale l_e lower than l_{e-e}. The mesoscopic scale include two types of regime depending on the lenght L of the sample with respect to the scattering length l_e:
- the ballistic regime where $L \ll l_e$: electrons do not face any scattering event when crossing the sample (no backscattering processes).

- the diffusive regime when $L \gg l_e$: electrons experience many scattering events when crossing the sample.

These two regimes are illustrated below for a mesoscopic two-dimensional conductor linked to the external circuit by two terminals (electronic reservoirs). By applying a

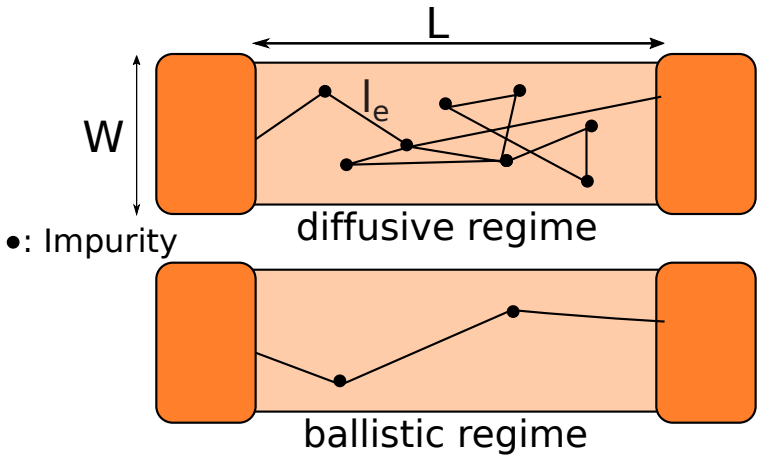

FIGURE 1.1: On the top: diffusive regime, the electrons scatter many times on impurities. On the bottom: quasi-ballistic regime, only few scattering events. This image is a very simplified scheme as electrons do not have a well defined trajectory. However, as far as they can be described by time-evolving wave functions (which is the case in both situations), we are in the mesoscopic regime.

bias V_{dc} between the two terminals, or by imposing a current I across this conductor, we can measure its resistance simply given by: $R = V_{dc}/I$. In 2D systems, the current is $I = JW/L$, where $J = \sigma V_{dc}$ is the current flux and W, L are respectively the width and the length of the conductor. Thus one particularity of 2D systems is that the resistivity $1/\sigma$ has the same unit as the resistance R.

Our experimental system is a bidimensional electron gas (2DEG) created at the interface of a heterostructure GaAs/AlGaAs (cf. Appendix B) and cooled down to temperatures around 20 mK. We will show that when applying a high magnetic field perpendicular to this 2DEG, the electronic transport can become ballistic over macroscopic lengths thanks to the formation of edge states. Thus 2DEG are particularly interesting when we need to control the trajectory of electrons (for interferometry experiments for example). Also, interesting physics can appear in 2D systems under high magnetic fields, as it will be detailed in Chapter 2.

In the diffusive regime, we can apply Drude model to calculate the conductance. In the ballistic one, it is not valid anymore, and we have to use a different approach that we now present.

1.3 Conductance quantization

Let's consider again a two-terminal and 2D mesoscopic conductor, across which we apply a bias V_{dc} (as illustrated in figure 1.2). The two terminals are electron reservoirs that inject particles in the conductor with a probability given by the Fermi distributions $f_R(E)$ and $f_L(E)$ (L and R refer to left and right reservoirs). Assuming that the conductor is ideal (no backscattering) and has a finite width W but infinite length L ($L \gg W$), the number of allowed modes is $N = W/\lambda_F$, where λ_F is the Fermi wavelength. In 2DEG systems, λ_F is of the order of tens of nanometers (while it is few Å in metals). The current flowing from the left contact to the conductor and carried by each mode is :

$$I_L = e \int_{-\infty}^{+\infty} v(E)\rho(E)(f_L(E) - f_R(E))dE$$

where we called $\rho(E)$ the density of states and $v(E)$ the velocity of electrons at energy E. We note that $I_L + I_R = 0$, ensuring current conservation. If we consider that each of the N modes corresponds to a perfect 1D non-interacting channel, the density of states is: $\rho(E) = 2/hv(E)$ (taking the spin degeneracy into account). This greatly simplifies the expression of the current at low temperatures ($k_BT \ll eV_{dc}$) which, for each of the N occupied modes, writes:

$$I_L = \frac{2e^2}{h} V_{dc} \tag{1.1}$$

As a consequence, the conductance takes discrete values depending on the number of allowed (or transmitted) modes: $G = N2e^2/h$. This conductance quantization has been observed in 2DEGs in many previous experimental works [8][7] using a Quantum Point Contact as a restriction in the transverse direction. The current being a number of charge per unit time, we can conclude from expression (1.1) that in each mode, one charge every h/eV_{dc} second crosses the conductor. Applying a DC bias to a conductor thus correspond to a periodic injection of charges from one terminal to the other. In

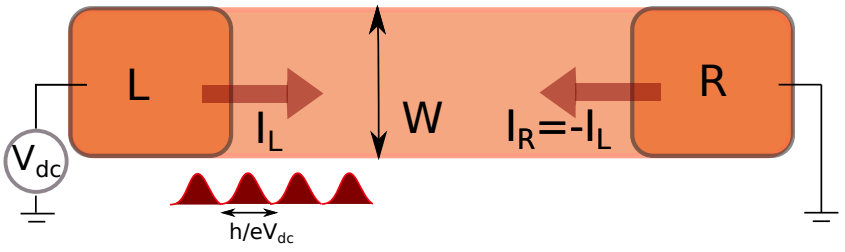

FIGURE 1.2: 2-terminal conductor across which we apply a voltage $V = V_{dc}$. The number of modes is given by $N = W/\lambda_F$ and each mode carries a current $\frac{2e^2}{h}V_{dc}$

.

our experimental system, the quantization of conductance is due to the edge states of

the Quantum Hall effect, and is very accurate thanks to the absence of backscattering. Here we only want to emphasise the necessity of taking into account the wave nature of electrons, that leads to very different results than the classical approach for the conductivity in mesoscopic systems.

One particularity of quantum mechanics is that a particle can be described as a wave and as a particle at the same time. The conductance measurement of a mesoscopic system highlights the wave nature of electrons, but not their particle nature. For this, it is necessary to measure not only the mean value of the current $\langle I \rangle$, but also the fluctuations of the current around this mean value $\langle (I - \langle I \rangle)^2 \rangle$ or in other words the noise, that we treat in the following paragraph.

1.4 Noise in mesoscopic systems

1.4.1 Definition of noise

More generally, we consider a classical random signal $V(t)$ with zero mean value (a situation we can always reach by subtracting the mean value of $V(t)$ if it is finite). The autocorrelation function of $V(t)$ is defined as:

$$C_{VV}(t, t') = \langle V(t)V(t') \rangle$$

whose sign and magnitude tell us whether the signal fluctuations at time t and time t' are correlated, anticorrelated or statistically independent. We assume that the noise process is stationary (i.e. the statistical properties are time-translation invariant) so that C_{VV} only depends on the time difference $t - t'$. We also assume that C_{VV} decays (sufficiently rapidly) to zero on some characteristic correlation time scale τ_c which is finite.

We can access to the Fourier components of $C_{VV}(t-t')$ by measuring the power spectral density (PSD), which represents the power of the signal $V(t)$ at different frequencies. Indeed, we can Fourier transform the signal $V(t)$ over a time T_{meas} (that corresponds to the measurement time of the spectrum analyser):

$$\tilde{V_n} = \frac{1}{2T_{meas}} \int_{-T_{meas}}^{T_{meas}} V(t) e^{i\pi nt/T} dt$$

Then the PSD is defined, after having done a large ensemble of statistically equivalent measurements, as the statistical mean (or ensemble average) value of the square of

the Fourier components: $S_{VV}(\omega_n) = \langle \tilde{V_n}^2 \rangle / \Delta f$ where $\Delta f = 1/2T_{meas}$ is the spectral resolution and $\omega_n = n\pi/T_{meas}$.

If $T_{meas} \gg \tau_c$ (which we assume to be always true), the Wiener-Khintchine theorem states that:

$$S_{VV}(\omega_n) = \int_{-\infty}^{+\infty} C_{VV}(t'-t) e^{i\omega_n(t'-t)} d(t'-t)$$

Taking the continuous limit $T_{meas} \to +\infty$ and the inverse transform, this theorem relates the autocorrelation function to the PSD:

$$C_{VV}(t'-t) = \int_{-\infty}^{+\infty} S_{VV}(\omega) e^{-i\omega(t'-t)} d\omega$$

We thus see that a short auto-correlation time implies a spectral density which is finite over a wide range of frequencies. In the limit of white noise $C_{VV}(t'-t) = \sigma^2 \delta(t'-t)$ and the spectrum is flat (frequency independent): $S_{VV}(\omega) = \sigma^2$.

Finally, we want to emphasise that as $V(t)$ is a classical variable, it commutes with its values at different times: $\langle V(t)V(t') \rangle = \langle V(t')V(t) \rangle$ and $C_{VV}(t,t')$ is a real value (which can be false for quantum operators that do not commute at different times). As a consequence, $C_{VV}(t,t')$ is symmetric in time and its Fourier transform is symmetric in frequency: $S_{VV}(\omega) = S_{VV}(-\omega)$. The PSD of voltage or current across a conductor can be explained by different physical phenomena. We will detail the main sources of noise in the next paragraph.

1.4.2 Thermal noise

The thermal noise, also called "Johnson-Nyquist Noise" [35][36], is due to the thermal agitation of the electrons at thermal equilibrium. This phenomenon exists independently of the bias applied to the conductor. The PSD of the voltage across the conductor at equilibrium depends only on the real part of the impedance $Z(\omega)$ of the conductor and on its temperature T:

$$S_{VV}(\omega) = 4k_B T Re(Z(\omega))$$

This formula is valid for low enough frequency or high enough temperature ($\hbar\omega \ll k_B T$). It can be demonstrated applying the fluctuation-dissipation theorem. In the case of a simple resistance ($Z(\omega) = R$), we obtain a white noise.

1.4.3 1/f noise

The $1/f$ noise can have many origins: for example impurities that deliver arbitrary charge carriers, or electron-hole recombinations. These types of phenomena can cause conductance fluctuations. The appellation "$1/f$ noise" is quite generic and used in opposition to the white noise: this noise is actually proportionnal to $1/f^{\alpha}$ where α is an empirical value between 0,8 and 1,3.

1.4.4 Shot noise

The shot noise in a mesoscopic conductor is due to the granularity of the charge carriers. Contrary to the thermal noise, it is necessary for the conductor to be out of equilibrium (applying a finite bias) to observe it.

To understand its origin, we use again the scheme of a 2D conductor in figure 1.3 with electrons flowing from the left to the right contact because of a finite bias V_{dc}. But now we add a potential barrier inside the conductor (caused for example by an impurity) that scatters the electrons coming from the left contact. Because electrons are quantum particles, they have a non zero probability $D(E)$ to tunnel whatever their energy E, and a probability $R(E)$ to be reflected. The particle state is thus a superposition between "transmitted" and "reflected".

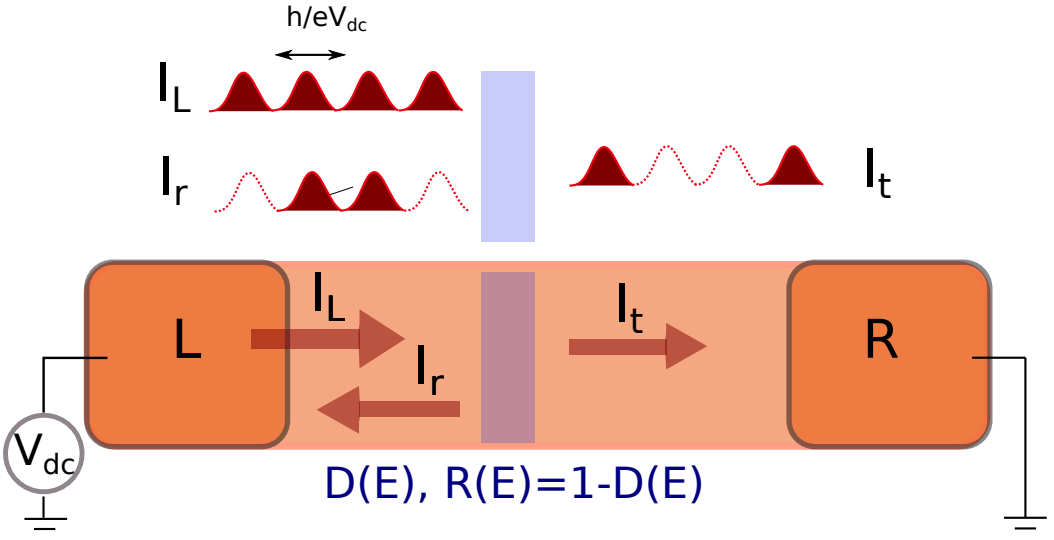

FIGURE 1.3: 2-terminal conductor on which we apply a bias V_{dc}. This generates a periodic charge injection from Left to Right. For an electron at energy E, the probability of being transmitted (resp. reflected) by the barrier is $D(E)$ (resp. $1 - D(E)$). The result is that a part I_t of the incoming current I_L is transmitted by the barrier, and the other part I_r is reflected.

The reservoirs' temperature T is finite such that an electron with energy between E and $E + dE$ is emitted from the left contact with a probability $f_L(E)$, and from the right contact with probability $f_R(E)$. We call N_L and N_R the occupation number of electrons emitted respectively from the left and the right. Pauli exclusion principle implies that $N_{L,R} = 0$ or 1, and: $\langle N_{L,R} \rangle = f_{L,R}(E)$. The notation $\langle X \rangle$ is used for the statistical average of the variable X. The current between the left and right contact is simply the sum over all the energies of the difference between left and right emitted charges per unit time : $I = \int e\langle N_L - N_R \rangle / \tau$ where $\tau = h/dE$ is the time of emission of the electron (given by Heisenberg principle). We recover the conductance quantization at low temperature. The fluctuations of $N_{L,R}$ can be calculated using $N_{L,R}^2 = N_{L,R}$:

$$\langle (\Delta N_{L,R})^2 \rangle = \langle N_{L,R}^2 \rangle - \langle N_{L,R} \rangle^2 = \langle N_{L,R} \rangle (1 - \langle N_{L,R} \rangle) = f_{L,R}(E)(1 - f_{L,R}(E)) \quad (1.2)$$

This term represents the fluctuations of the occupation number due to the finite temperature. We obtain the expected result for a binomial law with a number of experiments equal to one and a probability of success $f_{L,R}(E)$, that is the consequence of the Pauli exclusion principle.

Now we are interested in the fluctuations of the number of transmitted and reflected electrons by the barrier. We only take into account the contribution of electrons coming from the left contact, in order to give an idea on the origins of shot noise. We call N_t (resp. N_r) the occupation number of electrons coming from the left contact and transmitted (resp. reflected) by the barrier. Their mean value is: $\langle N_t \rangle = D f_L(E)$ and $\langle N_r \rangle = R f_L(E)$ (we omitted the energy dependence of D and R for simplicity). As $N_{t,r}$ takes values 0 or 1, $N_{t,r} = N_{t,r}^2$. Moreover, after each measurement the electron is either transmitted or reflected, so $N_t N_r = 0$. From this we can easily calculate the fluctuations of N_t and N_r (autocorrelations) as well as the cross correlation $\langle \Delta N_t \Delta N_r \rangle$:

$$\langle (\Delta N_t)^2 \rangle = \langle N_t^2 \rangle - \langle N_t \rangle^2 = \langle N_t \rangle (1 - \langle N_t \rangle) = D f_L(E)(1 - D f_L(E)) \quad (1.3a)$$

$$\langle (\Delta N_r)^2 \rangle = \langle N_r^2 \rangle - \langle N_r \rangle^2 = \langle N_r \rangle (1 - \langle N_r \rangle) = R f_L(E)(1 - R f_L(E)) \quad (1.3b)$$

$$\langle \Delta N_t \Delta N_r \rangle = \langle N_t N_r \rangle - \langle N_r \rangle \langle N_t \rangle = -\langle N_r \rangle \langle N_t \rangle = -DR f_L^2(E) \quad (1.3c)$$

Using $D + R = 1$ (the incident electron is either transmitted or reflected by the barrier) we get:

$$\langle (\Delta N_t)^2 \rangle = D f_L (1 - f_L) - \langle \Delta N_t \Delta N_r \rangle$$
$$\langle (\Delta N_r)^2 \rangle = R f_L (1 - f_L) - \langle \Delta N_t \Delta N_r \rangle$$

We see that the auto-correlation functions are the sum of two types of fluctuations: the first term comes from the finite temperature (thermal noise), and the second term (equal

to minus the cross-correlation term) comes from partition of particles at the barrier. This last contribution is called "shot noise".

To relate these electron numbers fluctuations to the fluctuations of the incident current I_i $(i = L, R)$, the transmitted and reflected current I_t and I_r, we have to take into account the measurement time T_{meas}. In the energy interval between E and $E + dE$, one electron every $\hbar/dE$ is emitted by the left and right contact with probability $f_{L,R}$. This means that the number of repeated events (or experiments) during the time T_{meas} is $T_{meas}dE/\hbar$. The number of transmitted (reflected) electrons $\tilde{N}_t$ ($\tilde{N}_r$) measured during the time T_{meas} follows a binomial law with a probability of success Df_L (Rf_L). Indeed, as the emission of particles from the left contact and the partition of the barrier are independent events, we can multiply their probabilities to get the probability of one electron transmitted (or reflected). We can easily deduce the variance of $\tilde{N}_{t,r}$:

$$\langle(\Delta\tilde{N}_t)^2\rangle = Df_L(1 - Df_L)\frac{dE}{h}T_{meas} \tag{1.4a}$$

$$\langle(\Delta\tilde{N}_r)^2\rangle = Rf_L(1 - Rf_L)\frac{dE}{h}T_{meas} \tag{1.4b}$$

$I_{t,r}$ is of course proportional to $\tilde{N}_{t,r}$:

$$I_{t,r} = e\tilde{N}_{t,r}/T_{meas} \tag{1.5}$$

which gives: $\langle(\Delta I_{t,r})^2\rangle = e^2\langle(\Delta\tilde{N}_{t,r})^2\rangle/T^2_{meas}$. The PSD of $I_{t,r}$ is: $S_{II} = \langle(\Delta I)^2\rangle 2T_{meas}$ (where we have omitted the prefixes t, r). We can make the same reasoning to calculate the fluctuations of the number of incident particles from left ($\tilde{N}_L$) and right ($\tilde{N}_R$), that follow a binomial law with probability of success $f_{L,R}$. From the last two equations and equation (1.4), we get the PSD of the incident, transmitted and reflected currents:

$$S_{I_iI_i} = \frac{2e^2}{h}\int f_i(E)(1 - f_i(E))dE \tag{1.6a}$$

$$S_{I_tI_t} = \frac{2e^2}{h}\int Df_L(E)(1 - Df_L(E))dE \tag{1.6b}$$

$$S_{I_rI_r} = \frac{2e^2}{h}\int Rf_L(E)(1 - Rf_L(E))dE \tag{1.6c}$$

$$S_{I_tI_r} = \frac{2e^2}{h}\int D(1 - D)f^2_L(E)dE \tag{1.6d}$$

Using the property of Fermi functions: $f_i(E)(1 - f_i(E)) = k_BTdf/dE$, we can show that the sum $S_{I_LI_L} + S_{I_RI_R}$ gives the Johnson Nyquist noise $4k_BTe^2/h$. For a perfect conductor ($D = 1$), the shot noise cancels and only thermal fluctuations remains.

The derivation of equation (1.6d) was a bit more complicated than the situation when we considered one experiment only, as $\tilde{N}_t\tilde{N}_r$ is not equal to zero anymore. Moreover,

as already said, the expressions for shot noise are not exact because we should also take into account the partition of electrons coming from the right. Despite this, with a proper derivation of the noise using the scattering approach in Chapter 4, we will find very similar expressions. In particular, the $D(1-D)$ term in the cross correlation is once again characteristic of a binomial distribution. In the limit $D \ll 1$ or $f_i \ll 1$, the factor $(1 - Df_L(E))$ can be replaced by 1 in expressions (1.6b) and (1.6c), and we find a Poissonian noise:

$$S_{I_{t,r}I_{t,r}} = 2eI_{t,r} \tag{1.7}$$

This PSD results from non-correlated arrivals of electrons on the barrier, with a distribution of the time Δt between two arrivals that is Poissonian: $P(\Delta t) = \tau^{-1} exp(-\Delta t/\tau)$, τ being the mean time between two incident particles. From this simple picture we can see that with non-interacting fermions, the shot noise is always sub-poissonian.

As a conclusion of this discussion, the low frequency current noise of a mesoscopic conductor is due to the number of particle fluctuations, that have two origins: thermal fluctuations (thermal noise), and partition on a barrier (shot noise). The shot noise we have derived corresponds to the variance of a binomial (or poissonian in the limit of low transmission) law for the number of transmitted and reflected particles. Indeed for each measurement this number is either 1 or 0, due to the Fermi statistics. But in order to have informations about a statistical phase different from 0 (bosons) π (fermions), we need to make two-particle collisions with interferometers. That is what we will detail next.

1.4.5 HOM experiment to reveal the statistics

Now we consider an experiment in which two particles x and y collide on a scatterer, and each of these particles have two possible outputs (it is either transmitted or reflected). These particles can be either bosons, fermions or more exotic particles such as anyons. The anyons are quasi-particles that appear in the fractional quantum Hall regime, when applying a strong perpendicular field to the 2D conductor. The physics of the Integer and Fractional quantum Hall will be detailed in Chapter 2. Here we consider the general case in which the spatial exchange of two particles gives rise to a phase $e^{i\theta}$. If we call (1) and (2) the two branches of the interferometer and $a(x, y)$ the 2-particle wave function with particle x in (1) and particle y in (2), we have that: $a(x, y) = e^{i\theta(y,x)}a(y, x)$. The physical situation is illustrated in figure 1.4. We first assume that we have perfect sources, such that there is always one particle incident on each branch. It follows that: $|a(x, y)|^2 + |a(y, x)|^2 = 1$. In view of the last two equations, we have: $|a(x, y)|^2 = |a(y, x)|^2 = 1/2$.

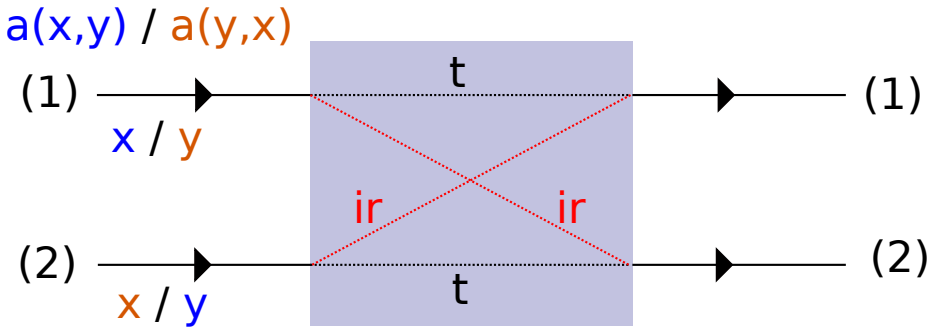

FIGURE 1.4: 2-particles collider with scattering amplitudes t and ir for particles x and y. The two possible initial situation are illustrated with an amplitude probability $a(x,y)$ and $a(y,x)$.

We call $P(x,y)$ the probability for having particle x in output (1) and particle y in output (2) and $P(xy,0)$ (resp. $P(0,xy)$) the probability of having both particles in output (1) (resp. (2)). Let's calculate these probabilities knowing the scattering matrix elements t and ir and taking $T = t^2 = 1/2, R = r^2 = 1/2$:

$$P(x,y) = |a(x,y)t^2 - a(y,x)r^2|^2 = |a(x,y)|^2|t^2 - r^2e^{i\theta}|^2 = \frac{1}{4}(1 - cos\theta) \tag{1.8a}$$

$$P(y,x) = |a(y,x)t^2 - a(x,y)r^2|^2 = |a(x,y)|^2|t^2e^{-i\theta} - r^2|^2 = \frac{1}{4}(1 - cos\theta) \tag{1.8b}$$

$$P(0,xy) = |-irt(a(y,x) + a(x,y))|^2 = r^2t^2|a(x,y)|^2|1 + e^{i\theta}|^2 = \frac{1}{4}(1 + cos\theta) \tag{1.8c}$$

$$P(xy,0) = P(0,xy) = \frac{1}{4}(1 + cos\theta) \tag{1.8d}$$

We can check that the sum of all the output configurations probabilities is equal to 1. From equations (1.8) we can calculate the mean value and the variance of the particle number N_1 and N_2 in branches (1) and (2) :

$$\langle N_1 \rangle = P(x,y) + P(y,x) + 2P(xy,0) = \frac{1}{2}(1 - cos\theta) + \frac{1}{2}(1 + cos\theta) = 1 \tag{1.9a}$$

$$\langle N_1^2 \rangle = P(x,y) + P(y,x) + 4P(xy,0) = \frac{1}{2}(1 - cos\theta) + (1 + cos\theta) \tag{1.9b}$$

$$\langle (\Delta N_1)^2 \rangle = \langle N_1^2 \rangle - \langle N_1 \rangle^2 = \frac{1}{2}(1 + cos\theta) \tag{1.9c}$$

We can easily find the same results for the variable N_2. As explained before, for an electronic systems (ie for fermions or anyons), the current PSD is directly related to the variance (or fluctuations) of particle number in each branch. In this experiment, we thus see that the statistical phase directly appear in the shot noise expression. For fermions, $\theta = \pi$ and the fluctuations of N_1 and N_2 (or "shot noise") vanish. Indeed, because of Pauli exclusion principle, the fermions make perfect anti-bunching, so we would always have $N_1 = N_2 = 1$. For bosons, $\theta = 0$ and the shot noise reaches its

maximum value as bosons make perfect bunching: the situation would be similar to the partition of 2 particles on a barrier ($N_1 = 0$ or 2, $N_2 = 0$ or 2). Let's now calculate the cross-correlation $\Delta N_1 \Delta N_2$:

$$\langle \Delta N_1 \Delta N_2 \rangle = \langle N_1 N_2 \rangle - \langle N_1 \rangle \langle N_2 \rangle = \frac{1}{2}(1 - cos\theta) - 1 = -\frac{1}{2}(1 + cos\theta) \tag{1.10}$$

As we have ignored the fluctuations of the incident particles, we find again (similarly to paragraph 1.4.4) that :

$$\langle (\Delta N_1)^2 \rangle = \langle (\Delta N_2)^2 \rangle = -\langle \Delta N_1 \Delta N_2 \rangle$$

In other words, the cross and the auto-correlations contains the same information about the particle statistics. Now let's consider that the sources from which particle x and y are emitted are noisy and emit particles with a probability $p < 1$ (that is the same for both sources), such that: $|a(x,y)|^2 = |a(y,x)|^2 = p$. Making the same calculations than before, we find:

$$P(x,y) = P(y,x) = \frac{p}{2}(1 - cos\theta)$$
$$P(0,xy) = P(xy,0) = \frac{p}{2}(1 + cos\theta)$$

which leads to :

$$\langle N_1 \rangle = \langle N_2 \rangle = 2p$$
$$\langle N_1^2 \rangle = \langle N_2^2 \rangle = p(1 - cos\theta) + 2p(1 + cos\theta) = p(3 + cos\theta)$$
$$\langle (\Delta N_1)^2 \rangle = \langle (\Delta N_2)^2 \rangle = \langle N_1^2 \rangle - \langle N_1 \rangle^2 = p(3 - 4p + cos\theta)$$
$$\langle \Delta N_1 \Delta N_2 \rangle = -p(1 + cos\theta)$$

We notice again that the cross-correlation term originates from the partition of particles that collide, whereas the auto-correlation also contains a part due the fluctuations of the source emitting particles. In paragraph 1.4.4, the fluctuations of the source were due to the finite temperature. Here, they can also be due to any noisy process of emission (such as poissonian sources). The sum of the auto and cross correlation term gives the fluctuations of the source (the noise we would have with a perfect transmission $D = 1$):

$$\langle \Delta N_1 \Delta N_2 \rangle + \langle (\Delta N_1)^2 \rangle = 2p(1 - 2p)$$

$2p$ is the probability that two particles collide on the scatterer (for perfect sources, $p = 1/2$), thus this term is similar to the $f(1 - f)$ thermal noise.
We emphasize that the cross-correlation cancels in the case of fermions, and is maximal for bosons. These results are coherent with the results of previous works [37], although

we used a different approach. But contrary to previous work (that were made for weak transmission probabilities only), we find a sub-poissonian noise that becomes poissonian for fermions. In the general case, the cross-correlation has a smaller value with noisy sources than with perfect sources. We will see that an anyon source is always noisy, which justify this last study. Indeed, as anyons are between bosons and fermions they inherit of the bosonic character which is known to make photon sources intrinsically noisy. Revealing the anyonic statistics is of central interest and is a motivation for this work.

Until now we have assumed that both particles always reach the collider at the same time. With only DC voltages, we would not have any temporal reference to ensure such situation. This is why we need a time-controlled particle emission for both sources, that would allow us to modify the time delay between the two particles' arrivals (or in other world, the overlap between the two particle wave functions). Modifying this delay, we could switch from a classical regime where the shot noise is independent of the particle statistics, to the quantum regime described above. If we call J the spatial recovery between the two wave functions incident on the scatterer, we can show (inspired by the review [38]) that the cross correlation (for perfect sources) becomes:

$$\langle \Delta N_1 \Delta N_2 \rangle = -\frac{1}{2}(1 + |J|^2 cos\theta)$$

Thus we can observe a minimum of noise when $|J| = 1$, and this minimum depends on the statistical phase θ. The $|J|$-dependence of the shot noise can thus give access to the statistical phase θ. It has been measured for fermions with a particular shape of incoming wave functions (called "levitons") in Ref [29]. We call this type of experiments "Hong-Ou-Mandel" (HOM) in analogy with the experiment made in [26] with photons.

The aim of this thesis is to make HOM experiments in the Integer and Fractional Quantum Hall regime. Although they give intuitive explanations, the results for shot noise derived in this chapter cannot be easily applied to our physical systems because of some reasons:
- Calculating the particle number fluctuation imply to use a one particle picture, which is not valid for fermions that interact with Coulomb interactions (in particular for strongly correlated systems such as the fractional quantum Hall effect).
- When we have to deal with time-dependent transport, we have non-stationary processes, such that the number of transmitted and reflected particles can not be calculated as easily. We have to use an appropriate formalism.
- The energy-dependence of the tunneling probability can lead to deviations from the last HOM experiments predictions.

We will treat these different points in the next chapters, starting with the physics of the Integer and Fractional Hall effect (and the creation of anyons). We will then explain how this regime can be reached experimentally, and describe the DC electronic transport in such setups. Also, we will present two different formalisms for treating the time-dependent transport, and present some theoretical predictions for the HOM experiments. The sample used in this PhD work will not allow us to make HOM experiments with anyons but only with fermions, that is the first step. After presenting the experimental setup and measurements principle, we will end by presenting the experimental results and discuss their interpretation.

Chapter 2

Physics in strong magnetic field

2.1 The classical Hall effect

Many figures and arguments of this chapter are taken from the David Tong's lecture [39] on Quantum Hall effect. The reader can refer to it for a deeper comprehension of the subject.

The original, classical Hall effect was discovered in 1879 by Edwin Hall. It is a simple consequence of the motion of charged particles of a 2D system in a perpendicular magnetic field. Electrons with charge $-e$ and mass m are accelerated by an electric field $\mathbf{E}$ and slowed down by collision on impurities (phonons or other electrons). The resulting equation of motion is:

$$m\frac{d\mathbf{v}}{dt} = -e\mathbf{E} - e\mathbf{v} \wedge \mathbf{B} - m\frac{\mathbf{v}}{\tau} \tag{2.1}$$

where τ is the mean scattering time (the average time between collisions). We are interested on equilibrium solution of equation (2.1). The velocity $\mathbf{v}$ of electrons must then satisfy:

$$\mathbf{v} + \frac{e\tau}{m}\mathbf{v} \wedge \mathbf{B} = -\frac{e\tau}{m}\mathbf{E} \tag{2.2}$$

The current density $\mathbf{J} = -en\mathbf{v}$, where n is the electronic density, can thus be written in matrix notation:

$$\begin{pmatrix} 1 & \omega_B\tau \\ -\omega_B\tau & 1 \end{pmatrix} \mathbf{J} = \frac{e^2 n\tau}{m}\mathbf{E} \tag{2.3}$$

where $\omega_B = eB/m$ is called the *cyclotron frequency*. We note that in presence of a magnetic field, the resisitivity, defined as: $\rho\mathbf{J} = \mathbf{E}$, is not a scalar but a matrix. From equation (2.3) we get :

$$\rho = \frac{1}{\sigma_D}\begin{pmatrix} 1 & \omega_B\tau \\ -\omega_B\tau & 1 \end{pmatrix} \tag{2.4}$$

where $\sigma_D = e^2 n\tau/m$ is the conductivity without magnetic field. We can also get the conductivity σ matrix simply by inverting the matrix ρ:

$$\sigma = \rho^{-1} = \frac{\sigma_D}{1+\omega_B^2\tau^2}\begin{pmatrix} 1 & -\omega_B\tau \\ \omega_B\tau & 1 \end{pmatrix} \tag{2.5}$$

The off-diagonal terms are responsible for the Hall effect and can be understood with simple argument: let's first switch on only an electric field in the x direction such that we get a current $\mathbf{J}$ flowing in the same direction. The physical situation is illustrated below. By switching on the magnetic field, an electric field $\boldsymbol{E_y}$ perpendicular to $\mathbf{J}$ is

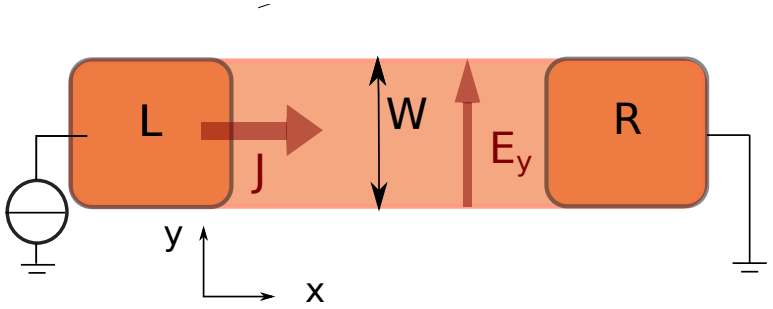

FIGURE 2.1: Classical Hall bar : we impose a current J flowing in the x direction. In the presence of a magnetic field, an electric field perpendicular to J is created: it is responsible for the Hall voltage.

developed in order to compensate the Lorentz forces: $\boldsymbol{E_y} = \frac{1}{ne}\mathbf{J} \wedge \mathbf{B}$. This gives the off-diagonal terms: $\sigma_{xy} = \frac{eB}{ne^2}$, that have the particularity of being independent of the scattering time τ (thus on microscopic properties of the sample). Another interesting property is that they are independent of the geometry factors of the sample, such that the transverse resistance R_{xy} and the transverse resistivity ρ_{xy} coincides. To see this, let's consider a sample of width W in the y-direction. The transverse resistance is:

$$R_{xy} = \frac{V_y}{I_x} = \frac{WE_y}{WJ_x} = \frac{E_y}{J_x} = \rho_{xy}$$

This is a point to keep in mind and will be also important in the universality and precision of the quantum Hall resistance. In contrast, if we measure the longitudinal resistance R_{xx} we have to divide by the appropriate lengths to extract the resistivity ρ_{xx}.

The classical predictions for the transverse and parallel resistivity are thus :

$$\rho_{xx} = \frac{m}{ne^2\tau} \quad \text{and} \quad \rho_{xy} = \frac{B}{ne}$$

We note that ρ_{xx} only depends on the scattering time and goes to zero when τ increases, as scattering processes become less and less important. If we plot the two resistivities as

a function of the magnetic field, then our classical expectation is that they should look as the figure 2.2.

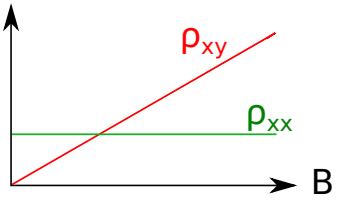

FIGURE 2.2: transverse and longitudinal resistivities

2.2 The Integer Quantum Hall effect

The first experiments exploring the quantum regime of the Hall effect were performed in 1980 by von Klitzing [40]. At low enough temperature, the two resistivities look like this:

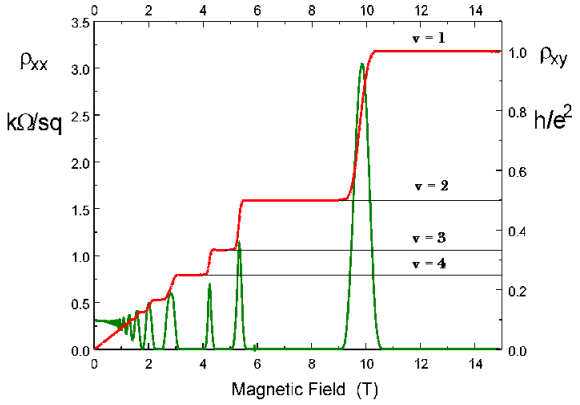

FIGURE 2.3: Integer quantum Hall effect ([1])

Both the Hall resistivity ρ_{xy} and the longitudinal resistivity ρ_{xx} exhibit interesting behaviour, very different from the classical predictions. Perhaps the most striking feature in the data is the that the Hall resistivity ρ_{xy} sits on a plateau for a range of magnetic field, before jumping suddenly to the next plateau. On these plateau, the resistivity takes the value:

$$\rho_{xy} = \frac{h}{\nu e^2}$$

The value of ν is measured with very high accuracy, in various materials and geometries. The quantity $\frac{h}{e^2} = 25.812807k\Omega$, called the *quantum of resistivity* or *von Klitzing constant*, has been the basis for new practical standard for electrical resistance.

When ρ_{xy} sits on a plateau, the longitudinal resistivity vanishes: $\rho_{xx} = 0$. It spikes only when ρ_{xy} jumps to the next plateau. We emphasize that when $\rho_{xy} \neq 0$, $\rho_{xx} = 0$ implies

$\sigma_{xx} = 0$. This weird property come actually from the Drude model: if $\tau \to \infty$, $\rho_{xx} = 0$, and the current is flowing perpendicular to the electric field, so $\mathbf{E}.\mathbf{J} = 0$. The fact that this quantity vanishes means that we have a steady current flowing without doing any work and, correspondingly, without any dissipation. This is the meaning of $\rho_{xx} = 0$. In contrast, $\sigma_{xx} = 0$ simply means that no current is flowing in the x-direction.

To understand the passage from the classical Hall effect to the quantum Hall effect, we have to recall the equations of motion of an electron with a magnetic field:

$$m\frac{d\mathbf{v}}{dt} = -e\mathbf{v} \wedge \mathbf{B} \tag{2.6}$$

When the magnetic field points in the z-direction, so that $B = (0, 0, B)$, and the particle moves only in the transverse plane, so $v = (\dot{x}, \dot{y}, 0)$, the general solution of (2.6) is:

$$x(t) = X - R\sin(\omega_B t + \Phi) \qquad y(t) = Y + R\cos(\omega_B t + \Phi) \tag{2.7}$$

We see that the particle moves in a circle. The centre of the circle, (X, Y), the radius of the circle R and the phase Φ are all integration constants. In contrast, the frequency at which the particle goes around the circle is fixed, and given by $\omega_B = eB/m$. It is called the *cyclotron frequency*. If we solve the equations of motion in presence of an electric field $\mathbf{E}$, we find that the center (X, Y) of the orbit now drifts along the equipotential lines. The drift velocity $v_D = (\dot{X}, \dot{Y})$ is given by :

$$\boldsymbol{v_D} = \frac{\mathbf{B} \wedge \mathbf{E}}{|\mathbf{B}|^2} \tag{2.8}$$

The trajectory of an electron can thus be decomposed into a cyclotron orbit and a drift of the center of the orbit, as illustrated in figure 2.4.

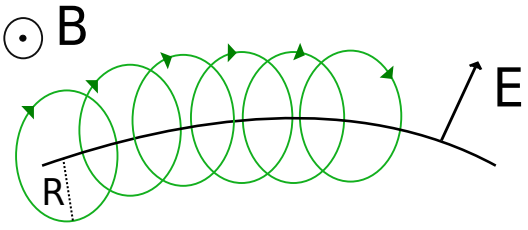

FIGURE 2.4: Trajectory of an electron under an electromagnetic field: the center of the orbit drifts along equipotential lines

The radius R is proportional to the velocity: $R = vm/eB$. Thus the quantization of the kinetic energy is equivalent to the quantization of the radius R of the orbit. When we increase the magnetic field, this radius decreases and the electron can make one entire cyclotron orbit without scattering events: $\omega_B \tau \geq 1$. Another consequence of increasing the magnetic field is that the energy scale $\hbar\omega_B$ becomes much higher than the

temperature. When both these conditions are satisfied (over a critical field $B_c = h/e\tau$) the quantization of the kinetic energy of electrons becomes visible. The critical field from which we can observe the quantum Hall effect is higher for dirty samples than for clean samples. However, we will see that we also need disorder to observe the plateaux of resistance.

2.2.1 Landau levels

We will be interested in large magnetic fields where large energies are needed to flip the spin. This means that, if we restrict to low energies, the electrons act as if they are effectively spinless. We will thus neglect the spin of electrons in this discussion.
In the presence of a magnetic field, the two canonical conjugate variables (derived from the Lagrangian) are: $\mathbf{x}$ and $\mathbf{p} = \dot{\mathbf{x}} - e\mathbf{A}$, where $\mathbf{A}$ is the vector potential associated to the magnetic field: $\mathbf{B} = \mathbf{rot}\mathbf{A}$. Of course, the definition of $\mathbf{A}$ is not unique. As emphasized, when the magnetic field increases, we need to treat the problem with quantum mechanics formalism, so that $\mathbf{x}$ and $\mathbf{p}$ become quantum operators. The fact that they are canonical means that:

$$[x_i, p_j] = \delta_{ij} \quad and \quad [x_i, x_j] = [p_i, p_j] = 0 \tag{2.9}$$

The one-particle Hamiltonian is :

$$H_0 = \frac{1}{2m}(\mathbf{p} + e\mathbf{A})^2 = \frac{1}{2m}\boldsymbol{\pi}^2 \tag{2.10}$$

Since the particle is restricted to lie in the plane, we write $\mathbf{x} = (x, y)$. Meanwhile, we take the magnetic field to be constant and perpendicular to this plane, $\mathbf{B} = B\mathbf{z}$. We have also defined the quantum operator: $\boldsymbol{\pi} = m\dot{\boldsymbol{x}} = \mathbf{p} + e\mathbf{A}$. The commutation rules derived from (2.9) are:

$$[\pi_x, \pi_y] = -ie\hbar B \tag{2.11}$$

Thus π_x and π_y are conjugate variables. We can identify them to the momentum P and the position X of a harmonic oscillator. This motivates the definition of raising and lowering operators, entirely analogous to those that we use in the harmonic oscillator:

$$a = \frac{1}{\sqrt{2e\hbar B}}(\pi_x - i\pi_y) \quad and \quad a^\dagger = \frac{1}{\sqrt{2e\hbar B}}(\pi_x + i\pi_y) \tag{2.12}$$

The commutation rules for $\boldsymbol{\pi}$ give:

$$[a, a^\dagger] = 1 \tag{2.13}$$

which are precisely the commutation relations obeyed by the raising and lowering operators of the harmonic oscillator. Written in terms of these operators, the Hamiltonian (2.10) even takes the same form as that of the harmonic oscillator:

$$H_0 = \hbar\omega_B(a^\dagger a + \frac{1}{2})$$

where $\omega_B = eB/m$ is the cyclotron frequency that we met previously. We can construct the eigenfunctions of H_0 as for the harmonic oscillator: from the ground state $|0\rangle$ obeying $a|0\rangle = 0$, we get the rest of the eigen-functions by acting with $a^\dagger$: $|n\rangle = (a^\dagger)^n|0\rangle$. Using the commutation rules (2.13), we can show that the state $|n\rangle$ (with n integer) has energy:

$$E_n = \hbar\omega_B(n + \frac{1}{2}) \tag{2.14}$$

These equally spaced energy levels are called *Laudau levels*. However, contrary to the harmonic oscillator levels, these are highly degenerated. To see this, let's define the center of orbit operators, that we derive from the classical results:

$$X = x(t) + R\sin(\omega_B t + \Phi) = x - \dot{y}/\omega_B = x - \pi_y/m\omega_B$$
$$Y = y(t) - R\cos(\omega_B t + \Phi) = y + \dot{x}/\omega_B = x + \pi_x/m\omega_B$$

From the commutation rules (2.11) we get:

$$[X, Y] = il_B^2 \tag{2.15}$$

where l_B is the magnetic length $l_B^2 = \hbar/eB$. The Heisenberg uncertainty principle now means that we cannot localise states in both the X coordinate and the Y coordinate. In general, the uncertainty is given by:

$$\Delta X \Delta Y = 2\pi l_B^2$$

A counting of the states then comes from taking the plane and parcelling it up into regions of area $2\pi l_B^2$ (that is the area occupied by one quantum state). The number of states in an area A is then

$$N = \frac{A}{2\pi l_B^2} = \frac{eBA}{h}$$

which gives the number of electrons per Landau levels (LL), or the degeneracy of each LL. The advantage of this approach is that is does not require any choice of magnetic gauge.

When turning on an electric field in the plane (such as the electric field on the edge confining the electrons), the translational invariance is broken, leading to gapless states

called edge states. To understand their formation in a rectangular sample, it is easier to work in a particular gauge.

2.2.2 The Landau gauge

The Landau gauge is useful for rectangular geometries. It correspond to the choice: $\mathbf{A} = xB\mathbf{y}$. By replacing this value of A in the Hamiltonian (2.10) and by looking for solutions invariant under y translation $\Phi_k(x, y) = e^{iky} f_k(x)$, we can show that H acts as:

$$H\Phi_k(x, y) = H_k\Phi_k(x, y)$$

where H_k is the Hamiltonian for a harmonic oscillator in the x direction, with the center displaced from the origin:

$$H_k = \frac{1}{2m}p_x^2 + \frac{m\omega_B^2}{2}(x + kl_B^2)^2$$

The momentum in the y direction, k, has turned into the position of the harmonic oscillator in the x direction, which is now centred at $x = kl_B^2$. The energy eigenvalues are again given by (2.14). By taking into account the finite length of the sample of x direction, we can recover the degeneracy of each LL: $N = \frac{eBA}{h}$.

But now we could also write down the explicit wave functions $\Phi_{n,k}(x, y)$ built from the solutions for a harmonic oscillator. They look like strips in the y direction but are localized in the x direction around $x = -kl_B^2$.
Let's now add a confining potential $V(x)$ to the Hamiltonian (2.10). If the potential is smooth over distance scales l_B, then for each state labeled by (n, k), we can Taylor expand the potential around its location $x_k = -kl_B^2$: $V(x) = V(x_k) + \frac{\partial V}{\partial x}(x - x_k)$. Writing $E = \frac{\partial V}{\partial x}$, we can show that we get again a Hamiltonian of a harmonic oscillator in the x direction. The new eigenfunctions have a shifted wave packet center:

$$\Phi'_{n,k}(x, y) = \Phi_{n,k}(x - mE/eB^2, y)$$

and the eigenvalues now depend on k:

$$E_{n,k} = \hbar\omega_B(n + 1/2) + eEkl_B^2 + C$$

where C is only a constant. This means that the states now drift in the y direction, with a velocity given by:

$$v_y = -\frac{1}{eB}\frac{\partial V}{\partial x}$$

Each wave function, labeled by momentum k, sits at different x positions $x = -kl_B^2$ and thus has a different drift velocity. In particular the modes at each edge are both chiral, travelling in opposite directions: $v_y > 0$ on the left, and $v_y < 0$ on the right. The states localised in the center (the bulk) have zero drift velocity as $\frac{\partial V}{\partial x} = 0$ in this region, unless we consider the potential caused by the disorder.

2.2.3 Conductance quantization

Let's now calculate the current flowing in the y direction when all the states of the first LL are occupied. We do this by introducing the chemical potential E_F . The states are labelled by y-momentum k but, as we have seen, this can equally well be thought of as the position of the state in the x-direction. This means that we are justified in drawing the filled states like this:

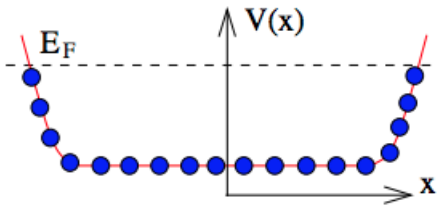

Now we introduce a potential difference $\Delta\mu$ between the two edges of the sample. As shown previously, this electric field tilts the Landau levels so that the effective potential looks like that

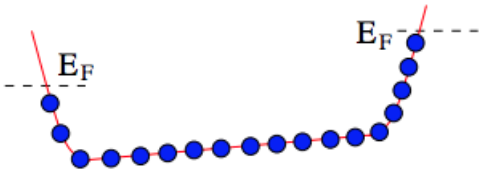

To compute the resulting current we simply need to sum over all filled states. But, at the level of our approximation, this is the same as integrating over x:

$$I_y = -e \int \frac{dk}{2\pi} v_y(k) = \frac{e}{2\pi l_B^2} \int dx \frac{1}{eB} \frac{\partial V}{\partial x} = \frac{e}{2\pi\hbar} \Delta\mu \tag{2.16}$$

The Hall voltage is $eV_H = \Delta\mu$, giving us the hall conductivity:

$$\sigma_{xy} = \frac{I_y}{V_H} = \frac{e^2}{2\pi\hbar}$$

This picture suggests that all the filled state contribute to the current as they have non-zero velocity. However, the real potential shape is more complicated because of impurities in the sample. This create localized states that will not contribute to the current. But the interesting aspect about calculation (2.16) is that whatever the shape of the effective potential, the resulting current I_y, and thus the Hall conductance σ_{xy}, remains the same.
The above discussion can easily be generalized for ν filled Landau levels. As long as the chemical potential E_F lies between Landau levels, we have ν filled LL, like this:

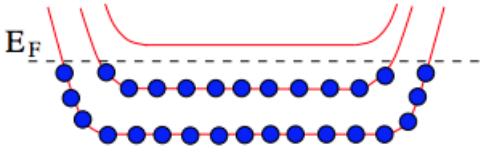

The number of filled LL ν is called the filling factor. Correspondingly, there are ν chiral mode on each opposite edge (also called edge channels). We find the current in presence of a difference of potential $\Delta\mu$ between the two edges to be: $I_y = \nu\frac{e}{2\pi\hbar}\Delta\mu$. This leads to the quantization of the transverse conductance:

$$\sigma_{xy} = \nu\frac{e^2}{2\pi\hbar}$$

However, this quantization should happen only for magnetic fields corresponding to an integer filling factor $\nu = nh/eB$, where n is the electronic density. Thus this is not enough to understand the presence of plateaux of resistance visible in figure 2.3.

2.2.4 The role of disorder

In this discussion we do not make any gauge choice. In absence of external potential, we emphasize that the center of orbit coordinates are constants of motion. Indeed, using the definition of (X, Y) coordinates and the expression (2.10) of H_0, we can check that under time evolution, we have

$$i\hbar\dot{X} = [X, H_0] = 0 \quad and \quad i\hbar\dot{Y} = [Y, H_0] = 0$$

The effect of disorder can be treated by adding an arbitrary potential $V(\mathbf{x})$ to the Hamiltonian H_0, such as $H = H_0 + eV(\mathbf{x})$. Now the (X, Y) operators are not constants

of motion anymore:

$$i\hbar\dot{X} = [X, H] = [X, eV(\mathbf{x})] = \frac{i\hbar}{B}\frac{\partial V}{\partial y} \tag{2.17}$$

$$i\hbar\dot{Y} = [Y, H] = [Y, eV(\mathbf{x})] = \frac{i\hbar}{B}\frac{\partial V}{\partial x} \tag{2.18}$$

We find the same result as in the classical case (equation (2.8)): the center of the cyclotron orbits drifts along equipotentials with a drift velocity

$$\boldsymbol{v_D} = \frac{\mathbf{B} \wedge \mathbf{E}}{|\mathbf{B}|^2}$$

We assume that the potential V varies smoothly enough so that the cyclotron orbit takes place in a region of constant potential, such that: $\frac{\partial V}{\partial x} = \frac{\partial V}{\partial X}$ and $\frac{\partial V}{\partial y} = \frac{\partial V}{\partial Y}$. We can then draw a schematic of center of orbit trajectory in presence of disorder: We see that

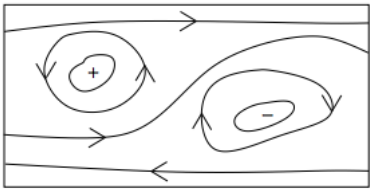

FIGURE 2.5: The localisation of states due to disorder. The drawn lines correspond to equipotentials.

localized states inside the bulk do not contribute to the current in the y-direction. We assume also that the strength of disorder is small relative to the splitting of the Landau levels: $V(\mathbf{x}) << \hbar\omega_B$. The energy spectrum in the presence of this weak disorder is the expected to change the quantized Landau levels from the familiar picture in the left-hand figure 2.6, to the more broad spectrum shown in the right-hand figure 2.6. Let's assume

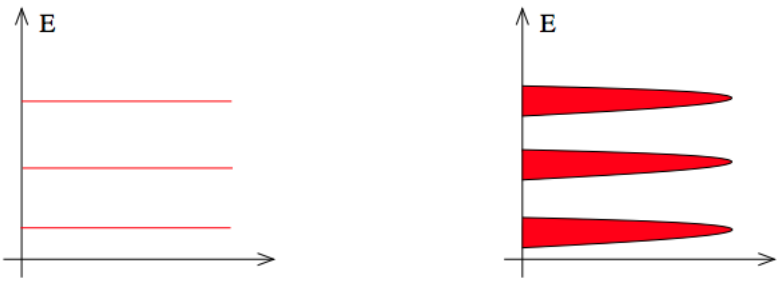

FIGURE 2.6: Energy spectrum without disorder (left-figure) and with disorder (right-figure)

that the Fermi energy sits at the second LL. When we decrease the magnetic field, the energy gap between LL decreases as well as the degeneracy of each LL. As the electron density is fixed, this means that we have to populate new available states. However, rather than directly populating the next LL, we will populate some localized states induced by the disorder. While populating these states, the value of the conductance is not modified: this is the explanation for the presence of plateaux in figure 2.3.

However we should revisit our argument for the conductance quantization, that we derived without taking into account this effect of disorder, and assuming that all the filled states contribute to the current. Now we know that many of these states are localised by impurities and do not transport charge. But remarkably, current carried by the extended states increases to compensate for the lack of current transported by localised states. This ensures that the resistivity remains quantized despite the presence of disorder. In order to understand why through a more solid argument, we need to introduce another gauge.

2.2.5 The symmetric gauge

We come back to the problem of electrons submitted to a magnetic field only, so to the Hamiltonian of (2.10). We have already noted that the center of orbit operators (X, Y) both commute with H_0, but not with each other (equation (2.15)). We can thus define a second pair of raising and lowering operators:

$$b = \sqrt{\frac{eB}{2\hbar}}(Y - iX) \quad and \quad b^\dagger = \sqrt{\frac{eB}{2\hbar}}(Y + iX) \tag{2.19}$$

These two obey:

$$[b, b^\dagger] = 1$$

It is this second pair of creation operators that provides the degeneracy of the Landau levels. To find the eigenfunctions of H_0, we will choose a particular gauge in which $[a, b] = 0$: the *symmetric gauge*. It corresponds to the choice:

$$\mathbf{A} = -\frac{1}{2}\mathbf{r} \wedge \mathbf{B} = -\frac{yB\mathbf{x}}{2} + \frac{xB\mathbf{y}}{2}$$

This choice of gauge does preserve rotational symmetry about the origin. This means that angular momentum is a good quantum number. In this gauge the guiding center coordinates are:

$$X = x/2 - p_y/eB, \quad Y = y/2 + p_x/eB \tag{2.20}$$

From which we deduce:

$$[\pi_x, X] = [\pi_y, Y] = [\pi_x, Y] = [\pi_y, X] = 0$$

Thus we have: $[a, b] = 0$. It is now easy to write the eigenfuctions of H_0. We first define a ground state $|0, 0\rangle$ to be anhilated by both lowering operators, so that: $a|0, 0\rangle = b|0, 0\rangle = 0$. We can show that the states $|n, m\rangle$ for integers m, n defined as

$$|n, m\rangle = \frac{a^{\dagger n} b^{\dagger m}}{\sqrt{n!m!}}|0, 0\rangle$$

are eigenfunctions of both H_0 and $b^\dagger b$:

$$H_0|n, m\rangle = \hbar\omega_B(n + \frac{1}{2})$$
$$b^\dagger b|n, m\rangle = m|n, m\rangle$$

Now let's try to write these wavefunctions, focusing on the first LL, $n = 0$, since this will be of primary interest when we come to discuss the fractional quantum Hall effect. The states in the lowest LL (that we sometimes write LLL) are annihilated by a, meaning $a|0, m\rangle = 0$. We introduce the complex coordinates:

$$z = x - iy \quad \text{and} \quad \bar{z} = x + iy$$

as well as the corresponding derivatives:

$$\partial_z = \frac{1}{2}(\partial_x + i\partial_y) \quad \text{and} \quad \partial_{\bar{z}} = \frac{1}{2}(\partial_x - i\partial_y)$$

In term of complex coordinates, a and $a^\dagger$ take the form

$$a = -i\sqrt{2}(l_B\partial_{\bar{z}} + \frac{z}{4l_B}) \quad and \quad a^\dagger = -i\sqrt{2}(l_B\partial_z - \frac{\bar{z}}{4l_B})$$

The lowest Landau level wavefunctions $\Phi_{LLL}(z, \bar{z})$ are then easily solved:

$$\Phi_{LLL}(z, \bar{z}) = f(z)e^{-|z|^2/4l_B^2}$$

where $f(z)$ is a holomorphic function. We can construct the specific states $|0, m\rangle$ in the lowest Landau level by similarly writing b and $b^\dagger$ as differential operators. We find

$$b = -i\sqrt{2}(l_B\partial_z + \frac{\bar{z}}{4l_B}) \quad \text{and} \quad b^\dagger = -i\sqrt{2}(l_B\partial_{\bar{z}} - \frac{z}{4l_B})$$

The ground state is annihilated by both a and b. There is a unique such state given by $|0, 0\rangle = \Phi_{LLL,m=0}(z, \bar{z}) = e^{-|z|^2/4l_B^2}$. We can now construct the higher states by acting

with $b^\dagger$. Each time we do this, we pull down a factor $z/2l_B$. This gives us a basis of lowest LL wavefunctions in terms of holomorphic monomials

$$\Phi_{LLL,m}(z,\bar{z}) = \left(\frac{z}{l_B}\right)^m e^{-|z|^2/4l_B^2} \tag{2.21}$$

This particular basis of states has an advantage: these are eigenstates of angular momentum. Indeed we can show that the angular momentum operator is nothing else than $\hbar b^\dagger b$:

$$J = i\hbar(x\partial_y - y\partial_x) = \hbar(z\partial_z - \bar{z}\partial_{\bar{z}}) = \hbar b^\dagger b$$

Then, acting on these lowest LL states we have

$$J\Phi_{LLL,m}(z,\bar{z}) = \hbar m \Phi_{LLL,m}(z,\bar{z})$$

In symmetric gauge, the profiles of the wavefunctions (2.21) form concentric rings. The wavefunction with angular momentum m is peaked on a ring of radius $r = \sqrt{2m}l_B$. This means that on a disc shaped a region of area A, the maximum value of momentum N is given by $A = 2\pi N l_B^2$. As each particle occupy one state, we recover the degeneracy of LL: $N = A/2\pi l_B^2$. The N-particle wave function can be constructed by taking the Slater determinant of the one-particle states (2.21). We obtain:

$$\Phi_{LLL}(z_1,..,z_N) = \prod_{i<j}(z_i - z_j)e^{-\sum_{i=1}^N |z_i|^2/4l_B^2} \tag{2.22}$$

It is interesting to note that this state is always an eigenstate in the presence of an interaction potential of the form $V(z_i - z_j)$. Indeed this form of potential commutes with the relative angular momentum operator $J_{ij} = \hbar b_{ij}^\dagger b_{ij}$, with b_{ij} defined as b before but replacing the variable z replaced by $z_i - z_j$. As $\Phi_{LLL}(z_1,..,z_N)$ is also an eigenfunction of J_{ij}, it remains a good ground state in presence of interactions, as far as the kinetic energy is frozen. In other words, the state (2.22) is stable because the repulsion forces between electrons are compensated by the Lorentz forces.

2.2.6 Laughlin's argument

We now come to our argument for the conductance quantization. As it should not depend on the geometry of the sample, we can consider electrons moving in an annulus as shown in the figure 2.7. This is sometimes called a *Corbino ring*. We apply a voltage around ring with the electromotive force of a time-dependent flux Φ that penetrates the sample. When Φ goes slowly (with a time $T >> 1/\omega_B$) from 0 to $\Phi_0 = h/e$, the induced emf is $V_H = -\partial\Phi/\partial t = \Phi_0/T$. As the change is done suitably slowly, the adiabatic

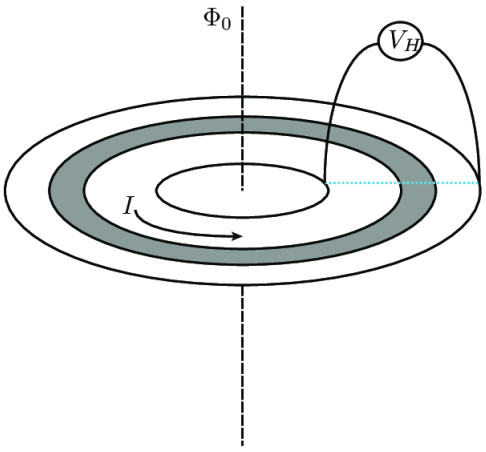

FIGURE 2.7: The Corbino disc ([2]). An emf V_H is induced by slowly introducing a quantum of flux.

theorem ensures that the final energy eigenstate must lie in the same LL as the initial state. The spectrum of H_0 is unaffected by such a modification, but the states (2.21) are affected: each state $\Phi_{LLL,m}$ is shifted to the state $\Phi_{LLL,m+1}$. This means that each state moves outwards, from radius $r = \sqrt{2\pi m} l_B$ to radius $r = \sqrt{2\pi(m+1)} l_B$. The net result is that, if all states in the LL are filled, a single electron is transferred from the inner ring to the outer ring as the flux is increased from $\Phi = 0$ to $\Phi_0 = h/e$. It is simple to check that the same result holds for higher LL. If ν LL are filled, then ν electrons are transferred from the inner to the outer ring. The resulting radial current is : $I = -\nu e/T$, from which we deduce the resisivity:

$$\rho_{xy} = \frac{V_H}{I} = \frac{h}{\nu e^2}$$

This is the result we want: it is the Hall resistivity. Now what happens in presence of disorder? We have shown that the disorder induce localized states in the sample. These states will be unaffected by the insertion of a quantum of flux Φ_0. But an extended state localised at one radius is transformed into an extended state at the next available radius. The presence of disorder means that there are fewer extended states, but this doesn't change the overall conclusion: if all extended states in a given Landau level are filled, then the net effect of adding this quantum of flux is to transport one electron from the inner to the outer edge. Thus as far as extended states exist (we can show that it is always the case), the resistivity is quantized.

Now that we have done a step in the understanding of the integer quantum Hall effect (IQHE), we will focus on the fractional Hall efect (FQHE), that is of particular interest. Indeed it is a strongly-correlated system formed by Coulomb interactions, in which the minimal excitations carry a fraction of charge and have an anyonic statistics.

2.3 The Fractional Quantum Hall effect

It came as a great surprise to the community when, in 1982, plateaux in the Hall resistivity were seen at non-integer filling fractions [3] in a high-mobility 2-dimensional electron gas. These plateaus were seen at filling fraction $\nu = \frac{1}{3}, \frac{2}{3}, \frac{1}{5}, \frac{2}{5}$ in the LL and $\nu = \frac{4}{3}, \frac{5}{3}, \frac{7}{5}$ in higher LL, as well as many others. Around 80 quantum Hall plateaux have been observed. A number of these are shown below:

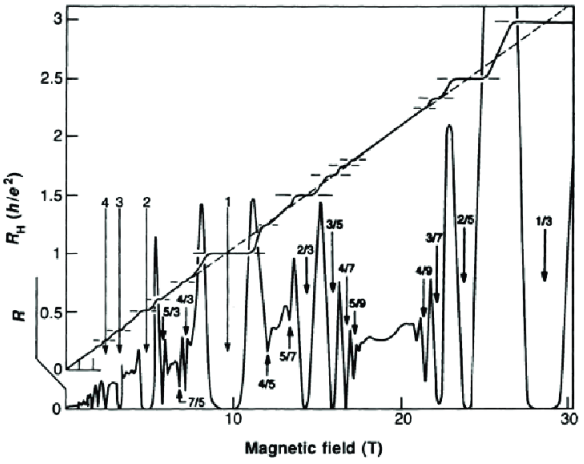

FIGURE 2.8: Integer and Fractional Quantum Hall effect conductance plateaus from [3]

The plateaus localised at $(1/m)e^2/h$ correspond to the formation of so-called "Laughlin's states".

2.3.1 Laughlin's filling factors

2.3.1.1 Many-particle ground state

Interactions between electrons must be playing some role in the formation of these plateaux. However, a direct diagonalisation of the Hamiltonian in presence of Coulomb interactions is almost impossible, especially because of the very high degeneracy of a partially filled LL. The first approach to the fractional quantum Hall effect was due to Laughlin [19], who described the physics at filling fractions $\nu = \frac{1}{m}$ with m an odd integer. Inspired by the many-particle ground state (2.22) derived at filling factor $\nu = 1$, Laughlin's proposal for the ground state wavefunction at filling fraction $\nu = \frac{1}{m}$ is:

$$\Phi_{LLL}(z_1, .., z_N) = \prod_{i<j}(z_i - z_j)^m e^{-\sum_{i=1}^{N}|z_i|^2/4l_B^2} \tag{2.23}$$

To respect the fermionic exchange properties of electrons m must be an odd integer. Being a holomorphic function of the coordinates, this wave function lies in the lowest

LL. The pre-factor vanishes with a zero of order m whenever two electrons come together, providing an efficient reduction of the repulsive Coulomb interaction.
Let's first show that this ground state has the good filling factor. For this we simply notice that the maximum power of each coordinate z_i is $m(N-1)$, which corresponds to the maximum angular momentum of each particle. So the maximal radius (in the thermodynamic limit) is $R = \sqrt{2\pi mN} l_B$ and the area occupied by this ground state is $A = 2\pi mN l_B^2$. As each state occupy an area $2\pi l_B^2$, the number of states in the area A is mN. Thus each electron occupies m quantum states, or the area of m quantum of flux. This gives the filling factor $\nu = \frac{1}{m}$, as promised.

We can show that the Laughlin state of (2.23) is the state that minimizes the energy in presence of Coulomb repulsion. A state with higher power of z_i would also minimize Coulomb interaction as it would be more extended, but it would higher the total angular momentum. Thus it would cost extra energy because of the confining potential. These two contributions (the Coulomb repulsion and the confining potential) make the Laughlin's state a stable state for a certain range of magnetic field. This explains the plateaux observed at filling factors $\nu = \frac{1}{3}, \nu = \frac{1}{5}$... The gap of the fractional Hall effect is due to the fact that in presence of a magnetic field, the relative momentum of two particles has to be an integer. For a deeper discussion, the reader can refer to Girvin's lecture note on Quantum Hall effect [41].

As electrons always interact through Coulomb repulsion, we can wonder why the effects of the Coulomb repulsion more important in the FQHE than in the IQHE. A first explanation is that the FQHE appears for higher magnetic fields. And when the magnetic field increases, the distance between single particles wave functions decreases. Indeed, from the symmetric gauge treatment the distance between a particle in state m and a particle in state $m+1$ is $(\sqrt{2\pi(m+1)} - \sqrt{2\pi m}) l_B$, that is proportional to $1/\sqrt{B}$. Thus the intensity of the Coulomb repulsion increases with the magnetic field.
The second explanation is that as far as the Coulomb repulsion is weak enough not to break the LL, in the $\nu = 1$ case we had "no other choice" for the ground state than (2.22). However for fractional filling factor, the electrons have "more freedom" to rearrange themselves in order to minimize Coulomb repulsion. This leads to the formations of states such as (2.23).

2.3.1.2 Charged excitations

We can now build the excitations of the Laughlin's state (2.23). For example, the wavefunction describing a quasi-hole at position z_0 is

$$\Phi_{LLL}(z_1,..,z_N,z_0) = \prod_{i=1}^{N}(z_i - z_0)\prod_{i<j}(z_i - z_j)^m e^{-\sum_{i=1}^{N}|z_i|^2/4l_B^2} \tag{2.24}$$

This is actually the excited state obtained when we slowly insert a quantum of flux Φ_0 at position z_0. But now, one electron occupy an area that corresponds to m quantum of flux. The quantum Hall system is always incompressible. Thus introducing this quantum of flux, we end up in a new eigenstate where a charge $\frac{-e}{m}$ have been transferred from the inner edge to the outer edge. We can thus repeat the Laughlin's argument of paragraph 2.2.6 to find the Hall resistivity :

$$\sigma_{xy} = \frac{1}{m}\frac{e^2}{2\pi\hbar} \tag{2.25}$$

Considering the excited state (2.24), and calculating the Berry phase associated to a closed trajectory of this hole excitation, we find two type of contributions:
- the first term is the Aharonov-Bohm phase picked up by the hole. It teaches us that it carries a charge $-e/m$.
- the second term tells about the statistics. It teaches us than when exchanging two holes positions, the wave function is affected by a phase factor: $\Phi(z_1,z_2) = e^{2i\pi/m}\Phi(z_2,z_1)$. Thus the quasiparticles have a statistics that is neither fermionic nor bosonic, but an intermediate between both. These quasiparticles created by these minimal excitations of the ground state are called "anyons", and they obey "anyonic" statistics.

Fractional charges at $\nu = 1/3$ [15],[42] and at more complex filling factors $\nu = 2/5$ [43],[16] and $\nu = 2/3$ [44] have already been measured in experiments in which quasiparticles tunnel between two opposite edge states. As it will be shown later, the measurement of the tunneling current as well as its fluctuations (the "shot noise") give access to the fractional charge. The fractional charge have also been measured through photo-assisted transport measurement [18] thanks to the injection of radio-frequency (RF) waves. Indeed, the "photo-assisted" shot noise shows some discontinuities at bias $e^*V_{dc} = \hbar\Omega$, where Ω is the RF pulsation. This is another way to measure the fractional charge, on which we will come back later. Finally, the fractional charge have been also measured through finite frequency shot noise measurements [45].

Regarding the fractional statistics, most efforts have focused on the implementation of single-particle interferometers [46],[47] where the output current is expected to be directly sensitive to the exchange phase. However, despite many experimental attempts

([20],[21],[22],[23]), clear signatures were difficult to obtain, because the observed modulations of the current result not only from the variation of the exchange phase, but also from Coulomb blockade and Aharonov-Bohm interference. A recent experiment [24] provided a clear signature of anyonic statistics using an electronic Fabry-Perot interferometer, and an efficient screening to reduce Coulomb interactions. Recently as well, an experiment [25] based on theoretical predictions [48], have put in clearer evidence the fractional statistics thanks to shot noise measurement in an anyon collider (using the same kind of ideas as the ones developed in section 1.4.4).

2.4 Description of edge states

2.4.1 Filling factors $\nu = 1/m$

In this section we will give a microscopic description for edge states that can be applied for both integer and fractional quantum Hall effect. X.G. Wen has first shown the deep connection between fractional edge channels and the concept of Tomonaga-Luttinger liquids. We will here repeat the phenomenological hydrodynamical approach of Wen in the simple case of a Laughlin state in the bulk, for filling factors $\nu = 1/m$, m odd. The basic idea is that the ground state forms an incompressible disc. The low-energy excitations of this state are deformations which change its shape, but not its area, as illustrated below.

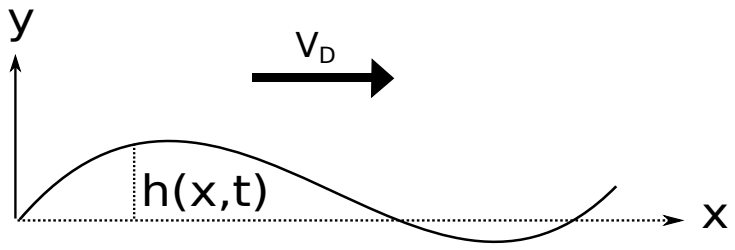

FIGURE 2.9: Edge of a quantum hole droplet. Excitations are described by the propagation of a deformation $h(x,t)$ of the droplet with a drift velocity $v_D = v = E/B$.

We describe the deformations of one edge state through variations of the height $h(x,t) = \frac{\rho(x,t)}{n}$ of the droplet, where n is the electronic density. n is related to the filling factor : $\nu = \frac{nh}{eB}$. $\rho(x,t)$ is the local excess charge per unit length. This deformation is a charged density wave that propagates along the x direction with a drift velocity $v = \frac{E}{B}$, E being the electric field induced by the confining potential $V(x,y)$. In order for this droplet picture to be correct, the confining potential has to be abrupt enough. However, $V(x,y)$ should vary slowly on the length scale of $h(x,t)$, such that we can write: $E =$

$\partial_y V(x,y) \approx V(x,y=0)/h(x)$ (as $\partial_x V(x,y)=0$). The Hamiltonian which describes the edge modes is simply an electrostatic term:

$$H = \frac{1}{2}\int_0^L V(x,y=0)e\rho(x)dx = \frac{1}{2}\int_0^L Eh(x)e\rho(x)dx = \frac{1}{2}\int_0^L v_D B h(x) e\rho(x)dx$$
$$= \frac{e}{2}\int_0^L v_D B\frac{\rho^2(x)}{n}dx = \frac{vh}{2\nu}\int_0^L \rho^2(x)dx$$

It is convenient to transform this Hamiltonian into Fourier space using:

$$\rho(x) = \frac{1}{\sqrt{L}}\sum_k e^{-ikx}\rho_k \quad , \quad H = \frac{vh}{2\nu}\sum_k \rho_k\rho_{-k}$$

Quantization requires first to identify a set of canonical conjugate variables which satisfy Hamiltons equations. Identifying $q_k = \rho_k$ we obtain:

$$\dot{p}_k = -\frac{\partial H}{\partial \rho_k} = -\frac{vh}{\nu}\rho_{-k} \tag{2.26}$$

The continuity equation for this chiral density reads $\dot{\rho}_{-k} = -vik\rho_{-k}$ Integrating over time equation (2.26) one thus get: $p_k = -i\frac{h}{\nu}\frac{\rho_{-k}}{k}$

Quantization is achieved by imposing the commutation relations: $[p_k, q_{k'}] = i\hbar\delta_{k,k'}$. Replacing p_k by its expression, one gets the Kac-Moody commutation relations:

$$[\rho_k, \rho_{k'}] = -\frac{\nu k}{2\pi}\delta_{k',-k} \tag{2.27}$$

Using these commutation rules, we get the time-evolution of the charge density in the Heisenberg picture: $i\hbar\dot{\rho}_k = [H,\rho_k] = v\hbar k\rho_k$. We thus recover the continuity equation. For later purposes, we introduce the Luttinger bosonic field:

$$\rho(x) = \frac{1}{2\pi}\partial_x\Phi(x) \tag{2.28}$$

From this definition and the commutation rules (2.27), we get the commutation rules for the bosonic fields:

$$[\Phi(x),\Phi(y)] = -i\pi\nu sgn(x-y) \tag{2.29}$$

From which we deduce: $[\rho(x),\Phi(y)/\nu] = -i\delta(x-y)$. We can check that the operator $\Psi(x) = \frac{1}{\sqrt{a}}e^{i\Phi(x)/\nu}$, where a is a cut-off distance, has the good property for being an electron anhilation operator:

$$[\rho(x),\Psi^\dagger(y)] = \delta(y-x)\Psi^\dagger(x) \tag{2.30}$$

The anhilation operator $\Psi(x)$ obviously depends on the filling factor. Fermion operators are known to anti-commute, which brings a constraint on this filling factor in order to

ensure that $\{\Psi(x), \Psi(y)\} = 0$. To find this constraint we use the Baker Campbell-Hausdorff relations $e^{iq\Phi(x)}e^{p\Phi(y)} = e^{ip\Phi(y)}e^{iq\Phi(x)}e^{pq[\Phi(x),\Phi(y)]}$, that lead to:

$$\Psi(x)\Psi(y) = e^{-i\frac{\pi}{\nu}sgn(x-y)}\Psi(y)\Psi(x)$$

In order to ensure anti-commutation relations, we need $\nu = 1/m$, with m odd integer. This conclusion is consistent with the Laughlin's filling factor. In the case $m = 1$, we recover the fermionic statistics expected IQHE at $\nu = 1$.

This description of edge states is useful to predict the value of experimental observables such as the tunneling current between two counter-propagating edge states. Indeed the current calculation involves the Green function $G(x,t) = i\langle\Psi^\dagger(x,t)\Psi(0,0)\rangle$, that can be found using the spectral decomposition of the bosonic fields

$$\Phi(x,t) = \phi + Qx + i\sum_{k>0}\sqrt{\frac{2\pi\nu}{Lk}}[a_k e^{ik(x-vt)} + a_k^\dagger e^{-ik(x-vt)}] \tag{2.31}$$

In the last expression, $a_k^\dagger = \sqrt{L/2\pi\nu k}\rho_k$ and $a_k = \sqrt{L/2\pi\nu k}\rho_{-k}$ are creation and anhilation operators that obey $[a_k^\dagger, a_{k'}] = \delta_{k,k'}$. Q is the zero mode operator : $Q = 1/L\int\rho(x)dx$ and ϕ is canonically conjugate to Q. Introducing the boson occupation number $f(k) = \frac{1}{e^{\beta v k}-1}$, where $\beta = 1/T$, we arrive at the following result (see for example Ref [49]):

$$G(x,t) \propto \frac{v}{\pi T}\sinh\left(\pi\frac{T(x-vt)}{v}\right)^{-1/\nu} \tag{2.32}$$

As expressed in equation (2.30), $\Psi^\dagger(x)$ creates one charge e at position x, and the Green function $G(x,t)$ can be used when electrons tunnel between two edges.

Now, how to create a quasiparticle with a fractional charge? The quasi-particle anhilation operator $\Psi_{qp}(x)$ has to be local with respect to the electron anhilation operator $\Psi(x)$. If we write $\Psi_{qp}(x) = e^{ip\Phi(x)}$, the statistical phase of such quasi-particle with respect to an electron is p: $\Psi_{qp}(x)\Psi(y) = e^{i\pi p}\Psi_{qp}(x)\Psi(y)$. Thus p has to be an integer. We can calculate in the same way the Green function associated to quasi-particles propagation. We find:

$$G_{qp}(x,t) \propto \frac{v}{\pi T}\sinh\left(\pi\frac{T(x-vt)}{v}\right)^{-p^2\nu} \tag{2.33}$$

The most dominant tunneling process is for $p = 1$, that is the most common choice in litterature. We can check that $\Psi_{qp}^\dagger(x)$ created a fractional charge $e^* = \nu e = e/m$ at position x:

$$[\rho(x), \Psi_{qp}^\dagger(y)] = \nu\delta(y-x)\Psi_{qp}^\dagger(x) \tag{2.34}$$

Finally, we also recover the fractional statistics as :

$$\Psi_{qp}(x)\Psi_{qp}(y) = e^{i\pi\nu}\Psi_{qp}(y)\Psi_{qp}(x) \tag{2.35}$$

2.4.2 Integer filling factors $\nu > 1$

Wen's approach can be generalized to the case of filling factors $\nu > 1$, where as explained before, we have ν co-propagating edge states on each side of the sample. We thus introduce the charge density operators and the associated bosonic fields for each edge state n : $\rho_n(x,t)$ and $\rho_n(x,t) = \frac{1}{2\pi}\partial_x\Phi_n(x,t)$. The Hamiltonian is now a sum of electrostatic terms due to the deformation of edge states:

$$H = \sum_n \frac{v_n h}{2}\int_0^L \rho_n^2(x)dx \tag{2.36}$$

v_n is the drift velocity of electrons of edge state n. It is linked with the electric field at the edge state position. This Hamiltonian can be derived in a more rigorous way thanks to the bozonisation technique for free fermions. ρ_n and Φ_n obey the same commutation rules as the one given by equations (2.27) and (2.29):

$$[\rho_{n,k}, \rho_{m,k'}] = -\frac{\nu k}{2\pi}\delta_{n,m}\delta_{k',-k}$$
$$[\Phi_n(x), \Phi_m(y)] = -i\pi\nu sgn(x-y)\delta_{n,m}$$

where he have introduced $\rho_{n,k}$, the Fourier components of $\rho_n(x)$. Similarly than before, we define the electron operators associated to the edge state n: $\Psi_n(x) = \frac{1}{\sqrt{a}}e^{i\Phi_n(x)}$. The expression of the Green functions $G_n(x,t) = i\langle\Psi_n^\dagger(x,t)\Psi_n(0,0)\rangle$ in absence of interactions is simple: these are given by equation (2.32), taking $\nu = 1$ and replacing the velocity v by v_n. They lead to a linear tunneling current between two counter-propagating edge states.

Now what happens if we add inter and intra-edge interactions? If we assume that the screening is good enough for the Coulomb potential to be short-ranged, we can write the Hamiltonian as:

$$\begin{aligned} H &= \sum_{n,m}\int dxdy V_{n,m}(x-y)\rho_n(x)\rho_m(y) = \sum_{n,m}\int dxdy V_{n,m}\delta(x-y)\rho_n(x)\rho_m(y) \\ &= \sum_{n,m}\sum_k V_{n,m}\rho_{n,k}\rho_{m,-k} = \sum_j v_j\tilde{\rho}_{n,k}\tilde{\rho}_{m,-k} \end{aligned} \tag{2.37}$$

where $V_{n,m} = U_{n,m} + \delta_{n,m}2\pi v_n$. For the purely chiral case of the IQHE we can express these matrix elements with an orthogonal matrix $q_{n,j}$ so that qq^T=1 and : $V_{n,m}$ =

$\sum_j q_{n,j} v_j q_{j,m}$. The diagonal density operators are thus defined as: $\tilde{\rho}_j(x) = \sum_n q_{n,j}\rho_n(x)$. From the expression of the hamiltonian (2.37) we can check that they propagate at the generalized velocity v_j: $\tilde{\rho}_j(x,t) = \tilde{\rho}_j(x - v_j t)$. We can replace the $\Phi_n(x,t)$ by their expression with respect to the $\tilde{\Phi}_j(x,t)$ in order to calculate the $G_n(x,t)$. We obtain:

$$G_n(x,t) \propto \prod_j \frac{v_j}{\pi T} \sinh\left(\pi \frac{T(x - v_j t)}{v_j}\right)^{-q_{j,n}^2}$$

It is important to note that at low temperature, the correlation function in chiral systems behaves as $G_n(0,t) \propto 1/t$ even in presence of interactions, because $\sum_j q_{j,n}^2 = 1$. The consequence is that the I-V characteristic of the tunneling current is linear even in presence of interactions.

2.4.3 Fractional filling factors $\nu = \frac{m}{2pm\pm1}$

Many different approaches have been proposed to describe the physics at filling factors $\nu = \frac{m}{2pm\pm1}$. One useful approach is the composite fermions theory [50], that makes a match between fractional filling factors of electrons and integer filling factors of "composite fermions" (CF). A CF is the topological bound state of an electron and an even number of quantized vortices, sometimes visually pictured as the bound state of an electron and, attached, an even number of magnetic flux quanta. The magnetic field seen by composite fermions is given by $B^* = B - 2pn\phi_0$, where n is the electronic density, and B the external magnetic field. More accurately, the vortices bound to electrons produce their own geometric phases which partly cancels the Aharonov-Bohm phase due to the external magnetic field, to generate a net geometric phase that can be modeled as an Aharonov-Bohm phase in an effective magnetic field B^*. We define the filling factor ν^* of composite fermions as $\nu^* = n\phi_0/|B^*|$. This gives the following relation between the electron and CF filling factors:

$$\nu = \frac{\nu^*}{2p\nu^* \pm 1}$$

Thus the filling factors $\nu = \frac{m}{2pm\pm1}$ correspond to integer CF filling factors $\nu^* = m$. The interaction between CF themselves is often negligible to a good approximation. Thus the formation of fractional edge channels is equivalent to the one described previously for the integer quantum Hall effect. Moving from the bulk to the edge, each time a CF Landau level crosses the Fermi energy a line of gapless excitation is built. These defines m chiral fractional edge channels. For $\nu = 1/3$, $\nu^* = 1$, leading to the formation of one edge state. For $\nu = 2/3$ and $\nu = 2/5$, we have $\nu^* = 2$, leading to the formation of two edge states.

The composite fermion picture is supported by experimental observations [51]. The

symmetric variations of the Shubnikov-de Has oscillations around $B_{1/2} = 2n\phi_0$ are very similar to that observed around $B = 0$.

The CF approach for edge channels is convenient for pedagogical presentation and gives a fair qualitative representation, but is certainly not complete. To predict the transport properties we need a microscopic description of edge states. A generalization of Wen's approach for $\nu = \frac{m}{2pm\pm1}$ shows that one must have p branches of bosonic modes (consistent with the CF picture). For example , the $\nu = 2/5$ FQH state consists of two droplets, one is the electron condensate with filling factor $\nu_1 = 1/3$ and radius r_1 and the other is the quasiparticle condensate with filling factor $\nu_2 = 1/15$ ($1/3+1/15 = 2/5$) and radius r_2. When $r_1 - r_2 >> l_B$ the two edges are independent. Generalizing the hydrodynamical approach previously described, we can show that there are two branches of the edge excitations whose low energy dynamics is described by:

$$\begin{aligned} [\rho_{n,k}, \rho_{m,k'}] &= -\frac{\nu_m k}{2\pi}\delta_{n,m}\delta_{k',-k} \\ H &= 2\pi \sum_{n,k>0} \frac{v_n}{\nu_n}\rho_{n,k}\rho_{n,-k} \end{aligned} \tag{2.38}$$

where $n = 1, 2$ labels the two branches, and v_n are velocities of edge excitations (that are determined by the effective electric fields from the edge potential and the electrons). In order for the Hamiltonian to be bounded from below, we require $\nu_n v_n > 0$. We find that the stability of the $\nu = 2/5$ FQH state requires both v_n to be positive, so that we have co-propagating edge states.

According to the hierarchical picture the $\nu = 2/3$ FQH state is also formed by two condensates, an electron condensate with filling factor 1 and a hole condensate with filling factor 1/3. Thus we have again two branches of edge excitations but now with *opposite* velocities: we have two counter-propagating states. Experimentally, the existence of fractional edge channels can be probed in transport experiments using the reflection induced by a QPC in a manner similar to the integer case. However, the co or counter-propagating nature of the edge states is more difficult to probe, although it has been the subject of some experimental works [52] [53].

Using the commutation rules of equation (2.38) and the same arguments as section 2.4.1, we find that the electrons operators on the two edges are given by:

$$\Psi_n(x) = e^{i\Phi_n(x)/\nu_n} \quad \text{for} \quad n = 1, 2 \tag{2.39}$$

with $\partial_x \Phi_n(x) = \frac{1}{2\pi}\rho_n(x)$. The electron propagator at zero temperature have the form: $G_n(x,t) = i\langle \Psi_n^\dagger(x,t)\Psi_n(0,0)\rangle \propto \frac{1}{(x-v_n t)^{-1/|\nu_n|}}$.

As we bring the two edges together ($r_1 - r_2 \approx l_B$), the interactions between edges can no longer be ignored. In this case we make the same treatment as in section 2.4.2 to diagonalize the Hamiltonian, and calculate $G_n(x,t)$ using the new eigenmodes. Remarkably, Wen's approach leads to a power law of the electrons propagation function $G_n(0,t)$ that is not modified by the interaction parameters: we always have $G_n(0,t) \propto 1/t^{-1/|\nu_n|}$. The power is determined only by the topological orders of the bulk FQH state. Once we know the electron operators, we can find the quasi-particle operators $\Psi_{qp}(x) = e^{i(p_1\Phi_1(x)+p_2\Phi_2(x))}$ (where Φ_1 and Φ_2 are the eigenmodes of the Hamiltonian with interactions). The $p_{1,2}$ factors are fixed by the fact that $\Psi_{qp}(x)$ and $\Psi(y)$ commute, using the same locality argument as in section 2.4.1. For quasiparticles, we find $G_{qp}(0,t) \propto 1/t^{(n_1\nu_1+n_2\nu_2)}$, where n_1 and n_2 are two arbitrary integers.
We can also determine the charge carried by quasi-particle operators on each edge state. Here we directly give the results:

$$[\rho_1(x), \Psi_{qp}(y)] = \delta(x-y)\nu_1 n_1$$
$$[\rho_2(x), \Psi_{qp}(y)] = \delta(x-y)\nu_2 n_2$$

We can choose different quasi-particle operators and thus charges thanks to the freedom on n_1, n_2. But comparing with experiments at $\nu = 2/5$ [43][16], where it was observed that quasiparticles on the inner edge channel have charge $e/3$ and the quasiparticles on the outer edge channel have charge $e/5$, the good choice would be $(n_1, n_2) = (1, 3)$ (knowing that $\nu_1 = 1/3$ and $\nu_2 = 1/15$).

We can also determine the statistical phase when exchanging two quasiparticle operators, that is found to be: $n_1^2/\nu_1 + n_2^2/\nu_2$. We thus recover the fractional statistics of quasi-particles. We note that the exchanging phase is here again linked to the charge carried by quasi-particles.

As a conclusion, the description of edge states in term of bosonic modes at integer filling factors of fractional filling factors (using Wen's approach) allows to make many interesting physical predictions:
- The calculation of the propagation function gives the I-V characteristics of tunneling experiments, that we will detail in the next chapter. However we will see that experimentally, the power laws derived in this section can hardly be observed. The reasons for this can be numerous: long range Coulomb interactions, tunneling that is not local, or tunneling amplitudes that are energy-dependent.
- We recover the fractional charge carried by quasi-particles on each edge states, that is particularly interesting at filling factors $\nu = \frac{m}{2pm\pm1}$. As we will also detail next, these fractional charges are accessible by shot noise measurements, and previous works have shown a good agreement with the theory.

- Finally, we demonstrated the fractional statistics of such quasi-particles, calculating the statistical phase associated to each of these.

Chapter 3

Quantum transport in tunneling experiments

In the last chapters, we have emphasized that electronic transport at the mesoscopic scale have to be treated with quantum mechanics. The probabilistic nature of the quantum transmission of electrons impinging on a barrier is responsible for a fundamental noise of the electrical current, the shot noise. We have emphasized the fact that the shot noise can reveal the statistics of the particles that collide in an interferometer, thanks to two-particle exchange interference. To control the trajectory of these particles, we work in the quantum Hall regime, where as we have seen, transport occurs only through the edges of the sample. We saw that the quantum dynamics of edge states is very similar to that of Tomonaga-Luttinger liquids (TLL) predicted for 1D interacting electrons [54], with remarkable simplifications for integer filling factors. The fractional Hall regime is of particular interest because it gives rise to quasi-particles that have a fractional (or "anyonic") statistics, as also showed. He have re-derived the propagation functions of such quasi-particles and shown that they mainly depend on the bulk filling factor.

Now we explicit the system we are working with and show how these propagation functions give access to the I-V characteristics of the tunnel junction, as well as the fluctuations of the current (the shot noise). We will use a perturbative approach with respect to the tunnelling amplitudes, following the works of I.Safi [33],[55], to express the current and the noise. Then we will present the scattering approach, mainly developed by Landauer, Imry and Büttiker [38]. We will see that both approaches lead to the same results for DC transport in the case of non-interacting fermions. For the time-dependent transport, we also get similar predictions within some assumptions.

3.1 Perturbative approach

3.1.1 DC transport

In this part, we describe tunneling experiments between two counter-propagating edge channels, which form at the periphery of a QH fluid. In our experiments, the charge tunneling occurs thanks to a Quantum Point Contact (QPC) on which we apply a voltage to control the electronic density. The QPC acts as a confining potential for the QH fluid, defining the geometry of edge channels. The latter can be easily connected to metallic contacts arranged at the periphery of the sample and then to an external circuit. In this section we do not use any specified model for the description of edge states: this approach is valid for arbitrary filling factor ν. For now we don't even assume initial thermalisation, thus including the case of noisy incoming current on the QPC (which is the case of the anyon collider or when we have non-perfect ohmic contacts). The only restriction is on the tunnelling amplitude: the tunneling current have to be weak with respect to the incoming current. The two physical situations (strong and weak barrier) included by this model are illustrated below, for the particular case of $\nu = 1/3$.

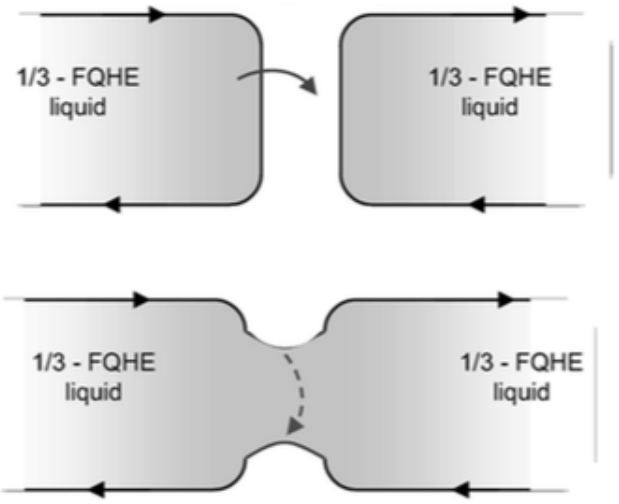

FIGURE 3.1: Schematic view of charge transfer in the case of a strong barrier (upper figure) and a weak barrier from [4]. In the first situation only electrons can tunnel as the regime of FQHE is destroyed in the QPC region. In the second situation, the FQHE fluid is weakly perturbed and fractional charge transfer may occur via the FQHE fluid.

The charge transport occurs between two edges that are more generally two systems with total charge Q_1 and Q_2. We impose a bias $V_{dc} = V_1 - V_2$ between both systems thanks to electronic reservoirs connected to the external circuit. The total Hamiltonian,

including coupling with the bias and tunneling between systems 1 and 2, thus writes:

$$H = H_0 + Q_1 V_1 + Q_2 V_2 + A + A^\dagger$$

The tunneling term $A + A^\dagger$ transfers the charge $Q = \frac{Q_2 - Q_1}{2}$ from a quantity q, that is the the charge of the quasi-particles that are exchanged. This charge q depends on the local filling factor under the QPC, as well as the choice for the quasi-particles operator (for complex filling factors, this choice is made from experimental observations!). The unperturbed Hamiltonian H_0 may include edge reconstruction or inhomogeneous Coulomb interactions, or even extended tunneling processes between co-propagating edges. Q has to commute with H_0 to ensure charge conservation in absence of tunneling, and it is incremented by q when acting upon by $A^\dagger$:

$$[Q, A] = qA \tag{3.1}$$

We can make a unitary transformation on H in order to absorb $V_{1,2}$ in the tunneling term [56]: $H' = UHU^\dagger - iU\partial_t U^\dagger$. Choosing $U(t) = e^{-it(V_1 Q_1 + V_2 Q_2)/\hbar}$ we get : $UAU^\dagger = e^{iqt(V_1 - V_2)/\hbar} A$. Thus the new Hamiltonian writes:

$$H' = H_0 + e^{iqtV_{dc}/\hbar} A + e^{-iqtV_{dc}/\hbar} A^\dagger \tag{3.2}$$

We emphasize that this transformation is possible assuming homogeneous voltages V_1 and V_2. This is the case in the quantum Hall regime when we assume that the edge states are equipotentials. It corresponds to a gauge choice, where the electric field is located at the tunneling point (the QPC). We could also allow the voltages V_1 and V_2 to be time-dependent, but now we are only interested by the DC case. Equations 3.1 and 3.2 imply that:

$$I(t) = \partial_t Q = \frac{iq}{\hbar}(e^{-i\omega_J t} A - e^{i\omega_J t} A^\dagger) \tag{3.3}$$

$I(t)$ is the backscattering current operator, and $\omega_J = qV_{dc}/\hbar$. We can calculate its dc value at second order in A using the two building blocks:

$$\hbar^2 X^>(t) = \langle A^\dagger_{H_0}(t) A_{H_0}(0) \rangle \tag{3.4}$$

$$\hbar^2 X^<(t) = \langle A_{H_0}(0) A^\dagger_{H_0}(t) \rangle \tag{3.5}$$

where $A_{H_0}(t) = e^{iH_0 t} A e^{-iH_0 t}$, and $\langle\rangle$ is the thermodynamic average of the expectation values taken on the unperturbed states of H_0. To second order in A, the mean DC current is given by:

$$I_{dc}(\omega_J) = q(X^>(\omega_J) - X^<(\omega_J)) \tag{3.6}$$

that can be interpreted as the difference between two transfer rates in opposite directions. We can now apply this result to the case of the FQHE with edge states described as chiral TLL. In the strong backscattering case, the FQHE regime is destroyed at the QPC level, such that only electrons can tunnel: $q = e$ and $A = \Psi_1^\dagger \Psi_2$ involves electron operators. However, in the weak tunneling regime, only quasi-particles can tunnel, such that $q = e^*$ and $\Psi_{1,2}$ are quasi-particle operators carrying a fractional charge. The I-V characteristic is thus different for these two regimes. Using the edge states description of section 2.4 at simple filling fractions $\nu = 1/m$ to calculate the propagation functions $\langle \Psi_{1,2}(x,t)\Psi_{1,2}(0,0)\rangle$, and assuming a local tunneling (at $x = 0$), we can derive the following expressions for the conductance $G = \partial I_{dc}/\partial V_{dc}$:

$$G(\omega_J) = \frac{\nu e^2}{h}(\frac{\omega_J}{T_B})^{2(1/\nu-1)} \quad \text{for} \quad \omega_J \gg T_B$$
$$G(\omega_J) = \frac{\nu e^2}{h}(\frac{\omega_J}{T_B})^{2(\nu-1)} \quad \text{for} \quad \omega_J \ll T_B$$

The first expression corresponds to the weak backscattering regime, and the second to the strong backscattering regime. T_B is the impurity strength in energy units. We can note the duality $\nu \longleftrightarrow 1/\nu$ in the power exponent. Increasing the energy (the voltage or the temperature), leads to a progressive transition from the strong backscattering regime to the weak backscattering regime. The curve $G(\omega_J)$ describing the whole transition can be calculated exactly to all perturbative order using conformal field theory [57].

The last expressions are valid within the description of edge states of section 2.4, treated as a Tomonaga-Luttinger liquid (TLL). Power-law behaviours have been measured for the tunneling current between a Laughlin state ($\nu = 1/3$) and a metal ($\nu = 1$), but the evolution of the exponent factor with the magnetic field does not show the predicted plateaux [58], [59]. The discrepancy between experiments and predictions may be due to the reconstruction of the edge. Wen's model assume a sharp density variation at the edge of the 2D sample. In real samples, the density decreases smoothly and some additional edge states corresponding to filling factor lower than the bulk filling factor may also strongly modify the exponents.

Hopefully, even when the description of edge states using the TLL model is not valid, general results for the noise can be derived using the expression (3.3) of the tunneling current. Letting $\delta I_{H'}(t) = I_{H'}(t) - I_{dc}(\omega_J)$ where the subscript H' refer to the Heisenberg representation with respect to $H'(t)$ (equation (3.2)), the current noise is defined as:

$$S(\omega_J, t-t') = \langle \delta I_{H'}(t)\delta I_{H'}(t')\rangle = \langle I_{H'}(t)I_{H'}(t')\rangle - \langle I_{H'}\rangle^2$$

The term $\langle I_{H'}\rangle^2$ involving only fourth order terms in A, it cancels at the second-order. To express S at second-order in A, we replace $I_{H'}(t)$ by $I_{H_0}(t)$, or $A_{H'}(t)$ by $A_{H_0}(t)$. We

obtain for the noise at frequency ω:

$$S(\omega_J,\omega) = q^2(X^>(\omega-\omega_J) + X^<(-\omega_J-\omega)) \tag{3.7}$$

At thermal equilibrium $T = 1/\beta$, we can show that the correlators are linked: $X^>(\omega) = e^{\beta\omega}X^<(\omega_J)$. Using this property, equations (3.7) and (3.6), we get:

$$S(\omega_J,\omega) = q\big[(1+N(\omega_J-\omega))I(\omega_J-\omega) - N(\omega_J+\omega)I(\omega_J+\omega)\big] \tag{3.8}$$

where $N(\omega) = 1/(e^{\omega\beta}-1)$ is the Bose-Einstein distribution at temperature T. This formula, derived in Ref [14],[60], generalizes previous derivations of the finite frequency noise [61] for independent electrons and assuming electron-hole parity. It has been experimentally checked in some experimental works such as Ref [62], where infrared photons emitted by a tunneling junction were probed. Closer to our subject, the fractional charge of quasiparticles in a QPC geometry was measured through the finite-frequency noise [63] using equation (3.8).

In our experiment, we are interested only by the zero-frequency noise:

$$S(\omega_J,0) = q^2(X^>(\omega_J) + X^<(\omega_J)) \tag{3.9}$$

From the spectral decomposition of $X^<(\omega_J)$ and $X^>(\omega_J)$, we can show that they are always positive. Thus the zero frequency noise 3.9, compared with Eq. 3.6, obeys:

$$S(\omega_J,0) \geq q|I_{dc}(\omega_J)| \tag{3.10}$$

From equations (3.9) and (3.6), we get:

$$S(\omega_J,0) = qcoth(\frac{\hbar\omega_J}{2k_BT})I_{dc}(\omega_J) \tag{3.11}$$

Experimentally, we have access to the symmetrized noise, that at zero frequency is simply $2S(\omega_J,0)$. Thus equation (3.11), derived in [64], usually appears with a factor 2 and is also known as "Schottky formula" [65]. It generalizes expression of shot noise based on Luttinger liquid model [66],[12],[13]. At zero temperature or more generally when the system described by H_0 is in its ground state, we recover the Poissonian noise: $S(\omega_J,0) = qI_{dc}(\omega_J)$. However we emphasize that following equation 3.10, the noise is super-poissonian for thermal states or for out of equilibrium initial states.

Equation (3.9) shows that it is possible to access to the tunnelling charge q through shot noise measurements. These measurements have started about 20 years ago in Saclay and in the Weizmann Institute, and revealed a charge $q = e/3$ at fraction filling factor $\nu = 1/3$ [15] [42]. In both experiments a QPC was used to implement a local

and controllable coupling between two $\nu = 1/3$ fractional edges (figure 3.3). The main difference between the two works resides in the shot noise detection technique, as in Ref [15] both auto and cross correlations were measured, whereas only auto-correlation measurements were made in Ref [42].
Fractional charge measurements at more complex filling factors such as $\nu = 2/3$ [44] and $\nu = 2/5$ [43],[16] were also performed. While at $\nu = 2/5$ the fractional charge was found to be $q = e/5$, an unexpected evolution of q with the temperature was measured at $\nu = 2/3$. Indeed, the measured charge from auto-correlations was $e^* = 2e/3$ at low temperature (25mK), and $e^* = e/3$ at higher temperature (125mK). Recent comparisons between auto and cross correlation noise at $\nu = 2/3$ and $\nu = 2/5$ [6] revealed that the this phenomenon is not the signature of a "charge evolution", but more probably of a non perfect coupling between the reservoirs and the edge states of the FQHE. When the reservoir injects a noisy current, the auto correlation is expected to be higher than the cross correlation. This difference was found to decrease when increasing the temperature [6]. This observation emphasizes the advantage of cross-correlation measurement technique, that is the most sensitive to the noise due to partitioning at the QPC, and is thus more suitable for fractional charge measurement.

For the weak tunneling regime of complex filling factors ($\nu = 2/3$ or $\nu = 2/5$), as showed in the last chapter, quasi-particle operators can involve the sum of bosonic fields related to different edge states. Thus the tunneling do not systematically occur from one physical edge state to the other (in contrast with the assumption made in Ref. [16]). However the strength of the perturbative approach is that it is independent of edge reconstruction picture, such as it include the more general situation illustrated in figure 3.3. We inject a current I_0 by imposing a bias between the two edge states (or

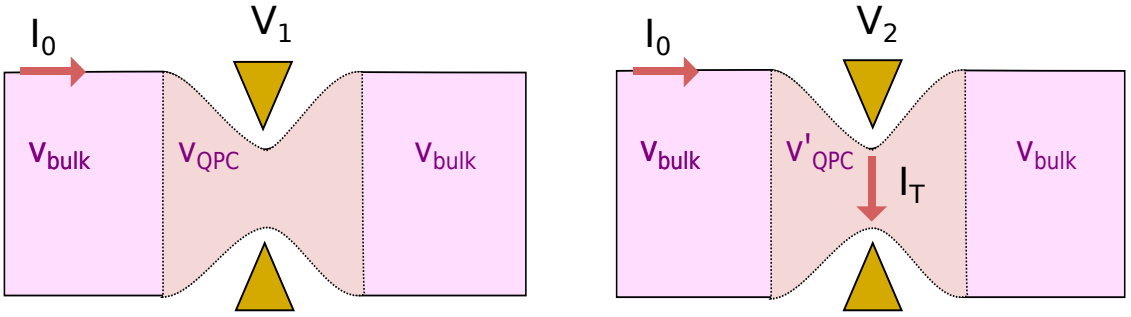

FIGURE 3.2: Schematic view of charge transfer in the case of weak tunneling through the QPC region. The left figure correspond to a stable QPC filling factor ν_{QPC}, such that no tunneling occurs between the two opposite edges of the sample. The right figure correspond to a non-stable filling factor ν'_{QPC}, allowing charge transport through the QPC region.

with a current source) and we control the QPC local filling factor ν_{QPC} by applying a voltage on the QPC. In the situation 1 (left image of figure 3.3), the QPC filling factor is stable, such that we see a plateau of conductance and there is no current transport in the QPC region. In the situation 2 (right image of figure 3.3), the voltage V_2 impose an electronic density corresponding to a non-stable filling factor ν'_{QPC} , such that transport can occur through the bulk at the QPC level. This transport does not necessarily occur from one edge state to the other but can involve the contribution of many edge states. However the tunneling process can involve only one effective charge q. The perturbative approach gives expression for the tunneling current I_T resulting from the situation 2 as well as its fluctuations, assuming that this current is weak enough $I_T \ll I_0$.

This approach thus leads to useful predictions for the tunneling current as well as its fluctuations in a very general context. In particular, we have confirmed the classical intuition that the fluctuations of a weak tunneling current are poissonian, thus proportional to the current. When we can use Wen's description of edge states as TLL, the I-V characteristic is predicted to follow a power law.

3.1.2 Time-dependent transport

The influence of a periodic driving field on the transport through tunnel barriers is an extensively studied subject. A paradigmatic result has been obtained more than three decades ago by Tien and Gordon for a superconducting tunnel junction [67]. A perturbative approach with respect to tunnelling amplitudes was first introduced by Wen to study quantum transport in the FQHE and in presence of an AC field [68]. However this work applies only to transport through simple filling factors $\nu = 1/m$, and results were derived for the current only. In order to describe time-dependent transport (current and noise) in a very general context that includes complex filling factors, we can extend the previous perturbative approach [33]. The AC signal is applied through metallic contacts linked with an external circuit. The metallic contacts, when properly coupled to the edge states, impose time-dependent potentials $V_1(t)$ (resp. $V_2(t)$) on the upper (resp. down) edge state. Assuming homogeneous $V_1(t)$ and $V_2(t)$ along the edge states, we can write the total Hamiltonian in the same form as equation (3.2):

$$\tilde{H}' = H_0 + e^{iqtV_{dc}/\hbar}E(t)A + e^{-iqtV_{dc}/\hbar}E^\dagger(t)A^\dagger \tag{3.12}$$

where $E(t) = e^{i\Phi(t)}$ and $\Phi(t) = e/\hbar \int_{-\infty}^{t}(V_1(t') - V_2(t'))dt'$. This expression of the Hamiltonian can be demonstrated properly using the quadratic form of the edge states Hamiltonian H_0, accounting for propagation effects between the reservoirs and the QPC. $V_1(t)$ and $V_2(t)$ correspond to the potential of edge states at the QPC level.

The tunneling current operator (in the Schrödinger picture) resulting from expression (3.12) and commutation rules (3.1) is:

$$\tilde{I}_S(t) = -\frac{q}{\hbar}\left(e^{iqV_{dc}t/\hbar}E(t)A - e^{-iqV_{dc}t/\hbar}E^\dagger(t)A^\dagger\right) \tag{3.13}$$

At the second order in A, the noise operator in the Heisenberg picture is equal to the one in the interaction picture: $\tilde{S}(t,t') = \langle\tilde{I}(t)\tilde{I}(t')\rangle$, where $\tilde{I}(t) = e^{iH_0t}\tilde{I}_S(t)e^{-iH_0t}$. Using expression (3.13) as well as the assumption $\langle A(t)A(t')\rangle = 0$, we get:

$$\tilde{S}(t,t') = -\frac{q^2}{\hbar^2}\left[e^{iqV_{dc}(t-t')/\hbar}E(t)E^\dagger(t')X^<(t'-t) + e^{-iqV_{dc}(t-t')/\hbar}E^\dagger(t)E(t')X^>(t-t')\right] \tag{3.14}$$

The correlators $X^<(t-t')$ and $X^>(t-t')$ are given by equation (3.4), in which $t' = 0$. Now we assume that $E(t)$ is T-periodic, and we note $\Omega = 2\pi/T$ its pulsation. Ω corresponds to the common pulsation of $V_1(t)$ and $V_2(t)$. We can Fourier-decompose $E(t)$:

$$E(t) = \sum_l p_l e^{-il\Omega t} \tag{3.15}$$

from which we deduce: $E(t)E^\dagger(t') = \sum_{l,m} p_l p_{l+m}^\dagger e^{-il\Omega t}e^{i(l+m)\Omega t'}$. Introducing this expression in equation (3.14), and making the variable change $u = t - t'$, we can calculate the zero-frequency noise:

$$\begin{aligned}\tilde{S}(V_{dc}) &= \sum_l |p_l|^2 \int du\left[e^{-iu(qV_{dc}-l\Omega)}X^<(u) + e^{iu(l\Omega-qV_{dc})}X^>(u)\right] \\ &= \sum_l |p_l|^2\left[X^<(l\Omega - qV_{dc}) + X^>(l\Omega - qV_{dc})\right]\end{aligned}$$

Leading to the main result:

$$\tilde{S}(V_{dc}) = \sum_l |p_l|^2 S(\omega_J = qV_{dc}/\hbar - l\Omega, 0) \tag{3.16}$$

where we recognized the expression of the DC zero-frequency noise given by equation (3.9) and (3.11). This result is quite striking: it reveals that the shot noise in presence of a time-dependent voltage only depends on the DC shot noise and the shape of the AC voltage. Using the same assumptions, similar results were found for the zero frequency current $\tilde{I}(V_{dc})$ in presence of an AC signal [69]:

$$\tilde{I}(V_{dc}) = \sum_l |p_l|^2 I_{dc}(qV_{dc}/\hbar - l\Omega) \tag{3.17}$$

This formula contains the results of numerous previous works based explicitly on a specific model within much more restrictive framework, for instance considering non-interacting systems [31], [32] or based on Tomonaga-Luttinger models [70],[71],[72].

Interestingly, one can interpret the previous expressions of $\tilde{S}(V_{dc})$ and $\tilde{I}(V_{dc})$ it by extending the "photo-assisted" transport picture (cf. paragraph 3.2.3) to complicated global many-body states. A tunneling charge q has a probability $|p_l|^2$ to absorb (emit) a energy $l\hbar\Omega < 0$ (> 0) (or l photons with energy $\hbar\Omega$), thus sees an effective voltage $V_{dc} - l\hbar\Omega/q$. The total current is given by the superposition of DC currents at $V_{dc} - l\hbar\Omega/q$ weighed by the probabilities $|p_l|^2$. The transport in presence of an AC voltage is called "photo-assisted" because it can be interpreted as the result of photons exchange processes. When $V_1(t) = V_1 \cos(\Omega t)$ and $V_2(t) = 0$, p_l corresponds to the l-th order Bessel function $J_l(\frac{qV_1}{\hbar\Omega})$. If there is a time delay τ between the two sine waves $V_1(t) = V_2(t+\tau)$, p_l also corresponds to a Bessel function but with argument $2qV_1 \sin(\Omega\tau/2)/\hbar\Omega$. This can be easily shown noticing that:

$$V_1(t) - V_2(t) = V_1 \sin(\Omega(t+\tau)) - V_1 \sin(\Omega t) = 2V_1 \sin(\Omega\tau/2) \sin(\Omega t + \phi/2)$$

This picture is thus useful to make predictions on HOM measurements, where we measure the shot noise $\tilde{S}$ while varying the delay τ.

"HOM" types of experiments were also theoretically addressed in different configurations, when the injection of quasi-particles is made by capacitive coupling [73][74]. Recently, the result (3.16) has been experimentally verified by photo-assisted shot noise (PASN) measurements in the FQHE [18]. The slope changes of the PASN $\tilde{S}(V_{dc})$ at $qV_{dc} = \hbar\Omega$, measured while irradiating the sample with microwave frequencies (Ω up to 18GHz), were found to be an alternative way to measure the fractional charge for $q = e/5$ and $q = e/3$. PASN measurements were also performed in a tunnel junction in the regime of dynamical Coulomb blockade [75]. In this regime, the strong non-linearity of the I-V curve makes it possible to observe photo-assisted processes in the current as well. However, a mismatch between the AC amplitude deduced from photo assisted current and from photo assisted noise measurement was observed, questioning the validity of equations (3.16) (3.17) in that regime.

3.2 The scattering approach

3.2.1 Conductance of a mesoscopic system

We are now going to introduce another very useful and widely-used approach for quantum transport, first initiated by Rolf Landauer and then generalized by M. Büttiker [38],[9]. The idea of the scattering approach is to relate transport properties of the system (in particular, current fluctuations) to its scattering properties, which are assumed to be known from a quantum-mechanical calculation. In its traditional form the method applies to non-interacting systems in the stationary regime. The system consists on a mesoscopic conductor linked to many particle reservoirs. It is assumed that the reservoirs are so large that they can be characterized by a temperature T_α and a chemical potential μ_α; the distribution functions of electrons in the reservoirs, defined via these parameters, are the Fermi distribution functions:

$$f_\alpha(E) = \frac{1}{1 + e^{(E-\mu_\alpha)/k_B T_\alpha}}$$

The total energy E of electrons is counted from the chemical potential of one of the reservoirs, that is supposed to be grounded.

3.2.1.1 Two-terminal case

We first consider a two-terminal geometry for simplicity. We put this system out-of equilibrium by applying a bias on one of the reservoir. We ignore internal potential variations that could be induced by external potentials. Thus the non-equilibrium state is introduced exclusively through the distribution functions of the electrons emitted by the reservoir. And the wavefunctions on the left and right sides of the sample are a simple superposition of plane waves incoming on the barrier, and reflected by the barrier. These two are linked through a scattering matrix s that is determined by solving the Schrödinger equation with a certain shape of the barrier potential. We can introduce the operators $a^\dagger_{L,n}(E)$ and $a_{L,n}(E)$ that act on the Fock states of the left reservoirs by creating and annihilating electrons in the transverse mode n and with energy E. These electrons are incident upon the barrier. In the same way, the creation $b^\dagger_{L,n}$ and annihilation $b_{L,n}$ operators describe electrons in the outgoing states, as illustrated below.
The operators a and b obey anti-commutation relations:

$$[a^\dagger_{L,n}(E), a_{L,n'}(E')] = \delta_{n,n'}\delta(E - E')$$
$$[a^\dagger_{L,n}(E), a^\dagger_{L,n'}(E')] = [a_{L,n}(E), a_{L,n'}(E')] = 0$$

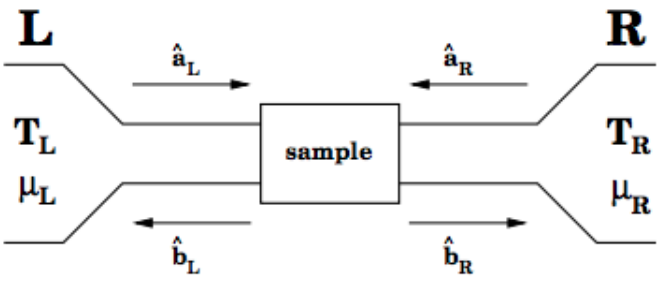

FIGURE 3.3: Example of two-terminal scattering problem for the case of one transverse channel.

and are related via the scattering matrix s, that is generally energy-dependent:

$$\begin{pmatrix} b_{L1} \\ \dots \\ b_{LN_L} \\ b_{R1} \\ \dots \\ b_{RN_R} \end{pmatrix} = s \begin{pmatrix} a_{L1} \\ \dots \\ a_{LN_L} \\ a_{R1} \\ \dots \\ a_{RN_R} \end{pmatrix} \tag{3.18}$$

N_L and N_R being the number of modes on the left and right lead. The matrix s has dimensions $(N_L + N_R) \times (N_L + N_R)$. The current conservation implies that the matrix s is unitary: $s^\dagger s = s s^\dagger = 1$.

We can express the current flowing from the left and right side of the sample when we apply a finite bias V_{dc} on the left side, such that $\mu_L = \mu + eV_{dc}$, μ being the equilibrium potential (or the energy reference, fixed by the ground). We find (the reader can refer to Ref. [38] for the derivation):

$$I_L(t) = \frac{e}{2\pi\hbar} \sum_n \int dE dE' e^{i(E-E')t/\hbar} (a^\dagger_{L,n}(E) a_{L,n}(E') - b^\dagger_{L,n}(E) b_{L,n}(E'))$$

To find this expression, we have assumed that the velocity of electrons contributing to the current vary slowly with the energy. Using equation (3.18), we can express the current in term of a and $a^\dagger$ operators alone:

$$I_L(t) = \frac{e}{2\pi\hbar} \sum_{\alpha,\beta} \sum_{m,n} \int dE dE' e^{i(E-E')t/\hbar} a^\dagger_{\alpha,m}(E) A^{m,n}_{\alpha,\beta}(L, E, E') a_{\beta,n}(E') \tag{3.19}$$

where the indices α, β label the reservoirs and may assume values L or R, whereas the indices n and m label the transport channels. We note that the current is uniform along the lead. The matrix A is defined as:

$$A^{m,n}_{\alpha,\beta}(L, E, E') = \delta_{m,n}\delta_{\alpha,L}\delta_{\beta,L} - \sum_k s^\dagger_{L,\alpha;mk} s_{L,\beta;kn}$$

We can first derive the average current from equation (3.19). For a system at thermal equilibrium the quantum statistical average of the product of an electron creation operator and annihilation operator of a Fermi gas is:

$$\langle a^{\dagger}_{\alpha,m}(E)a_{\beta,n}(E')\rangle = \delta_{n,m}\delta_{\alpha,\beta}\delta(E-E')f_{\alpha}(E) \tag{3.20}$$

Using equations (3.20) and (3.19) and taking into account that the scattering matrix s is unitary, we obtain:

$$\langle I_L\rangle = \frac{e}{2\pi\hbar}\int dE \mathrm{Tr}\,(t^{\dagger}(E)t(E))(f_L(E)-f_R(E)) \tag{3.21}$$

Here the matrix t is the off-diagonal block of the scattering matrix (3.18), $t_{mn} = s_{RL;mn}$. In the QH regime, the transport modes correspond to edge channels, and the scattering between edge channels is suppressed: $t_{mn} = \delta_{mn}t_n$. Thus the matrix t is diagonal and the expression of the mean current simplify as $\mathrm{Tr}\,(t^{\dagger}(E)t(E)) = \sum_n D_n(E)$, with $D_n = t_n^{\dagger}(E)t_n(E)$. At zero temperature and if the transmission coefficients t_n vary slowly on the energy scale $\mu_L - \mu_R = eV_{dc}$ this gives:

$$\langle I_L\rangle = \frac{e^2}{2\pi\hbar}\sum_n D_n V_{dc}$$

which leads to the quantization of the conductance when an integer number of channels is transmitted. In the non-interacting case limit, the current can thus be expressed only in term of transmission probabilities for each channel independently.

3.2.1.2 Multi-terminal case

This approach can be easily generalized to a multi-terminal case. We introduce, for each lead α, creation and annihilation operators of electrons in an incoming $a^{\dagger}_{\alpha,n}$, $a_{\alpha,n}$ and outgoing $b^{\dagger}_{\alpha,n}$, $b_{\alpha,n}$ state on the transverse channel n. These operators are again related via the scattering matrix. We write down this relation, similar to Eq. (3.18):

$$b_{\alpha m}(E) = \sum_{\beta n} s_{\alpha\beta,mn}a_{\beta n}(E)$$

In other words, we define a scattering matrix from contact β to contact α that have dimensions $M_\alpha \times M_\beta$. If we apply a voltage V_β to the reservoir β, we modify its electrochimical potential: $\mu_\beta = \mu + eV_\beta$, where μ is the equilibrium potential. We still neglect the variations of potential inside the conductor, assuming that this bias only modify the Fermi distribution of electrons in the reservoir β. Then, similarly to the two-terminal case, we can express the wave function of electrons in any lead α as a superposition of

plane waves emitted from the reservoir α and incoming on the reservoir α after reflexion on the barrier or after having been transmitted from other reservoirs. We obtain the current flowing in the lead α:

$$I_\alpha(t) = \frac{e}{2\pi\hbar}\sum_{\beta\gamma}\sum_{mn}\int dEdE' e^{i(E-E')t/\hbar} a^\dagger_{\beta,n}(E) A^{mn}_{\beta,\gamma}(\alpha, E, E') a_{\gamma,m}(E') \tag{3.22}$$

where the number $A^{mn}_{\beta,\gamma}$ are the matrix coefficients:

$$A^{mn}_{\beta\gamma}(\alpha, E, E') = \delta_{m,n}\delta_{\beta,\alpha}\delta_{\gamma,\alpha} - \sum_k s^\dagger_{\alpha\beta;mk}(E) s_{\alpha\gamma;kn}(E') \tag{3.23}$$

The signs of currents are chosen to be positive for electrons incoming on the sample. Then we obtain the average current incoming on the contact α:

$$\langle I_\alpha\rangle = \frac{e}{h}\int dE(N_\alpha - R_{\alpha\alpha}) f_\alpha(E) - \sum_{\alpha\neq\beta} T_{\alpha\beta}(E) f_\beta(E)$$

where $R_{\alpha\alpha}$ is the total probability for an electron from contact α to be reflected in the same contact:

$$R_{\alpha\alpha}(E) = \sum_{m,n=1}^{N_\alpha} |S_{\alpha\alpha,mn}|^2$$

and $T_{\alpha\beta}$ is the probability for an electron incident from β to be transmitted to contact α:

$$T_{\alpha\beta}(E) = \sum_{m,n=1}^{N_\alpha,N_\beta} |S_{\alpha\beta,mn}|^2$$

The conservation of the mean current gives $N_\alpha = R_{\alpha\alpha}(E) + T_{\alpha\beta}(E)$, and $\sum_\alpha \langle I_\alpha\rangle = 0$.

3.2.2 Noise of a mesoscopic system

We are concerned with fluctuations of the current away from their average value. We thus introduce the operators $\Delta I_\alpha(t) = I_\alpha(t) - \langle I_\alpha\rangle$. We define the correlation function of the current in contact α and the current in contact β as:

$$S_{\alpha\beta}(t-t') = \frac{1}{2}\langle \Delta I_\alpha(t)\Delta I_\beta(t') + \Delta I_\beta(t')\Delta I_\alpha(t)\rangle$$

Note that in the absence of time-dependent external fields the correlation function must be function of only $t - t'$. Its Fourier transform is thus expressed as:

$$2\pi\delta(\omega+\omega')S_{\alpha\beta}(\omega) = \langle \Delta I_\alpha(\omega)\Delta I_\beta(\omega') + \Delta I_\beta(\omega')\Delta I_\alpha(\omega)\rangle$$

In this expression, $I_\alpha(\omega) = \int dt I_\alpha(t) e^{i\omega t}$ and $\Delta I_\alpha(\omega) = I_\alpha(\omega) - \langle I_\alpha(\omega) \rangle$. From expression (3.22), we obtain:

$$I_\alpha(\omega) = \frac{e}{2\pi\hbar} \sum_{\beta\gamma} \sum_{mn} \int dE a^\dagger_{\beta,n}(E) A^{mn}_{\beta,\gamma}(\alpha, E, E+\hbar\omega) a_{\gamma,m}(E+\hbar\omega)$$

To find the noise power we need the quantum statistical expectation value of products of four operators a. Using Wick's theorem as well as the thermal average of $a^\dagger a$ in equation (3.20), we find for the zero-frequency noise:

$$S_{\alpha\beta}(\omega=0) = \frac{e}{2\pi\hbar} \sum_{\gamma\delta} \sum_{mn} \int dE A^{mn}_{\gamma\delta}(\alpha, E, E) A^{nm}_{\delta\gamma}(\beta, E, E) (f_\gamma(E)(1-f_\delta(E)) + f_\delta(E)(1-f_\gamma(E)))$$

Let's apply these results for a sample similar to the experimental setup, that has six ohmic contacts. Two of them are grounded, so that we can consider a 4-contact geometry to calculate the auto and cross-correlation functions. The bulk filling factor ν is integer, thus also corresponds to the number of edge channels. We consider that T channels are completely transmitted by the QPC, $\nu - T - 1$ channels are completely reflected by the QPC, and one channel is partially transmitted with a transmission coefficient D and a reflexion coefficient $R = 1 - D$ (we don't write the energy dependence for simplicity). The physical situation is illustrated below with the example of $\nu = 2$ and $T = 1$.

The reader can refer to Ref. [6] for more details on the auto and cross-correlation

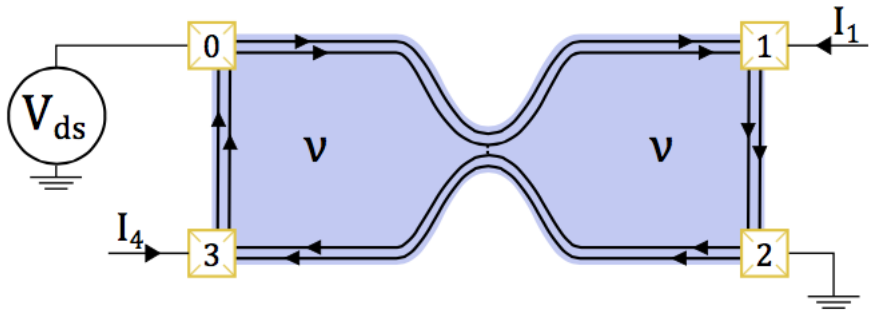

FIGURE 3.4: 4-contacts geometry. We apply a voltage on the reservoir 0 and we are interested in the current flowing in contacts 1 and 2 as well as their auto and cross correlation functions.

calculations. Here we simply give the results, using the labels of Fig. 3.4:

$$\begin{aligned} S_{11}(\omega=0) = 2\frac{e^2}{h} \int dE \nu f_1(1-f_1) + (T+D^2) f_0(1-f_0) + (\nu - T - 1 + R^2) f_2(1-f_2) \\ + RD(f_2(1-f_0) + f_0(1-f_2)) \end{aligned} \tag{3.24}$$

$$\begin{aligned} S_{13}(\omega=0) &= 2\frac{e^2}{h}\int dERD(f_0(1-f_0)+f_2(1-f_2)-f_2(1-f_0)-f_0(1-f_2) \\ &= -2\frac{e^2}{h}\int dERD(f_2-f_0)^2 \end{aligned} \tag{3.25}$$

We apply a voltage V_{dc} only on the contact 0, such that $f_1 = f_2 = f_3 = f$ and $f_0(E) = f(E + eV_{dc})$. Knowing this, we can easily show: $S_{11}(\omega = 0) = S_{33}(\omega = 0)$.

Let's first study the equilibrium state, where $V_{dc} = 0$ and $f_0 = f$. Then the expression of the auto-correlation functions (3.24) can be simplified as:

$$\begin{aligned} &S_{11}(\omega=0) = S_{33}(\omega=0) = 2\frac{e^2}{h}\int dEf(1-f)(D^2+R^2+2\nu-1+2RD) \\ &= 2\frac{e^2}{h}\int dEf(1-f)(2\nu+(D+R)^2-1) \\ &= 4\frac{\nu e^2}{h}\int dE\nu f(1-f) \end{aligned}$$

Using the property of Fermi-Dirac functions: $f(1-f) = k_BT\frac{\partial f}{\partial E}$, we get simply the thermal (or Johnson-Nyquist) noise :

$$S_{11}(\omega=0) = S_{33}(\omega=0) = 4k_BT\nu\frac{e^2}{h}$$

While it is clear from equation (3.25) that the cross-correlation $S_{13}(\omega = 0)$ cancels at $V_{dc} = 0$. Indeed, the cross-correlation only contains information about (anti-)correlated partition noise, and is insensitive to the fluctuations of the incoming current such as thermal fluctuations due to the finite temperature of the reservoirs as they are uncorrelated.

Let's now add a finite bias V_{dc} on the reservoir 0. We can show from equations (3.24) and (3.25) that the auto-correlation functions can be re-expressed as a thermal noise minus the cross-correlation function:

$$S_{11}(\omega=0) = 2\frac{e^2}{h}\int dE\nu f_1(1-f_1)+(T+D)f_0(1-f_0)+(\nu-T-1+R)f_2(1-f_2)+RD(f_0-f_1)^2$$

As already emphasized in the Chapter 1, the auto-correlation functions contain two contributions:

- The first one corresponds to the fluctuations of the incoming currents due to the finite temperature of the reservoirs from which they are emitted (independently on the bias applied).
- The second one is due to the partition of charge carriers at the QPC. This term correspond to the cross-correlation term, with a minus sign.

From equation (3.25) and using $\int dEf(E)(1-f(E+\Delta)) = \frac{\Delta}{exp(\Delta/k_BT)-1}$, we can give

an integrated expression for the cross-correlation:

$$S_{13}(\omega = 0, V_{dc}) = -2e\frac{e^2}{h}D(1-D)V_{dc}\big[\coth(\frac{eV_{dc}}{2k_BT}) - \frac{2k_BT}{eV_{dc}}\big] \tag{3.26}$$

Experimentally, we have access to the auto as well as the cross-correlations. The main interest will be on measuring the shot noise, that as we have emphasized, can reveal interesting informations.

For interacting systems, it is possible to link the cross-correlation noise to the zero-frequency noise $S(\omega_J, 0) = S(V_{dc})$ of equation (3.9) (where $\omega_J = eV_{dc}/\hbar$) using the Luttinger Liquid description of edge states. Theoretical works for two-terminal systems [66], [76] can be extended to many-terminal systems, leading to the very useful relation:

$$S_{13}(V_{dc}) = S(V_{dc}) - 2k_BTG_B(V_{dc}) \tag{3.27}$$

where $G_B(V_{dc}) = \frac{\partial I_B}{\partial V_{dc}}$ is the conductance of the reflected current.

3.2.3 Photo-assisted transport

In this part we are going to extend the previous scattering approach to the case where the applied voltage is time-dependent. The theory of fluctuations in presence of an oscillating field originating from a variable magnetic flux was initially studied by Lesovik and Levitov [31]. This was later extended to the case of ac voltage by Pedersen and Büttiker [32]. Here we present this theory based on a single-particle picture and semi-classical approach.

The initial Hamiltonian (in the Schrödinger picture) describing reservoir α can be expressed using the second quantization for independent particles:

$$H_\alpha = \sum_k \epsilon_{\alpha,k} a^\dagger_{\alpha,k} a_{\alpha,k}$$

In the Heisenberg picture, the time-dependence of annihilation operators is thus: $a_{\alpha,k}(t) = e^{i\epsilon_k t/\hbar} a_{\alpha,k}(0)$. In the presence of an oscillating potential $V_\alpha(t)$ applied on reservoir α, each electron "feels" an additional potential, leading to:

$$\tilde{H}_\alpha = \sum_k (\epsilon_{\alpha,k} + eV_\alpha(t)) a^\dagger_{\alpha,k} a_{\alpha,k}$$

And the resulting annihilation operators in the Heisenberg picture are:

$$\tilde{a}_{\alpha,k}(t) = e^{i\epsilon_k t/\hbar + i\Phi_\alpha(t)} a_{\alpha,k}(0)$$

where $\Phi_\alpha(t) = e/\hbar \int_{-\infty}^{t} dt' V_\alpha(t')$. Assuming a sine shape $V_\alpha(t) = V_\alpha \sin(\Omega t)$ and using the spectral decomposition of $e^{i\Phi_\alpha(t)}$

$$e^{\imath\Phi_\alpha(t)} = \sum_l J_l(\frac{eV_\alpha}{\hbar\Omega}) e^{-il\Omega t}$$

where J_l is the l-th order Bessel function, we get :

$$\tilde{a}_{\alpha,k}(t) = \sum_l J_l(\frac{eV_\alpha}{\hbar\Omega}) e^{i(\epsilon_k - l\hbar\Omega)t/\hbar} a_{\alpha,k}(0)$$

Re-expressed in the energy domain, this gives :

$$\tilde{a}_\alpha(\epsilon) = \sum_l J_l(\frac{eV_\alpha}{\hbar\Omega}) a_\alpha(\epsilon - l\hbar\Omega) \tag{3.28}$$

To calculate the current flowing into contact α, we can replace the operators a in equation (3.22) by the operators $\tilde{a}$. We also let the possibility for each sign wave be out of phase with respect to a certain reference signal: $V_\alpha(t) = V_\alpha \sin(\Omega(t + \tau_\alpha))$. This time-delay is accounted for by making the substitution $J_l(\frac{eV_\alpha}{\hbar\Omega}) \to e^{-il\Omega\tau_\alpha} J_l(\frac{eV_\alpha}{\hbar\Omega})$. Considering only one mode for simplicity, we find:

$$\langle \tilde{I}_\alpha(t) \rangle = -\frac{e}{h} \int dE \sum_{\gamma,lk} Tr(A_{\gamma,\gamma}(\alpha, E, E+(k-l)\hbar\Omega)) e^{-i(k-l)\Omega(\tau_\gamma + t)} J_l^\dagger(\frac{eV_\gamma}{\hbar\Omega}) J_k(\frac{eV_\gamma}{\hbar\Omega}) f_\gamma(E - l\hbar\Omega)$$

Calling $T_{\alpha,\gamma}(E) = -Tr(A_{\gamma,\gamma}(\alpha, E, E)$ (A is defined in equation (3.23)), we get for the zero-frequency current:

$$\langle \tilde{I}_\alpha \rangle = -\frac{e}{h} \int dE \sum_{\gamma,l} T_{\alpha,\gamma}(E) |J_l(\frac{eV_\gamma}{\hbar\Omega})|^2 f_\gamma(E - l\hbar\Omega) \tag{3.29}$$

The Fermi functions originates from quantum statistical average of $a^\dagger(E)a(E')$ for an equilibrium system. It is thus assumed that the modulation imposed on the system is so slow that the contacts can still be regarded as being in a dynamic equilibrium state.

We now apply equation (3.29) to a two-terminal geometry, on which we apply time-dependent voltages $V_L(t)$ and $V_R(t)$. We note that the photo-assisted current has the same form as equation (3.21), with the Fermi functions $f_\gamma(E)$ replaced by $\sum_l |J_l(\frac{eV_\gamma}{\hbar\Omega})|^2 f_\gamma(E - l\hbar\Omega)$:

$$\langle \tilde{I}_L \rangle = \frac{e}{h} \int dE D(E) \sum_l \left[|J_l(\frac{eV_L}{\hbar\Omega})|^2 f_L(E - l\hbar\Omega) - |J_l(\frac{eV_R}{\hbar\Omega})|^2 f_R(E - l\hbar\Omega) \right] \tag{3.30}$$

To understand better this equation, let's analyse it at zero temperature and with $V_{dc} = V_{L,dc} - V_{R,dc}$, or $f_L = f_R$. We get:

$$\langle \tilde{I}_L \rangle = \frac{e}{h} \sum_l \int_0^{l\hbar\Omega} dE D(E) \sum_l \left[|J_l(\frac{eV_L}{\hbar\Omega})|^2 - |J_l(\frac{eV_R}{\hbar\Omega})|^2 \right]$$

If $D(E)$ is energy-independent, the property $\sum_l l P_l(x) = 0$ ensures that the photo-current cancels. Indeed, the photo-current can be finite only if the electron-hole pairs created by the AC voltage have different tunneling probabilities due to an energy-dependent transmission coefficient. In the case of a small dependence of $D(E)$ on the energy, its expansion $D(E) = D(0) + \frac{\partial D}{\partial E} E$ leads to:

$$\langle \tilde{I}_L \rangle = \frac{e}{h} \sum_l \frac{(l\hbar\Omega)^2}{2} \frac{\partial D}{\partial E} \left[|J_l(\frac{eV_L}{\hbar\Omega})|^2 - |J_l(\frac{eV_R}{\hbar\Omega})|^2 \right] = \frac{e}{h} \frac{e^2}{2} \frac{\partial D}{\partial E} (\langle V_L^2 \rangle - \langle V_R^2 \rangle)$$

In contrast with the results of the perturbative approach and with a commonly adopted "gauge invariance" argument, the transport is not determined by the difference $V_L(t) - V_R(t)$. Instead, $\langle \tilde{I}_L \rangle$ cancels as far as the amplitude of the two sines V_L and V_R are equal, independently on the phase difference between the two sines. In that sense, the scattering approach cannot be used to interpret our photo-assisted current measurements in the HOM configuration (see paragraph 5.9). The limits of such approach to describe AC transport are discussed in Ref [32], that emphasizes the necessity to take into account the internal potential of the conductor in the presence of static and oscillating contact voltages.

If the AC voltage is applied on one contact only (that is the case for most of previous photo-current measurements), let's say the left contact, equation (3.30) leads to:

$$\langle \tilde{I}_L \rangle = \frac{e}{h} \sum_l |J_l(\frac{eV_L}{\hbar\Omega})|^2 \int E D(E) (f_L(E - l\hbar\Omega) - f_R(E)) \tag{3.31}$$

$$= \sum_l |J_l(\frac{eV_L}{\hbar\Omega})|^2 \langle I_L \rangle (V_{dc} - l\hbar\Omega/e) \tag{3.32}$$

We thus recover the same result as equation (3.17): the photo-assisted current at V_{dc} corresponds to the superposition of the DC current at $V_{dc} - l\hbar\Omega/e$ weighted by the probability to emit ($l < 0$) or absorb ($l > 0$) photons. Photo-assisted current measurements were done in a QPC geometry at zero magnetic field [77] and were in good agreement with the theory.

3.2.4 Photo-assisted shot noise (PASN)

Still considering a two-contacts geometry, we can also calculate the PASN while applying sine waves on both contacts. We have to be careful when calculating the zero-frequency noise: with an AC signal, the noise $S(t,t')$ is a function of both $\tau' = t+t'$ and $\tau = t-t'$. As we average the signal over times that are longer than the period $2\pi/\Omega$ of the AC signal, we can consider the average:

$$S(\tau) = \frac{\Omega}{2\pi}\int_0^{2\pi/\Omega} S(\tau,\tau')d\tau'$$

In other words, we don't have access to the very rapid oscillations of the signal. Using the previous expression of $\tilde{I}(t)$, we can show that the shot noise at zero frequency (subtracting the thermal noise) is given by:

$$\langle \tilde{S}_{L,L}(\omega=0)\rangle = \frac{e^2}{\hbar}\int dE \sum_{l,k,l'} t(E+k\hbar\Omega)r(E+k\hbar\Omega)t(E)r(E)* \tag{3.33}$$

$$\big[p^\dagger_{R,l+k}p_{L,l'+k}p^\dagger_{R,l'}p_{L,l}f_R(E-l\hbar\Omega)(1-f_L(E-l'\hbar\Omega)) \tag{3.34}$$

$$+ p^\dagger_{L,l+k}p_{R,l'+k}p^\dagger_{L,l'}p_{R,l}f_L(E-l\hbar\Omega)(1-f_R(E-l'\hbar\Omega))\big] \tag{3.35}$$

where $t(E)$ and $r(E)$ are the transmission and reflection amplitude probabilities, and $p_{L/R,l} = J_l(\frac{eV_{L/R}}{\hbar\Omega})$ refers to the l-th order Bessel function. As for the photo-assisted current, the noise is not simply a function of $V_1(t)-V_2(t)$ when the transmission coefficient are energy-dependent. Instead, it is reminiscent of many wave-packets interference. This aspect was discussed by previous theoretical works [78] through charge and energy fluctuations studies. In the case of energy-independent scattering matrix and in-phase signals ($\tau_L = \tau_R$), we recover the results of the perturbative approach:

$$\langle \tilde{S}_{L,L}(\omega=0)\rangle = \sum_l |J_l\big(\frac{e(V_L-V_R)}{\hbar\Omega}\big)|^2 \langle S_{L,L}(\omega=0, V_{dc}-l\hbar\Omega/e)\rangle \tag{3.36}$$

where $\langle S_{L,L}(\omega=0,V_{dc})\rangle$ is the DC shot noise:

$$\langle S_{L,L}(\omega=0,V_{dc})\rangle = \frac{e^2}{h}D(1-D)eV_{dc}\coth(\frac{eV_{dc}}{2k_BT}) \tag{3.37}$$

Of course, to get the total noise we need to add the thermal contribution $\frac{e^2}{h}4k_BTD^2$, that is independent of the DC or AC voltage. In case N modes contributes to the transport, we get very similar results replacing D by $\sum_n D_n$ and $D(1-D)$ by $\sum_n D_n(1-D_n)$.

Let's first interpret the PASN at $V_{dc}=0$, and zero temperature limit. Then electrons and holes contributes both with the same amount to the shot noise. Indeed, even though they are created together as an electron-hole pair, they can be transmitted or reflected

by the barrier independently. The electrons that are at energy higher than the Fermi level E_F after having absorbed l photons were initially in a an energy band $l\hbar\Omega$ under the Fermi level, their contribution is thus:

$$S_l = 2\frac{e^2}{h}D(1-D)l\hbar\Omega P_l$$

The PASN corresponds to the sum over the contribution of all these l-photon absorption processes.

In the case where V_{dc} is finite, electrons and holes do not contribute in the same way to the PASN, and the situation strongly depends the ratio $eV/\hbar\Omega$, explaining the change in slopes. The reader can refer to L.-H. Reydellet PhD thesis for a deeper discussion on the subject.

Historically, the PASN was first measured in a diffusive conductor [79], in a diffusive normal metalsuperconductor junction [80], in a QPC [81], and finally in a simple junction [82] where finite-frequency noise measurements were also in agreement with the theory. More recently, the works on noise minimization using Lorentzian pulses [27] as well as PASN measurements in the IQHE [83] also supported this model of "photo-assisted" transport.

To describe our "Hong -Ou-Mandel" experiments, we consider that the Left and Right applied voltages are sine waves out of phase but with the same amplitude: $V_R(t) = V_L(t+\tau)$. This leads to the simple relation: $p_{R,l} = e^{-il\tau\Omega}p_{L,l}$ for any integer l. For simplicity, we also assume that the scattering matrix is energy-independent. In that case, equation (3.33) leads to:

$$\langle\tilde{S}_{L,L}(\omega=0)\rangle = \frac{e^2}{\hbar}D(1-D)\int dE \sum_{l,k,l'} p^\dagger_{L,l+k}p_{L,l'+k}p^\dagger_{L,l'}p_{L,l}*$$

$$\left[e^{i(k+l+l')\Omega\tau}f_R(E-l\hbar\Omega)(1-f_L(E-l'\hbar\Omega)) + e^{-i(k+l+l')\Omega\tau}f_L(E-l\hbar\Omega)(1-f_R(E-l'\hbar\Omega))\right]$$

We introduce the Fourier transform $\tilde{p}$ of $e^{i(\Phi_L(t)-\Phi_R(t))}$ (we recall $\Phi_{L/R}(t) = e/\hbar\int_{-\infty}^{t}V_{L/R}(t)$), that can be expressed as:

$$\tilde{p}_l = \sum_k p_{L,k-l}p_{R,k} = \sum_k p_{L,k-l}e^{-ik\tau\Omega}p_{L,k}$$

The previous expression of $\langle\tilde{S}_{L,L}(\omega=0)\rangle$ can be simplified noticing that:

$$\sum_k p^\dagger_{L,l+k}p_{L,l'+k}e^{ik\Omega\tau} = e^{-il'\Omega\tau}\sum_{k'} p^\dagger_{L,k'+l-l'}p_{L,k'}e^{ik'\Omega\tau} = e^{-il'\Omega\tau}\sum_{k'} p^\dagger_{L,k'+l-l'}p^\dagger_{R,k'} = e^{-il'\Omega\tau}\tilde{p}_{l'-l}$$

where we made the variable change: $k' = l' + k$. In the same way, we can show that:

$$\sum_k p^\dagger_{L,l+k} p_{L,l'+k} e^{-ik\Omega\tau} = e^{il'\Omega\tau} \tilde{p}^\dagger_{l'-l}$$

Combining the last four equations, we get:

$$\langle \tilde{S}_{L,L}(\omega = 0) \rangle = \frac{e^2}{\hbar} D(1-D) \sum_n |\tilde{p}_n|^2 \int dE \Big[f_R(E)(1-f_L(E-n\hbar\Omega)) + f_L(E-n\hbar\Omega)(1-f_R(E)) \Big]$$

Finally, we recover the same kind of expression as equation 3.36:

$$\langle \tilde{S}_{L,L}(\omega = 0) \rangle = \sum_l |\tilde{p}_l|^2 \langle S_{L,L}(\omega = 0, V_{dc} - l\hbar\Omega/e) \rangle \tag{3.38}$$

When the scattering matrix is energy-independent, applying a voltages $V_L(t)$ ($V_R(t)$) on the left (right) contact leads to the same shot noise as when a voltage $V_L(t) - V_R(t)$ is applied on one contact only.
When the scattering elements are energy-dependent, $\langle \tilde{S}_{L,L}(\omega = 0) \rangle$ depends on the time delay τ in a complicated way. The situation is not simply equivalent to the one where $V_L(t) - V_R(t)$ is applied on one contact only.

The perturbative theory and the Floquet scattering theory lead to different predictions on electronic HOM experiments. The first approach treats a large variety of systems including strongly-correlated systems (FQHE), however it applies only to the weak backscattering regime, and energy-independent tunneling amplitudes. The gauge choice that is made leads to transport properties (current and noise) determined only by the difference $V_L(t) - V_R(t)$. The scattering approach is able to treat energy-dependent scattering processes at arbitrary transmissions, but for non-interacting electrons. This approach generally leads to more complicated expressions of the noise, that simplify only in the energy-independent scattering matrix limit. It leads also to time-delay independent photo-current in the HOM configuration. This last result is not coherent with experimental observations (cf paragraph 5.14). We hope this short study will motivate a deeper work to understand the origin of such a discrepancy.

Now that we have described the useful approaches to deal with DC and time-dependent transport in a ballistic mesoscopic conductor, and particularly in the quantum Hall regime, we will turn to experimental aspects and results.

Chapter 4

Experimental setup

Photo-assisted transport and HOM experiments are performed on a Quantum Point Contact (QPC) device. The voltage applied on the QPC modifies the local electronic density of a two-dimensional electron gas (2DEG) built in a GaAs-AlGaAs heterostructure. Varying the gate voltage and the intensity of the perpendicular magnetic field, we can study quantum transport in various Hall regimes. In this chapter, we present the main characteristics of the sample and the whole experimental setup, highlighting some of the experimental challenges. In particular, we present how we apply DC and radiofrequency (RF) voltage to the sample, as well as the principle of conductance and noise measurements. Most of the experimental techniques have been developed in the past, thus the reader can refer to previous PhD thesis [84] [77] for more details.

4.1 Sample geometry and characteristics

The sample we used is a 2DEG made from hetero-structures of $GaAS$ and $GaAs - Al_xGa_{1-x}As$, where x defines the Aluminium mole fraction and is typically around 30%. The sample electronic density $n_S = 1.11 * 10^{11} cm^{-2}$ and the mobility is $\mu = 3 * 10^6 V^{-1} cm^2 s^{-1}$. This high mobility enables us to reach the fractional Hall effect regime at accessible magnetic fields (lower than 14 T). Details on the sample fabrication are given in Appendix B. The 2DEG is bound to the external circuit thanks to ohmic contacts (see figure 4.1). Co-planar 50Ω wave-guides designed by CST microwave studio and etched on a PCB (printed circuit board) bring the RF and DC signal to contacts (0) and (3) of the sample. The 6 contacts-geometry shown in figure 4.1 enables to measure separately the transmitted and reflected currents. The latter are accessible by voltage measurements on contact (1) and (4). Contacts (2) and (5) are grounded to avoid unwanted transmissions of the current from contacts (1) to (3), or (4) to (0).

It is important to note that the impedance mismatch between the co-planar wave-guides and the sample resistance (Hall resistance) is responsible for strong reduction of the RF power sent to the sample, as well as strong oscillations with the frequency (see Appendix C).

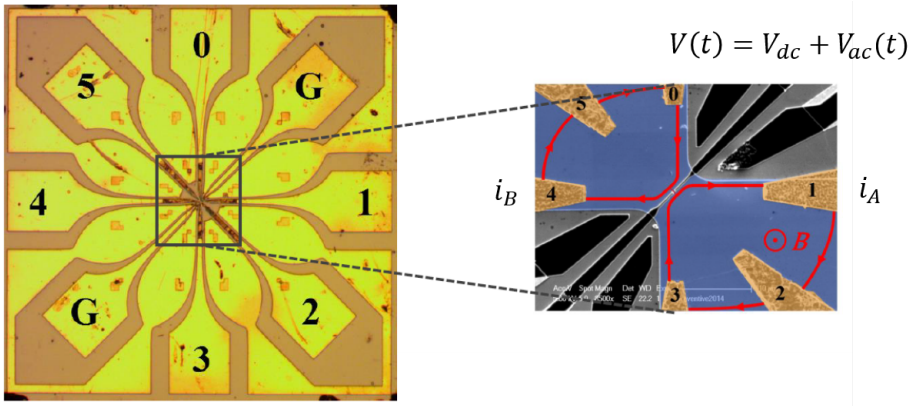

FIGURE 4.1: Left: PCB co-planar wave-guides, on which coaxial cables are connected to bring DC and RF signals. Right: SEM (scanning electron microscope) image of the sample. The blue part represents the 2DEG, the yellow part corresponds to the ohmic contacts.

4.2 General considerations on the setup

The range of temperature we need is fixed by many constraints:

- We need the temperature to be lower than the gap of the integer or fractional quantum Hall effect. This excitation gap depends crucially on the quality of the material in which the 2DEG resides. The state of the art technology currently yields samples with an excitation gap of the of the order of a few meV [85]. Thus the temperature has to be lower than approximately $10K$. This excitation gap also limits the range of bias that can be applied, leading to tunneling currents levels of the order of few $10nA$ and shot noise levels in the $10^{-28}A^2/Hz$ range.

- Within this range of bias (below $1mV$), we need to observe a regime for which the shot noise dominates the thermal noise. As the two contributions becomes equal when $2eV = k_BT$, we need temperatures lower than 1 K.

- Finally, in order to observe photo assisted effects, we need the frequency of the RF waves to be higher than the temperature: $hf >> k_BT$. The maximal frequency delivered by the AC source and for which the coaxial cables and circuit elements are well suited is 18 GHz, which means that the temperature has to be much lower than approximately 300

mK. Of course, the lower the temperature, the more relevant will be these photo-assisted effects.

We work with a Cryoconcept Helium free dilution refrigerator equipped with a 14.5 T Cryomagnetics coil, that enables to cool down the sample to a temperature of 18 mK, the temperature of the coolest stage. As the sample is connected to the room temperature instruments through coaxial lines and circuit elements, it is important for each of these components to be well thermalized with the different stages of the dilution fridge. The heat flow and voltage fluctuations brought by these elements lead to an effective temperature higher than 18mK. This so-called "electronic temperature" (to distinguish it from the actual temperature of the sample) is observable using shot noise measurements and is of the order of 30 mK. The reduction of this effective temperature is an experimental difficulty mainly treated in J.Dubois thesis [77].

A global scheme of the experimental setup is shown in figure 4.2. The DC voltage bias are delivered by voltage sources Yokogawa 7651 attenuated by a voltage divider to realize the DC polarization of the sample (see Appendix D). The RF source is a DC to 20 GHz microwave synthezizer Agilent N5183A MXG Analogic signal generator. Well-thermalized coaxial cables bring the DC and the RF signals from room temperature to the PCB. These two signals are added up thanks to a "bias-tee", as also illustrated in figure 4.2. The second RF line was added recently in order to perform Hong-Ou-Mandel measurements.

The DC-line from which a voltage is applied on the QPC is not shown. The V_{dc} source is actually a mixing of a DC signal plus a very-low frequency (270Hz) signal, needed for conductance measurements. Transmitted and reflected current fluctuations are transformed into voltage fluctuations across RLC resonators that are resonant around 2.5 MHz. These voltages V_A, V_B are first amplified by home made cryogenic amplifier (HEMT) at 3.6 K. A splitter then separates the low-frequency (kHz) signal from high-frequency (MHz) signal. The high frequency signal is amplified at room temperature by low noise commercial amplifiers NF SA-421F5 and go through a Chebyshev filter to finally be sent to a digital acquisition card ADLink 9826. The PC then computes the cross-correlation and auto-correlation spectra. The low frequency signal is amplified at room temperature by commercial amplifiers LI-75A and sent to the two lockins.

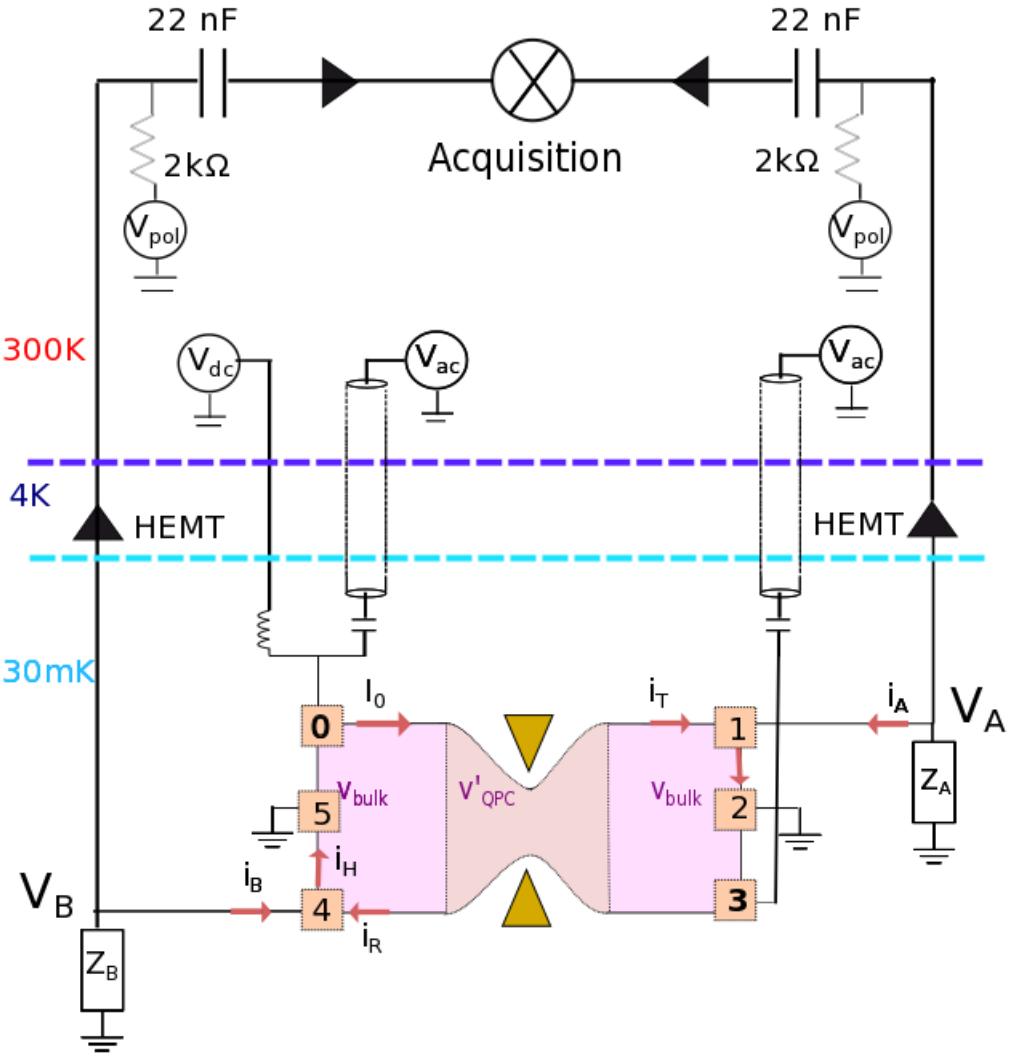

FIGURE 4.2: Global scheme of the experimental setup.

4.3 Power brought by the external circuit

Coaxial cables can be described by transmission lines designed to transfer electromagnetic energy towards one dominant mode of propagation that is the transverse electromagnetic mode (TEM), ensuring small energy losses. Two important aspects have to be considered when choosing the material of the coaxial cables bringing DC and RF signals to the sample. The first one is limiting the heat conduction between different stages of the Cryostat, while ensuring a good thermalisation of the inner conductor at the same time. Depending on its temperature, each stage of the cryostat is designed to accept a maximum heating power. The lower the temperature is, the smaller is the acceptable

power that mainly comes from the thermal short-cut introduced by the electrical wiring. If the set-up brings too much power, then the base temperature of the cryostat establishes at much higher temperature than the nominal base temperature (about $17mK$). Consequently, the heat flow carried by the coaxial cables must be estimated in order to ensure a base temperature as low as possible. This estimation, as well as the estimation of the thermalization length of coaxial cables and the choice of material, were done in J.Dubois PhD thesis [77].

The second aspect is to limit the electromagnetic radiation of circuits elements (voltage source connectors, attenuators, connectors, etc) on the sample. Photons associated to Johnson-Nyquist noise coming from the hot parts of the external circuit affect directly the electronic temperature of the sample, because they induce broadband voltage fluctuations ΔV^2. These fluctuations increase the effective electronic temperature by $\Delta T = e\Delta V^2/k_B$. Nyquist has derived the power spectrum of photons associated to resistor at a temperature T [35]. It is given by the energy of photon hf multiplied by the photon occupation number at frequency f:

$$S_V(f) = \frac{2Rhf}{e^{hf/k_BT} - 1} \tag{4.1}$$

The voltage fluctuations are : $\Delta V^2 = \int_0^\infty S_V(f)df$. The cut-off frequency of DC lines is estimated around $40kHz$, making the radiated power on the sample negligible (see Appendix D). At the opposite, the loss of the RF lines is weak until GHz frequencies, therefore the voltage noise is directly transmitted on a large bandwidth $\Delta f = 20GHz$ which corresponds to the loss specifications of the constructor. To estimate the voltage fluctuations seen at the end of RF lines on the sample, we have to sum of the contribution of each impedance R_k at temperature T_k over the bandwidth $\Delta f = 20GHz$, attenuated by a factor A_k:

$$\Delta V^2 = \sum_k \int_{\Delta f} df \frac{2R_k hf}{e^{hf/k_BT} - 1} A_k \tag{4.2}$$

Three $20dB$ attenuators are set respectively on the 3.6 K, 1 K and 100 mK stages, and are considered as 50Ω impedances. The $20dB$ attenuation corresponds to a reduction by a factor $A = 100$ of the PSD. The calculations made in M.Santin PhD thesis [83] showed that the main contribution to the thermal noise comes from the 100 mK stage. It was estimated that $\sqrt{\Delta V^2} = 1\mu V$, corresponding to a temperature of 12 mK. As a consequence, the thermal noise brought by RF lines considerably increases the electron temperature.

Now that we have briefly described the voltage (DC and RF) injection lines, we will focus on the measurement setup, starting by noise measurements.

4.4 Noise measurements

4.4.1 Data acquisition

The currents transmitted and reflected by the QPC are treated as a random classical stationary and ergodic variables $i(t)$ (corresponding to $i_T(t)$ and $i_R(t)$ in figure 4.2). The set of values taken by $i(t)$ corresponds to the current operator eigenvalues. The mean value and the variance give informations about the distribution of the variable $i(t)$. The fluctuations of $i(t)$ give rise to voltage fluctuations across the RLC resonators. These voltages $V_A(t)$ and $V_B(t)$ are amplified and recorded simultaneously by a digitizer (Acquiris U1071A-HZ4 from agilent instruments) that uses a memory size of Ns = 65472 points at a rate of 20Ms/s. As explained in Chapter 1, the Fourier components of the cross and auto correlation function are equal to the PSD $S_{V_AV_A}$ $S_{V_BV_B}$ and $S_{V_AV_B}$ at frequencies $f_n = n/2T$ (where T is the measurement time):

$$S_{V_AV_A}(f_n) = \langle \tilde{V}_A^2(f_n) \rangle / \delta f \tag{4.3}$$

$$S_{V_BV_B}(f_n) = \langle \tilde{V}_B^2(f_n) \rangle / \delta f \tag{4.4}$$

$$S_{V_AV_B}(f_n) = \langle \tilde{V}_A(f_n) \tilde{V}_B^*(f_n) \rangle / \delta f \tag{4.5}$$

Which allows to reconstruct the auto and cross-correlation spectra. In order to save time, the memory size is divided into two blocks: one stores new incoming data, a second operates fast Fourier transform (FFT) on the measured voltages in order to compute the PSD. Then 32732 points of V_A and V_B at a rate of 20 Ms/s (one measure every 50 ns) are measured in real-time. Therefore, the maximum frequency is 10MHz, and the resolution of the PSD spectra is $\delta f = 10 * 10^6 Hz/32732 = 305 kHz$. The FFT are computed thanks to a C++ software with high time-efficiency: 10000 averaged PSD takes 35 s experimentally whereas a pure data acquisition needs 33 s.

4.4.2 RLC resonator

The acquisition card works on a wide range of frequencies, but we are interested only by the signal in the MHz range in order to avoid 1/f noise and to make faster measurements. Taking into account the cable capacitance from the sample to the head of the fridge which is about $C_l = 200pF$, we need an inductance $L = 22\mu H$ in parallel with C_l to get a resonance frequency $1/\sqrt{LC_l}$ around 2 MHz. The resistance $R = 20k\Omega$ defines the height and width of the resonance peak of the equivalent impedance. Finally $C_1 = 9.4nF$ capacitance aims to cut the low frequency part in its branch, and the capacitance $C_2 = 100nF$ together with the resistance R act as a high pass filter with a cut off

frequency of 500Hz in order to avoid very low-frequency components. A schematic of the RLC resonator is shown in figure 4.3.

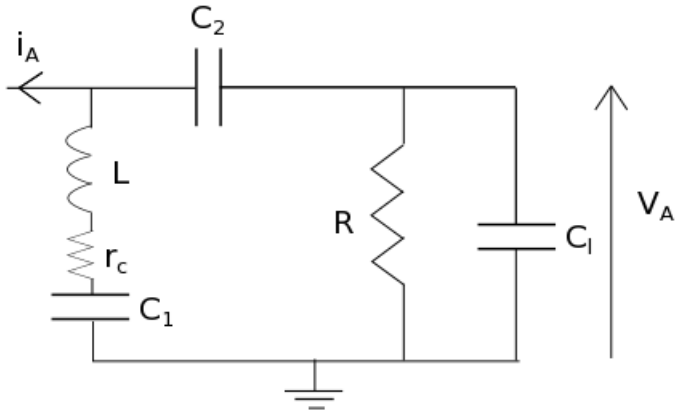

FIGURE 4.3: Scheme of the RLC resonator. r_c is the inner conductance of the Coil, that competes with the value of R to define the height of the impedance resonance peak.

Passive components are chosen so that they maintain a constant value from room temperature to 20 mK and are stable under high magnetic field. For resistance we use 0805 thin film resistor SMC whose value measured at 4 K varied of less than 5% from room temperature. Capacitors are also SMC 0805. The inductance is a Coilcraft ceramic chip inductor with no magnetic core. This inductor has a finite inner resistance r_c, that was measured to be equal to 9.5Ω at 300 K and zero magnetic field.

For MHz frequency, C_2 can be neglected, and the whole circuit is treated as an equivalent impedance and used to convert current fluctuations to noise fluctuations. The equivalent impedance $Z_{RLC}(\omega)$ is plotted in figure 4.4 for frequencies around the resonance, and for both RLC circuits (A and B).

We note that the RLC impedance has the same order of magnitude than the Hall resistance, so a non-negligible part of the current is flowing into it. To relate the measured voltage PSD of equation 4.3 to the transmitted and reflected current PSD (that are the quantities of interest), one can refer to the scheme of figure 4.2 and simply apply the current conservation (or Kirchoff laws) at contacts (1) and (4) to write: $i_A + i_T - i_H = 0$ and $i_B + i_R - i_H = 0$. This gives:

$$i_T(\omega) = V_A(\omega)(1/R_H + 1/Z_A(\omega)) = V_A(\omega)/Z_{eq,A}(\omega)$$
$$i_R(\omega) = V_B(\omega)(1/R_H + 1/Z_B(\omega)) = V_B(\omega)/Z_{eq,B}(\omega)$$

Where $\frac{1}{Z_{eq,A}} = \frac{1}{R_H} + \frac{1}{Z_A}$ (and same for line B). We call $V_{A,out} = G_A V_A$ and $V_{B,out} = G_B V_B$ the voltages after amplification ($G_{A,B}$ being the total amplification factors of

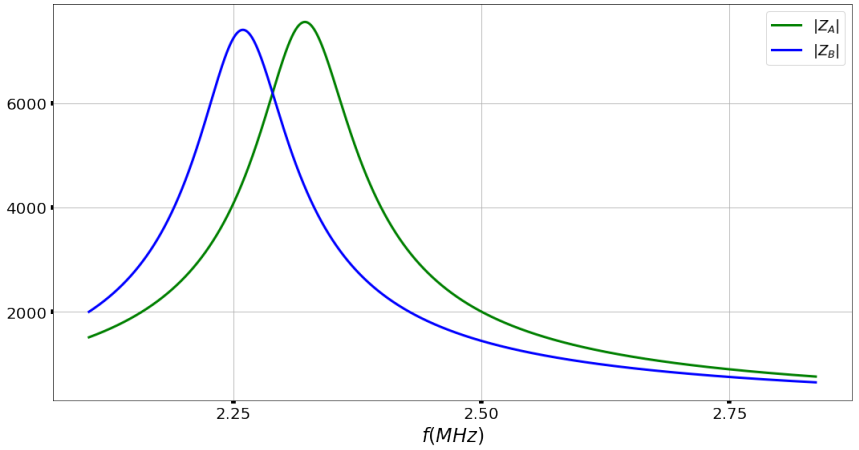

FIGURE 4.4: Absolute value of the RLC impedance for the two lines (in Ω). Because of the mismatch between the C_l values (that are found to be $219pF$ for line B and $231pF$ for line B), resonance frequencies are not equal. The RLC parameters were found from the noise calibration of paragraph 4.5.

measurements lines A and B). From the last equation we easily link the PSD of i_T and i_R to the PSD of $V_{A,out}$, $V_{B,out}$:

$$|V_{A,out}(\omega)|^2 = G_A^2|Z_{eq,A}(\omega)|^2|i_T(\omega)|^2$$
$$|V_{B,out}(\omega)|^2 = G_B^2|Z_{eq,B}(\omega)|^2|i_R(\omega)|^2$$
$$V^*_{A,out}(\omega)V_{B,out}(\omega) = G_A G_B Z^*_{eq,A}(\omega)Z_{eq,A}(\omega)i^*_T(\omega)i_R(\omega)$$

The MHz frequencies range being smaller than all other energy scales, $S_{ii}(\omega)$ is independent of the frequency in the bandwidth of RLC resonators, and is simply proportional to the variance of $i(t)$. Thus if we take the integral of $V^*_A V_B$ over the RLC bandwidth we get:

$$|i_T|^2 = \int |V_{A,out}(\omega)|^2 d\omega / C_{aa} \tag{4.6}$$
$$|i_R|^2 = \int |V_{B,out}(\omega)|^2 d\omega / C_{bb} \tag{4.7}$$
$$i^*_T i_R = \int V^*_{A,out}(\omega)V_{B,out}(\omega)d\omega / C_{ab} \tag{4.8}$$

Where $C_{aa} = G_A^2 \int |Z_{eq,A}|^2 d\omega$, $C_{bb} = G_B^2 \int |Z_{eq,B}|^2 d\omega$, and $C_{ab} = G_A G_B \int Z^*_{eq,A} Z_{eq,B} d\omega$. As for MHz frequency range and 17 mK temperature $\hbar\omega \ll k_B T$, the cross correlation $i^*_T i_R$ should correspond to the zero-frequency current noise, that is of course a real value. Then from the previous expression of $i^*_T i_R$, we should have:

$$i^*_T i_R = \frac{Re(\int V^*_{A,out} V_{B,out} d\omega)}{Re(C_{ab})} = \frac{Im(\int V^*_{A,out} V_{B,out} d\omega)}{Im(C_{ab})} \tag{4.9}$$

allowing us to convert voltages cross-correlation to the current cross-correlation.

The final PSD of $V_{A,out}$ and $V_{B,out}$ include the noise of the amplification chain, that we will detail in the next section. It is actually the dominant part of the auto correlation spectra, but we can get rid of it thanks to ON-OFF measurement technique. An example of spectra for auto-correlations functions (or PSD) of $V_{A,out}$ and $V_{B,out}$ is shown in figure 4.5. The main source of noise is due to the amplifiers and does not appear in the cross-

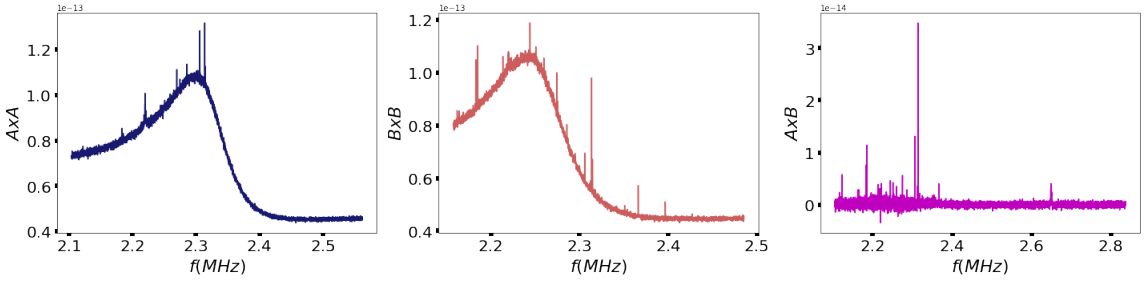

FIGURE 4.5: Noise spectra for $\nu = 2/5$ and $T = 100mK$, for AutoA (left figure) AutoB (middle) and Cross correlation (right figure).

correlation spectra (as the fluctuations on both measurement lines are uncorrelated). On top of this white noise, we can observe the resonance due to the thermal noise of the RLC circuit in parallel with the sample resistance. The 1/f noise contribution is also visible and responsible for the observed asymmetry with respect to the resonance frequency. One interesting thing to note in the cross-correlation spectrum is that the noise increases proportionally to the mean value of the PSD, as it is expected for a Gaussian variable.

Next we will present the technique used to determine the RLC parameters, in particular the inner resistance of the coil r_c and the capacitance of the lines C_l. To calculate the conversion factors C_{aa}, C_{bb}, C_{ab} we also need to know the total gains G_A and G_B of the two amplifiers on lines A and B.

4.5 Noise calibration

In order to determine the RLC parameters and the total gains G_A and G_B, we measure the Johnson-Nyquist noise $S_{A,A} = S_{V_AV_A}$ (resp. $S_{B,B} = S_{V_BV_B}$) given by the PSD of V_A (resp. V_B) when $V_{dc} = 0$. Thanks to the chirality of edge states and the 6-contact geometry of our sample, when $i_T = i_R = 0$, the equilibrium noise $S_{A,A}$ is decorrelated from $S_{B,B}$ (and independent of the gate voltage). The sample behaves as a simple Hall resistance $R_H = \frac{h}{\nu e^2}$ in parallel with the RLC resonators Z_A (resp. Z_B), as illustrated in figure 4.6. We note $1/Z_{eq,A} = 1/Z_A + 1/R_H$ and $1/Z_{eq,B} = 1/Z_B + 1/R_H$. When the

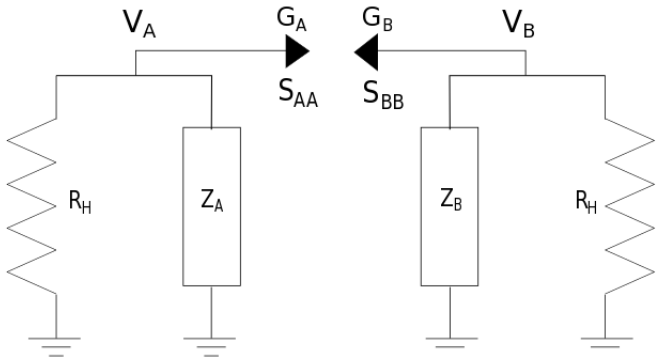

FIGURE 4.6: Equivalent circuit of the sample and the RLC resonators at equilibrium ($V_{dc} = 0$).

RLC resonators and the sample are at the same base temperature T_0, we get:

$$S_{A,A}(\omega, T_0) = G_A^2 4k_B T_0 Re(Z_{eq,A}(\omega)) + S_{G_A} \tag{4.10}$$

$$S_{B,B}(\omega, T_0) = G_B^2 4k_B T_0 Re(Z_{eq,B}(\omega)) + S_{G_B} \tag{4.11}$$

where S_{G_A} and S_{G_B} are white noises brought by the amplifiers of lines A and B. T_0 is ideally the temperature of the mixing chamber, that is the coolest stage of the dilution fridge to which the sample as well as the RLC resonators are thermalized. The thermometer indicates $T_0 = 17mK$, but the actual temperature of the sample T_s may be higher than T_0 because of a bad thermalization. As far as $T_s - T_0 << T_0$, equation (4.11) holds. The mixing chamber temperature can be increased by injecting current on a resistive heater. The injected current (or power) is regulated in order to reach the target temperature T thanks to a PID system. In order to cancel the noise of the amplifiers (that is independent of the mixing chamber temperature), we consider the quantities:

$$\Delta S_{A,A}(\omega, T - T_0) = S_{A,A}(\omega, T) - S_{A,A}(\omega, T_0) = G_A^2 4k_B (T - T_0) Re(Z_{eq,A}(\omega)) \tag{4.12}$$

$$\Delta S_{B,B}(\omega, T - T_0) = S_{B,B}(\omega, T) - S_{B,B}(\omega, T_0) = G_B^2 4k_B (T - T_0) Re(Z_{eq,B}(\omega)) \tag{4.13}$$

We measure $S_{eq,A/B}(\omega, T)$ for different values of T between $40mK$ and $100mK$, and we plot the mean value of $\Delta S_{eq,A/B}(\omega, T - T_0)$ over a large interval $\Delta f = [2.1, 2.8]MHz$ versus T. This plot is shown in figure 4.7 for $\nu = 2$. The points of figure 4.7 are well aligned, in agreement with equation (4.13) and thus with a good thermalization of the sample with the mixing chamber. A deviation from the linear behaviour is often observed for temperatures below $50mK$, indicating that the thermalization is less efficient for low temperatures. In that case we consider the slope given by the points at $T > 50mK$ to

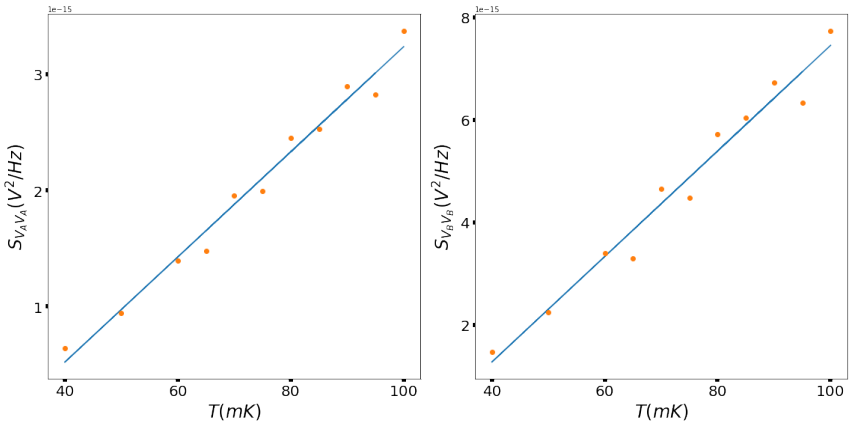

FIGURE 4.7: $\langle \Delta S_{A,A}(T - T_0) \rangle$ (left figure) and $\langle \Delta S_{B,B}(T - T_0) \rangle$ (right figure) versus mixing chamber temperature T

.

determine the base temperature T_0. The latter is given by the crossing point between the x-axis and the blue straight lines of figure 4.7. It is found to be equal to $28mK$ for line A and $27mK$ for line B (with around 5% incertitude).

With the knowledge of the base temperature T_0, we can now use the spectra of $\Delta S_{eq,A/B}(\omega, T - T_0)$ to determine the gains G_A and G_B, as well as r_c and C_l values for lines A and B. These are fitting parameters, while the other parameters of the RLC circuits are fixed to their values measured at room temperature: $R = 20k\Omega$, $L = 22\mu H$, $C_1 = 9.4nF$ (cf figure 4.3). The plot of $\Delta S_{A,A}(\omega, T - T_0)$ and $\Delta S_{B,B}(\omega, T - T_0)$ using equation (4.13) is shown in figure 4.8 for $\nu = 2$ and $T = 100mK$. The fit reproduces well the

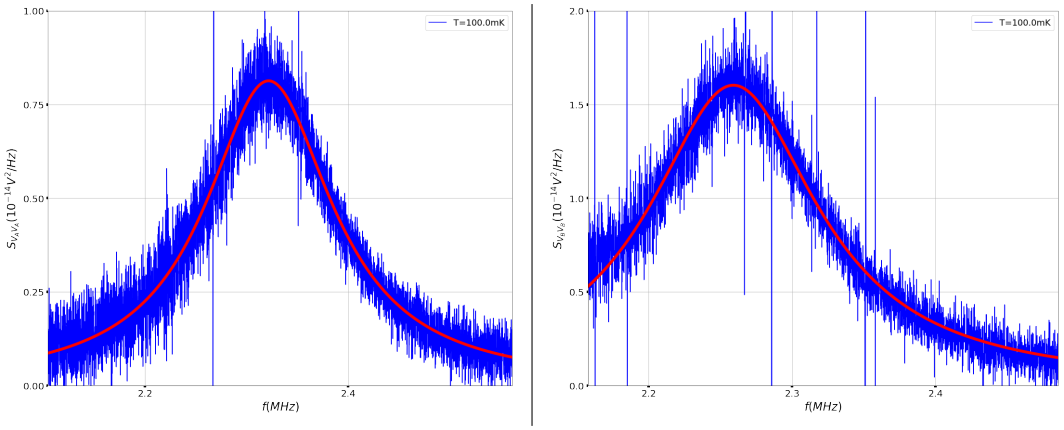

FIGURE 4.8: $\Delta S_{A,A}(\omega, T - T_0)$ (left figure) and $\Delta S_{B,B}(\omega, T - T_0)$ (right figure) at $T = 100mK$ and fit using equation (A.2) and r_c,C_l and $G_{a/b}$ as fitting parameters.

noise spectra. We make this fit for various values of T, from which we extract values of $r_c, G_{A/B}, C_l$ reported on figure 4.9 (for line A only). We note that the fitting parameters seems to converge at high temperature, but show more fluctuations at low temperature. This indicates that the fit of $\Delta S_{eq,A/B}(\omega, T - T_0)$ is more accurate for high values of T,

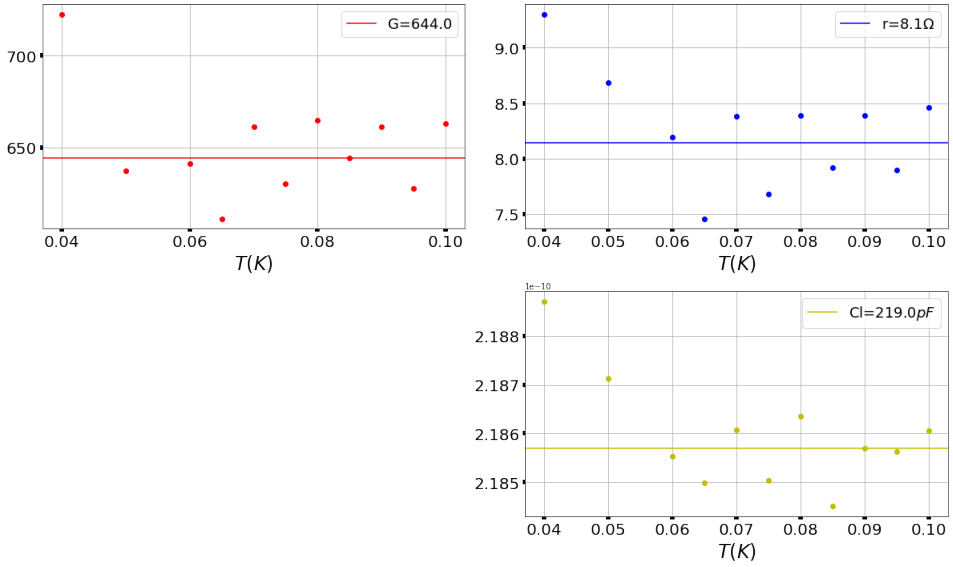

FIGURE 4.9: RLC parameters r_c,C_l and G_A found from the fit of $\Delta S_{A,A}(\omega, T - T_0)$ at different temperatures T.

where the signal over noise ratio is higher. Thus we take the mean value of the fitting parameters found for $T > 50mK$ only (indicated in the legend).
Using these mean values of r_c (8.1Ω for line A and 7.9Ω for line B) and C_l (219pF for line A and 231pF for line B), we plot the the quantities $|Z_{eq,A}|^2$, $|Z_{eq,B}|^2$ and $Re(Z^*_{eq,A}Z_{eq,B})$ versus frequency (figure 4.10). To get $C_{aa} = G_A^2 \int |Z_{eq,A}|^2 d\omega$, $C_{bb} = G_B^2 \int |Z_{eq,B}|^2 d\omega$,

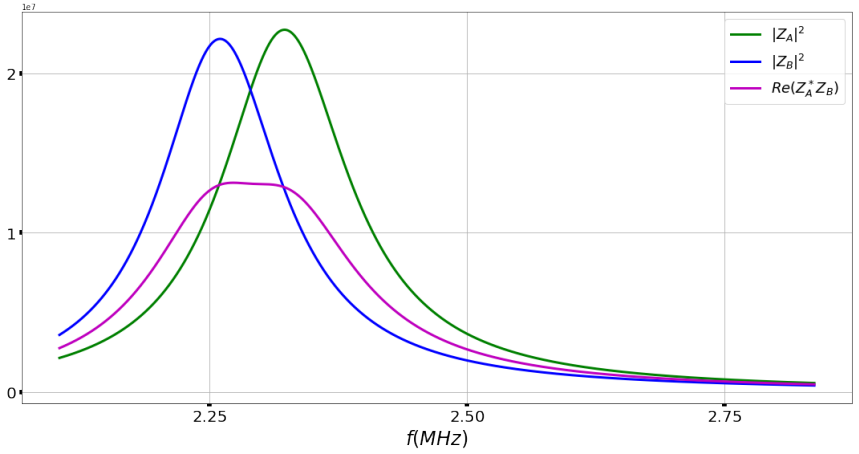

FIGURE 4.10: $|Z_{eq,A}|^2$, $|Z_{eq,B}|^2$ and $Re(Z^*_{eq,A}Z_{eq,B})$ for $\nu = 2$ and RLC parameters found from the fit of $\Delta S_{A,A}(\omega, T - T_0)$.

and $C_{ab} = G_A G_B \int Z^*_{eq,A} Z_{eq,B} d\omega$, we only have to integrate the curves of figure 4.10 over Δf. We get:

$$C_{aa} = 2.59 * 10^{12}\Omega^2, \quad C_{bb} = 4.74 * 10^{12}\Omega^2, \quad C_{ab} = (2.89 - 1.49j) * 10^{12}\Omega^2$$

These values were determined with around 6% accuracy, estimated from the spreading of the gain and RLC parameters shown in figure 4.9. The inner resistance r_c and the line capacitance C_l found from the calibration at $\nu = 2$ are fixed for next calibrations at other filling factors. However the gain of the amplifiers $G_{A,B}$ can vary from one calibration to the other because of the instability of the low-temperature amplifiers. In table 4.1, we report the gain found at different filling factors ν.

	G_A	G_B
$\nu = 2$	651	907
$\nu = 2/3$	903	958
$\nu = 2/5$	915	940

TABLE 4.1: Gain factors from noise calibration at different filling factors ν.

4.6 Amplification chain

The amplification chain is composed of two voltage-to-voltage amplifiers in series. The first is a hand made cryogenic amplifier thermally fixed to the 3.6 K stage in the cryostat. The second one is a commercial amplifier NF SA-421F5 at room temperature, powered with external battery. It has a gain of $46dB$ (400) and a low noise density: $0.5nV/\sqrt{Hz}$. Cryogenic amplifiers used for the experiments presented in this thesis have been developed by Thibaut Jullien [84], here we report only the general principle. It is is based on the sensitivity of a High Electron Mobility Transistor (HEMT) to its gate voltage V_G. A polarization resistance R_{pol} imposes a current I through the HEMT, thus: $V_{HEMT}(V_G) = IR_{HEMT}(V_G)$. The resistance of the HEMT $R_{HEMT}(V_G)$ strongly depends on the voltage applied to the gate V_G, that modify the electron density of the 2DEG. V_G is modulated by the input voltage V_{in} ($V_G = V_{in}$). The capacitance C_2 of the RLC circuits (figure 4.3) cuts DC components coming from the sample, so that V_{in} is composed of only voltage fluctuations. These fluctuations δV_{in} makes the resistance R_{HEMT} fluctuates as well. In the case of small variations δV_{in}, we can write:

$$R_{HEMT}(V_{in}) = R_{HEMT}(V_{in} = 0) + \frac{\partial V_G}{\partial V_{in}}\delta V_{in}$$

As the current I through the HEMT is constant, voltage fluctuations of V_{in} are recovered in V_{HEMT}:

$$V_{HEMT} = IR_{HEMT}(V_{in}) = IR_{HEMT}(V_{in} = 0) + I\frac{\partial R}{\partial V_{in}}\delta V_{in}$$

The 22 nF capacitance before the commercial amplifier at 300 K cuts the DC voltage (cf figure 4.2). Thus, the output voltage V_{out} is:

$$V_{out} = I\frac{\partial R}{\partial V_{in}}\delta V_{in}$$

The gain of this amplifier is thus $G = I\frac{\partial R}{\partial V_{in}}$. It is proportional to the injected current, thus to the polarisation voltage V_{pol}. However, the quantity $\frac{\partial R}{\partial V_{in}}$ also depends on the current I, thus the gain G has actually non-trivial variations with V_{pol}. We choose $V_{pol} = 7.89V$ for cryo-amplifier A and $V_{pol} = 8.1V$ for cryo-amplifier B for most of the measurements presented here.

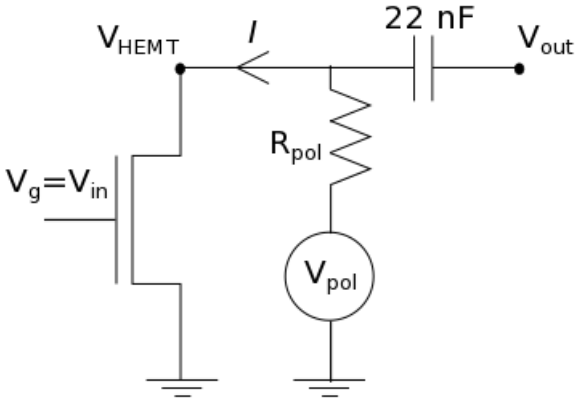

FIGURE 4.11: Simplified schematic of HEMT amplifiers. V_{in} is the voltage to be amplified, thus V_A or V_B.

4.7 Measurements accuracy

A good estimation of the uncertainty on the mean value of one noise spectrum over a frequency window Δf is given by the effective standard deviation $\sigma_{eff} = \sigma/\sqrt{N_{freq}}$, where N_{freq} is the number of frequency points in the spectrum ($N_{freq} = \Delta f/\delta f$, with $\delta f = 305Hz$). Indeed, on the frequency range Δf, the current noise is frequency-independent. Thus the precision of noise measurements should increase with Δf (or N_{freq}). However, we are limited by the 1/f noise. Moreover, it is useless to include large frequencies for which the signal is very weak (far from the RLC resonance).
For the next study, we choose: $\Delta f = [2.1, 2.83]MHz$. We want to estimate the uncertainty on the mean value of the spectra for different values of N, that is the number of PSD measurements done by the acquisition card (or number of averages). According to the standard limit theorem and to the previous considerations, the mean value of a noise spectrum averaged N times is a variable that follows a Gaussian distribution with

standard deviation $\sigma_N = \sigma_{eff}/\sqrt{N} = \sigma/\sqrt{N * N_{freq}}$. To estimate σ_N, we first take a noise spectrum averaged during a long time (around 40 min), corresponding to $N = 10^5$. This study was made at filling factor $\nu = 4$, and for an intermediate value of reflection by the QPC and of V_{dc} such as the cross- correlation is finite. We measure the noise

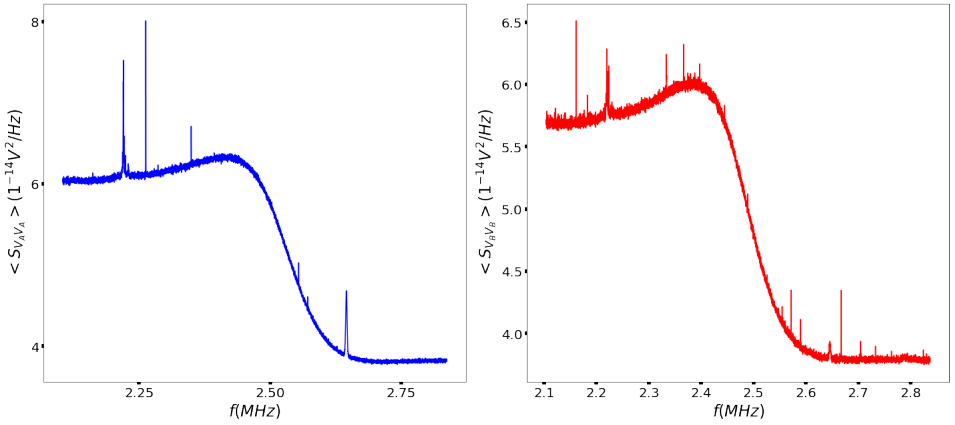

FIGURE 4.12: Auto correlation $S_{VV}(f)$ spectra for $N = 10^5$. Left figure: Auto A, right figure: Auto B.

for N between 1000 (30 s of measurement time) and 15 000 (around 10 min), and we subtract the spectra obtained for $N = 10^5$ to estimate the standard deviation. These differences are plotted in figure 4.13. We clearly see that the spreading of the points is reduced while increasing the number of averages N.

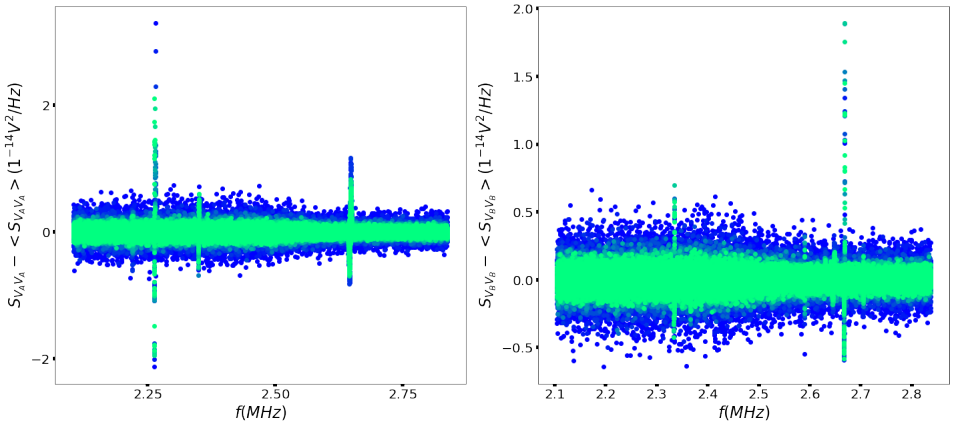

FIGURE 4.13: $S_{VV}(N) - S_{VV}(N = 10^5)$ for N between 1000 and 15 000 (auto correlation spectra). Left figure: Auto A, right figure: Auto B.

The values of $\sigma_N \sqrt{N_{freq}}$ found from these noise measurements versus the number of averages N are plotted in log scale in figure 4.14.

We see the expected linear behaviour, with small deviations for the Auto A at small N. These deviations may be due to the noisy peaks that are more pronounced in Auto A than in Auto B spectrum, increasing the value of σ_N independently of N. The slopes

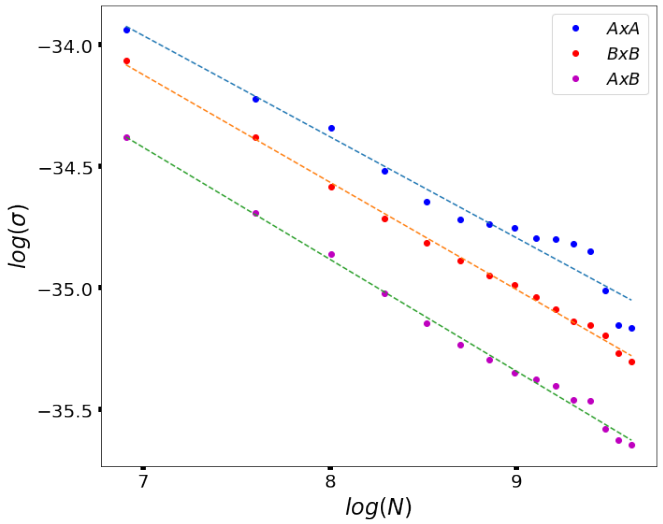

FIGURE 4.14: $\sigma_N\sqrt{N_{freq}}$ values extracted from the spectra of figure 4.13), versus number of averages N in log scale.

extracted from the linear fit of figure are 0.42 for Auto A, 0.44 for Auto B and cross correlation. These values are close to the expected value of 0.5 for $\sigma_N \propto 1/\sqrt{N}$. Some values of σ_N for auto and cross-correlations are reported in table 4.2. These values have

N	σ_N(AxA)	σ_N(BxB)	σ_N(AxB)
4000	1 e-17	8.6 e-18	6.3e-18
8000	8.2 e-18	6.5 e-18	4.5 e-18
14 000	5.4 e-18	4.7e-18	3.3 e-18

TABLE 4.2: σ_N in V^2/Hz for some values of N, for the auto and cross-correlations.

to be compared with the level of the shot noise to be measured, around $10^{-17}V^2/Hz$ and $5 * 10^{-16}V^2/Hz$ approximately (depending on the filling factor ν and the reflected current). From table 4.2, we need at least $N = 14000$ to have an acceptable signal over noise ratio.

Instead of one long PSD measurement, we prefer to average many short-time (few seconds) "ON-OFF" measurements with small values of N (around N=700). The standard deviation is multiplied by $\sqrt{2}$ due to the "ON-OFF" operation. But the advantage of such a technique is to avoid time deviations of the background noise (mainly due to the HEMT), that can occur within few minutes. These time-deviations limit the precision of an entire noise curve (bias sweep), that is typically measured within one night (or 9 hours) with not more than few $10^{-18}V^2/Hz$ precision.

The exact evaluation of the uncertainty on a shot noise measurement is a quite complicated task. Indeed, we have to take into account not only the error given by the standard deviation, but also the error on the estimated gains of the amplifiers through the noise calibration procedure described in paragraph 4.5. The determination of the

conversion factors C_{aa}, C_{bb}, C_{ab} can sometimes be the largest source of error, especially at low filling factors ν where the RLC resonance is short-circuited by the low sample resistance $R_H = h/\nu e^2$. Moreover, the HEMT gain can deviate within one or a few days. To make sure that the gain did not vary during one shot noise measurement, we usually make many bias sweeps (that takes around one hour each) and we average similar curves only. Moreover, we make as regular noise calibration as possible (around one per week).

Now that we have a good overview on noise measurements technique, that is the most challenging point of the experiment, we will detail DC conductance measurements.

4.8 Conductance measurements

Conductance measurements are made at kHz frequency (270 Hz more precisely) thanks to a lockin technique which is very efficient to filter all other components of the signal. At this frequency the capacitance of the cable C_l is not relevant anymore. C_2 being approximately ten times higher that C_1, we replace the RLC circuit by a simple high pass filter with a cutoff frequency $1/RC_2 = 500Hz$, as illustrated in figure 4.15.

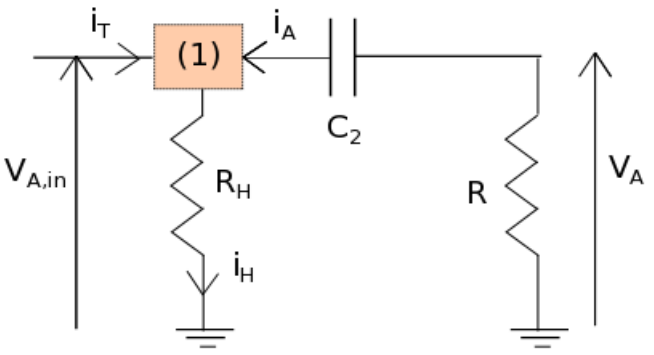

FIGURE 4.15: Equivalent circuit at kHz frequencies for the transmitted current measurements. We could draw the same scheme for the reflected current measurements (on line B).

The voltage V_A across the resistance R is amplified and measured by the lock-in on both measurement lines. To relate V_A to the transmitted (or reflected) current by the QPC, we can again apply the current conservation (or Kirchoff laws) at contacts (1) and (4)

to write $i_A + i_T - i_H = 0$ and $i_B + i_R - i_H = 0$. This gives:

$$i_T(\omega) = \frac{V_{A,in}(\omega)}{R_H} + \frac{V_A(\omega)}{R} = V_A(\omega)(\frac{1}{R} + \frac{1}{R_H}(1 + \frac{1}{RC_2\omega j}))$$
$$i_R(\omega) = \frac{V_{B,in}(\omega)}{R_H} + \frac{V_B(\omega)}{R} = V_B(\omega)(\frac{1}{R} + \frac{1}{R_H}(1 + \frac{1}{RC_2\omega j}))$$

where $R_H = h/\nu e^2$ is the Hall resistance. The voltage after amplification is called $V_{out,A/B} = G_{A/B}V_{A/B}$. We note that although we used the same notations, the gains of the low-frequency part of the signal (conductance measurements) are not the same than the gains of the high-frequency part (used for noise measurements), as we use different kind of room-temperature amplifiers.

The transmitted (resp. reflected) current is thus proportional to $V_{out,A}$ (resp. $V_{out,B}$) with a prefactor that depends on the filling factor ν:

$$i_{T,R}(\omega) = y_{A,B}(\omega)V_{out,A/B}(\omega) \quad \text{with} \quad y_{A,B}(\omega) = (\frac{1}{R} + \frac{1}{R_H}(1 + \frac{1}{RC_2\omega j}))/G_{A,B} \quad (4.14)$$

Now let's focus on the lockin technique used for conductance measurements. The lockin amplifier deliver a small AC signal in addition to the DC bias on contact 0, at a chosen frequency $\omega = 2\pi f$. This generates a transmitted and reflected current that can have components at the frequency f and eventually higher harmonics. The lockin takes the input signal $V_{out,A}$ (or $V_{out,B}$), multiplies it by the reference signal that has the same frequency f (either provided from the internal oscillator or from an external source), and integrates it over a specified time. The integration time τ has to be higher than the period $1/f$, for $f = 270Hz$ we usually choose $\tau = 0.1s$. Noise at frequencies very close to the reference frequency will result in very low frequency AC outputs from the phase-sensitive detector. Their attenuation depends upon the low pass filter bandwidth. A narrower bandwidth will remove noise sources very close to the reference frequency; a wider bandwidth allows these signals to pass. The low pass filter bandwidth determines the bandwidth of detection. The resulting signal is a DC signal, where the contribution from any signal that is not at the same frequency as the reference signal is attenuated close to zero.

The amplitude V_0 of the signal delivered by the lockin on the sample is small enough (around some μV) so that we can linearize the transmitted (or reflected current) at the lockin frequency ω: $i_T(\omega) = \frac{\partial I(eV_{dc},\omega)}{\partial V_0}V_0$. The work of Ref [86] relates the generalized admittance $G(eV_{dc},\omega) = \frac{\partial I(V_{dc},\omega)}{\partial V_0}$ to the DC current (for low enough AC amplitude V_0):

$$G(V_{dc},\omega) = \frac{e}{\hbar\omega}(I_{dc}(eV_{dc} + h\omega) - I_{dc}(eV_{dc} - h\omega)) \quad (4.15)$$

The step of the voltage applied on the sample being of the order of μV, we have $h\omega \ll eV_{dc}$, thus equation 4.15 gives: $G(V_{dc},\omega) = \frac{\partial I_{dc}}{\partial V_{dc}}$. Thus the lockin measurement

of $V_{out,A}(\omega)$ (resp. $V_{out,B}(\omega)$) gives access to the DC-conductance of the transmitted current $\frac{\partial I_T}{\partial V_{dc}}$ (resp. the reflected current $\frac{\partial I_R}{\partial V_{dc}}$) :

$$V_{out,A}(\omega) = \frac{i_T(\omega)}{y_A(\omega)} = \frac{V_0}{y_A(\omega)} \frac{\partial I_T}{\partial V_{dc}}, \qquad V_{out,B}(\omega) = \frac{i_R(\omega)}{y_B(\omega)} = \frac{V_0}{y_B(\omega)} \frac{\partial I_R}{\partial V_{dc}}$$

From equation (4.14), the conversion factor $y_A(\omega)/V_0$ is proportional to the Hall conductance $\nu e^2/h$. We determine it thanks to conductance plateau measurements, assuming that $\frac{\partial I_T}{\partial V_{dc}} = \frac{\nu e^2}{h}$ when the QPC is open, and $\frac{\partial I_R}{\partial V_{dc}} = \frac{\nu e^2}{h}$ when the QPC is closed. An example of conductance calibration is given in Chapter 2 for $\nu = 2$. In figure 4.16 we report the values of $y_{A/B}(\omega)/V_0$ found from the calibration at filling factors $\nu = 4, 3, 2, 2/3$, for $\omega = 2\pi * 270Hz$ and $V_0 = 4\mu V$ (corresponding to $V = 0.5V$ at the lockin output). The

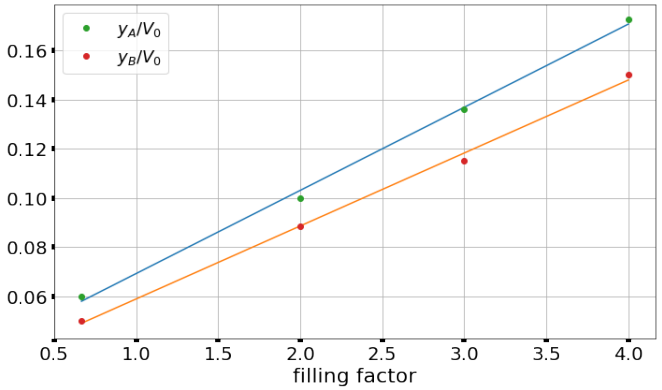

FIGURE 4.16: y_A/V_0 and y_B/V_0 versus filling factor ν, from lockin measurements at frequency $f = 270Hz$ and output amplitude $V = 0.5V$.

uncertainty on $y_{A,B}/V_0$ being of only 1%, we did not represent the error bars on the figure. The alignment of the points of figure 4.16 give us confidence on the measured Hall conductance, even though our experimental setup is not as accurate as a Hall bar.

Chapter 5

Experimental results at $\nu = 2$

We first made measurements at filling factor $\nu = 2$, reached for a magnetic field of 2.3T. Before making HOM measurements, we first need to recover previous results [83][6], checking that:
- The DC transport can be well described by the scattering approach described in part 3.2.2.
- The transport with an AC signal can be well described by photo-assisted effects using the Floquet formalism detailed in paragraph 3.2.3.

5.1 Conductance plateaus

We first need to characterise the regime $\nu = 2$ by checking that the conductance plateaus are separated by the quantum of conductance e^2/h. This requires conductance measurements while sweeping the gate voltage V_{gate}. We call $G_T = \frac{\partial I_T}{\partial V_{dc}}$ (resp. $G_R = \frac{\partial I_R}{\partial V_{dc}}$) the conductance measured on line A (resp. B). We perform lockin measurements at $270Hz$, and with an excitation amplitude of $1V$, that corresponds to approximately $5\mu V$ on the sample (see Appendix D). In figure 5.1, we observe two conductance plateaus spaced by e^2/h, confirming that we are in the regime of the integer Hall effect with $\nu = 2$. We did not deplete more the QPC region in order to avoid an irreversible electronic density modification (that would be problematic for studies in the FQHE). The conversion factors y_A, y_B between lockin voltages and G_T, G_R (cf. part 4.8) are determined assuming that $G_T = 2e^2/h$ at open QPC, and $G_R = e^2/h$ on the second plateau. They are found to be:

$$y_A = 0.0956\frac{e^2}{Vh} \quad y_B = 0.0884\frac{e^2}{Vh}$$

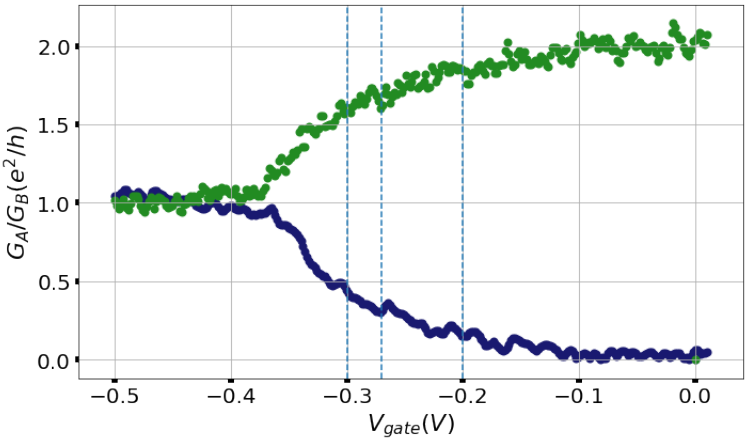

FIGURE 5.1: Conductance plateaux at zero DC bias. The dashed lines correspond to the gate voltages chosen to make noise measurements.

The accuracy on y_A, y_B (a few %) is limited by the leak on information on the transverse conductance (or transport through the bulk), that may be small but finite. This defines the level of accuracy for the next conductance measurements.

At $\nu = 2$, we can use the picture of two edge states that are transmitted one by one (without mixing between them) by the QPC. On a given plateau, an integer number of edge states is completely reflected or transmitted. In between the two first plateau shown in figure 5.1, the inner edge state is partitioned while the outer edge state is completely transmitted by the QPC. This situation is illustrated in figure 5.2. We can define transmission D and reflection R coefficients of the inner edge state such as: $G_T = (1 + D)\frac{e^2}{h}$, and $G_R = R\frac{e^2}{h}$. Current conservation implies that $G_T + G_R = 2e^2/h$, or $D + R = 1$ for all V_{gate} and bias V_{dc}. Next, we detail the measurements at different reflection coefficients R corresponding to various gate voltages ($V_{gate} = -0.2V, -0.27V, -0.3V$).

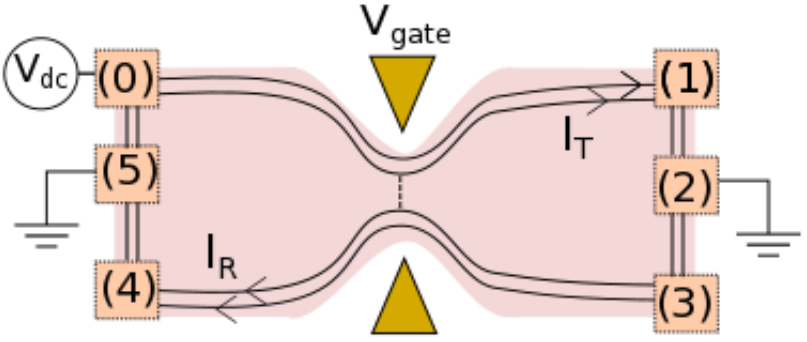

FIGURE 5.2: Sample schematic at $\nu = 2$: we work in the regime where only the inner edge state is partitioned by the QPC.

5.2 Measurements at $V_{gate} = -0.2V$

5.2.1 Conductance

We first look at the I-V characteristic by sweeping the bias V_{dc} from $-88\mu V$ to $88\mu V$. This bias range has been evaluated using the DC injection line circuit (cf Appendix D), it corresponds to voltages delivered by the DC source between -0.2V and 0.2V. We

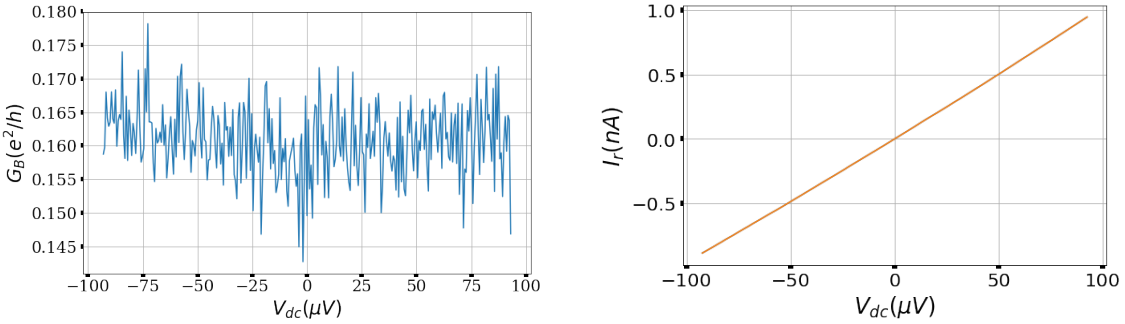

FIGURE 5.3: Conductance and reflected current for $V_{gate} = -0.2V$. The small non linearity visible in the conductance (left figure) is not visible anymore in the integral of it, that is the backscattered current (right figure).

see from figure 5.3 that the I-V characteristic is linear, and approximately 16% of the current carried by the inner edge state is reflected. In figure 5.4, we plot G_R, G_T as well as the sum $G_R + G_T$.

As expected from current conservation, $G_T + G_R = 2e^2/h$ independently of V_{dc}.

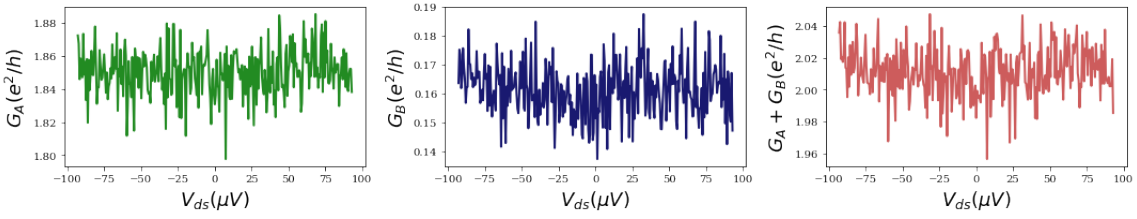

FIGURE 5.4: Transmitted and reflected conductance $G_A = G_T$ and $G_B = G_R$), as well as the sum of both for $V_{gate} = -0.2V$.

5.2.2 DC shot noise (DCSN)

Let's now turn to shot noise measurements (or measurements of the fluctuations of I_T and I_R). Using the noise calibration technique described in part 4.5, we determined the RLC parameters and the total gains of line A and B: $G_A = 640$, $G_B = 907$. Taking an integration interval of $\Delta f = [2.1, 2.8]MHz$ (that widely includes the resonance of both RLC circuits), the conversion factors between noise fluctuations and current fluctuations

are:

$$C_{aa} = 2.59 * 10^{12}\Omega^2, \quad C_{bb} = 4.74 * 10^{12}\Omega^2, \quad C_{ab} = (4.9 - 2.56j) * 10^{12}\Omega^2 \tag{5.1}$$

These conversion coefficients have been estimated with a maximum error of 5%. The results for the cross and auto-correlations are shown in figure 5.5.

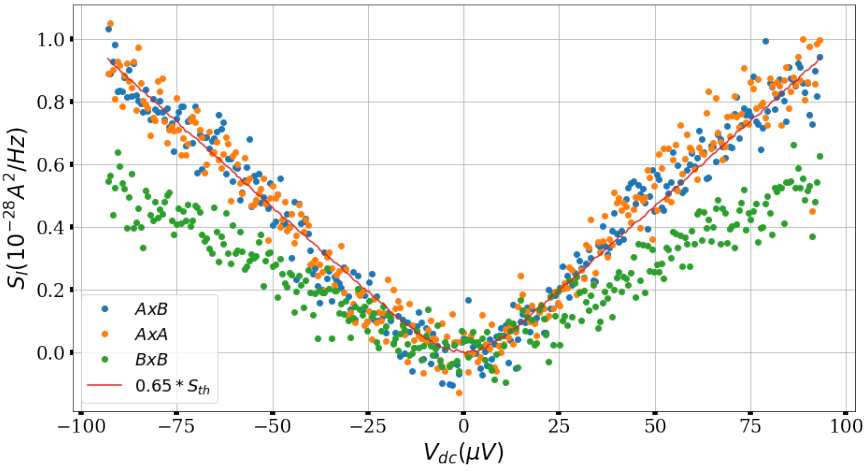

FIGURE 5.5: Cross and auto-correlation functions versus DC bias V_{dc} at $V_{gate} = -0.2V$.

At this stage, two important precisions are needed:

- Each experimental point of figure 5.5 corresponds to the mean value over Δf of a noise spectrum averaged $N = 700$ times by the acquisition card. Three more averaging are done over three identical bias sweeps. This method makes it possible to detect any variations of the gains G_A, G_B during the measurements while inspecting each bias sweep separately. The number of averages for each point is thus 2100, which gives a sufficient accuracy for this regime. Moreover, we always take the difference between the noise at finite V_{dc} and the noise at $V_{dc} = 0$. In this way, we cancel the thermal noise in the auto correlations, as well as undesired spurious peaks in the spectra of the auto and cross-correlations.

- If the imaginary part of the cross correlation was only due to the mismatch between the two RLC resonances, we would have: $\frac{Re(S_{cross})}{Re(C_{ab})} = \frac{Im(S_{cross})}{Im(C_{ab})}$ (equation (4.9)). However in figure 5.6 we see a clear difference between both quantities. It may be due to an additional phase rotation in the measurement lines. To take it into account, we found the angle γ satisfying: $\cos(\gamma)Re(A \times B) - \sin(\gamma)Im(A \times B) = |A \times B|$. The angle γ was found to be identical for all noise measurements. We always plot the quantity $\cos(\gamma)Re(A \times B) - \sin(\gamma)Im(A \times B)$.

Now that we have solved these experimental details, we can focus on physical results. The continuous red curve of figure 5.5 is a fit of the cross-correlation using the scattering

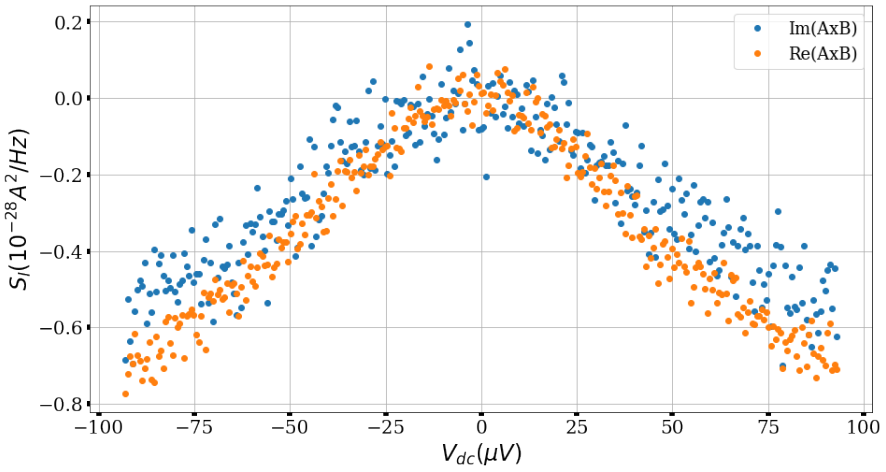

FIGURE 5.6: Real part $Re(A \times B) = \frac{Re(S_{cross})}{Re(C_{ab})}$ and imaginary part $Im(A \times B) = \frac{Im(S_{cross})}{Im(C_{ab})}$ of the current noise. As the current noise is measured at zero frequency, both quantities are supposed to be equal. But this is not confirmed by the datas.

approach of paragraph 3.2.2, but including a multiplication factor g:

$$S_{exp}(V_{dc}) = -g\frac{2e^2}{h}\int dE R(E)(1-R(E))(f_0(E)-f_3(E))^2 \tag{5.2}$$

where f_0 and f_3 are the Fermi functions of reservoirs (0) and (3) (see figure 5.2). They inject electrons at an electronic temperature $T = 40mK$ and with chemical potential $\mu = eV_{dc}$ for reservoir (0), $\mu = 0$ for reservoir (3). The multiplication factor g is found to be equal to 0.65, indicating that the cross correlation is roughly 35% smaller than the theoretical value. Moreover, we notice that while Auto A ($A \times A$) is equal to the cross-correlation ($A \times B$), Auto B ($B \times B$) is roughly 40% lower.

These results do not confirm the ones of previous works and are thus surprising. A difference between auto and cross correlation was measured by M.Kapfer [6] specifically in the fractional Hall regime. It was mainly attributed to non-perfect coupling between edge states and ohmic contacts. But in the integer Hall regime, measurements were consistent with the predictions of the scattering approach with perfect ohmic contacts. We expect that one source of error is a bad estimation the calibration factors C_{aa}, C_{bb}, C_{ab}, due to a bad thermalization of the RLC circuits and/or the sample with the mixing chamber. This bad thermalization can lead to underestimations of the amplifier gains. This hypothesis is developed in Appendix C.
Moreover, we noticed that the HEMT gain can vary from days to days, which make it difficult to ensure their value during the measurements. This can also represent an important source of error.

We want to check if it is still possible to use the PASN picture to describe the cross-correlation in presence of a radio-frequency (RF) signal. We preferred to work with the

cross-correlation only, in order to avoid eventual photo-assisted processes due to noisy incoming currents. In other words, we think that the photo-assisted picture is better established for the cross correlation than for the auto-correlation.

5.2.3 Photo-assisted shot noise (PASN)

We now present the cross-correlation measurements with a sine voltage $V_{ac}(t) = V_{ac}sin(2\pi ft)$ injected on contact (0) only. Indeed, it is important to confirm that we can use the "photo-assisted" picture described in paragraph 3.2.3 to describe AC transport, before sweeping to the more complicated HOM configuration. We use a source "Agilent N5181A MXG" that delivers radio-frequency (RF) from 0.04GHz to 20GHz, and powers from -20 dBm to 20 dBm. We recall that the power in dBm correspond to:

$$P_{dBm} = 10log(P/P_0)$$

where $P_0 = 1mW$. One of the most difficult task is to estimate the power that is effectively sent to the sample, after attenuation and many reflections at each connector (see appendix C).

We recall that in the case of energy-independent scattering matrix, a simple relation between the noise in presence of a time-dependent voltage $V_{dc} + V_{ac}(t)$ ($S_{ON}(V_{dc})$) and the noise in presence of the DC component V_{dc} only ($S_{OFF}(V_{dc})$) can be derived:

$$S_{ON}(V_{dc}) = \sum_{l=-\infty,+\infty} P_l(\alpha) S_{OFF}(V_{dc} + \frac{lhf}{e}) \tag{5.3}$$

where $P_l(\alpha)$ are the square of Bessel functions and $\alpha = eV_{ac}/hf$. However, we noted that the RF sine wave can induce a heating of contact (0). In this case, the noise is enhanced because of a temperature difference between the two counter-propagating edge states. Calling T_0 (resp. T_3) the temperature of contact (0) (resp. (3)), we have to use the DC shot noise $S_{OFF}(T_0, T_3, V_{dc})$ evaluated by taking $T_0 \neq T_3$ in expression (5.2) to get a right evaluation of $S_{ON}(V_{dc})$. Equation (5.3) becomes:

$$S_{ON}(V_{dc}) = \sum_{l=-\infty,+\infty} P_l(\alpha) S_{OFF}(T_0, T_3, V_{dc} + \frac{lhf}{e}) \tag{5.4}$$

For PASN measurements we choose a frequency $f = 10GHz$, for which we have $V_J = hf/e = 41.4\mu V$ and $hf/k_B = 480mK$, and two values of the RF power: 3 and 6 dBm. In that way, the ratio between two consecutive delivered power is equal to 2. We use the notation V_J for "Josephson voltage", with analogy with the AC Josephson effect where the bias and the frequency of emitted photons are linked.

We use the same "ON-OFF" technique as previously: after a measurement with $V_{dc} + V_{ac}(t)$ ("ON"), we take another measurement with V_{dc} only ("OFF"). If these two are close enough in time, we can get rid of the drift of spurious peaks in the spectra (that can evolve within few minutes). The results of these measurements are presented in figure 5.7 for the excess cross correlation $\Delta S(V_{dc}) = S_{ON}(V_{dc}) - S_{OFF}(V_{dc})$. The red vertical lines correspond to $\pm V_J = \pm hf/e$. To fit the excess noise $\Delta S(V_{dc})$, we used equation

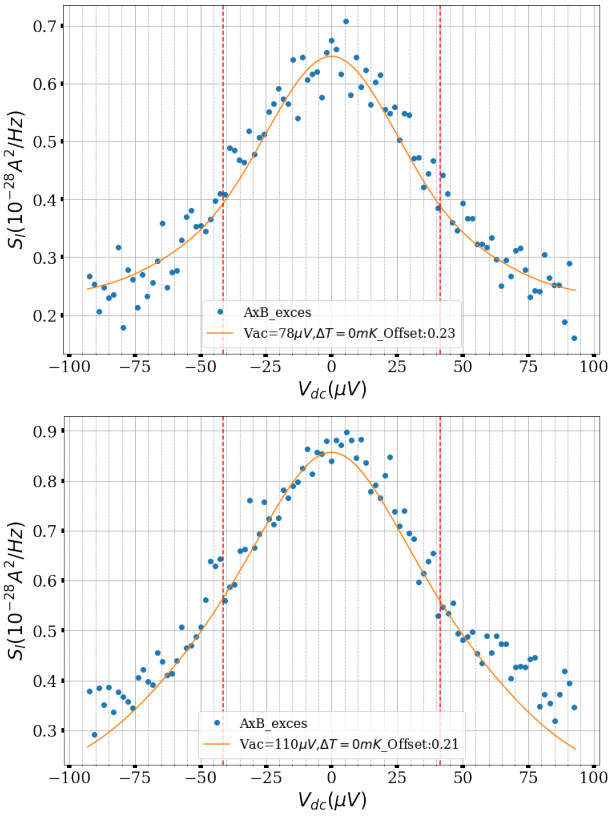

FIGURE 5.7: $\Delta S(V_{dc})$ at $V_{gate} = -0.2V$ for $f = 10GHz$, $P = 3dBm$ (top figure), $P = 6dBm$ (bottom figure)

(5.4), with $S_{OFF}(V_{dc}) = S_{exp}(V_{dc})$ obtained by equation (5.2) and $g = 0.7$. The fitting formula is thus:

$$\Delta S(V_{dc}) = \sum_{l=-\infty,+\infty} P_l(\alpha) S_{exp}(T_0, T_3, V_{dc} + \frac{lhf}{e}) - S_{exp}(T_3, T_3, V_{dc}) \tag{5.5}$$

where $\alpha = eV_{ac}/hf$, V_{ac}, T_0 and T_3 are fitting parameter. We also used the property of Bessel functions $P_l(\alpha) = P_{-l}(\alpha)$. The sum should theoretically be made on all l integers, but we considered only the terms corresponding to $-5 < l < 5$, which is widely enough for $\alpha < 4$. The last fitting parameter is an offset (also indicated in the legend), that is found to vary with power.

The excess noise shows the expected variations with V_{dc}: it is maximal at $V_{dc} = 0V$, and decreases when $|V_{dc}|$ increases. As explained in paragraph 3.2.3, this results from

electron-hole pair contributions to the shot noise. At fixed frequency f, the higher the bias V_{dc}, the higher is the number of photons that electrons at a certain level under the Fermi sea should absorb in order to contribute to the shot noise. This is why the excess noise decreases when V_{dc} increases. The slope breaks at $V_{dc} = \pm hf/e$ are hardly visible in figure 5.5 because of the high electronic temperature. Indeed, the values extracted from the fit of $\Delta S(V_{dc})$ are $T_0 = T_3 = T = 65mK$, thus a high value for both "ON" and "OFF" measurements and both contacts (0) and (3). The range of V_{ac} and the corresponding $\alpha = eV_{ac}/hf$ values extracted from the fits of figure 5.5 are reported in table 5.2. The values of V_{ac} are spaced by the expected factor $\sqrt{2}$ when increasing the

	P=3 dBm	P=6 dBm
$V_{ac}(\mu V)$	76-80	106-112
α	1.8-1.9	2.5-2.7

TABLE 5.1: V_{ac} and α values at $f = 10GHz$ and $V_{gate} = -0.2V$, deduced from the fits of figure 5.5.

RF power by 3dB steps. Thus our results seem coherent with the photo-assisted picture, provided that we include high electronic temperatures.

However, we can notice that the fit of the curves of figure 5.5 is not accurate for large bias V_{dc} (in particular for $P = 6dBm$). The fitting parameters were chosen to optimize the fit in the interval $[-V_J, V_J]$. At higher bias, the fit of the excess noise requires the knowledge of $S_{exp}(V_{dc} \pm lV_J)$ for $l > 2$. The weight of these terms is enhanced when increasing the RF power. Experimentally, we have access to the DC cross correlation only between $-88\mu V$ and $88\mu V$ (cf figure 5.5), thus we had to extrapolate the linear variations of S_{exp} at higher V_{dc}. This extrapolation may not correspond to the actual behaviour of the DCSN, and is probably the reason for which it is hard to fit the excess noise for $|V_{dc}| > V_J$.

We now present another way to treat the PASN that put into evidence the slope changes of $\Delta S(V_{dc})$ at $V_{dc} = \pm V_J = \pm hf/e$. For this, we notice that the sum $\sum_{l\neq 0} P_l(\alpha) S_{exp}(V_{dc} + \frac{lhf}{e})$ should give a flat variation between $-V_J$ and V_J when $S_{exp}(V_{dc})$ is symmetric and linear with V_{dc} (that is presently the case). We thus look for the P_0 value that minimizes the quantity $S_{ON}(V_{dc}) - P_0 S_{exp}(V_{dc})$ over an interval smaller than $[-V_J, V_J]$ (in order not to add artificial interpretations). The result of this minimization is shown in figure 5.8, for the same measurements at $f = 10GHz$ and $P = 0, 3, 6dBm$.

We clearly see the slope change at V_J and $-V_J$, confirming the validity of the photo-assisted picture in this regime. However, we note that the value of P_0 found with this method (indicated in the legend) fluctuates by approximately 10% with the interval of optimization. If we assume P_0 to be a Bessel function, we extract V_{ac} values of $45\mu V$, $49\mu V$ and $64\mu V$, which is not consistent with the values of table 5.2. Moreover, the ratio

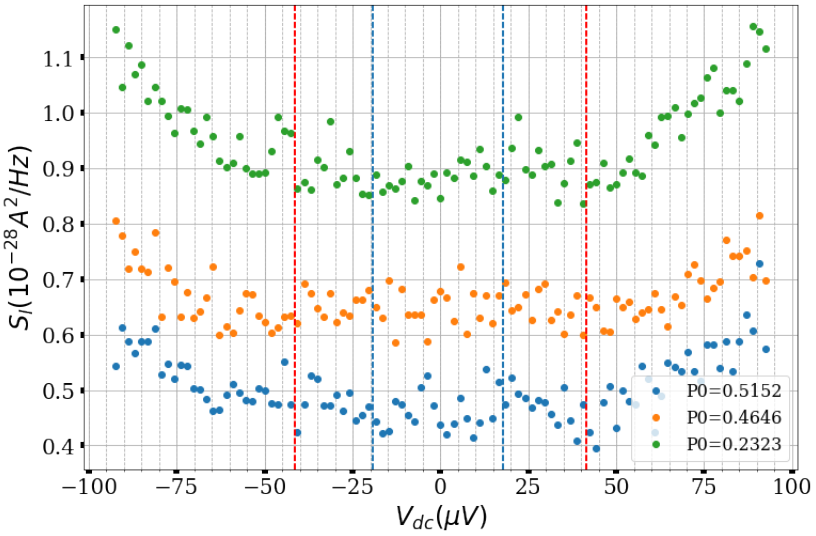

FIGURE 5.8: $S_{ON}(V_{dc}) - P_0 S_{OFF}(V_{dc})$ for $f = 10GHz$ and $P = 0, 3, 6dBm$. The blue dashed lines correspond to the minimisation interval, and he red dashed lines correspond to $\pm V_J$.

between these values is much lower than $\sqrt{2}$. This would mean that Bessel functions do not give the right photons absorption and emission probabilities. One possible reason for this deviation from Bessel functions is developed in Appendix E.

Despite some complications due to heating effects, PASN measurements at $V_{gate} = -0.2V$ could be understood within the "photo-assisted" picture. We now use this same picture to interpret HOM measurements.

5.2.4 HOM measurements

We are now going to present the "HOM" measurements, where we inject sine waves $V_1(t) = V_{ac,1} sin(2\pi ft)$ and $V_2(t) = V_{ac,2} sin(2\pi ft + \Phi)$ on contacts (0) and (3) of the sample. To inject power on both RF lines, we use a splitter at the outpout of the RF source, that splits the delivered power into two equal parts when plugged to 50 Ω impedance lines. We can control the phase difference Φ between the two sine waves thanks to a mechanical phase shifter that varies the length of one of the RF line. As explained in the main introduction, "HOM" measurements consist in measuring the cross correlation while sweeping the phase Φ (or the delay $\tau = \Phi/2\pi f$).

As shown in paragraph 3.1, in the weak backscattering regime, it is possible to show properly that the noise and the current only depend on the difference $V_1(t) - V_2(t)$ (neglecting propagation effects between the reservoirs and the QPC). As emphasized in paragraph 3.2.4, the extension of this result to arbitrary transmissions is not obvious.

Nevertheless, we expect the visibility of the "HOM" photo-assisted noise and current to be maximal when $V_{ac,1} = V_{ac,2}$.

5.2.4.1 Visibility optimisation

To maximize the visibility and to find the condition for equal $V_{ac,1} = V_{ac,2}$, we choose to make photo-assisted current measurements, that are much faster than noise measurements. For that, we had to modulate the RF power with a low-frequency signal also used as a reference for the lockin. This reference signal $V_{mod}(t)$ is delivered by a low frequency "agilent" source. The RF power is modulated by mixing the RF signal and $V_{mod}(t)$ with non-linear mixer. A schematic of the experimental device is shown in figure 5.9. The signal at the output of the mixer has the form $V_{ac}(t) = A(t)\cos(2\pi f t)$, where

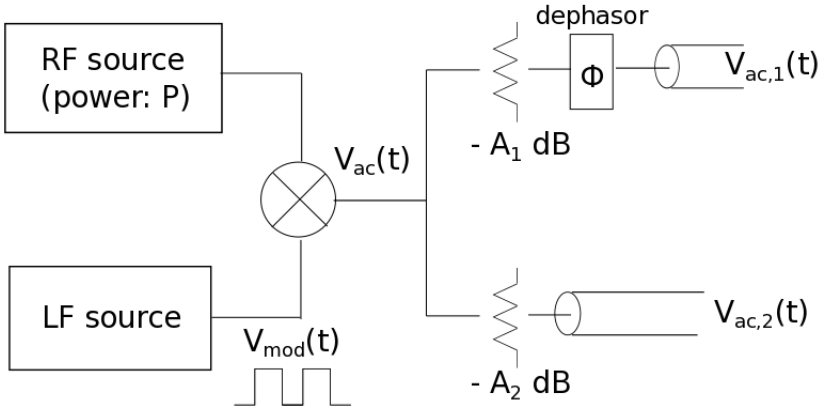

FIGURE 5.9: Experimental setup used for photo-assisted current measurements, including the low-frequency (LF) and radio-frequency (RF) sources. The LF source is also used as a reference for the lockin.

f is the frequency of the RF source and $A(t)$ is the 270Hz envelope, whose amplitude depends on both the RF power and the amplitude of $V_{mod}(t)$. On top of this signal, we can add a DC voltage V_{dc} on contact (0). The lock technique gives access to the 270 Hz components of the transmitted and reflected "photo-assisted" currents.
At third order the DC current I_{dc} (that refers to I_T or I_R) is given by :

$$I_{dc}(V_{dc}) = G_0 + G_1 V_{dc} + G_2 V_{dc}^2 + G_3 V_{dc}^3$$

From the perturbative approach (paragraph 3.1), we can show that the photo-assisted current writes:

$$I_{photo}(V_{dc}, V_{ac}) = G_1 V_{dc} + G_2\langle V^2(t)\rangle + G_3\langle V^3(t)\rangle \tag{5.6}$$

where $V(t) = V_1(t) - V_2(t)$, $V_1(t) = V_{dc} + V_{ac,1}sin(2\pi ft)$, $V_2(t) = V_{ac,2}sin(2\pi ft + \Phi)$, and $\langle\rangle$ stands for the mean value over one period of $V(t)$. With the above-described lockin measurement, we have access to the quantity:

$$\Delta I_{photo}(V_{dc}) = I_{photo}(V_{dc}, V_{ac}) - I_{photo}(V_{dc}, V_{ac} = 0) = (G_2 + 3G_3V_{dc})\langle V_{ac}^2(t)\rangle \quad (5.7)$$

where $V_{ac}(t)$ the AC part of $V(t)$ ($V_{ac}(t) = V_{ac,1}(t) - V_{ac,2}(t)$), and where we used $\langle V_{ac}^p(t)\rangle = 0$ for p odd. Obviously, we need a non-linearity (or finite values of G_2 or G_3) to observe a finite $\Delta I_{photo}(V_{dc})$. This is why we choose a gate voltage for which we measured a V_{dc}-dependent conductance: $V_{gate} = -0.3V$. In figure 5.10, we see a small instability of the conductance, as well as G_R variations of approximately 15%.

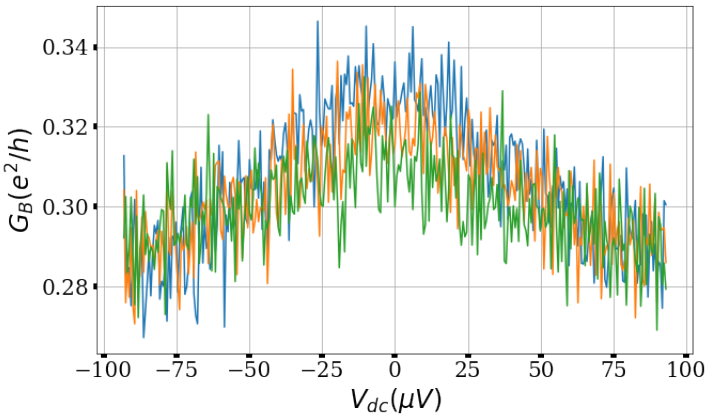

FIGURE 5.10: $G_R(V_{dc})$ at $V_{gate} = -0.3V$ for three consecutive sweeps in bias.

From equation 5.7, we also expect the signal to increase with V_{dc}. For the next photo-assisted current measurements, we thus choose a finite value $V_{dc} = -40\mu V$. Finally, the frequency $f = 14.15GHz$ was fixed after maximisation of the photo-current signal.
We measure the photo-current $\Delta I_{photo}(-40\mu V)$ while sweeping the phase difference Φ with the mechanical phase shifter (or "dephasor"). We then compare the contrast that we get with various values of the attenuation factors A_1,A_2 (see figure 5.9), corresponding to various ratios $V_{ac,1}/V_{ac,2}$. The results for some configurations are shown in figure 5.11. In figure 5.12, we compare the visibility obtained for various configurations.

The maximal value of visibility at this particular frequency is obtained for 3dB attenuation difference between both RF lines ($A_1 = A_2 + 3dB$). In this configuration, we expect $V_{ac,1} = V_{ac,2}$. This simplifies the analysis of "HOM" noise measurements, on which we now focus.

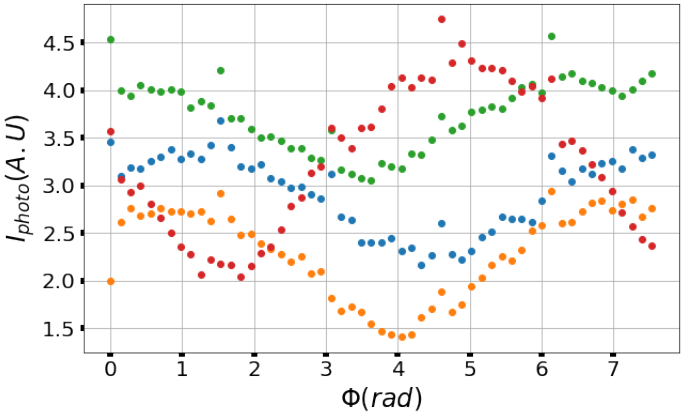

FIGURE 5.11: Photo-current versus phase difference for $V_{gate} = -0.3V$ and $V_{dc} = -40\mu V$, and total RF power P=9dBm. The different curves correspond to different attenuation factors $A_1 - A_2$.

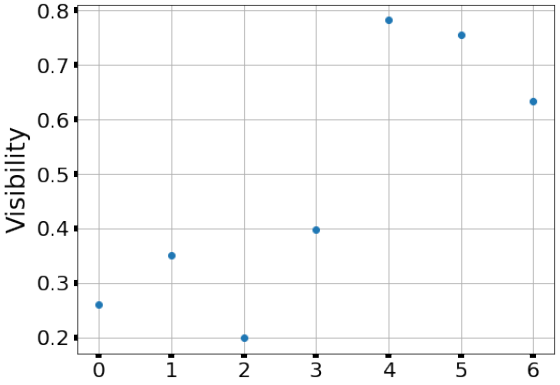

FIGURE 5.12: Visibility versus difference of attenuation between the two RF lines $A_1 - A_2$ (in dBm), calculated from the points of figure 5.11

5.2.5 HOM noise

We now present HOM noise measurements, done at $V_{dc} = 0V$. We remove the low-frequency modulation of the RF signal, needed only for photo-current measurements. Thus the experimental setup is the same as the one of figure 5.9, except that the power P delivered by the RF source is directly split and sent on the two RF lines. We come back to the initial gate voltage $V_{gate} = -0.2V$ (for which we already presented DCSN and PASN measurements). Remaining in the configuration for which $V_{ac,1} = V_{ac,2} = V_{ac}$ at $f = 14.15GHz$, we make HOM measurements for two powers of the RF source: $P = 5dBm$ and $P = 8dBm$. In order to fit the experimental data, we use equation 3.38:

$$S^{HOM}(\tau) = \sum_l P_l(\alpha_{eff}) S_{exp}(\frac{lhf}{e}) \tag{5.8}$$

where the τ dependence is contained in $\alpha_{eff} = 2eV_{ac}\sin(\pi f\tau)/hf$, and the delay τ is simply linked to the phase Φ by: $\Phi = 2\pi f\tau$. Equation (5.8) can be derived within

the Floquet formalism (paragraph 3.2.3), in the limit of energy-independent reflection coefficient (that is a good approximation at $V_{gate} = -0.2V$, see figure 5.3). As for PASN measurements, we study the cross-correlation only, and we use the fitting function $S_{exp}(V_{dc})$ of figure 5.5 in order to fit $S^{HOM}(\tau)$. From equation (5.8), we see that varying the time delay τ leads to the same effect as varying the effective AC amplitude α_{eff} of a sine wave applied on one contact only. It is thus useful to first simulate the variations of the PASN (equation (5.3)) with α, at $f = 14.14GHz$ and using the DCSN given by $S_{exp}(V_{dc})$. The curve is plotted in figure 5.13, for $V_{dc} = 0$. The quadratic departure is a signature of quantum effects, whereas the linear behaviour corresponds to an adiabatic regime.

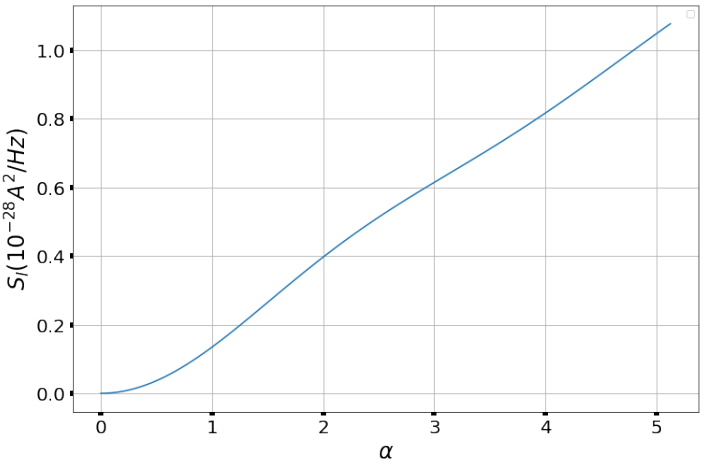

FIGURE 5.13: Simulation of the PASN $S_{ON}(V_{dc} = 0, \alpha)$ at $V_{gate} = -0.2V$, using equation (5.3) and the DC characteristic $S_{exp}(V_{dc})$.

The HOM measurements for $P = 5dBm$ and $P = 8dBm$ are presented in figure 5.14, where we plot the "excess" cross correlation obtained from "ON-OFF" measurements. More precisely, each point is the mean value over Δf of eight "ON-OFF" noise spectra. The accuracy on the V_{ac} amplitudes extracted from the manual fit of figure 5.14 and reported in table 5.2 is a few μV. It is limited by the experimental phase drift that can be significant within a few hours, the time duration range of these measurements. We are also limited by apparent drifts of the HEMT gains or of the power delivered by the RF source. We try to fit well at least one period over the 2.25 periods that are plotted. We note that the ratio between the two extracted AC amplitudes V_{ac} is 1.44, very close

	P=5dBm	P=8dBm
$V_{ac}(\mu V)$	50	72
α	0.4	0.576

TABLE 5.2: AC amplitudes V_{ac} in μV and corresponding $\alpha = eV_{ac}/hf$ values extracted from the fits of figure 5.14, for $f = 14.15GHz$.

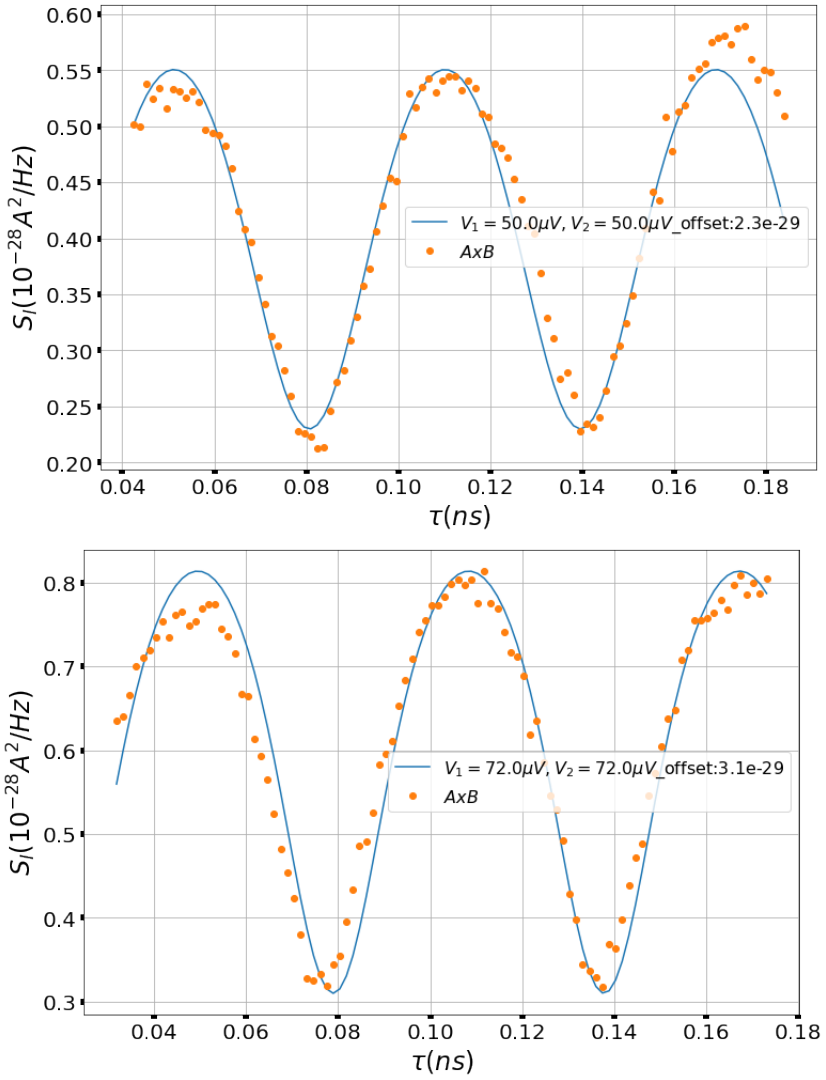

FIGURE 5.14: HOM measurements at $V_{gate} = -0.2V$ and $V_{dc} = 0V$, $f = 14.15GHz$, $P = 5dBm$ (top figure) and $P = 8dBm$ (bottom figure). From the fit we extract the V_{ac} amplitudes (as well as an offset value).

to the ratio $\sqrt{2}$ expected for 3dB power increase. This confirms that we can use the photo-assisted picture leading to formula 5.8 in order to describe HOM measurements.

As a conclusion, PASN as well as HOM measurements at $V_{gate} = -0.2V$ could also be interpreted within the Floquet theory of photo-assisted transport. PASN measurements analysis revealed a high electronic temperature $T = 65mK$ independent of the RF power. A precise study of the heating due to RF power should be carried out by measuring the auto-correlations on a plateau (that include only thermal contributions). During HOM measurements, we heat both edge states roughly in the same manner as we inject the same RF power on both sides of the sample. Our data were well fitted using a smaller electronic temperature $T = 40mK$. However, we do not observe a cancellation of the HOM noise expected for $\tau = 0$ and from the "fermionic behaviour".

In order to support the results found at $V_{gate} = -0.2V$, it is useful to make measurements at other gate voltages. We now present the results at $V_{gate} = -0.27V$.

5.3 Measurements at $V_{gate} = -0.27V$

5.3.1 Conductance

As done previously for $V_{gate} = -0.2V$, we first measure the conductance $G_R(V_{dc})$ and $G_T(V_{dc})$ within the same V_{dc} interval as previously ($-88\mu V$ to $88\mu V$), and using the same lockin parameters. The results are shown below. The mean reflection of the

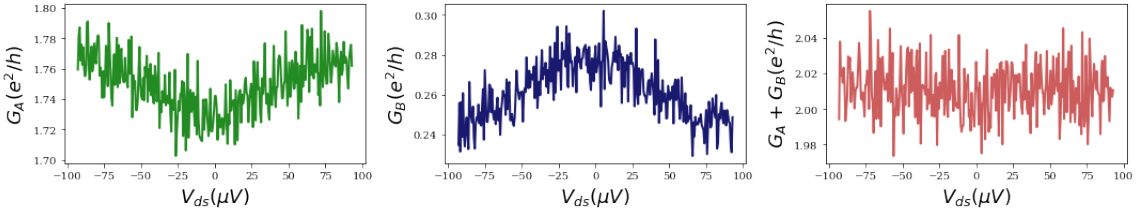

FIGURE 5.15: $G_R(V_{dc})$, $G_T(V_{dc})$, and the sum $G_R(V_{dc}) + G_T(V_{dc})$ for $V_{gate} = -0.27V$.

internal channel is now 26%, and it shows variations of 13% around this mean value. We also observe that the sum $G_R + G_T$ is constant and equal to $2\frac{e^2}{h}$, as expected from current conservation.

5.3.2 DCSN

For noise measurements, we integrate the spectra of the auto and cross correlation over the same interval $\Delta f = [2.1, 2.8]MHz$, thus we use the same conversion coefficients as the one indicated in equation (5.1). We also use the same "ON-OFF" technique, and the same number of averages. The DCSN results (auto and cross correlation) are shown in figure 5.16. The difference between auto and cross correlation is still visible, with Auto B ($B \times B$) and Auto A ($A \times A$) that are lower than the cross correlation.
Moreover, there is a mismatch of 55% between the theoretical cross-correlation evaluated with the reflection coefficient of figure 5.15 and the measured one. The cross correlation is fitted using equation (5.2) with the measured reflection $R = G_R h/e^2$ coefficient (plotted figure 5.15) and with a multiplication factor $g = 0.55$. The electronic temperature used for the fit is $T = 30mK$.
As for $V_{gate} = -0.2V$, we attribute these non-expected DCSN values to errors of estimation of the HEMT gains, either because of bad thermalizations (see Appendix C), or because of time-drifts of the gains. Despite these experimental difficulties, we can use

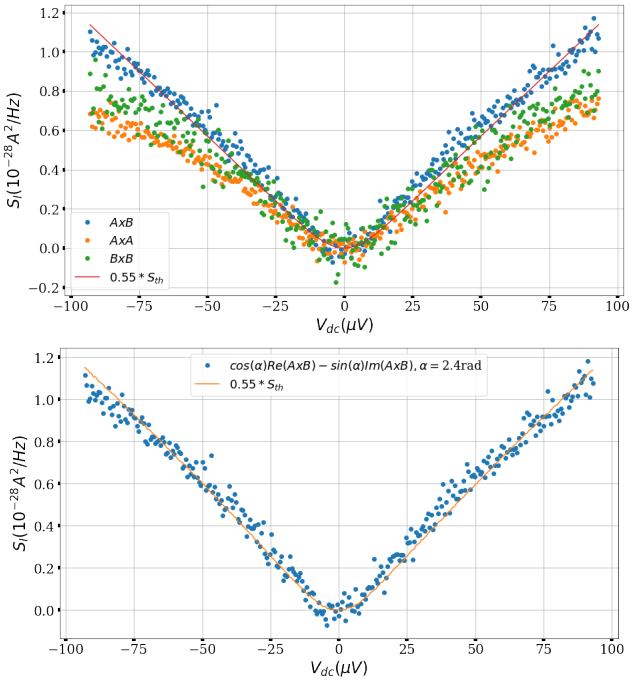

FIGURE 5.16: Cross and auto correlation functions versus DC bias V_{dc} for $V_{gate} = -0.27V$. The bottom figure focuses on the Cross correlation only.

our knowledge on the DCSN in order to interpret the noise in presence of a sine voltage. We want to check if it is possible to treat it as a consequence of emission and absorption processes, as suggested by formula (5.3).

5.3.3 PASN

We now present the PASN measurements, injecting power on the same RF line and at the same frequency as previously ($f = 10GHz$), but with lower powers: $P = -1.5dBm$ and $P = 1.5dBm$. Reducing the power, we hope to reduce eventual heating effects and to have a correct estimation of the PASN over a larger V_{dc} window. As previously, we focus on the cross-correlation only. Assuming that corrections due to the energy-dependence of the reflection coefficient (figure 5.15) are small enough, the excess noise should be given by:

$$\Delta S(V_{dc}) = \sum_{l=-\infty,+\infty} P_l(\alpha) S_{exp}(T_0, T_3, V_{dc} + \frac{lhf}{e}) - S_{exp}(T_3, T_3, V_{dc}) \tag{5.9}$$

where $S_{exp}(V_{dc})$ the new cross-correlation fitting function at $V_{gate} = -0.27V$ (cf figure 5.16), and the temperatures T_0 and T_3 may differ due to an eventual heating of contact (0) brought by the RF power. The amplitude V_{ac} and the offset are the other fitting parameters. The excess noise measurements and the fits with $T_0 = 65mK$, $T_3 = 30mK$ are presented in figure 5.17.

As previously noticed, the fit is not accurate for $|V_{dc}| > V_J$, especially for the highest

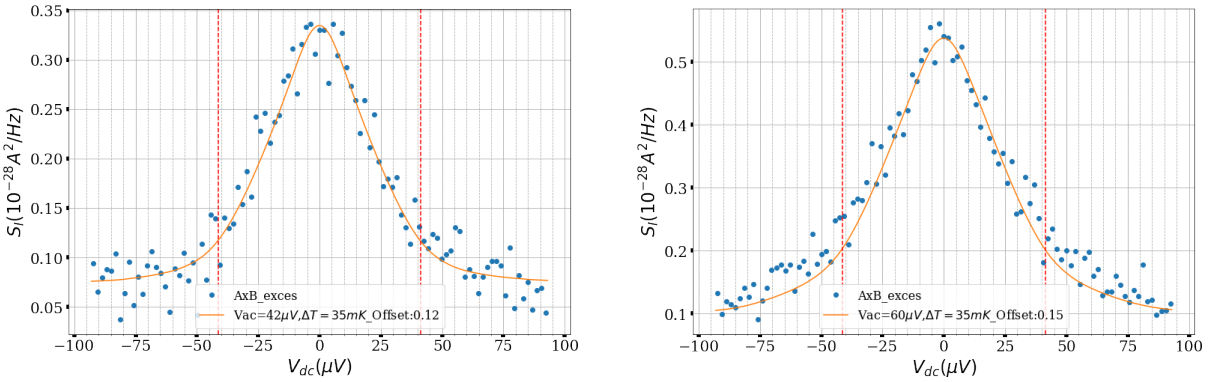

FIGURE 5.17: Excess noise $\Delta S(V_{dc})$ at $V_{gate} = -0.27V$, for $f = 10GHz$, $P = -1.5dBm$ (left figure) and $P = 1.5dBm$ (right figure).

power $P = 1.5dBm$. One possible reason is the lack of information on the DCSN at high V_{dc}, that is more limiting in the case of high powers. V_{ac} values were found trying to fit correctly the excess noise between V_J and $-V_J$, using equation (5.9). The results of the excess noise fit are reported in table 5.3.

Taking into account the uncertainties, we find the expected $\sqrt{2}$ ratio between V_{ac} values

	$P = -1.5dBm$	$P = 1.5dBm$
$V_{ac}(\mu V)$	40-44	58-62
α	0.96-1	1.4 -1.5

TABLE 5.3: V_{ac} and $\alpha = eV_{ac}/hf$ values at $f = 10GHz$ and $V_{gate} = -0.27V$, deduced from the fits of figure 5.17.

at $P = -1.5dBm$ and $P = 1.5dBm$. These results are in agreement with the photo-assisted transport picture, and confirm the PASN study at $V_{gate} = -0.2V$ (as well as many previous studies [83][6]). We now present HOM measurements, that we will try to interpret using the same picture.

5.3.4 HOM measurements

We now present HOM noise measurement, applying $V_1(t) = V_{ac,1}sin(2\pi ft)$ on contact (0) and $V_2(t) = V_{ac,2}sin(2\pi ft + \Phi)$ on contact (3) of the sample (see figure 5.9). As for $V_{gate} = -0.2V$, we work in the configuration that equals the AC amplitudes at $f = 14.15GHz$: $V_{ac,1} = V_{ac,2} = V_{ac}$. We also use the same RF powers as for previous HOM measurements: $f = 14.15GHz$ and $P = 2, 5, 8dBm$. Even though the conductance G_R is not constant at $V_{gate} = -0.27V$, the reflected current as well as the shot noise are roughly linear with V_{dc} (see figure 5.16). Thus we assume that equation (5.8) is still valid, and we use it to fit the HOM noise. We use the $S_{exp}(V_{dc})$ function determined from

DCSN measurements at $V_{gate} = -0.27V$, letting V_{ac} and an offset as fitting parameters. Experimental HOM results and theoretical simulations are compared in figure 5.18.

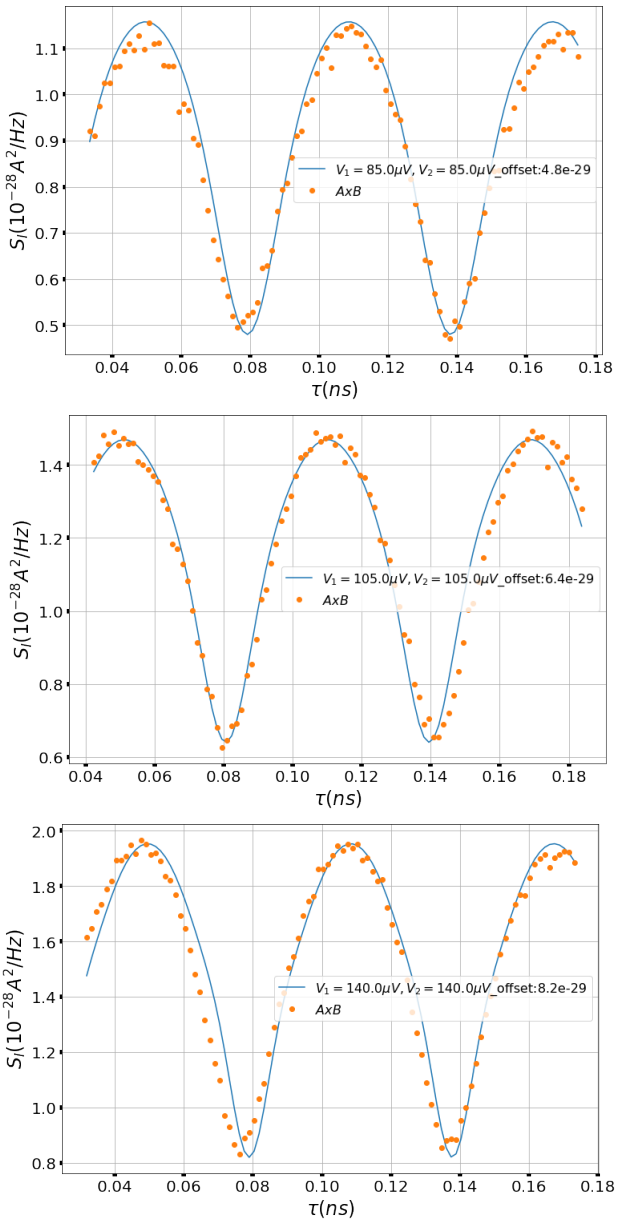

FIGURE 5.18: HOM noise measurements at $V_{gate} = -0.27V$, $f = 14.15GHz$, and powers $P = 2dBm$ (top), $P = 5dBm$ (middle) and $P = 8dBm$ (bottom figure). From the fit we extract the V_{ac} amplitude as well as an offset value.

We observe the expected shape for the HOM measurements, with minima that are sharper than the maxima. The V_{ac} values, determined with $3\mu V$ uncertainty, and the corresponding α values are reported in table 5.4. As previously noted, the measurements accuracy is limited by time-drifts of the relative phase between the two RF lines.

The ratio between $V_{ac} = 140\mu V$ and $V_{ac} = 105\mu V$ is equal to the expected $\sqrt{2}$ factor, but the HOM at $P = 2dBm$ gives too high AC amplitude (we would expect around

	P=2dBm	P=5 dBm	P=8dBm
$V_{ac}(\mu V)$	85	105	140
α	0.69	0.58	0.42

TABLE 5.4: V_{ac} in μV ($\pm 3\mu V$) and $\alpha = eV_{ac}/hf$ from HOM measurements at $f = 14.15GHz$ and $V_{gate} = -0.27V$, deduced from the fits of figure 5.18

$73\mu V$).

The values of table 5.4 do not coincide with the ones extracted from HOM measurements at $V_{gate} = -0.2V$, that were roughly two times smaller ($50\mu V$ for $P = 5dBm$ and $72\mu V$ for $P = 8dBm$). The reason for this mismatch is probably a variation of the HEMT gains between the date of DCSN measurements and the one of HOM measurements, that makes the V_{ac} determination inaccurate.

Despite this experimental artefact, the comparison between HOM measurements at various RF powers P brings us to the same conclusion as at $V_{gate} = -0.2V$: it confirms the validity of formula (5.8) to describe HOM measurements.
However, one important incoherence with equation (5.8) remains. Indeed, for equal amplitudes $V_{ac,1} = V_{ac,2}$, we would expect that the HOM noise $S^{HOM}(\tau)$ cancels at $\tau = 0$. But previous HOM measurements showed that $S^{HOM}(\tau)$ remains finite for all τ values. This effect is not due to the energy dependence of the reflection coefficient R, as it was also observed at $V_{gate} = -0.2V$ (where R is constant). If we assume the heating due to RF power to be identical on both sides of the sample (as $V_{ac,1} = V_{ac,2}$), we can neither explain it by this heating effect. Indeed, only a temperature difference between contacts (0) and (3) can induce additional noise. Until now, the origin of such an offset is not understood.

5.4 Measurements at $V_{gate} = -0.3V$

To conclude the study at filling factor $\nu = 2$, we present measurements at $V_{gate} = -0.3V$. We did not make HOM measurements at this gate voltage, but only PASN measurements in order to confirm the results obtained at $V_{gate} = -0.2V$. The technique, parameters and averaging of lockin and noise measurements being exactly the same as at $V_{gate} = -0.2V$, the presentation is shorter.

5.4.1 DC measurements

We start by looking at the reflection factor as well as the DCSN for the same V_{dc} window ($-88\mu V$ to $88\mu V$). The results are shown in figure 5.19.

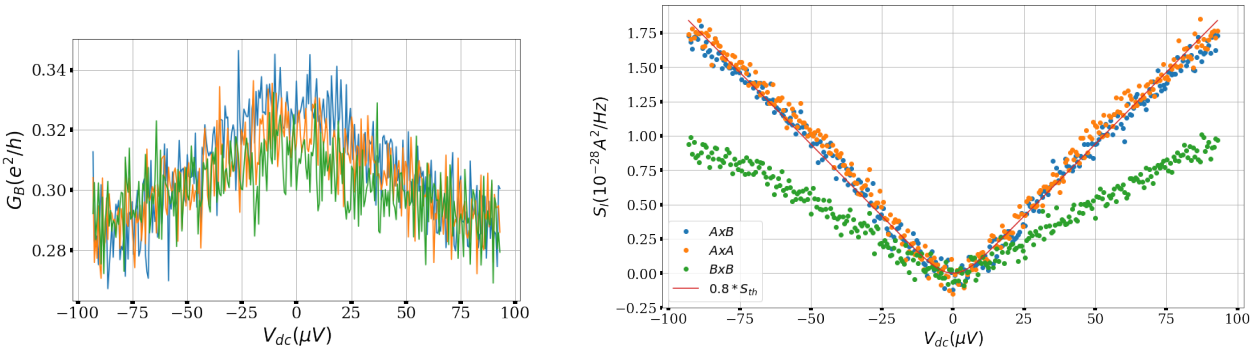

FIGURE 5.19: Reflection conductance $G_B(V_{dc}) = G_R(V_{dc})$ (left figure) as well as DCSN (right figure) verse DC bias V_{dc}. The three curves of $G_R(V_{dc})$ correspond to three successive measurements.

We first notice from conductance measurements that the sample may show small instabilities over time. Nevertheless they are not significant and we can estimate that 30% of the current carried by the inner edge state is reflected, with variations of 13% around the mean value. In the DCSN, we recover the same tendency as at $V_{gate} = -0.2V$: Auto A equals the cross-correlation, but Auto B is lower. We can fit the cross-correlation with equation (5.2), taking the measured reflection coefficient of figure 5.19 and $g = 0.8$. This corresponds to the smallest deviation to theory for the cross-correlation at $\nu = 2$. Once we have extracted the fitting function $S_{exp}(V_{dc})$ from these DCSN measurements, we can use it to study the PASN.

5.4.2 PASN

We use the same measurement technique and parameters as described in paragraph 5.2.3. We measure the excess noise at $f = 10GHz$ and $P = 0, 3, 6dBm$, and fit it using equation (5.9). The amplitude V_{ac}, the temperatures T_0 and T_3 and the offset are fitting parameters. Now $S_{exp}(V_{dc})$ corresponds to the continuous plot of figure 5.19. We assume $S_{exp}(V_{dc})$ to be linear with the bias for a large window of V_{dc}. The range of V_{dc} on which this extrapolation is made in order to estimate the excess noise $\Delta S(V_{dc})$ depends on the applied RF power. Practically, the fitting functions include all the $|l| < 5$ terms of the sum (5.9). The results on PASN are shown in figure 5.20.

From these PASN measurements, and using Bessel functions, we recover roughly the same V_{ac} values as at $V_{gate} = -0.2V$ (cf paragraph 5.2.3): $V_{ac} = 71\mu V, 83\mu V, 102\mu V$ ($\pm 3\mu V$) for $P = 0, 3, 6dBm$ respectively. Thus we can say that our results are consistent with the photo-assisted picture. Small deviations between the results at $V_{gate} = -0.2V$ and $V_{gate} = -0.3V$ may be due to the energy-dependence of the reflection coefficient, that is more pronounced at $V_{gate} = -0.3V$ (figure 5.19).

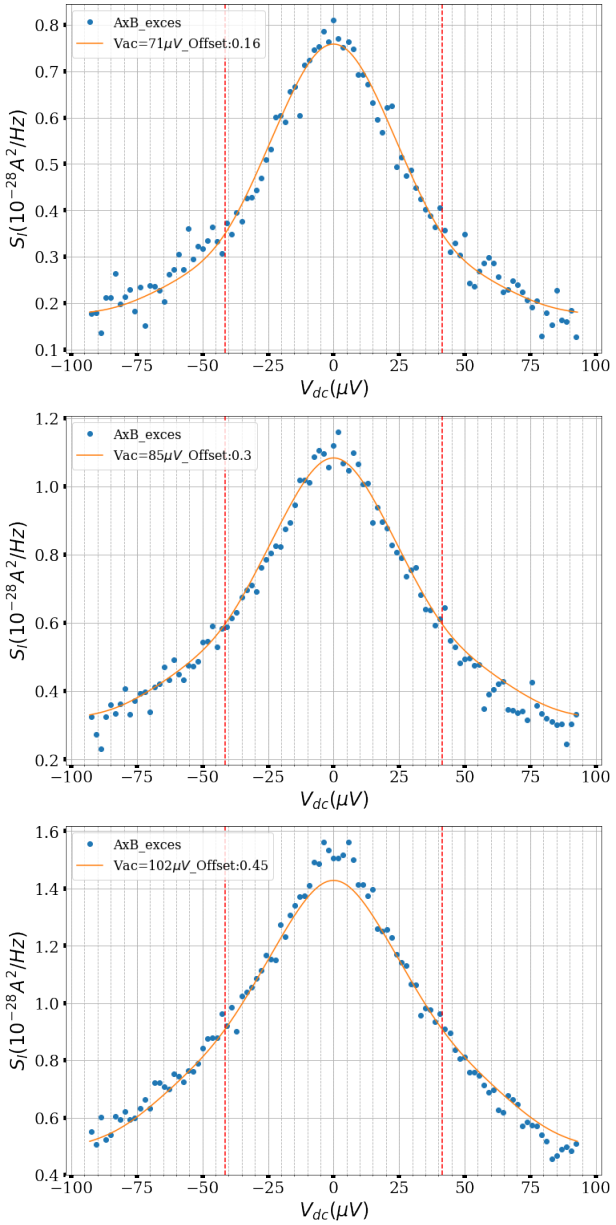

FIGURE 5.20: PASN at $V_{gate} = -0.3V$, $f = 10GHz$, and powers $P = 0dBm$ (top), $P = 3dBm$ (middle) and $P = 6dBm$ (bottom figure). From the fit we extract the V_{ac} amplitude and an offset value.

5.5 Conclusion

Even though we do not recover the expected values of DCSN, most probably because of experimental artefacts, we could use our knowledge on the DCSN to interpret measurements in presence of sine voltages. We first studied the case where a sine wave was applied on one contact only (PASN measurements), and then the case where sine waves with a well-controlled time delay were applied on contacts (0) and (3) (HOM measurements). The comparison between measurements at different RF powers showed that

our results could globally be interpreted within the "photo-assisted" transport picture. However, heating effects brought by RF waves complicate the data analysis.

However, no cancellation of the shot noise (nor of the photo-current) could be observed in the HOM configuration. The maximal visibility of HOM measurements is roughly 50%. The cancellation of the shot noise at $\tau = 0$, naively expected for fermions, is actually difficult to observe. The reasons may be linked with experimental artefacts, but also with fundamental aspects of transport. For example, when the reflection coefficient is energy-dependent, the transport does not depend only on the difference $V_1(t) - V_2(t)$. Applying AC voltage on both sides of the sample encourages a deeper understanding of AC transport, and to reconsider the meaning of "gauge invariance" in mesoscopic conductors.

Chapter 6

Experimental results at $\nu = \frac{2}{3}$

As already discussed in paragraph 2.4 a close analogy between edge states of the fractional Hall effect and Luttinger liquids (LL) [54] was established already in the 90's. MacDonald [87], following an extension of the Haldane-Halperin hierarchy [88],[89], predicted that current transport at filling factor $\nu = \frac{2}{3}$ occurs through two counter-propagating edge states, that are formed by two incompressible droplets of filling factors $\nu_1 = 1$ (internal droplet) and $\nu_2 = 1/3$ (external droplet). This approach was developed by Wen [90], [91], and has been successful in explaining fractional charge in a QPC geometry observed through shot noise measurements [42],[15][44]. Indeed, the charge carried by quasi-particles on the internal edge state is predicted to be $e^* = e/3$, while the charge carried by quasi-particles on the external edge state is expected to be integer. However, this picture could not predict the experimentally observed conductance plateau $G = (2/3)e^2/h$. This conductance was recovered in a pioneering paper of Kane, Fisher and Polochinski (KFP) [92], who considered random disorder-induces tunneling between edge states. They showed that at $\nu = 2/3$, interactions and incoherent disorder-tunneling between modes is necessary to recover the conductance quantization $G = (2/3)e^2/h$. They predicted the formation of two counterpropagating charged and neutral mode, that received experimental support [93] [94]. These experimental works also motivated the elaboration of new models [95] based on the chiral LL theory.

However, KFP approach was still inefficient to explain the emergence of a conductance plateau $G = (1/3)e^2/h$ in QPC geometries [44],[96]. This motivated Wang, Meir and Gefen (WMG) [97] to propose a different edge structure, based on earlier work [98] of edge reconstruction [99]. The starting point of the WMG theory is the edge reconstruction of the 2/3 edge due to a sufficiently small slope of the edge confinement potential. The corresponding edge structure includes, in addition to the two counter propagating modes $\nu_1 = 1$ and $\nu_2 = -1/3$ of the "conventional" 2/3 edge, two counter-propagating

modes $\nu_{3,4} = \pm 1/3$. It was shown that, under certain assumptions, disorder can drive such an edge towards renormalization-group fixed point with two downstream $\nu = \pm 1/3$ charged modes and two upstream neutral modes. At this fixed point, the presence of the $G = (1/3)e^2/h$ plateau is accounted for by assuming that in certain ranges of the gate voltage, the outermost charged channel is transmitted by the QPC while the inner charged one is reflected. More recently, Ref [100] performed a systematic study of the electric and thermal transport for the incoherent $\nu = 2/3$ edge. A more general study [5] at arbitrary Abelian filling factors showed that conductance plateau are found whenever the QPC locally depletes the 2DEG to a stable region with filling factor ν_{QPC} lower than that of the bulk ν_B, and the resulting edge states equilibrate.

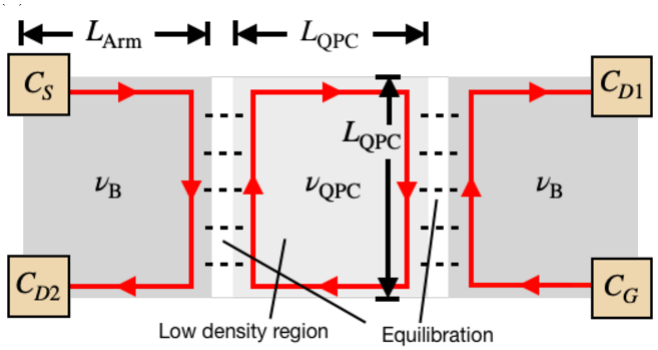

FIGURE 6.1: Model of a QPC device in the FQHE from Ref [5], similar to our experimental device. The filling factor ν_{QPC} depends on the density of the 2DEG under the QPC, that can be controlled through V_{gate}. In the incoherent regime where $l_{eq} << L_{QPC} << L_{arm}$ (where l_{eq} is the equilibration length, L_{arm} is the device length and L_{QPC} is the QPC length scale), stable conductance plateaus at recovered.

A very useful result of this study is that the conductance measured at contact C_{D1} and C_{D2} of figure 6.1 when applying a bias on C_S only depends on ν_{QPC}:

$$G_{D1} = \nu_{QPC}\frac{e^2}{h}, \quad G_{D2} = (\nu_B - \nu_{QPC})\frac{e^2}{h} \tag{6.1}$$

In our experimental setup, G_{D1} and G_{D2} corresponds to the conductance G_T and G_R measured on contacts (1) and (4) of figure 4.2. Furthermore, it was predicted that the auto correlation noise on plateaus depends on few topological numbers: the difference between the number of upstream and downstream modes in the different branches of figure 6.1. It was found that heating points induce thermally activated tunneling between edge modes and electron-hole pairs excitations that can reach different contacts, leading to a finite shot noise. This heating is due to the voltage profile of edge states during the equilibration process. A shot noise proportional to $\sqrt{L_{Arm}/l_{eq}}$ was found at $\nu_B = 2/3$, $\nu_{QPC} = 1/3$, while 0 shot noise is expected at $\nu_B = 2/5$, $\nu_{QPC} = 1/3$.

Having in mind this complexity of edge states structure at $\nu = 2/3$ (and more generally in the FQHE), we now present DCSN, PASN and HOM measurements in this regime. We try to interpret our result in the framework of the perturbative approach described in paragraph 3.1, that has the advantage to be independent of the microscopic description of edge states. We recall that the only restrictions is that the tunneling current is weak ($I_R << I_0$) and that only one charge tunneling process is involved. We present experiments similar to the one that we have done at $\nu = 2$, starting by DC measurements to characterize the regime of $\nu = 2/3$, reached for a magnetic field around $7T$. In figure 6.2, we show conductance measurements while sweeping the gate voltage V_{gate}, using the same lockin amplitude (around $5\mu V$) and frequency ($270Hz$) as previously.

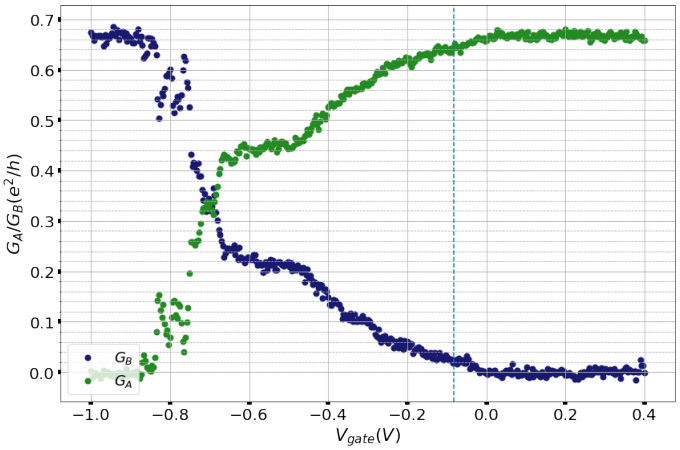

FIGURE 6.2: Conductance $G_R(V_{dc})$ and $G_T(V_{dc})$ at $V_{dc} = 0V$ and $B = 7T$. The dashed line correspond to the gate voltage chosen to make noise measurements.

The first observation is that, contrary to what is theoretically expected and measured in previous cited works, the second plateau is located at $0.44e^2/h$ and not $(1/3)e^2/h$. Following the approach of Ref [5], we could attribute this to deviations from the incoherent regime, probably due to the small length scale of the QPC region $L_{QPC} \approx 200nm$, that may be lower than the equilibration length l_{eq}. In that case, the conductance G_R could depend on other factors than only the QPC filling factor ν_{QPC}, such as the degree of backscattering between edge modes. Of course, this complex edge structure involving exchange processes between edge states may have consequence on the DCSN (DC shot noise) as well.

6.1 DCSN

The shot noise was found to be finite for all V_{gate} values (or QPC configuration). This is illustrated in figure 6.3, where the excess cross correlation $S_I(V_{dc})$ is plotted for $V_{dc} = \pm 48\mu V$ and $V_{dc} = \pm 96\mu V$, and for various values of the gate voltage V_{gate}. By "excess

noise" we refer to the "ON-OFF" technique previously mentioned, where we make the difference between the shot noise at finite V_{dc} and the shot noise at $V_{dc} = 0$. We observe

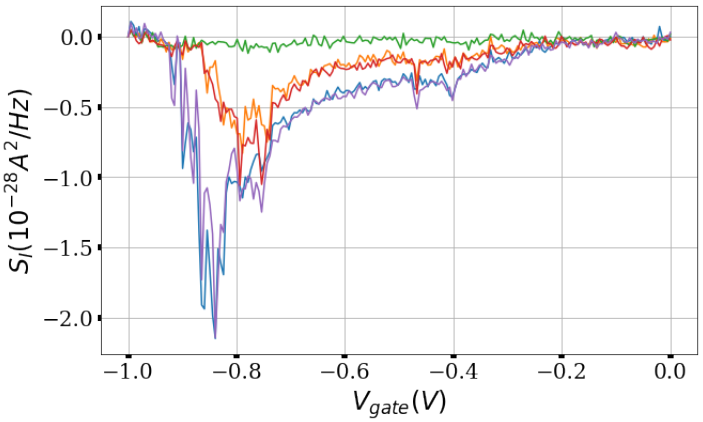

FIGURE 6.3: "ON-OFF" cross correlation versus V_{gate} at $V_{dc} = \pm 96\mu V$ (blue and magenta curves) and $V_{dc} = \pm 48\mu V$ (red and orange curves). The green curve is a reference for $V_{dc} = 0V$.

that $S_I(V_{dc})$ increases with V_{gate} and reaches maximal values in the strong backscattering regime. This behaviour is reminiscent for the increase of the tunneling charge from $e^* < e$ in the weak backscattering regime, to e in the strong backscattering regime. The strong backscattering is also the regime where we observe the strongest non-linearities of the reflected current.

$S_I(V_{dc})$ seems symmetric with the bias V_{dc} for most of V_{gate} values. However, no cancellation of the shot noise is visible except for closed QPC. Instead, $S_I(V_{dc})$ clearly increases with the DC bias V_{dc} even on the $0.44\frac{e^2}{h}$ plateau (around $V_{gate} = -0.4V$). A finite shot noise on intermediate plateau was already measured in previous works [6][94] and could be explained by theoretical models mentioned above [5].

In order to be able to compare our results to theoretical predictions, we decided to study the shot noise in the weak backscattering regime corresponding to a gate voltage $V_{gate} = -0.0815V$. The mean value of the reflected conductance is $G_R = 0.024\frac{e^2}{h}$, and the I-V characteristic is slightly non-linear (see figure 6.4).

We present DCSN measurements for V_{dc} between $-293\mu V$ and $293\mu V$, which corresponds to delivered voltage between -0.8 V and 0.8 V by the room-temperature DC source. Each point of figure 6.5 corresponds to the mean value of a noise spectrum over a smaller frequency interval than previously: $\Delta f = [2.2, 2.38]MHz$. Reducing this interval around the resonance of the RLC circuits, it can be shown that we increase the signal to noise ratio. Each point is averaged $N = 2000$ times by the acquisition card, and then four more times over consecutive bias sweeps. We use the thermal calibration

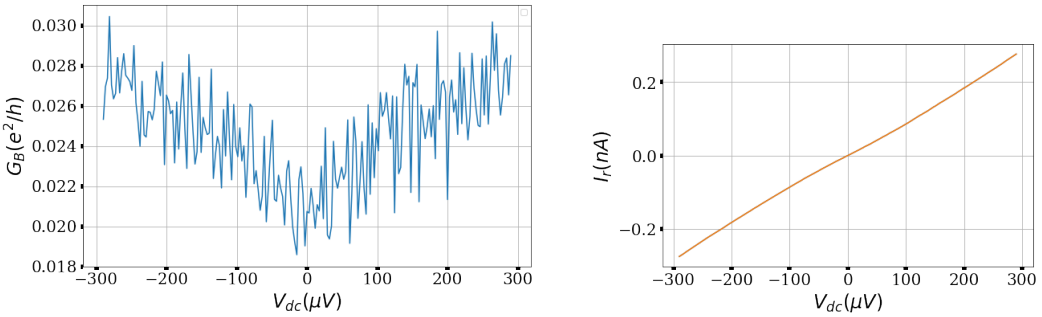

FIGURE 6.4: Conductance $G_B(V_{dc}) = G_R(V_{dc})$ (left figure) and backscattered current $I_B = I_R$ (right figure) for $V_{gate} = -0.0815V$. The non linearity visible G_R is almost not visible anymore in the integral of it, I_R.

technique described in paragraph 4.5 to find the conversion factors:

$$C_{aa} = 2.01 * 10^{13}\Omega^2, \quad C_{bb} = 2.3 * 10^{13}\Omega^2 \quad C_{ab} = (1.44 + 1.32j) * 10^{13}\Omega^2$$

The corresponding total amplification gains are $G_A = 948$ for line A and $G_B = 1008$ for line B. To compare our results with the theoretical cross-correlation, we use the expression (see [66],[76] for a derivation):

$$S_I(V_{dc}) = 2e^* I_R(V_{dc}) coth(\frac{e^* V_{dc}}{2k_B T}) - 2k_B T G_R(V_{dc}) \tag{6.2}$$

where $e^* = e/3$, and the conductance $G_R(V_{dc}) = \frac{\partial I_R}{\partial V_{dc}}$ corresponds to the experimental points of figure 6.4.

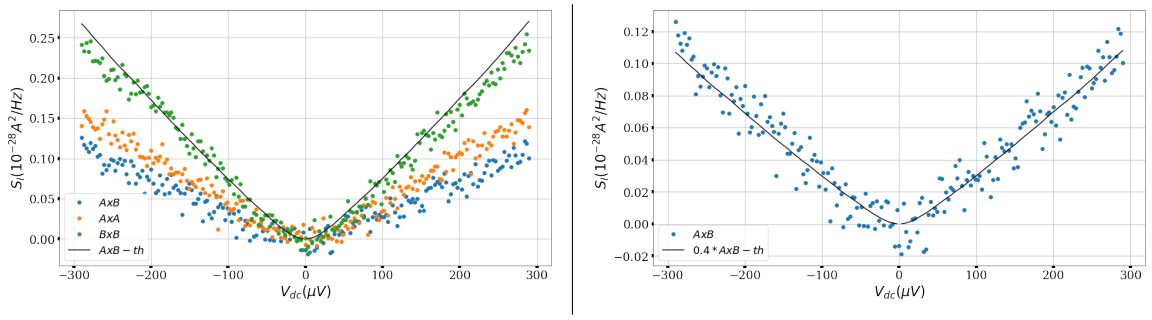

FIGURE 6.5: Cross and auto-correlation functions versus DC bias V_{dc}. (left figure) and cross-correlation only (right figure). The black continuous curve corresponds to $S_I(V_{dc})$ given by equation (6.2) (left figure) and to $0.4S_I(V_{dc})$ (right figure).

We observe that Auto B fits well with equation (6.2), while there is a factor 0.4 of difference for the cross correlation, that is better fitted with $e^* = 0.4e/3$.
The fact that the auto-correlations are higher than the cross-correlation is not surprising as it has already been observed at $\nu = 2/3$ and $\nu = 2/5$ [6]. However, the main difference with previous works [44] is that the charge e^* found from the cross-correlation was $e^* = 0.35$, and not $e^* = 0.4e/3$. One possible source of error is a bad thermalization of

the RLC circuits, that would lead to errors in the determination of the amplifier gains G_A and G_B and thus on the conversion factors C_{aa}, C_{bb}, C_{ab}. This effect is detailed in the last paragraph of Appendix A.

It is also possible that these DCSN result from non-perfect coupling between edge states and ohmic contacts. Finding a microscopic model to describe the injection of electrons from a reservoir to the edge states of $\nu = 2/3$ is a quite difficult task and have been the subject of theoretical works [101],[102]. It can be shown that a non-perfect coupling of fractional edge states to reservoirs would modify the quantization of the conductance, and would lead to power-law behaviour of the current even on a plateau. This could bring errors in the calibration of the transmitted and reflected current, as well as in the noise calibration. Indeed, these calibrations were made assuming that each ohmic contact at chemical potential eV_{dc} is perfectly coupled to the edge states, in which a current $\frac{2}{3}\frac{e^2}{h}V_{dc}$ is injected. If the coupling to reservoirs is non-perfect and the value of the injected current is reduced, the conductance and noise calibrations would give wrong estimations of the noise.

However, the linear behaviour of the conversion factors y_A, y_B with ν (see figure 4.16) proofs the consistency of the conductance calibration: the first measured plateau in figure 6.2 is indeed situated at $(2/3)e^2/h$ (and not only fixed in order to calibrate the lockin measurements). This means that an eventual bad coupling to reservoirs does not modify the conductance plateau at $(2/3)e^2/h$. However it could make the current injected in contact (0) noisy, and this would naturally induce a difference between auto and cross-correlations.

Even without evoking bad coupling to reservoirs, let's emphasize that the previously cited descriptions of the $\nu = 2/3$ edge states (KFP or WMG approach) do not give predictions on the shot noise induced by quasi-particle tunneling. To our knowledge, the tunneling of charges $e^* = e/3$ is usually described by the old "conventional" description of edge states involving two bosonic counterpropagating modes $\nu_1 = 1$ and $\nu_2 = 1/3$. As already mentioned, this picture is becoming obsolete as it could not account for the observed conductance plateau. These unexpected results on DCSN could motivate the study of shot noise outside of conductance plateaus within the most recent approaches.

Even with a partial comprehension of the DCSN, it is possible to use the fit $S_{exp}(V_{dc})$ of the cross correlation (figure 6.5) to interpret the noise measurements in presence of a RF sine wave.

6.2 PASN

We call the shot noise in presence of an AC signal "photo-assisted" shot noise (PASN), extending the single-particle picture of absorption and emission of photons by quasi-particles to a strongly-correlated system. This can be justified by the idea that even though quasi-particles in the FQHE results from excitation of a many-body ground state, they interact independently of each other with the electromagnetic field created by the AC voltage, thus exchanging photons of energy hf (where f refers to the frequency of the sine wave).
To study the PASN, we apply a signal $V_1(t) = V_{dc} + V_{ac}sin(2\pi ft)$ on contact (0), choosing the same frequency as for HOM measurements: $f = 14.15GHz$. We focus on the cross-correlation only, as it should be insensitive to the noise eventually brought by non-perfect coupling to reservoirs. The measurements with RF power ("ON"), without RF power ("OFF"), as well as the excess noise ("ON-OFF") $\Delta S(V_{dc})$ are shown in figure 6.6, for a power $P = 1dBm$ delivered by the RF source.

We recall the "OFF" noise $S_{exp}(V_{dc})$ determined from the last DCSN measurements:

$$S_{exp}(V_{dc}) = g(2e^*I_R(V_{dc})coth(\frac{e^*V_{dc}}{k_BT}) - 2k_BTG_R(V_{dc}))$$

where $e^* = e/3$, $g = 0.4$. This same e^* enters in the PASN formula, giving for the excess noise:

$$\Delta S(V_{dc}) = \quad = (P_0(\alpha) - 1)S_{exp}(V_{dc}) + \sum_{l>0} P_l(\alpha)(S_{exp}(V_{dc} + \frac{lhf}{e^*}) + S_{exp}(V_{dc} - \frac{lhf}{e^*})) \tag{6.3}$$

where $\alpha = e^*V_{ac}/hf$, $P_l(\alpha)$ are l-th order Bessel functions, and the fitting parameters are V_{ac} as well as an offset. The two continuous curves of figure 6.6 give an estimation of V_{ac} between $240\mu V$ and $270\mu V$, which corresponds to $1.3 < \alpha < 1.5$. As for $\nu = 2$, equation (6.3) fits well the excess noise except for the extreme V_{dc} values, as the fit in this region requires information on $S_{exp}(V_{dc})$ for $|V_{dc}| > 300\mu V$ (to which we do not have access). We can distinguish a slope variation around $V_{dc} = \pm hf/e^*$, confirming that the fractional charge entering in the PASN formula is $e^* = e/3$.

Now that we have checked that PASN measurements can be interpreted within the picture leading to equation 6.3, we can study HOM measurements - carried out for the first time in the fractional Hall regime.

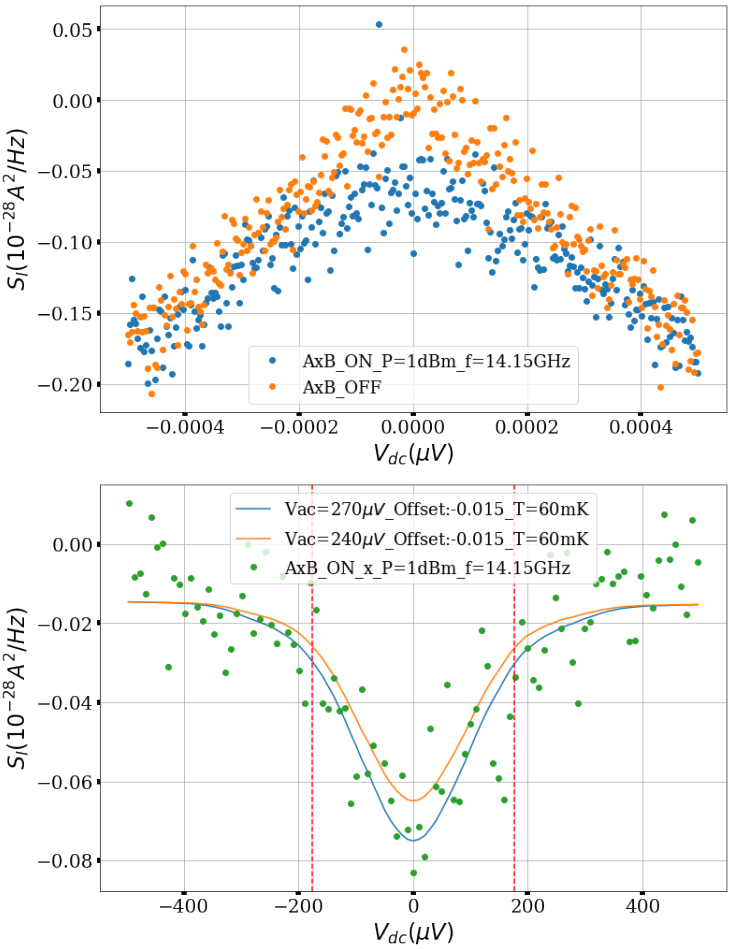

FIGURE 6.6: Comparison between the cross-correlation at $P = 1dBm$ ("ON") and the DCSN called "OFF", measured at $P = -20dBm$ (top figure), and excess cross-correlation $\Delta S(V_{dc})$ (bottom figure). The red dashed lines correspond to $\pm\frac{hf}{e^*}$

.

6.3 HOM measurements

Keeping $V_{gate} = -0.0815V$ and RF frequency $f = 14.15GHz$, we now send sine waves $V_{ac,1}(t) = V_{ac,1}sin(2\pi ft)$ and $V_{ac,2}(t) = V_{ac,2}sin(2\pi ft + \Phi)$ on both sides of the QPC, more precisely on contacts (0) and (3). This is achieved thanks to two identical "Agilent N5181A MXG" sources (delivering powers P_1 and P_2), that are synchronized to the same 10MHz clock. In that way, we can inject twice more power than with only one RF source. These high powers are needed in view of the low values of DC cross-correlation measured in this regime. A schematic of the experimental setup is shown in figure 6.7. We use the difference between the delivered powers $P_1 - P_2$ (expressed in dBm) that provides almost equal amplitudes on contacts (0) and (3): $V_{ac,1} = V_{ac,2} = V_{ac}$. This optimal ratio is found from a visibility optimization at $f = 14.15GHz$ that we will present in the next chapter (paragraph 7.3.1).

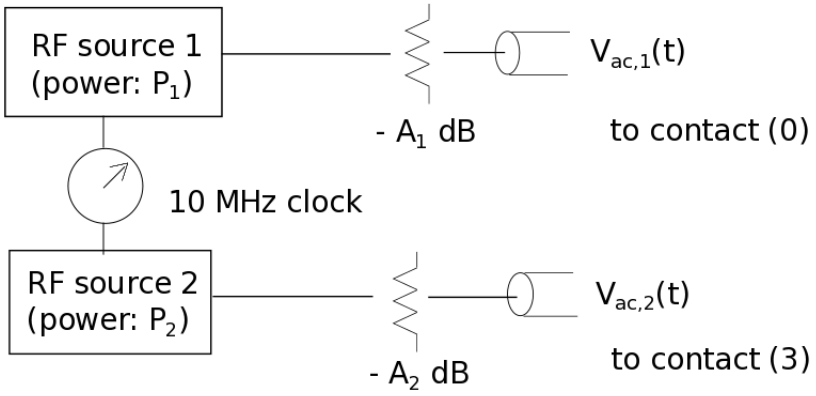

FIGURE 6.7: Experimental setup used for "HOM" measurements. A_1 and A_2 are the attenuations of both RF lines (that may differ). The RF powers P_1 and P_2 are regulated in order to ensure equal amplitudes $V_{ac,1} = V_{ac,2}$ on contacts (0) and (3) of the sample, when $f = 14.15GHz$.

We can vary V_{ac} by a factor $\sqrt{2}$ applying RF powers separated by 3dB: we choose $P_1 = 12, 9, 6dBm$. Thanks to the 10MHz source synchronisation, the phase difference between the two RF signals can be automatically swept, which is much faster than the mechanical phase shifter. For each value of the power P_1, three phase sweeps have been performed. From each sweep, we extract the value of V_{ac} that gives the best fit of the experimental curve, using equation (discussed in part 3.1):

$$S^{HOM}(\tau) = \sum_l P_l(\alpha_{eff}) S_{exp}(\frac{lhf}{e^*}), \quad \alpha_{eff} = \frac{2e^* V_{ac} \sin(\pi f \tau)}{hf} \tag{6.4}$$

In figure 6.8, we show a single τ-sweep for each value of P_1. The delay τ of the x-axis is actually a phase difference $\Phi = 2\pi f\tau$ (modulo 2π) in arbitrary units.

The fits are not perfect for all the Φ (or τ) values because of an experimental phase drift that limits the measurements accuracy. The V_{ac} amplitudes in μV found from the HOM measurements at different powers are summarized in table 6.1. They are determined with about 5% accuracy.

Taking the uncertainty into account, we do not recover the $\sqrt{2}$ ratio expected between

	P=6dBm	P=9dBm	P=12dBm
sweep 1	600	790	930
sweep 2	630	800	900
sweep 3	820	950	

TABLE 6.1: V_{ac}values in μV extracted from HOM measurements at different powers.

two power values separated by 3 dB. This ratio is instead smaller, between 1.15 and 1.3. Thus the HOM measurements cannot be interpreted within the model leading to

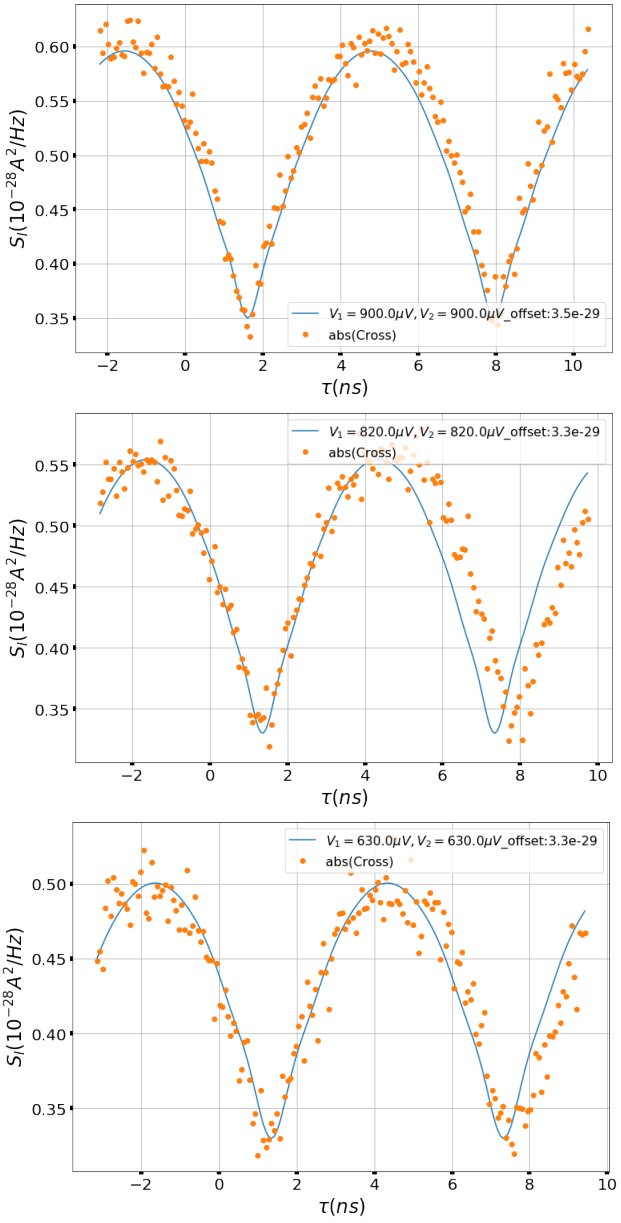

FIGURE 6.8: HOM measurements and fit using equation (6.4) for $P_1 = 12dBm$ (top), $P_1 = 9dBm$ (middle), $P_1 = 6dBm$ (bottom) and always $f = 14.15GHz$.

.

expression (6.4).

One possible reason for this mismatch is the high value of $\alpha = e^* V_{ac}/hf$ corresponding to $3.5, 4.5, 5.26$ (deduced from V_{ac} values of table 6.1) for $P = 6, 9, 12dBm$ respectively. During one HOM measurement, the effective AC amplitude $V_{ac,eff} = 2V_{ac}\sin(f\pi\tau)$ varies from 0 to $2V_{ac}$, thus involving α_{eff} values that can reach 7 for $P = 6dBm$, and 11 for $P = 12dBm$. For this range of α_{eff}, we need to consider a large number of terms in the sum of equation 6.4 (making the sum at least from $l = -5$ to $l = 5$). However, for $l > 2$, we do not have access to $S_{exp}(\frac{lhf}{e^*})$: we simply assume that its variation is linear. If this was not the case, our simulations of $S^{HOM}(\tau)$ could be wrong.

We could also think that this mismatch is due to fundamental limits of the theory leading to (6.4). In particular, the complex structure of edge modes at $\nu = 2/3$ may complicate the definition of the edge state potential at the QPC level, that is crucial to calculate the current as well as the shot noise. In absence of a good equilibration between edge state (that was a possible reason evoked to explain the $0.44e^2/h$ conductance plateau), the potential of edge states at the QPC level cannot be well-defined. Furthermore, equilibration processes between edge states could modify the sine shape of the potential during the propagation between the reservoir and the QPC.

For all these reasons, the interpretation of the HOM measurements is much harder at $\nu = 2/3$ than at $\nu = 2$. At $\nu = 2$ HOM measurements were globally coherent with the picture of "photo-assited" shot noise. At $\nu = 2/3$, complications may arise from bad coupling to reservoirs, or from equilibration processes between edge states. Because of the complexity of the edge states structure, the description of DC as well as photo-assisted shot noise is difficult and not well-established.
As for $\nu = 2$, and despite the expected fermionic behaviour of electrons, the HOM noise do not cancels at $\tau = 0$, and the visibility remains close to 26%. From another point of view, this finite visibility is a proof of coherent transport through the edge states of the fractional Hall regime $\nu = 2/3$. This first demonstration of HOM measurements at $\nu = 2/3$ provides information on fractional edge states.

Chapter 7

Experimental results at $\nu = \frac{2}{5}$

We now present the experimental results obtained at $\nu = 2/5$, corresponding to a magnetic field of 11.3 T. In this regime, Wen's picture and the composite fermions approach both predict that transport should occur through two co-propagating edge states. Wen describes the QH liquid as two droplets of different radius, corresponding to filling factor $\nu_1 = 1/15$ for the inner one and $\nu_2 = 1/3$ for the outer one. This approach can explain the $2/5(= 1/15+1/3)e^2/h$ conductance plateau, as well as the second $(1/3)e^2/h$ plateau observed when depleting the QPC (see figure 7.1). The presence of a conductance plateau is linked to the formation of a local QPC filling factor ν_{QPC} [5], as illustrated in figure 6.1.

Together with the bozonisation technique, Wen's picture also allows for the construction quasi-particle operators that carry charges $n_1\nu_1 e$ on the inner edge state and $n_2\nu_2 e$ in the outer edge state (n_1 and n_2 are arbitrary integers, see paragraph 2.4.3 for more details). These fractional charges have been measured in previous experiments through DCSN measurements [17] [43] as well as PASN measurements [6], using either the proportionality between the backscattered current I_R and the DCSN S_{dc} ($S_{dc} = 2e^*I_R$ at zero temperature), or the singularities of the PASN at $hf = e^*V_{dc}$. These two methods revealed that the fractional charge carried by the inner edge state was $e^* = e/5$, and the one carried by the outer edge state was $e^* = e/3$ (in consistency with the theory).

First of all, we need to characterize the regime of $\nu = 2/5$ by precise conductance measurements while sweeping the gate voltage V_{gate} (figure 7.1).

The conversion factors y_A, y_B between the lockin signal and the transmitted and reflected conductance are determined by assuming that $G_T = (2/5)e^2/h$ at open QPC, and $G_R = (2/5)e^2/h$ at closed QPC. We recall that $G_{T/R} = \frac{\partial I_{T/R}}{\partial V_{dc}}$, where I_T and I_R are the transmitted and reflected current by the QPC. The "open" QPC configuration

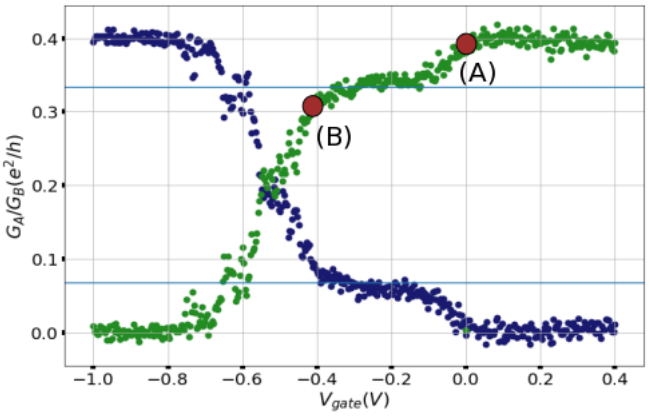

FIGURE 7.1: Conductance plateau at $\nu = 2/5$. The green dots are the transmitted conductance $G_A = G_T$, and the blue dots are the reflected conductance $G_B = G_R$. The horizontal lines correspond to the values $1/3e^2/h$ and $(2/5-1/3)e^2/h$. The regions (A) and (B) are the regimes in which we performed precise DCSN measurements.

corresponds roughly to $V_{gate} = 0.1V$, for which the reflected conductance G_R cancels. For higher V_{gate} values, G_R slightly increases (while G_T slightly decreases), probably due to a density inhomogeneity at the QPC. The second plateau of transmission G_T is slightly higher than the expected $(1/3)e^2/h$ value, and the second plateau of G_R is a bit lower than the expected $(2/5-1/3)e^2/h = 0.067e^2/h$ value. The sum $G_T + G_R$ remains equal to $(2/5)e^2/h$ for all V_{gate}. Sweeping the magnetic field around 11.3T does not lead to a better quantization.

The position of the conductance plateaus is linked with the structure of edge states at $\nu = 2/5$, that makes the link between the measured conductance $G_{T/R}$ and the QPC filling factor ν_{QPC} less obvious than in the IQHE. The model of Ref. [5] requires a good equilibration between edge states in order to ensure that $G_T = \nu_{QPC}e^2/h$ and $G_T + G_R = \nu_B e^2/h$. The slight deviations from the expected $(1/3)e^2/h$ plateau could be due to an equilibration length higher than the QPC length scale (around 200nm).

7.1 DCSN

We now present D.C. shot noise (DCSN) measurements. From the noise calibration at $\nu = 2/5$ (see Appendix A), we find for the amplifier gains: $G_A = 948, G_B = 1008$. Choosing the reduced frequency integration interval $\Delta f = [2.1, 2.38]MHz$, we get for the calibration factors:

$$C_{aa} = 2.32 * 10^{13}\Omega^2, \quad C_{bb} = 1.95 * 10^{13}\Omega^2, \quad C_{ab} = (1.38 + 1.35j) * 10^{13}\Omega^2$$

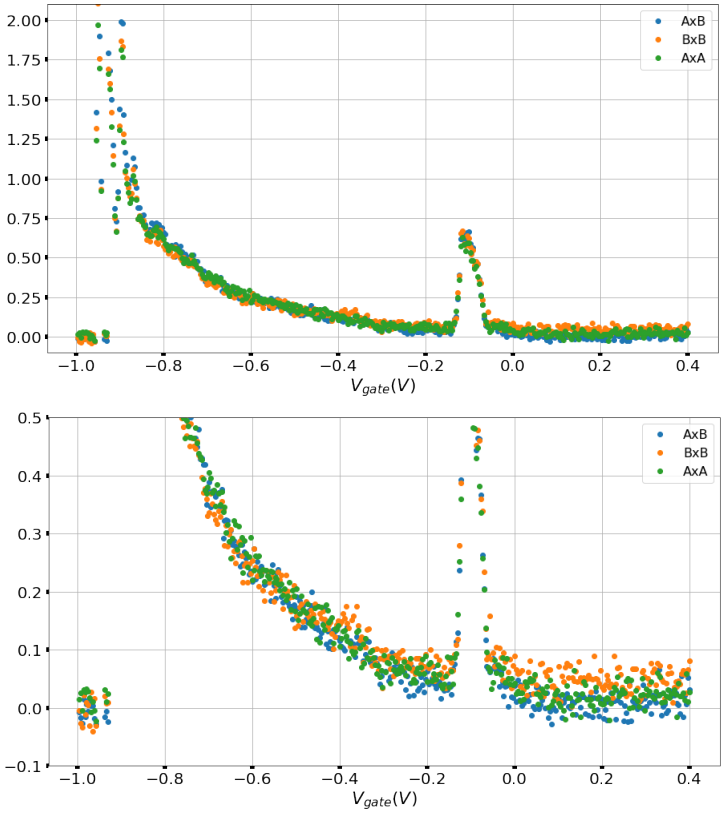

FIGURE 7.2: Cross and auto correlation for $V_{dc} = 400\mu V$ at various V_{gate} values. Bottom figure: zoom of the top figure.

We first show shot noise measurements at fixed $V_{dc} = 400\mu V$ while sweeping V_{gate} (figure 7.2). The expected value of the tunneling charge varies from e to $e/5$ depending on V_{gate}, thus the energy e^*V_{dc} may reach values of the order of the fractional gap. As done previously, we plot the "ON-OFF" cross and auto-correlation.

The shot noise shows two maxima around $V_{gate} = -0.9V$ and $V_{gate} = -0.1V$. Looking at figure 7.1, we notice that these V_{gate} values correspond respectively to the beginning of the last and of the intermediate plateau, thus to the regime of strong backscattering of the inner edge state (for $V_{gate} = -0.1V$) and of the outer edge state (for $V_{gate} = -0.9V$). This behaviour is reminiscent for the increase of the tunnelling charge while moving from the weak backscattering regime to the strong backscattering regime [16]. The transport at $\nu_B = 2/5$ through two edge states is illustrated in figure 7.3. While reaching the intermediate plateau, that corresponds to $\nu_{QPC} = 1/3$ (around $V_{gate} = -0.18V$), the noise abruptly decreases. However it does not cancel, contrary to what is expected for two co-propagating edge states (see for example Ref [5]). The cross correlation and Auto A cancel at open and close QPC, while Auto B remains finite and higher for a large range of V_{gate}.

The finite value of the shot noise on conductance plateau regions and the difference

between auto and cross correlations could both be explained by a bad coupling of edge states with the reservoirs. If the two co-propagating edge states couple differently to the reservoirs, they would have different potentials, and particle exchange between them would lead to additional shot noise. This hypothesis of a bad coupling to reservoirs will be confirmed by more precise DCSN study with V_{dc} in two different regimes illustrated in figure 7.3: $\nu_B = \nu_{QPC} = 2/5$ (configuration (A)), and $\nu_B = 2/5$, $\nu_{QPC} = 1/3$ (configuration (B)). In both regimes, tunneling currents I_T are weak, so the local FQH regime ν_{QPC} is maintained and fractional charges are expected to tunnel.

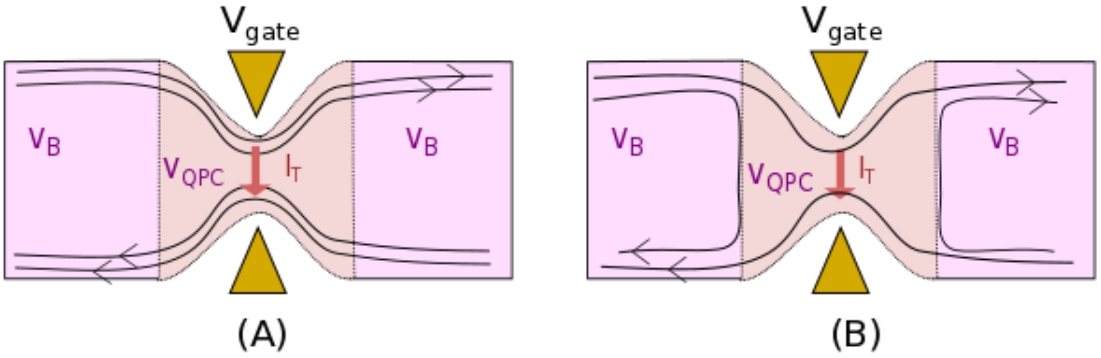

FIGURE 7.3: Schematic of the sample at $\nu_B = 2/5$ and two co-propagating edge states. In the configuration (A) the tunneling of fractional charge occurs through a region with local filling factor $\nu_{QPC} = 2/5$, while in configuration (B) it occurs through a region with local filling factor $\nu_{QPC} = 1/3$.

7.1.1 Results at $\nu_B = \nu_{QPC} = 2/5$

We now present DCSN measurements sweeping the DC bias V_{dc} in the regime $\nu_B = \nu_{QPC} = 2/5$. We can try to interpret our measurements in the framework of the theory presented in paragraph 3.1 as we are in the weak backscattering regime $I_R << I_H$ ($I_H = \frac{2}{5}\frac{e^2}{h}V_{dc}$). Indeed, at $V_{gate} = 0V$ the reflected conductance G_R is low: it varies between $0.012e^2/h$ and $0.02e^2/h$ (see figure 7.4).

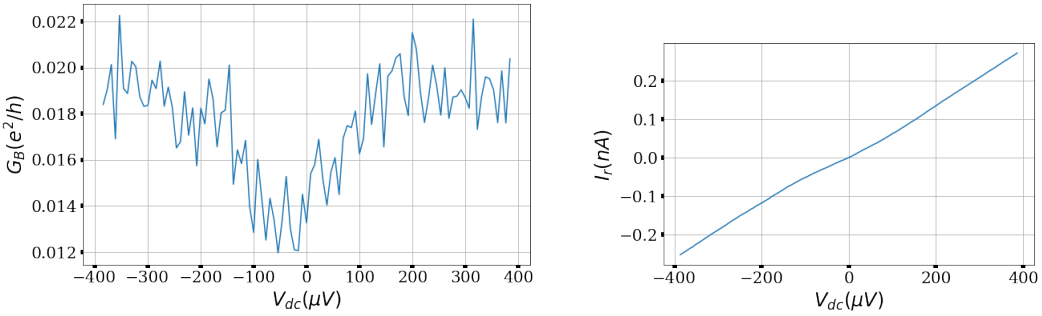

FIGURE 7.4: $G_R(V_{dc})$ and $I_R(V_{dc})$ for $V_{gate} = -0.01V$

The DCSN measurements are presented in figure 7.5, where the curves are the mean value of the noise over 8 bias sweeps.

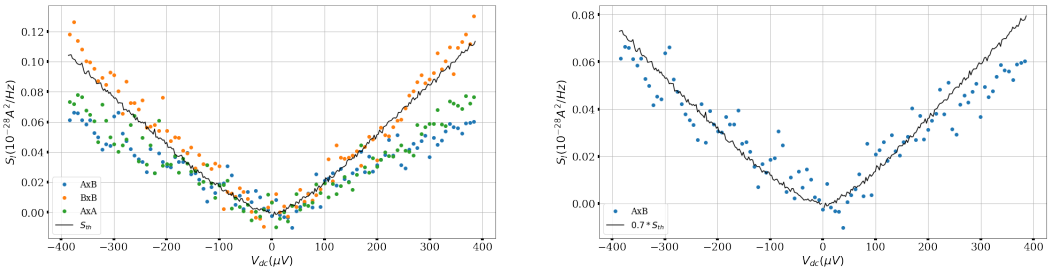

FIGURE 7.5: Left figure: cross and auto correlation for $V_{gate} = -0.01V$. The continuous curve corresponds to $S_I(V_{dc})$ (equation (7.1)) with $e^* = e/5$. Right figure: cross correlation only. The continuous curve corresponds to $0.7S_I(V_{dc})$.

As already noticed from figure 7.2, Auto B is higher than Auto A and cross correlation. Auto B fits well with the theoretical expectation (continuous lines of figure 7.5):

$$S_I(V_{dc}) = 2(1-R)\Big[e^* I_R(V_{dc}) coth(\frac{e^* V_{dc}}{2k_B T}) - k_B T G_R(V_{dc})\Big] \tag{7.1}$$

where $e^* = e/5$, and $T = 30mK$. The reflection factor R is estimated from conductance measurements (figure 7.4). It becomes non-negligible away from the weak backscattering regime, where previous works based on chiral LL model [103] showed that it is possible to use equation (7.1). The value of R depends on the picture chosen to describe edge states at $\nu = 2/5$: if we assume that only the inner edge state is partitioned, we get $R = 0.27$. Indeed, the mean value of G_R corresponds to 27% of the conductance of the inner edge state - the latter being equal to $(2/5 - 1/3)e^2/h = 0.066e^2/h$. This is the picture we choose for the fits of figure 7.5.

We see from figure 7.5 that the cross-correlation is around 30% lower than the theoretical expectation of equation (7.1). Once again, this result does not coincide with previous ones obtained with the same sample, where the fractional charge extracted from the cross correlation was $e^* = e/5$. We can again raise a problem of noise calibration leading to errors on the evaluation of the amplifier gains, as explained in Appendix A.

Another possible explanation is the already mentioned bad coupling of edge states to the reservoirs. Non-perfect contacts would reduce the value of the injected current from contact (0), and thus lead to a bad estimation of both the current and the noise (as calibrations were made assuming a perfect coupling). Also, the auto-correlation would be enhanced by shot noise coming from this non-perfect coupling. This difference between Auto and cross correlations have already been measured in Ref [6], and it was found to decrease while increasing the temperature. However, the reason for which

the Auto B is higher than Auto A is hard to understand. It could be due again to bad thermalization of the RLC circuit of channel B, thus affecting our estimation of Johnson-Nyquist noise during the calibration. An asymmetry in the coupling to the edge states between contacts (1) and (4) could also explain that Auto B is higher than Auto A.

These results of DCSN are partly understood and would need a deeper study of the difference between Auto and cross correlation to confirm the hypothesis of non-perfect coupling between edge states and reservoir. The study of the DCSN at different gate voltages could provide us more information.

7.1.2 Results at $\nu_B = 2/5$, $\nu_{QPC} = 1/3$

We now present DCSN measurements in the weak backscattering regime of the outer edge state (configuration (B) of figure 7.3), for two close gate voltages $V_{gate} = -0.4V$ and $V_{gate} = -0.42V$. Once again, we assume the existence of two independent edge states to interpret our results. To evaluate the reflected current I_R, we thus have to subtract the contribution of the inner edge state to the total measured conductance G_R. From figure 7.1, this contribution is found to be equal to $0.06e^2/h$ (instead of the expected $0.067(= 2/5 - 1/3)e^2/h$ value).

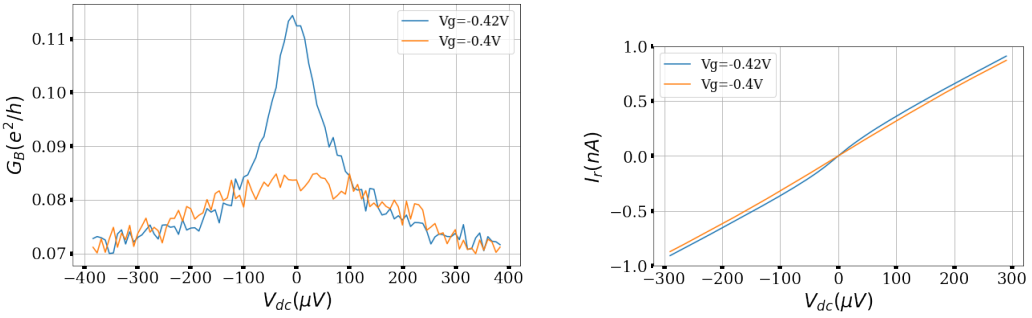

FIGURE 7.6: $G_R(V_{dc})$ and $I_R(V_{dc})$ for $V_{gate} = -0.42V$ and $V_{gate} = -0.4V$

We observe stronger non-linearity of I_R for $V_{gate} = -0.42V$ than for $V_{gate} = -0.4V$, as this last value is closer to the intermediate plateau where I_R is expected to be linear with V_{dc}. The observed increase of G_R at low V_{dc} is reminiscent of a Luttinger liquid behaviour. We see from the comparisons between $V_{gate} = -0.42V$ and $V_{gate} = -0.4V$ that these variations of the conductance do not significantly affect the reflected current I_R. More precisely, I_R corresponds roughly to 23% of the current carried by the outer edge state - the latter being roughly equal to $0.34e^2V_{dc}/h$ (from figure 7.1). The shot noise is expected to be given by expression (7.1) with $e^* = e/3$, $G_R(V_{dc})$ and $I_R(V_{dc})$ extracted from conductance measurements shown in figure 7.6.

In figure 7.7, we compare DCSN measurements to theoretical expectations. The experimental technique is the same as previously: we averaged the curves obtained from 8 bias sweeps, and 3 adjacent V_{dc} points. Each point is thus the results of N=19 200 PSD averages.

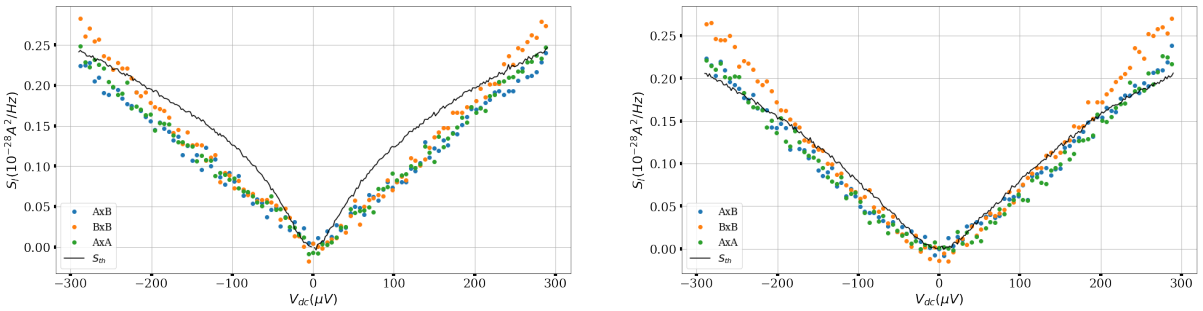

FIGURE 7.7: Cross correlation for $V_{gate} = -0.42V$ (left figure) and $V_{gate} = -0.4V$ (right figure). The black continuous line is the theoretical fit using equation (7.1), $R = 0.23$ and $e^* = e/3$.

Surprisingly, the difference between auto and cross correlation is much lower than at $V_{gate} = -0.01V$ and the shot noise has the expected order of magnitude. However, the measured non-linearity of I_R is less visible in the shot noise, that shows smoother variations than the theoretical prediction. The difference between the measured shot noise and the theory is more pronounced at $V_{gate} = -0.42V$ than at $V_{gate} = -0.4V$.

Before going through PASN measurements at $V_{gate} = -0.44V$, we show DC measurements at this same gate voltage (figure 7.8).

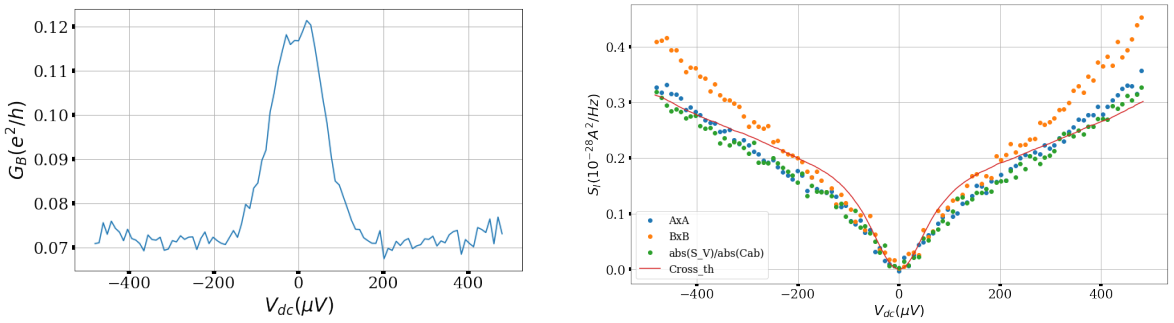

FIGURE 7.8: $G_R(V_{dc})$ (left figure) and auto and cross-correlation (right figure) for $V_{gate} = -0.44V$

The reflected conductance G_R is similar to the one measured at $V_{gate} = -0.42V$, showing quite strong non linearity and LL-like behaviour. The cross correlation has the expected order of magnitude, as for $V_{gate} = -0.42V$ and $V_{gate} = -0.4V$. But once again, it does not reproduce the non-linearity or I_R (instead, it has smoother variations). We could argue that this mismatch is due to the high value of G_R around $V_{dc} = 0V$, which shows the limit of the perturbative formula. We recover the good value of cross-correlation

for large V_{dc} values, where G_R is small. The difference between Auto B and cross correlation is more pronounced than at $V_{gate} = -0.42V$, while Auto A always follows the cross-correlation evolution.

Apart from the hypothesis of bad coupling of edge states to the reservoir, other possible reasons may explain deviations from equation 7.1. Indeed, this expression has been derived [103] for tunneling between Laughlin states ($\nu_B = \nu_{QPC} = 1/m$), using chiral Luttinger liquid (LL) model. Firstly, this model is not successful to describe most of I-V characteristic measured in the FQHE and QPC geometries. Secondly, the description of edge states at filling factor $\nu_B = 2/5$ is more complex. Some descriptions [99] involve equilibration processes between the two co-propagating edge states to explain conductance plateaus. But they do not give predictions on the shot noise due to fractional charge tunneling. The fractional charge is better described by Wen's approach (see paragraph 2.4.3), where quasi-particle operators are created from a linear combination of the two bosonic fields (they are of the form $e^{in_1\Phi_1+n_2\Phi_2}$). However this approach is not coherent with the image of two independently partitioned edge states (used by previous works [17][16]). This is the reason why we preferred to refer to tunneling of fractional charges through a local QPC factor $\nu_{QPC} = 1/3$ or $\nu_{QPC} = 2/5$, than to tunneling through the "outer" or "inner" edge state (even though this assumption was made to fit the DCSN curves).
Despite the difficulties to understand the origins of the measured DCSN, its knowledge is useful to interpret PASN and HOM measurements.

7.2 PASN

Keeping the same gate voltage $V_{gate} = -0.44V$, we have performed shot noise measurements while applying RF power on one side of the sample only (contact (0)). In order to be able to compare our results to those of paragraph 6.2 (at $\nu = 2/3$), we choose exactly the same RF parameters : $P = 1dBm$ and $f = 14.15GHz$. As previously, we made successive measurements with RF power "ON" (setting $P = 1dBm$) and RF power "OFF" (setting $P = -20dBm$). The difference (or excess noise) $\Delta S(V_{dc}) = S_{ON}(V_{dc}) - S_{OFF}(V_{dc})$ is plotted in figure 7.9, where we also compare the "ON" and "OFF" cross-correlation (the "OFF" curve corresponds to the DC cross correlation of figure 7.8). As expected, the PASN noise is higher than the DCSN for small V_{dc}, and this difference decreases for large V_{dc}. In figure 7.9, the DCSN is fitted using a variation of $G_R(V_{dc})$ flatter than the measured one, in order to reproduce correctly its shape. Calling S_{exp} this fitting function, we then fit the excess noise $\Delta S(V_{dc})$ using the expression

derived in paragraph 3.1.2:

$$\Delta S(V_{dc}) = \quad = (P_0(\alpha) - 1)S_{exp}(V_{dc}) + \sum_{l>0} P_l(\alpha)(S_{exp}(V_{dc} + \frac{lhf}{e^*}) + S_{exp}(V_{dc} - \frac{lhf}{e^*})) \tag{7.2}$$

where $e^* = e/3$, $\alpha = e^* V_{ac}/hf$, and $P_l(\alpha) = J_l^2(\alpha)$ is the square of the l-th order Bessel function. The effect of a heating of contact (0) brought by the RF signal can less easily be taken into account than at $\nu = 2$, because it requires the knowledge of the DCSN when $T_0 \neq T_3$. We simply fit the excess noise was fitted using $T_0 = T_3 = 20mK$ for RF "OFF" and $T_0 = T_3 = 60mK$ for RF "ON".

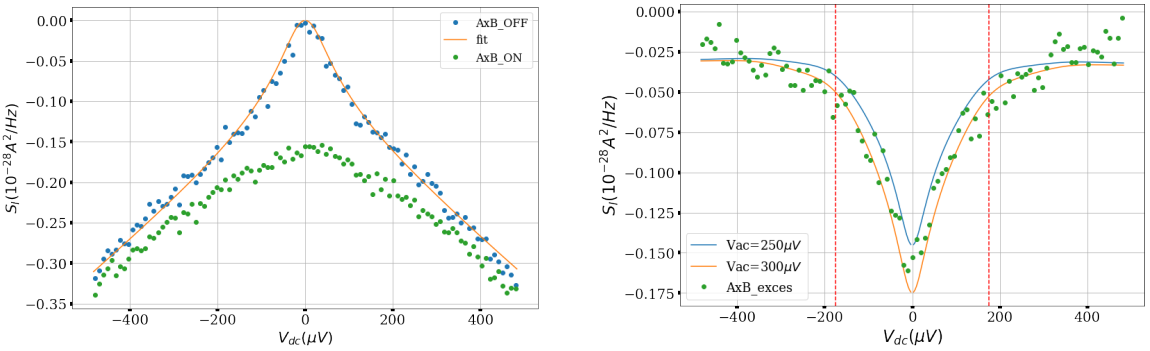

FIGURE 7.9: $S_{ON}(V_{dc})$ and $S_{OFF}(V_{dc})$ (left figure) and excess cross-correlation $\Delta S(V_{dc})$ (right figure) for $V_{gate} = -0.44V$. The horizontal red lines correspond to $\pm hf/e^*$, $e^* = e/3$.

The fit of the excess noise reproduces well its variations between $-hf/e^*$ and hf/e^* (red vertical lines of figure 7.8), but is not accurate for higher V_{dc} values. This can be due to various reasons:

- as previously explained, the lack of information on the DCSN for large bias V_{dc} can lead to wrong estimations of $\Delta S(V_{dc})$.
- deviations from equation (7.2) could be due to the heating of one side of the sample (contact (0)) by the RF wave. The DC shot noise $S_{exp}(V_{dc})$ should actually be replaced by its value in presence of a temperature difference ΔT on top of the bias V_{dc}. While in the IQHE it was easy to estimate this contribution (called "ΔT noise"), it is harder to estimate it in the FQHE without a precise microscopic model of edge states.

Despite these complications, using Bessel functions, we find from the fit of $\Delta S(V_{dc})$: $270\mu V < V_{ac} < 315\mu V$. This V_{ac} range is close to the one found from similar PASN measurements at $\nu = 2/3$ ($240\mu V < V_{ac} < 270\mu V$). This confirms the possibility to use equation (7.2) with fractional charge $e^* = e/3$ to describe the transport with AC voltage. Using similar arguments as the one presented for results at $\nu = 2/3$, we call this noise "photo-assisted shot noise" (PASN). This is the first evidence of the fractional

charge $e^* = e/3$ at $\nu = 2/3$ using PASN measurements. We will now use the picture of "photo-assisted" transport to analyse the HOM noise.

7.3 HOM measurements

7.3.1 Results at $\nu_B = 2/5$, $\nu_{QPC} = 1/3$

For HOM measurements, we come back to the gate voltage $V_{gate} = -0.42V$, where we already presented DCSN measurements (figure 7.7). This regime corresponds to weak tunneling of the external edge state through $\nu_{QPC} = 1/3$ (configuration (B) in figure 7.3). The RF frequency is always fixed to $f = 14.15GHz$. In order to send sine waves $V_{ac,1}(t) = V_{ac,1}sin(2\pi ft)$ and $V_{ac,2}(t) = V_{ac,2}sin(2\pi ft + \Phi)$ on contacts (0) and (3) with a well controlled time-delay $\tau = \Phi/2\pi f$, we use two synchronized RF sources. We call P_1 the power injected by the first source and P_2 the power injected by the second source (in dBm). The experimental setup used for RF injection is perfectly similar to the one illustrated in figure 6.7.

7.3.1.1 Visibility optimisation

Because of the asymmetry between the two RF lines, equalling P_1 and P_2 do not lead to equals $V_{ac,1}$ and $V_{ac,2}$ amplitudes on both sides of the QPC. Thus the first work is to optimize the contrast of HOM measurements, that is maximal for $V_{ac,1} = V_{ac,2}$. For this purpose, we make HOM measurements with fixed value of P_1, and varying P_2 by $1dBm$ steps. We then calculate the visibility of each curve plotted in figure 7.10. The phase shift Φ between the two RF signals is automatically controlled thanks to the common 10MHz clock between the two sources.

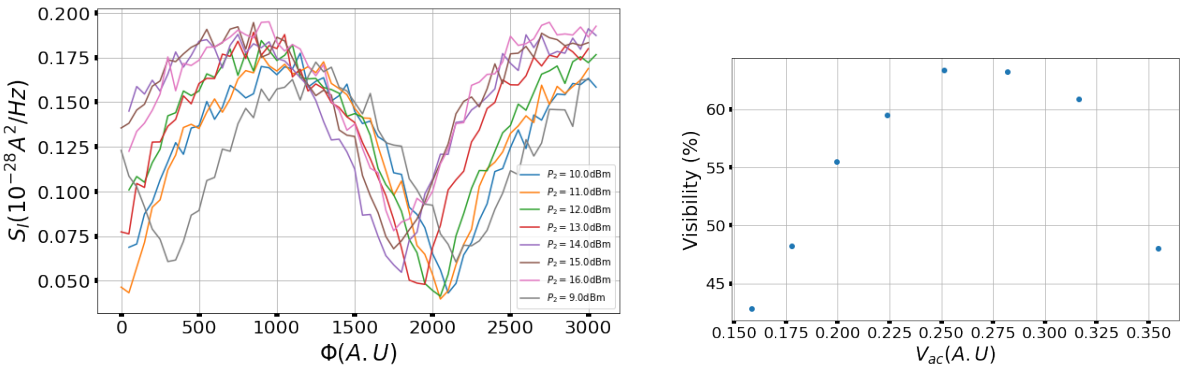

FIGURE 7.10: Left: S^{HOM} (cross-correlation) for $P_1 = 12dBm$ and P_2 between 9 dBm and 16 dBm. Right: evolution of the visibility with $V_{ac} = 10^{P_2/20}$.

This visibility optimization is more precise than the one made from photo-current measurements at $\nu = 2$ (paragraph 5.2.4) as the ratio between the two RF powers can be varied by smaller steps thanks to the second RF source. We see from figure 7.10 that the visibility reaches a maximum for $P_2 = 11dBm$. As these measurements were performed with an additional attenuation of $3dB$ on the line connected to the source injecting $P_1 = 12dBm$, we conclude that there are $2dB$ difference in the cables attenuation of the two RF lines at $f = 14.15GHz$. This result is coherent with the $3dB$ difference found from photo-current measurements at $\nu = 2$ (see paragraph 5.2.4).

When $P_1 - P_2 = 1dBm$, the AC amplitudes injected from the two RF lines are equal: $V_{ac,1} = V_{ac,2} = V_{ac}$. In that case, and when the $I - V$ characteristic is linear, we expect the HOM noise to be given by:

$$S^{HOM}(\tau) = \sum_l P_l(\alpha_{eff}) S_{exp}(\frac{lhf}{e^*}), \quad \alpha_{eff} = 2e^* V_{ac} \sin(\pi f \tau)/hf \tag{7.3}$$

where $e^* = e/3$, τ is the time delay between the two sine-waves: $V_1(t) = V_2(t + \tau)$, and $S_{exp}(V_{dc})$ the fitting function of the measured DCSN.
According to equation (7.3), $S^{HOM}(\tau)$ should cancel at $\tau = 0$ (as $S_{exp}(0) = 0$ and $P_{l\neq 0}(0) = 0$). However, similarly to what observed at $\nu = 2$ and $\nu = 2/3$, we see from figure 7.10 that the measured $S^{HOM}(\tau)$ is finite for all τ values. As we always plot the "ON-OFF" shot noise, this cannot be due to a power-independent offset in the cross-correlation. The exact reason is still not understood, but we could have reached the limit of validity of the model leading to equation (7.3) at $V_{gate} = -0.42V$.

7.3.1.2 HOM measurements

To interpret HOM measurements, we need to know the DCSN dependence with V_{dc}. The DC cross correlation is plotted in figure 7.11.

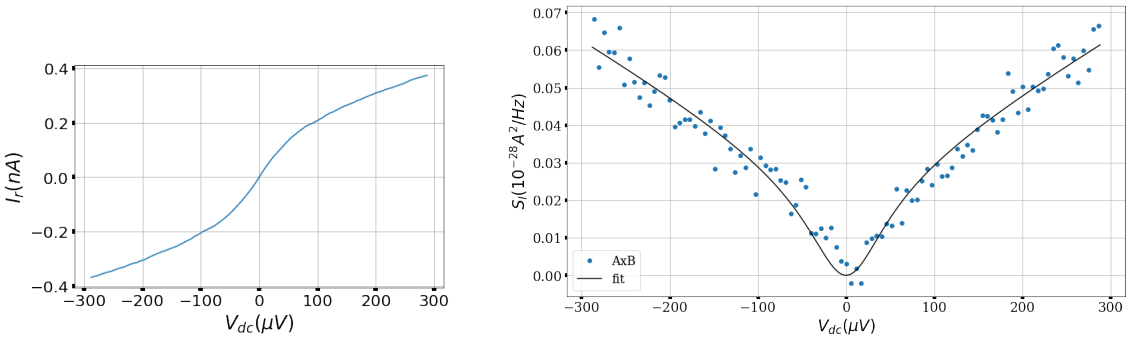

FIGURE 7.11: Reflected current I_R and DC cross correlation at $V_{gate} = -0.42V$.

These measurements were done approximately one month before the last DCSN and PASN measurements at $V_{gate} = -0.42V$, however the cross-correlation is more than two times smaller than the one of figure 7.7. The reflected current being identical, we think that this is due to the HEMT gains time-drift. The fit $S_{exp}(V_{dc})$ was done considering smoother variations of the conductance of G_R, and multiplying the expected shot noise by a factor 0.2.

We are now going to attempt to fit the HOM curves based on our knowledge of the DCSN S_{exp}, and on equation (7.3). The HOM measurements that we present now were taken within few days after the DCSN measurement of figure 7.11, reducing the probability of the HEMT time-drifts. They were carried out with $P_1 - P_2 = 1dBm$, thus ensuring $V_{ac,1} = V_{ac,2} = V_{ac}$. We compare HOM measurements for three V_{ac} amplitudes spaced by $\sqrt{2}$, corresponding to $P_1 = 8, 11, 14dBm$. For each P_1 value, we performed two consecutive HOM measurements in order to improve the accuracy on the extracted V_{ac} values. These measurements are shown in figures 7.12,7.13,7.14. The HOM noise simulations are done using expression (7.3), letting V_{ac} and an offset as fitting parameters.

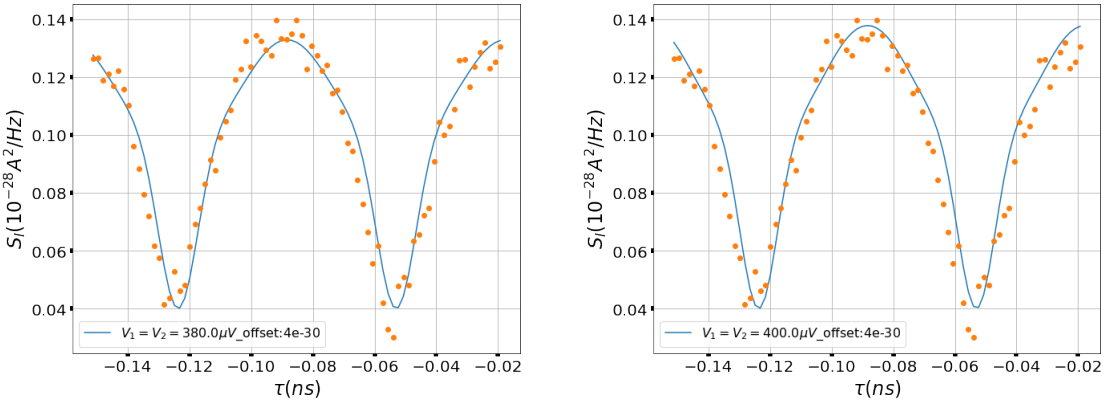

FIGURE 7.12: HOM measurements for $V_{gate} = -0.42V$, $P_1 = 8dBm$, $f = 14.15GHz$

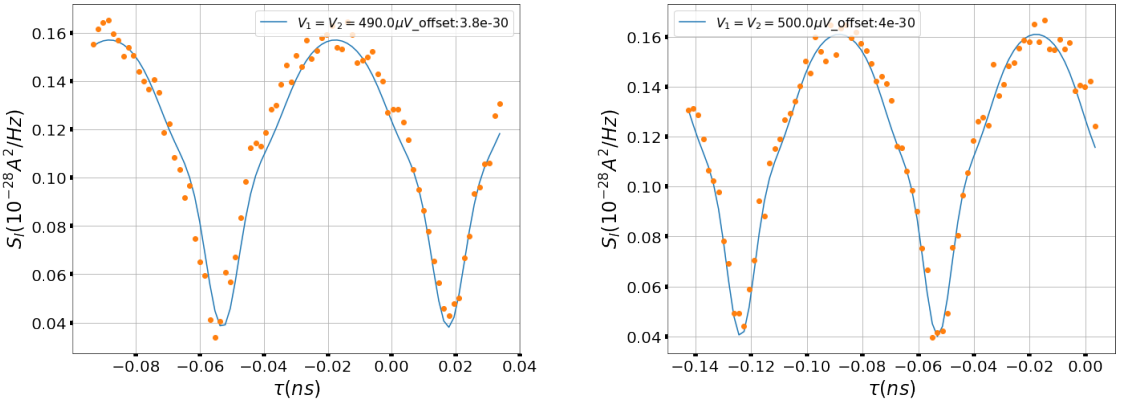

FIGURE 7.13: HOM measurements for $V_{gate} = -0.42V$, $P_1 = 11dBm$, $f = 14.15GHz$

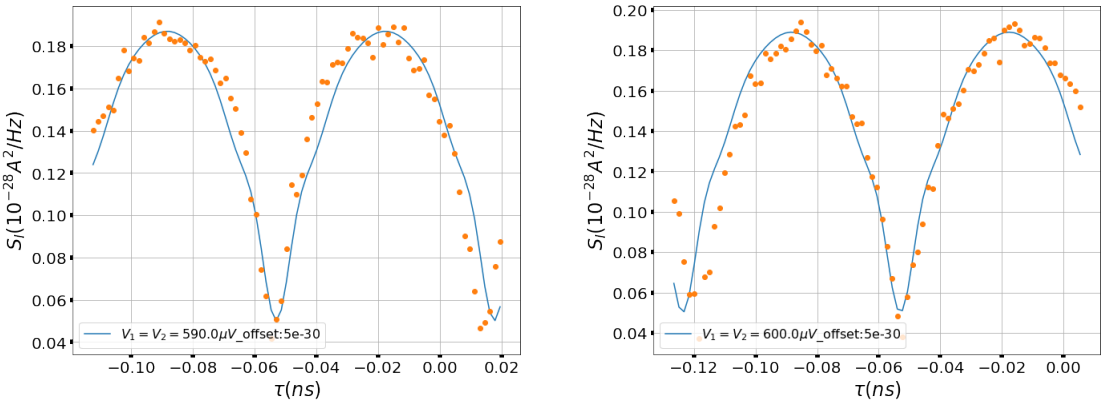

FIGURE 7.14: HOM measurements for $V_{gate} = -0.42V$, $P_1 = 14dBm$, $f = 14.15GHz$

The noise $S^{HOM}(\tau)$ shows the expected variations with the time delay τ. In particular, the structures with minima that are more peaked than the maxima are reminiscent of the DCSN variations. The experimental curves show break in slopes also visible from the theoretical simulations. These structures in the HOM curve are expected when the DCSN shows non-linearity with V_{dc} (see Ref [104] for the case of Levitons), which is the case at $V_{gate} = -0.42V$. The physical interpretation of such a structure is still subject of discussions.

As previously, the accuracy of our measurements is limited by experimental time drifts of the phase Φ, or of the HEMT gains. A single HOM measurement as presented in figures 7.12, 7.13 and 7.14, usually takes around 10 hours. In table 7.1, we report the range of V_{ac} and α values found from the analysis of the HOM measurements:

	$P_1 = 8dBm$	$P_1 = 11dBm$	$P_1 = 14dBm$
$V_{ac}(\mu V)$	380 - 400	490-500	590-600
α	2.16-2.27	2.78-2.84	3.35- 3.41

TABLE 7.1: V_{ac} range in μV and corresponding $\alpha = e^* V_{ac}/hf$ with $e^* = e/3$ and $f = 14.15GHz$ extracted from HOM measurements at various powers P_1.

The V_{ac} amplitudes are multiplied by a factor 1.31 when increasing the power from $P_1 = 8dBm$ to $P_1 = 11dBm$, and by 1.22 when switching from $P_1 = 11dBm$ to $P_1 = 14dBm$. We do not recover the ratio $\sqrt{2}$ expected for $3dB$ steps in the power. Thus HOM noise data cannot be totally interpreted within the picture leading to equation (7.3). Various explanations can be given for this mismatch:

- At $V_{gate} = -0.42V$, roughly 23% of the current carried by the outer edge state is reflected, meaning that we may have reached the limits of the weak backscattering regime. Out of this regime, no extension of equation (7.3) is known.
- The perturbative approach (see paragraph 3.1) used to derive equation (7.3) is valid

for strongly correlated systems, but energy-independent tunneling amplitudes. Energy-dependent tunneling could also lead to non-negligible deviations from equation (7.3). To our knowledge, a theory for strongly correlated systems that includes the energy-dependence of tunneling amplitudes is still lacking.
- The lack of information on $S_{exp}(V_{dc})$ for $V_{dc} > 300\mu V$ can also induce errors on the fit of HOM measurements using equation (7.3). Indeed when $\alpha_{eff} = 2e^* V_{ac} \sin(\pi f \tau)/hf$ is high (from the V_{ac} amplitudes of table 7.1, we can reach $\alpha_{eff} = 7$ for $P_1 = 14dBm$ and $\Phi = 2\pi f\tau = \pi/4$), we need to know $S_{exp}(V_{dc})$ for $V_{dc} = lhf/e$ with $-5 < l < 5$ - or equivalently for $-900\mu V < V_{dc} < 900\mu V$ - in order to calculate S^{HOM}. However, we have access to the DCSN $S_{exp}(V_{dc})$ only for $|V_{dc}| < 300\mu V$ (see figure 7.11). The linear extrapolation made for $|V_{dc}| > 300\mu V$ may lead to errors in the estimation of S^{HOM}.

7.3.2 Results at $\nu_B = 2/5$, $\nu_{QPC} = 2/5$

We now show results at $V_{gate} = 0V$, for which the DCSN is very close to the one presented in paragraph 7.1.1. The advantage of working in this regime is that we can interpret our measurements without assuming a particular edge state structure. The inconvenience is that the DC cross correlation is very low, and consequently the signal over noise of HOM measurement is low as well. We keep the RF frequency $f = 14.15GHz$, as well as the configuration for which $V_{ac,1} = V_{ac2}$, that is obtained for $P_1 - P_2 = 1dBm$. As previously, the phase shift Φ between two synchronized RF sources are automatically swept, and we make 400 steps of 1 radiant. For more accuracy, we carried out two HOM measurements for $P_1 = 12dBm$, and for $P_1 = 15dBm$.

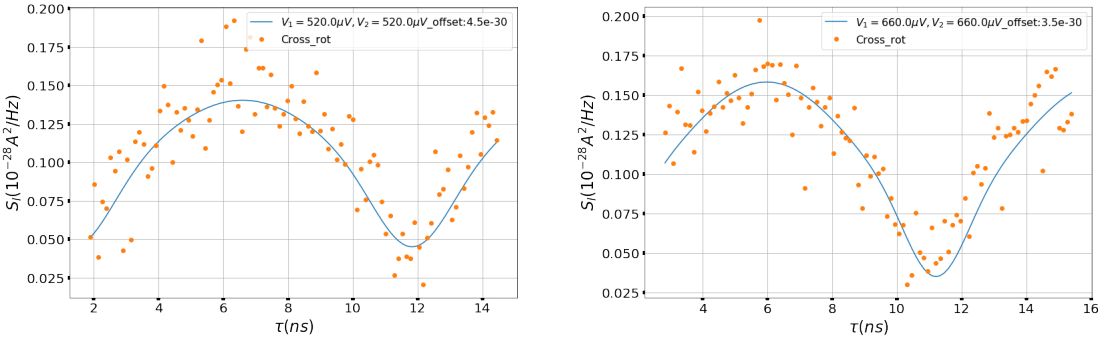

FIGURE 7.15: HOM measurements for $V_{gate} = 0V$, $P_1 = 12dBm$, $f = 14.15GHz$

The fit is made using equation (7.3), with $e^* = e/5$ and $S_{exp}(V_{dc})$ given by DCSN measurements (figure 7.5). Once again, we are limited by experimental phase shifts between the two RF sources. Because of the very low value of DC cross-correlation, it is hard to obtain a good signal over noise ratio within reasonable time measurements (to avoid experimental drifts). Consequently, the accuracy on the extracted V_{ac} is not very satisfying. We report these values in table 7.2.

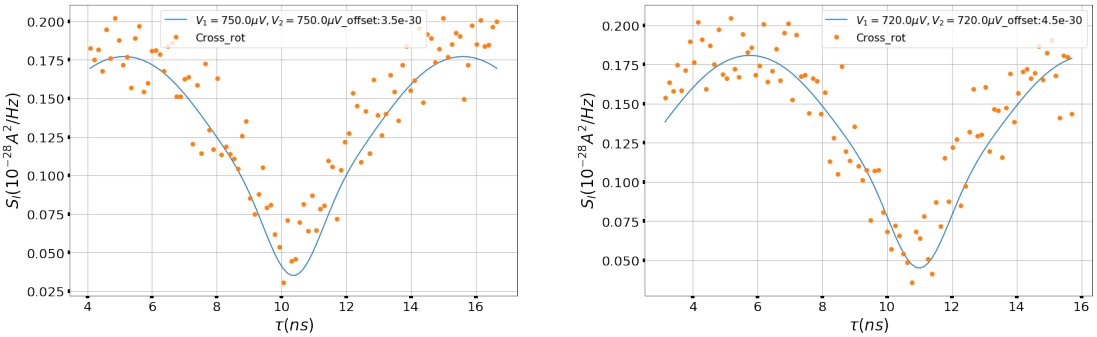

FIGURE 7.16: HOM measurements for $V_{gate} = 0V$, $P_1 = 15dBm$, $f = 14.15GHz$

	$P_1 = 12dBm$	$P_1 = 15dBm$
$V_{ac}(\mu V)$	520-660	720-750

TABLE 7.2: V_{ac} range in μV extracted from HOM measurements at different powers.

Taking into account the 20% uncertainty on the V_{ac} value for $P_1 = 12dBm$, we can recover the expected factor $\sqrt{2}$ between the V_{ac} amplitudes corresponding to $P_1 = 12dBm$ and $P_1 = 15dBm$. However, better accuracy is needed in order to be able to conclude on these HOM measurements.

7.4 Conclusion

DCSN measurements at $\nu = 2/5$ showed unexpected results, that we attribute most probably to errors due to bad thermalization during the noise calibration process. At $V_{gate} = 0V$, the cross correlation corresponds roughly to 70% of the expected $2e^*I_R$ value with $e^* = e/5$. A much smaller difference between experimental datas and theory was observed at $V_{gate} = -0.42V$ and $V_{gate} = -0.4V$. This variable difference makes us think that the problem does not only come from the noise thermal calibration, that would induce a systematic error on the calibration factor. Two other reasons were envisaged:

- Non-perfect coupling between edge states and ohmic contacts can induce errors in the estimation of the transmitted and reflected current, and possibly on the noise. It could lead to a non perfect definition of edge states potentials, or to different potentials for the two co-propagating edge states. The effect of this bad coupling on the auto and cross-correlation noise is difficult to estimate.
- The complexity of edge states at $\nu = 2/5$, that involves possible edge-reconstruction and tunneling processes between edge states, make it difficult to make exact predictions on the DCSN. This difficulty is enhanced in the presence of non-perfect ohmic contacts.

Of course, these two reasons have an impact on the PASN and HOM interpretation as well. From one hand, a good coupling between edge states and ohmic contacts is needed

so that the sine wave sent on reservoir (0) (and on contact (3) for HOM) propagates without deformation to the QPC. From the other hand, theoretical predictions of HOM noise are known only in the weak backscattering regime. At $V_{gate} = -0.4V$ or $V_{gate} = -0.42V$, this regime can be defined only assuming that the transport at $\nu = 2/5$ occurs through two independent edge states (with no tunneling events between both). However we did not find any clear evidence for this assumption from our experimental data.

Moreover, in presence of RF signals, experimental complications are linked to the intrinsic drifts of the RF source as well as a power-dependent noisy signal. These effects can considerably complicate the data analysis.

For all these reasons, the HOM measurements at $\nu_B = 2/5$ do not allow to conclude unambiguously on the validity of equation (7.3) to describe such measurements. Contrary to what is naively expected for fermions, the HOM noise does not cancel at $\tau = 0$ (or for $V_1(t) = V_2(t)$). The visibility is limited to 65%. This is not due to the non-fermionic nature of electrons pulses, but more probably to fundamental reasons linked with the complexity of FQHE edge states structure, or to energy-dependent tunneling processes. It can also be due to experimental artefacts, that should be analysed more deeply.
All these difficulties justify the necessity of performing HOM experiments in a single QPC geometry, where fermionic statistics is expected, before considering a more complex geometry (3 QPC) to explore the anyonic statistics. Despite these difficulties, HOM measurements were performed for the first time in the FQHE, and they show the expected qualitative behaviour.

Conclusion and prospects

In this work, we presented first measurements of HOM correlations in the fractional Hall effect. We used a QPC-beam-splitter, on which quasi-particles are sent by voltage pulses applied on both QPC sides. For simplicity, we applied sine voltages instead of "pure" electronic excitations (levitons), at either $10GHz$ or $14.15GHz$, and with a well-controlled time-delay τ. "HOM correlations" correspond to the cross-correlation between the transmitted and reflected current, measured while sweeping the delay τ. In the integer Hall effect, a good agreement with "photo-assisted" transport picture could be established through a comparison between HOM correlations at various sine amplitudes. The same study carried on in the fractional Hall showed deviations from known theoretical models, the origin of which needs to be clarified.
For both integer and fractional Hall regimes, we observe a large HOM dip at $\tau = 0$, but not as deep as the expected 100% dip of pure fermionic correlations. This points towards the need of improving the experimental measurements before addressing the study of anyonic correlations.

For the latter purpose, the idea is to send anyons on both sides of the QPC-beam-splitter, created by two other QPCs in the fractional Hall regime. Applying lorentzian pulses on each of these two QPCs, we inject electrons that, after tunneling through the FQH region, can be considered as anyons. The time-delay between the arrival of these two anyons on the QPC-beam-splitter can be controlled in the same way as in our experiments. As intuited in Chapter 1 by a simple single-particle approach, the cross correlation measurement could give information on the statistical phase of anyons. A simplified scematic of the 3-QPCs experimental setup is shown in figure 7.17.

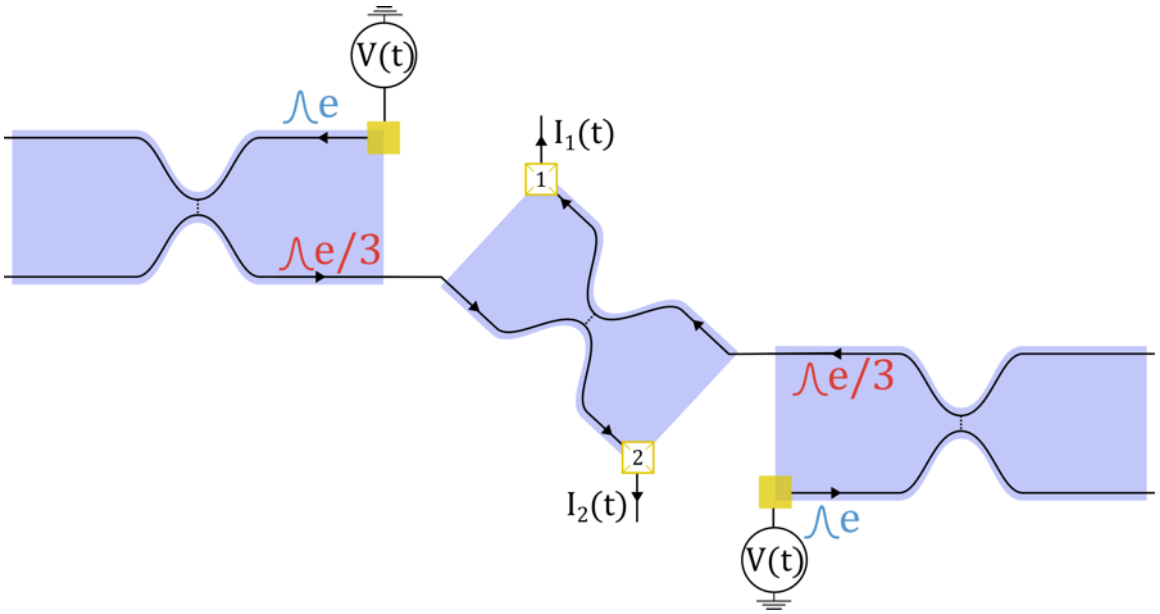

FIGURE 7.17: A Lorentzian pulse carrying integer charge e is applied on a QPC in the FQHE in the regime of weak backscattering regime, where charges $e/3$ tunnel. On a second QPC, also in the FQHE, in the WBS regime of transmission, a Lorentzian pulse of integer charge is applied with a delay τ. The two leviton-like fractional charges are sent to a third QPC playing the role of a beam-splitter. Correlations between $I_1(t)$ and $I_2(t)$ are measured.

Appendix A

Appendix A: Noise calibration

The noise calibration is made measuring the thermal noise that is emitted by two impedances in parallel: the RLC circuit and the Hall resistance. As explained in paragraph 4.5, we consider the difference between the Johnson Nyquist noise measured at $T > T_0$ and at base temperature T_0:

$$\Delta S_{A,A}(\omega, T - T_0) = S_{A,A}(\omega, T) - S_{A,A}(\omega, T_0) = G_A^2 4k_b(T - T_0)Re(Z_{eq,A}(\omega)) \quad \text{(A.1)}$$

$$\Delta S_{B,B}(\omega, T - T_0) = S_{B,B}(\omega, T) - S_{B,B}(\omega, T_0) = G_B^2 4k_b(T - T_0)Re(Z_{eq,B}(\omega)) \quad \text{(A.2)}$$

The inner resistance r_c of the Coil was already found to be equal to 8.1Ω in branch A and 9.1Ω in branch B from the the noise calibration at $\nu = 2$ (paragraph 4.5). It is thus fixed for the next calibrations at $\nu = 2/5$ and $\nu = 2/3$, that we present here. The other fixed parameters are $R = 20k\Omega, L = 22\mu H, C1 = 9.4nF$.

A.1 Calibration at $\nu = 2/3$

We first determine the base temperature T_0 by plotting the mean value of $\Delta S_{A,A}(\omega, T - T_0)$ over a frequency interval $\Delta f = [2.2MHz, 2.8MHz]$ versus temperature T in figure A.1. As expected from equation A.2, we find a linear dependence. However, we see a saturation for temperatures below 50mK. This probably comes from the effect of a bad thermalization of the sample or of the RLC circuit to the mixing chamber (the coolest stage of the fridge). This temperature gradient is more visible at low temperature than at high temperature. From the linear fit of figure A.1, we extract $T_0 = 32mK$ for line A and $T_0 = 31mK$ for line B.

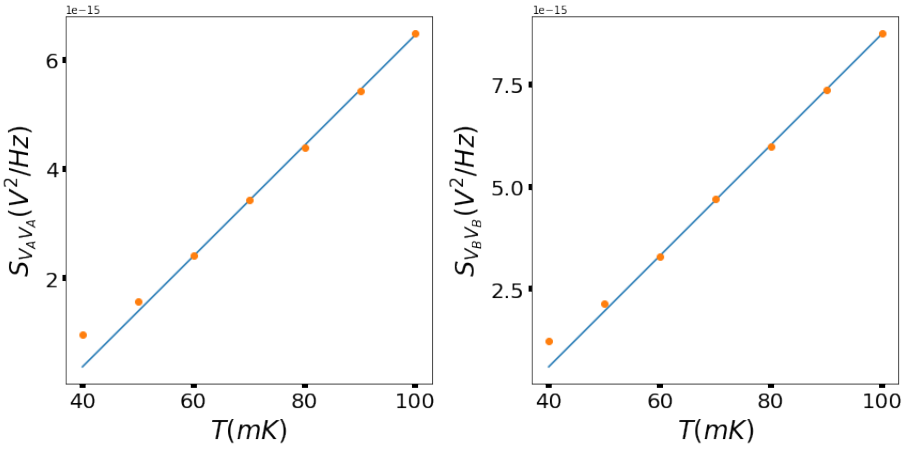

FIGURE A.1: $\langle \Delta S_{A,A}(T - T_0) \rangle$ versus T for $\nu = 2/3$

Then, the value of C_l (the line capacitance) and of the amplifier gains $G_{A/B}$ are determined from the fit of $\Delta S_{A/B}(\omega, T - T_0)$ for T values between 40 mK and 10 mK. The parameters extracted from these fits at different temperature are reported in figure A.3.

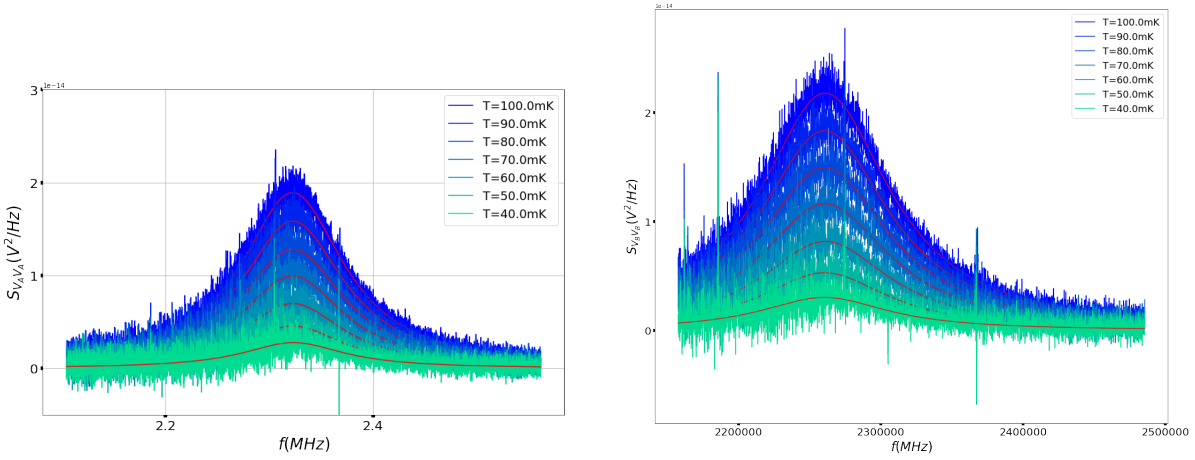

FIGURE A.2: $\Delta S_{A,A}(\omega, T - T_0)$ (left figure) and $\Delta S_{B,B}(\omega, T - T_0)$ (right figure) for $\nu = 2/3$ and T between $40mK$ and $100mK$

The simulation of $|Z_A(f)|^2$, $|Z_B(f)|^2$ and $Re(Z_A^* Z_B)$ using the previously determined RLC parameters is shown in figure A.6.

Finally, choosing an integration interval of $[2.2, 2.38]MHz$, we can calculate the calibration factors C_{aa}, C_{bb} and C_{ab} using the parameters of figure A.3 . The results and the accuracy are indicated below. The accuracy determined from the variance of these points is very good. These C_{aa}, C_{bb} and C_{ab} factors are used to convert the measured voltage fluctuations to current fluctuations according to equation (4.6).

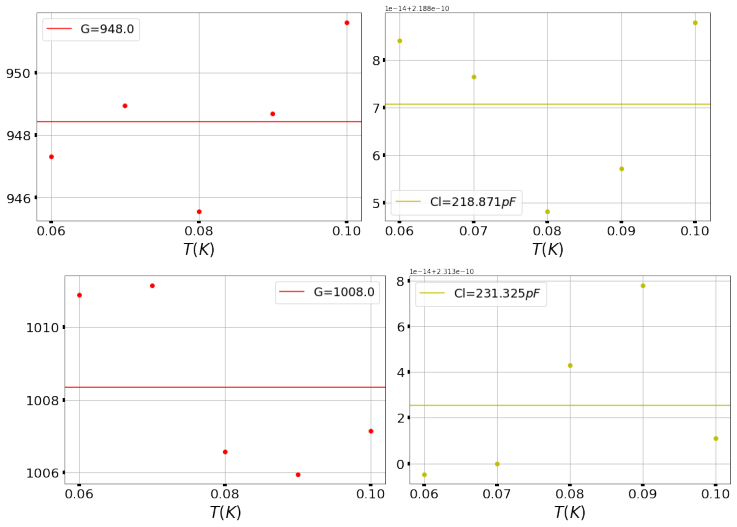

FIGURE A.3: C_l and gains $G_{A/B}$ for lines A and B found from the fits of figure A.2.

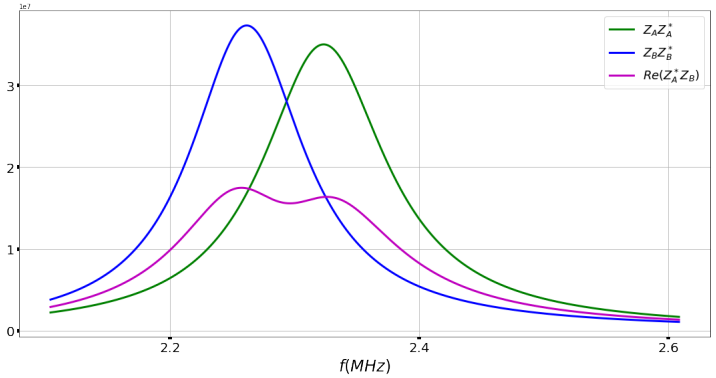

FIGURE A.4: $|Z_A|^2$, $|Z_B|^2$ and $Re(Z_A^* Z_B)$ versus frequency f

A.2 Calibration at $\nu = 2/5$

We use exactly the same technique than previously described to first determine the base temperature T_0 using the the linear fit of $\langle \Delta S_{A,A}(T - T_0) \rangle$ versus T (figure). We find $T_0 = 31mK$ for line A and $T_0 = 33mK$ for line B.

We then fit the spectra of $\Delta S_{A/B}(\omega, T - T_0)$ to find the line capacitance C_l and the gains $G_{A/B}$, for T between 60 mK and 100 mK. The parameters extracted from these fits at various temperatures are reported inf figure A.8. Of course, Cl do not depend on the filling factor and thus we find the same values than at $\nu = 2$ and $\nu = 2/3$. But the interesting parameters are the gains $G_{A/B}$, that need to be checked regularly because of time drifts.

Finally, choosing the same integration interval than previously [2.2,2.38]MHz and the parameters of figure A.8, we can calculate the calibration factors Caa,Cbb and Cab. The results and the accuracy are indicated in the legend of figure A.9.

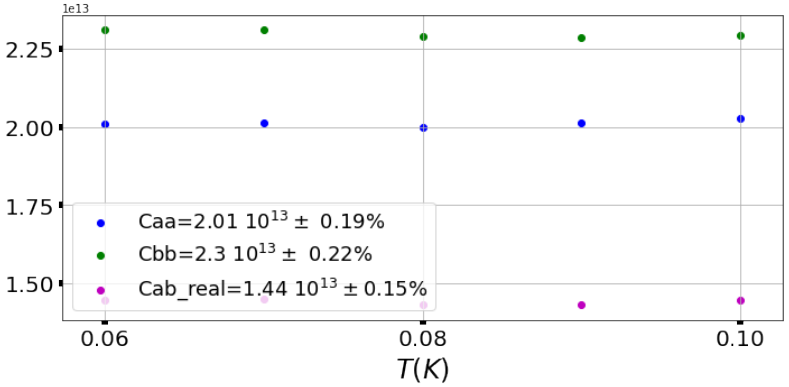

FIGURE A.5: C_{aa}, C_{bb} and C_{ab} values found from noise calibration at $\nu = 2/3$.

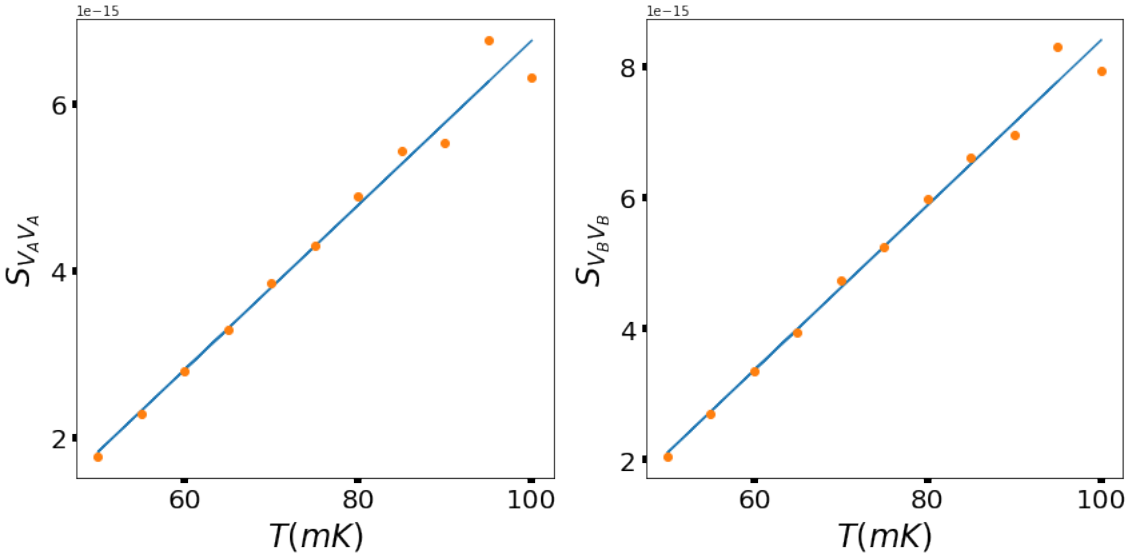

FIGURE A.6: $\langle \Delta S_{A,A}(T - T_0) \rangle$ versus T for $\nu = 2/5$

A.3 Effects of a bad thermalization

One of the main source of discordance of our results on DC shot noise with the literature is probably a bad thermalization of the sample (at temperature T_2) or of the RLC circuit (at temperature T_1) with the mixing chamber temperature. This effect leads to errors in the determination of the amplifier gains G_A and G_B and thus on the conversion factors C_{aa}, C_{bb}, C_{ab}. Indeed, in this case the Johnson-Nyquist noise would write:

$$S_{JN}(T_1, T_2) = 4k_B|Z_{eq}|^2(Re(\frac{T_1}{Z_{RLC}}) + \frac{T_2}{R_H}) = T_1 Re(Z_{eq}) + \Delta T \frac{|Z_{eq}|^2}{R_H} \tag{A.3}$$

where $\Delta T = T_2 - T_1$ and $1/Z_{eq} = 1/R_H + 1/Z_{RLC}$. During the thermal calibration, we heat up the mixing chamber up to temperature $T' > T_1, T_2$. Assuming that for high enough T', the thermalization of is efficient and T' corresponds to the temperature of

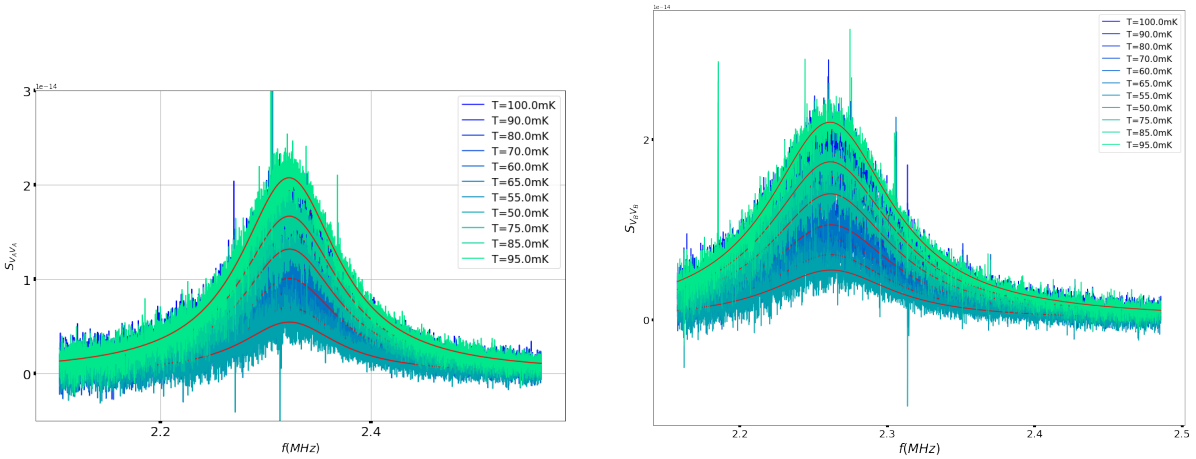

FIGURE A.7: $\Delta S_{A,A}(\omega, T - T_0)$ (left figure) and $\Delta S_{B,B}(\omega, T - T_0)$ (right figure) for $\nu = 2/5$ and T between $40mK$ and $100mK$

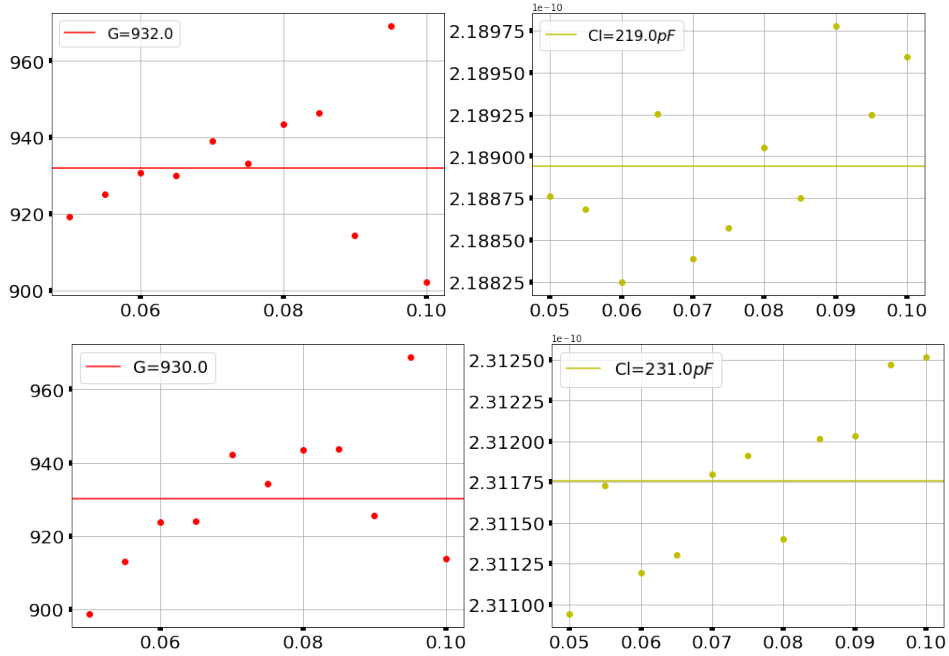

FIGURE A.8: C_l and gains $G_{A/B}$ for lines A and B found from the fits of figure A.7.

both the RLC and the sample, the excess Johnson-Nyquist noise would write:

$$\Delta S(T') = S_{JN}(T', T') - S_{JN}(T_1, T_2) = (T_1 - T')Re(Z_{eq}) + \Delta T \frac{|Z_{eq}|^2}{R_H} \tag{A.4}$$

Equation (A.4) implies a linear variation of $\Delta S(T')$, as experimentally observed for $T' > 40mK$ in most of the noise calibrations. At high enough T', the second term of equation (A.4) can be neglected, allowing for a good fit of $\Delta S(T')$ spectra using only the first term (see for example figure 4.8 at $T' = 100mK$ and $\nu = 2$). However, the value of T_1 in this first term is overestimated by a quantity $\delta = \Delta T \frac{|Z_{eq}|^2}{R_H Re(Z_{eq})}$ (as the solution of $\Delta S(T') = 0$ is not T_1 but $T_1 + \delta$). T_1 being overestimated, the gains G_A and G_B are

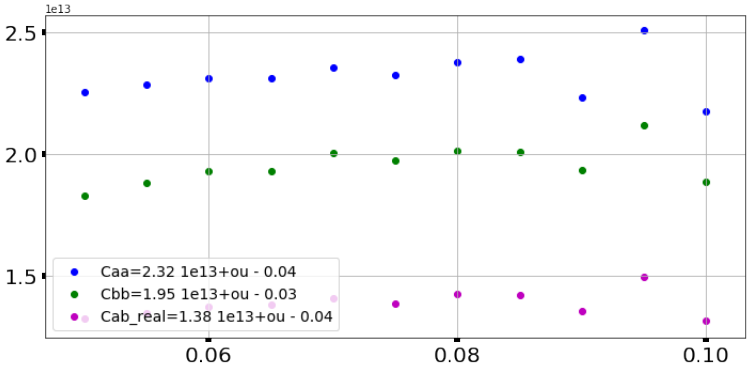

FIGURE A.9: C_{aa}, C_{bb} and C_{ab} values found from noise calibration at $\nu = 2/5$.

underestimated, leading to too low values of shot noise.

Appendix B

Sample characteristics

The sample we used are made from hetero-structures of $GaAS$ and $GaAs-Al_xGa_{1-x}As$, where x defines the Aluminium mole fraction and is typically around 30%. These are semiconductor crystals with only a slightly different lattice constant, a convenient property to build a multi-layer heterostructure without crystalline defects. A molecular beam epitaxy technique is used in order to control very precisely the thinkness of each layer. The wafer was supplied by I. Farrer and D.A. Ritchie from the Cavendish in Cambridge.

B.1 Formation of the two-dimensional electron gas (2DEG)

The hetero-structure is schematized in figure B.1. Some electrons introduced by the silicium populate the surface states of $GaAs$, others are trapped at the interface between the two semi conductors. These last electrons form the 2DEG, that is localized 90 nm under the sample surface. The position of the doping silicium is an important parameter of the fabrication. Indeed, if it is too far from the interface, the 2DEG will not exist as there will be no donors, while if it is too close, the 2DEG density will be high, but the mobility will be reduced. For the sample used here, an undoped AlGaAs layer of 40 nm is placed between GaAs and n-AlGaAs in order to increase the distance between the donors and the 2DEG to obtain higher mobility [105]. This high mobility is needed to reach the fractional Hall effect regime at accessible magnetic field (lower than 14 T).

When the two semiconductors with different energy gaps are put in contact, the Fermi energy homogenizes: electrons flow from AlGaAs to GaAs, creating charge inhomogeneity at the interface. This charge inhomogeneity creates an electric field that will tend to stop this effect. When the electric field is high enough to compensate for the diffusion current of charges, the equilibrium state is reached, and the band structure can be

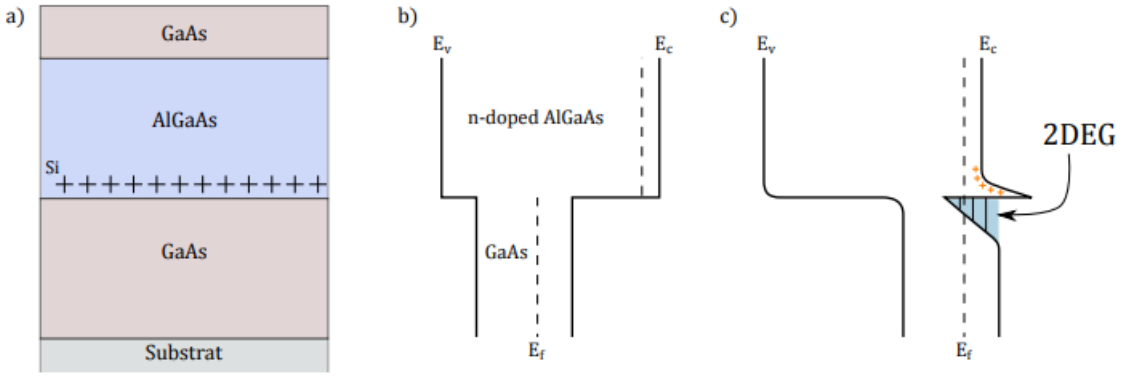

FIGURE B.1: a) Heterostructure scheme. Si donors are in the AlGaAs layer allowing the formation of the 2DEG. b) Band structure at the n-AlGaAs/iGaAs interface before charge equilibration. The dotted line represents the Fermi Energy in each structure, it is more important in AlGaAs than in GaAs. Solid lines are valence and conduction bands. c) Band structure after charge equilibration. The 2DEG, colored in blue, is formed at the interface of AlGaAs and GaAs while positively charged donors, in orange, accumulate at the AlGaAs side.

represented by figure B.1 c). A triangular shaped potential is created at the interface, where electrons are confined. Thus their wave vector is quantized in the direction perpendicular to the interface. The energy levels are discrete, distant of several tenth of meV [106]. At the working temperature ($< 100mK$), only the first level is occupied.

The sample electronic density $n_S = 1.11 * 10^{11} cm^{-2}$ and the mobility is $\mu = 3 * 10^6 V^{-1} cm^2 s^{-1}$. At two dimensions the density of states is constant and thus the electronic density is proportional to the Fermi energy:

$$n_S = \frac{m^*}{\pi \hbar^2} E_F$$

where m^* is the effective mass of one electron in the GaAs: $m^* = 0.067 m_0$, m_0 being the electron mass. The resulting Fermi energy is $4meV$, that results in Fermi temperature $T_F = E_F / k_B = 45K$. In our measurements, the necessary condition $T << T_F$ is satisfied as $T = 20mK$. The mean collision time and the mean free path can be estimated from the mobility:

$$\tau_e = \frac{m^* \mu}{e} = 112ps, \quad l_e = v_F \tau_e = 16\mu m$$

However in the Hall regime the transport is ballistic and such expression is not useful. The value of the coherence length in the FQHE has never been measured, but it was done for electrons in AsGa in the IQHE. The coherence length has been measured at 20 mK to be ot the order of tenth of μm [107].

B.2 QPC realization

Once the 2DEG was supplied, the nanofabrication of the sample was realized by M.Santin and M.Kapfer using exclusively electronic lithography. Here we report only the main steps:
- The mesa etching is first performed to define the surface on which we need the 2DEG to be defined. The etching of the nanostructure away from the mesa avoid the donors to fill the states at the interface between the two semiconductors, and thus there the 2DEG to be formed. This is a chemical etching using H_3PO_4.

- Ohmic contacts were then deposited in order to make the link between the surface of the sample and the 2DEG, 90 nm below. For that, we deposit on the mesa a mixture of gold, nickel and germanium. The sample is the heated at 470 in order for the alloy to penetrate the heterostructure and reach the 2DEG.

- Finally the gates are done by evaporating aluminium on the surface of the sample after an electronic lithography. The gates are separated by 300 nm.
The sample is later connected to the PCB by aluminium wires.

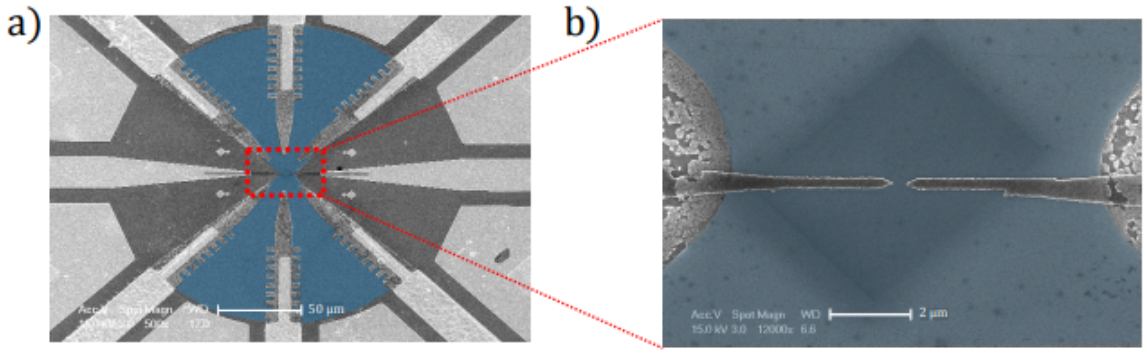

FIGURE B.2: SEM image of the finished sample from Ref [6]. a) Image realized by electron microscope of the sample. The 2DEG is artificially colored in blue. The large bright circuit are golden leads connecting the ohmic contact in grey to the external circuit. The black lines are the gates. A zoom (figure b)) is realized at the center of the mesa where the gates are placed.

Appendix C

Interference phenomena with RF waves

In this chapter we want to emphasize some aspects on which one should pay attention when working with radio frequency (RF) waves. High frequencies mean short wavelengths: for GHz frequencies, the wavelengths are in the cm range, meaning that wave phenomena arise over distances comparable to the connectors length. A transmission line is characterized by its characteristic impedance, that is commonly 50Ω for all the RF systems. The reflection coefficient for a wave travelling from a medium with characteristic impedance Z_1 to a medium with characteristic impedance Z_2 is given by:

$$r = \frac{Z_1 - Z_2}{Z_1 + Z_2}$$

The RF coaxial lines as well as the circuit on which the sample is connected (PCB) are designed to be 50Ω matched. However, small reflections can occur because of non-perfect connections between two RF coaxial cables through 'SMA' connectors. Moreover, almost all the power is reflected when it reaches the sample, as the Hall resistance R_H is many order of magnitude higher than $Z_0 = 50\Omega$. This impedance mismatch is impossible to avoid when working in the Hall regime. The reflection at both ends of a transmission line creates a standing wave, which leads to further power waste and cause frequency-dependent loss. This situation is schematized in figure C.1 for a coaxial cable of length L, connected to the sample resistance R_H at one end and to a non-perfect connector at the other end.

Calling r_1, t_1 (resp. r_2, t_2) the reflection and transmission amplitudes at the interface between the transmission line and the connector (resp. the sample resistance R_H), the

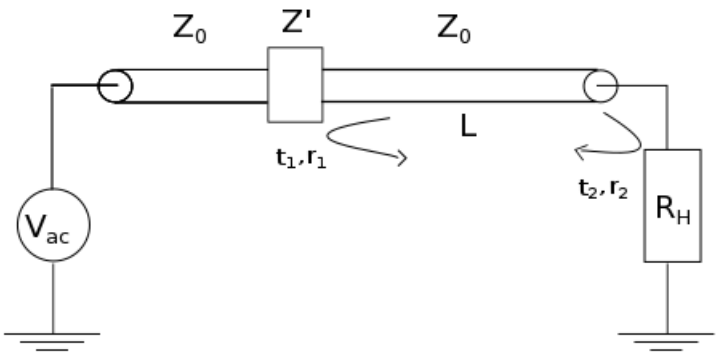

FIGURE C.1: A standing wave is created by a reflection at both ends of a transmission line of length L and characteristic impedance $Z_0 = 50\Omega$. As $R_H >> Z_0$, the reflection coefficient $|r_2|^2$ is close to one. $|r_1|^2$ depends on non-perfect connector modeled by an impedance $Z' \neq Z_0$

total transmission amplitude T is given by:

$$T = t_1 t_2 e^{i\phi} + t_1 e^{i\phi} r_2 r_1 e^{2i\phi} + ... = t_1 t_2 e^{i\phi} \sum_{n=0}^{+\infty} (r_1 r_2 e^{2i\phi})^n = t_1 t_2 \frac{e^{i\phi}}{1 - r_1 r_2 e^{2i\phi}}$$

where $\phi = 2\pi f L / v_p$, v_p being the propagation velocity in the cable. From the transmission line theory it can been shown that $v_p = c/\sqrt{\epsilon} = 2.07 * 10^8 m/s$, where $\epsilon = 2.1$ is the dielectric constant of Teflon, used in our coaxial cables. This leads to:

$$|T|^2 = \frac{|t_1 t_2|^2}{|1 - r_1 r_2 e^{2i\phi}|^2}$$

We see that the transmission coefficient $|T|^2$ strongly depend on the frequency f. Assuming that t_1, t_2, r_1, r_2 are frequency-independent, taking $|r_2|^2 = 0.99$, $|r_1|^2 = 0.01$, and $L = 20cm$, we can simulate the variations of $|T|^2$ over a frequency interval of 1GHz (figure C.2).

We see that a small reflection probability of 1% at the connector can already be responsible for oscillations of the power transmitted to the sample with 30% visibility.
This was confirmed by experimental observations: a strong dependence of the RF power sent on the sample with the frequency was observed through photo-current measurements. The principle of such measurement was detailed in paragraph 5.9. The photo-current shows strong oscillations with the RF frequency. This is illustrated in figure C.3, for $\nu = 2$ and in the strong back-scattering regime $V_{gate} = -0.97V$. In this regime, we often observe the strongest non-linearities of the I-V characteristic, and thus the higher photo-current values.

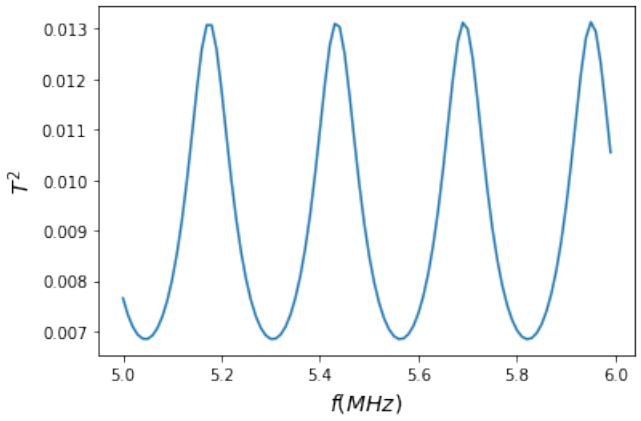

FIGURE C.2: Transmission probability $|T|^2$ vs frequency for $|r_2|^2 = 0.99$, $|r_1|^2 = 0.01$, and $L = 20cm$

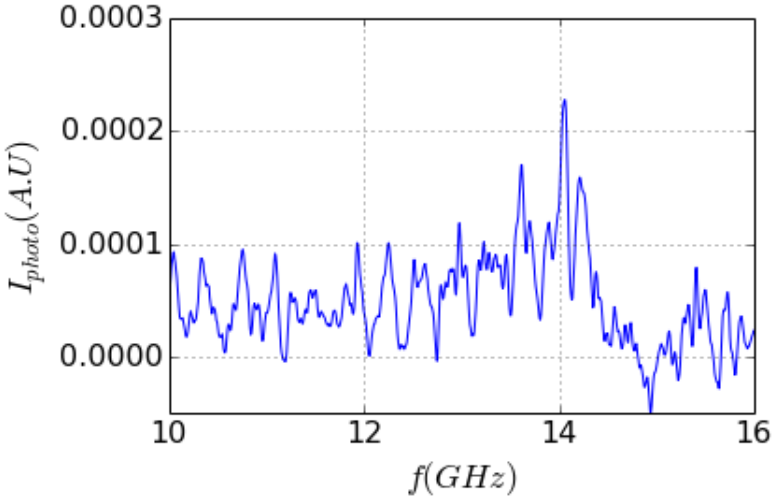

FIGURE C.3: Photo-current vs RF frequency for $\nu = 2$ (B=2.4T), $V_{gate} = -0.97V$.

The oscillation period is around $0.3GHz$, indicating that the interferometer length is approximately $L = 20cm$ (as simulated in figure C.2). This corresponds to the length scale of our RF cables. Moreover, this period was found to be independent on the gate voltage or the filling factor. These are the reasons why, after a long study trying to interpret these oscillations as the mark of charged and neutral modes due to interaction between edge states, we were finally convinced that this effect originates from the experimental setup.

Appendix D

DC polarisation of the sample

DC voltages delivered by Yokogawa 7651 (commonly called "Yoko") are brought to the sample by coaxial cables stainless steel. Those wires have a linear resistance of $23.6\Omega/m$ and a capacitance of $173.9pF/m$. They can carry signal up to a cutoff frequency of approximately $40kHz$. Their cut-off frequency is estimated around $40kHz$, which is suitable as only DC or low-frequency voltages are to be sent through those wires.

The outer conductor is made of braided stainless, the inner conductor is stainless steel while the dielectric is Teflon. The wires are anchored at each stages of the cryostat through SMA connectors, thermalizing the outer conductor at the stage temperature.
From one hand, the relatively high resistivity of the inner conductor limits the heat conductivity of the wires, that is proportional to the electrical conductivity at low temperature. The heating power brought by the wires have been estimated to $10pW$ using the Wiedemann-Franz law (see M.Kapfer PhD thesis [6]). This value is much lower than the cooling power of the mixing chamber stage which is of $2\mu W$, ensuring that there is no overheating due to the wires.
From the other hand, the low cut-off frequency makes the noise brought by DC cables negligible, around $\Delta V = 1\mu V$.

A schematic of the DC injection line is shown in figure D.1. In order to decrease the electronic temperature, we added a supplementary filter that consists on a 1.5 m long resistive wire enrolled in "epoxy" glue that contains some silver. Its high thermal conductivity favors the thermalization of the DC line to the lowest stage of the Cryostat. A voltage divider is thermalized to the 100 mK stage in order to ensure ensure a good voltage source (with no current flowing into the sample resistance $R_{sample} = R_H$). The $1k\Omega$ resistance placed after the voltage divider was used to lower the cutoff frequency of the DC lines. However, she makes the voltage V_0 slightly dependent on R_{sample}. These corrections were taken into account using numerical simulations of the circuit to

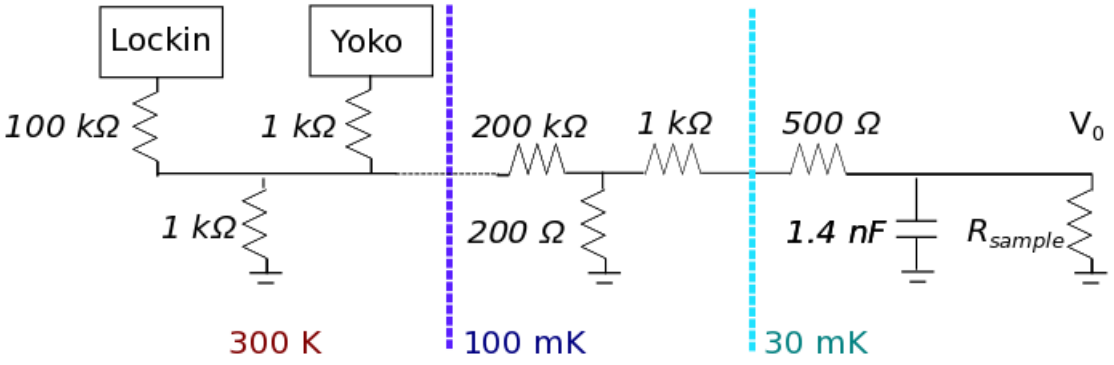

FIGURE D.1: DC injection lines

calculate V_{sample} for 1V at the output of the Yokoyawa ("Yoko") source. The results are shown in table D.1.

ν	$R_H(k\Omega)$	$V_0(\mu V)$
4	6.45	392
2	12.9	438
1	25.8	465
2/3	38.72	475
2/5	64.5	483

TABLE D.1: V_0 for an output voltage of 1V on the Yoko, for different falling factors ν.

Appendix E

Appendix E: Effects of the environmental noise on the PASN measurements

Some measurements made at various filling factors seemed to not agree with the use Bessel functions to describe PASN. This can be due to experimental reasons: on top on the mono-frequency main signal, the RF source may deliver an aleatory signal $V_{al}(t)$ that has a broadened spectra. In that case, we have to consider the total signal $V(t) = V_{ac}sin(2\pi ft)+V_{al}(t)$ to calculate the spectra of $e^{i\Phi(t)}$, where $\Phi(t) = \int_{-\infty}^{t} V(t')dt'$. If we call $\Phi_{al}(t) = \int_{-\infty}^{t} V_{al}(t')dt'$ the noisy phase and $g(\omega)$ the Fourier transform of $e^{-i\Phi_{al}(t)}$, the new weight (that may be interpreted as the new emission and absorption probabilities) would be given by $|\tilde{p}(\omega,\alpha)|^2$, $\tilde{p}$ being the convolution product between Bessel functions and $g(\omega)$:

$$\tilde{p}(\omega,\alpha) = \sum_{l} p_l(\alpha) g(\omega - 2\pi l f) \tag{E.1}$$

This aleatory signal being present only in presence of a finite RF signal, the "ON" measurements are linked to the "OFF" measurements (or to S_{exp}) by:

$$S_{ON}(V_{dc}) = \int d\omega |\tilde{p}(\omega,\alpha)|^2 S_{exp}(V_{dc} + \frac{\hbar\omega}{e}) \tag{E.2}$$

Indeed, the Floquet scattering approach as well as the perturbative approach (see paragraphs 3.2.3 and 3.1) can be adapted to any shape of the AC signal.

To observe the slope changes of figure 5.7, the function $g(\omega)$ needs to be peaked around 0 with a width much smaller than f. In other words, the thermal broadening due to

the finite temperature in $S_{exp}(V_{dc})$ is much more important than the spectra broadening of $g(\omega)$. From numeric simulations, we can show that this hypothesis considerably simplifies equation (E.1):

$$\tilde{p}(lf, \alpha) = \tilde{p}_l(\alpha) = p_l(\alpha)g(0) \tag{E.3}$$

In other words, the correction brought by the noisy signal can be taking into account simply by multiplying the DCSN by $|g(0)|^2$. From equation (E.2) and (E.3), the excess noise becomes:

$$\Delta S(V_{dc}) = \sum_{l=-\infty,+\infty} P_l(\alpha)|g(0)|^2 S_{exp}(T_{ON}, V_{dc} + \frac{lhf}{e}) - S_{exp}(T_{OFF}, V_{dc}) \tag{E.4}$$

In our analysis of the excess noise, we assumed $|g(0)|^2 = 1$ and we determined an effective α_{eff} such as : $|p_l(\alpha)g(0)|^2 = |p_l(\alpha_{eff})|^2$. We understand that this results in $\alpha_{eff} \neq \alpha$, and we do not conserve the ratio between two different values of α and two different values of α_{eff}. This may explain why we don't find the good $\sqrt{2}$ ratio when applying $\sqrt{2}$-spaced V_{ac} amplitudes.

We can try to be quantitative on the power noise brought by the RF source. We assume that the amplifier of the RF source has a noise temperature of $T_N = 300K$. We recall that the noise temperature is a unit for noise: it corresponds to the temperature at which we should bring a 50Ω impedance to get the same amount of noise. Each amplifier has a finite noise temperature. $T_N = 300K$ noise temperature is one of the best value that is possible to reach for an amplifier that works in such a wide range of frequencies ($0.2GHz - 20GHz$). As the delivered power can vary from $-20dBm$ to $20dBm$, the maximal gain of this amplifier should be $G = 10^4$ for $P = 20dBm$. Integrating over the whole frequency range $\Delta f = 20GHz$, the power brought by the RF source connected to a 50Ω impedance line (ended by a 50Ω resistance) is:

$$P_N = k_b G T_N \Delta f = 2\mu W = -27dBm \tag{E.5}$$

As $R_H >> 50\Omega$, the 50Ω impedance line that brings the RF signal to the sample is connected to an open circuit instead of a 50Ω resistance. Thus the power is multiplied by a factor 4: $P_N = -21dBm$. For the maximal delivered power $P = 20dBm$, the ratio $\frac{P_N}{P}$ is around $10^{-4.1}$. This ratio can vary with the delivered power P (or the variable gain G), but this gives an order of magnitude that can be used for simulations.

Bibliography

[1] Daniel Cooper, Benjamin D'Anjou, Nageswara Ghattamaneni, Benjamin Harack, Michael Hilke, Alexandre Horth, Norberto Majlis, Mathieu Massicotte, Leron Vandsburger, Eric Whiteway, and Victor Yu. Experimental review of graphene. *ISRN Condens. Matter Phys.*, 2012, 10 2011. doi: 10.5402/2012/501686.

[2] Mirco Milletari. *Non-Equilibrium transport in quantum Hall edge states*. PhD thesis, 06 2013.

[3] D. C. Tsui, H. L. Stormer, and A. C. Gossard. Two-dimensional magnetotransport in the extreme quantum limit. *Phys. Rev. Lett.*, 48:1559–1562, May 1982. doi: 10.1103/PhysRevLett.48.1559. URL https://link.aps.org/doi/10.1103/PhysRevLett.48.1559.

[4] D. Christian Glattli. *Tunneling Experiments in the Fractional Quantum Hall Effect Regime*, pages 163–197. Birkhäuser Basel, Basel, 2005. ISBN 978-3-7643-7393-1. doi: 10.1007/3-7643-7393-8_5. URL https://doi.org/10.1007/3-7643-7393-8_5.

[5] Christian Spanslätt, Jinhong Park, Yuval Gefen, and A. Mirlin. Conductance plateaus and shot noise in fractional quantum hall point contacts. *Physical Review B*, 101, 02 2020. doi: 10.1103/PhysRevB.101.075308.

[6] M. Kapfer, P. Roulleau, M. Santin, I. Farrer, D. A. Ritchie, and D. C. Glattli. A josephson relation for fractionally charged anyons. *Science*, 363(6429):846849, Jan 2019. ISSN 1095-9203. doi: 10.1126/science.aau3539. URL http://dx.doi.org/10.1126/science.aau3539.

[7] B. J. van Wees, H. van Houten, C. W. J. Beenakker, J. G. Williamson, L. P. Kouwenhoven, D. van der Marel, and C. T. Foxon. Quantized conductance of point contacts in a two-dimensional electron gas. *Phys. Rev. Lett.*, 60:848–850, Feb 1988. doi: 10.1103/PhysRevLett.60.848. URL https://link.aps.org/doi/10.1103/PhysRevLett.60.848.

[8] DA Wharam, Trevor John Thornton, R Newbury, M Pepper, H Ahmed, JEF Frost, DG Hasko, DC Peacock, DA Ritchie, and GAC Jones. One-dimensional transport and the quantisation of the ballistic resistance. *Journal of Physics C: solid state physics*, 21(8):L209, 1988.

[9] M. Büttiker. Scattering theory of current and intensity noise correlations in conductors and wave guides. *Phys. Rev. B*, 46:12485–12507, Nov 1992. doi: 10.1103/PhysRevB.46.12485. URL https://link.aps.org/doi/10.1103/PhysRevB.46.12485.

[10] A. Kumar, L. Saminadayar, D. C. Glattli, Y. Jin, and B. Etienne. Experimental test of the quantum shot noise reduction theory. *Phys. Rev. Lett.*, 76:2778–2781, Apr 1996. doi: 10.1103/PhysRevLett.76.2778. URL https://link.aps.org/doi/10.1103/PhysRevLett.76.2778.

[11] M. Reznikov, M. Heiblum, Hadas Shtrikman, and D. Mahalu. Temporal correlation of electrons: Suppression of shot noise in a ballistic quantum point contact. *Phys. Rev. Lett.*, 75:3340–3343, Oct 1995. doi: 10.1103/PhysRevLett.75.3340. URL https://link.aps.org/doi/10.1103/PhysRevLett.75.3340.

[12] C. de C. Chamon, D. E. Freed, and X. G. Wen. Tunneling and quantum noise in one-dimensional luttinger liquids. *Phys. Rev. B*, 51:2363–2379, Jan 1995. doi: 10.1103/PhysRevB.51.2363. URL https://link.aps.org/doi/10.1103/PhysRevB.51.2363.

[13] P. Fendley, A. W. W. Ludwig, and H. Saleur. Exact nonequilibrium dc shot noise in luttinger liquids and fractional quantum hall devices. *Phys. Rev. Lett.*, 75:2196–2199, Sep 1995. doi: 10.1103/PhysRevLett.75.2196. URL https://link.aps.org/doi/10.1103/PhysRevLett.75.2196.

[14] Benjamin Roussel, Pascal Degiovanni, and Inès Safi. Perturbative fluctuation dissipation relation for nonequilibrium finite-frequency noise in quantum circuits. *Phys. Rev. B*, 93:045102, Jan 2016. doi: 10.1103/PhysRevB.93.045102. URL http://link.aps.org/doi/10.1103/PhysRevB.93.045102.

[15] L. Saminadayar, D. C. Glattli, Y. Jin, and B. Etienne. Observation of the $e/3$ fractionally charged laughlin quasiparticle. *Phys. Rev. Lett.*, 79:2526–2529, Sep 1997. doi: 10.1103/PhysRevLett.79.2526. URL https://link.aps.org/doi/10.1103/PhysRevLett.79.2526.

[16] T. G. Griffiths, E. Comforti, M. Heiblum, Ady Stern, and V. Umansky. Evolution of quasiparticle charge in the fractional quantum hall regime. *Phys. Rev. Lett.*, 85:

3918–3921, Oct 2000. doi: 10.1103/PhysRevLett.85.3918. URL https://link.aps.org/doi/10.1103/PhysRevLett.85.3918.

[17] M. Heiblum. Measuring the fractional charge and its evolution. In Bernhard Kramer, editor, *Advances in Solid State Physics 40*, pages 21–34, Berlin, Heidelberg, 2000. Springer Berlin Heidelberg. ISBN 978-3-540-44560-9.

[18] M. Santin, M. Kapfer, P. Roulleau, I. Farrer, D. A Ritchie, and D. C Glattli. The Josephson frequency of fractionally charged anyons. *Science*, 363 (6429):846 – 849, 2019. doi: 10.1126/science.aau3539. URL https://hal-cea.archives-ouvertes.fr/cea-02167003.

[19] R. B. Laughlin. Anomalous quantum hall effect: An incompressible quantum fluid with fractionally charged excitations. *Phys. Rev. Lett.*, 50:1395–1398, May 1983. doi: 10.1103/PhysRevLett.50.1395. URL https://link.aps.org/doi/10.1103/PhysRevLett.50.1395.

[20] D. T. McClure, W. Chang, C. M. Marcus, L. N. Pfeiffer, and K. W. West. Fabry-perot interferometry with fractional charges. *Phys. Rev. Lett.*, 108:256804, Jun 2012. doi: 10.1103/PhysRevLett.108.256804. URL https://link.aps.org/doi/10.1103/PhysRevLett.108.256804.

[21] F. E. Camino, Wei Zhou, and V. J. Goldman. $e/3$ laughlin quasiparticle primary-filling $\nu = 1/3$ interferometer. *Phys. Rev. Lett.*, 98:076805, Feb 2007. doi: 10.1103/PhysRevLett.98.076805. URL https://link.aps.org/doi/10.1103/PhysRevLett.98.076805.

[22] R. L. Willett, K. Shtengel, C. Nayak, L. N. Pfeiffer, Y. J. Chung, M. L. Peabody, K. W. Baldwin, K. W. West, and . Interference measurements of non-abelian e/4 abelian e/2 quasiparticle braiding. 2019.

[23] Nissim Ofek, Aveek Bid, Moty Heiblum, Ady Stern, Vladimir Umansky, and Diana Mahalu. Role of interactions in an electronic fabry–perot interferometer operating in the quantum hall effect regime. *Proceedings of the National Academy of Sciences*, 107(12):5276–5281, 2010. ISSN 0027-8424. doi: 10.1073/pnas.0912624107. URL https://www.pnas.org/content/107/12/5276.

[24] J. Nakamura, S. Liang, G. C. Gardner, and M. J. Manfra. Direct observation of anyonic braiding statistics. *Nat. Phys.*, 16:931–936, Mars 2020. doi: 10.1038/s41567-020-1019-1. URL https://doi.org/10.1038/s41567-020-1019-1.

[25] H. Bartolomei, M. Kumar, R. Bisognin, A. Marguerite, J.-M. Berroir, E. Bocquillon, B. Plaçais, A. Cavanna, Q. Dong, U. Gennser, Y. Jin, and G. Fève.

Fractional statistics in anyon collisions. *Science*, 368(6487):173–177, 2020. ISSN 0036-8075. doi: 10.1126/science.aaz5601. URL https://science.sciencemag.org/content/368/6487/173.

[26] C. K. Hong, Z. Y. Ou, and L. Mandel. Measurement of subpicosecond time intervals between two photons by interference. *Phys. Rev. Lett.*, 59:2044–2046, Nov 1987. doi: 10.1103/PhysRevLett.59.2044. URL https://link.aps.org/doi/10.1103/PhysRevLett.59.2044.

[27] J. Keeling, I. Klich, and L. S. Levitov. Minimal excitation states of electrons in one-dimensional wires. *Phys. Rev. Lett.*, 97:116403, Sep 2006. doi: 10.1103/PhysRevLett.97.116403. URL https://link.aps.org/doi/10.1103/PhysRevLett.97.116403.

[28] T Jullien, P Roulleau, B Roche, A Cavanna, Y Jin, and Christian D.C. Glattli. Quantum tomography of an electron. *Nature*, 514:603 – 607, 2014. doi: 10.1038/nature13821. URL https://hal-cea.archives-ouvertes.fr/cea-01409215.

[29] J. Dubois, T. Jullien, F. Portier, P. Roche, A. Cavanna, Y. Jin, W. Wegscheider, P. Roulleau, and D. C. Glattli. Minimal-excitation states for electron quantum optics using levitons. *Nature*, 502(7473):L659 – 663, 2013. doi: 10.1038/nature12713. URL https://hal-cea.archives-ouvertes.fr/cea-01481175.

[30] Johnson N. Locane E. et al. Fletcher, J.D. Continuous-variable tomography of solitary electrons. *Nat Commun*, 5298, 2019. doi: 10.1038/s41467-019-13222-1. URL https://doi.org/10.1038/s41467-019-13222-1.

[31] G. B. Lesovik and L. S. Levitov. Noise in an ac biased junction: Nonstationary aharonov-bohm effect. *Phys. Rev. Lett.*, 72:538–541, Jan 1994. doi: 10.1103/PhysRevLett.72.538. URL https://link.aps.org/doi/10.1103/PhysRevLett.72.538.

[32] Morten Holm Pedersen and Markus Büttiker. Scattering theory of photon-assisted electron transport. *Phys. Rev. B*, 58:12993–13006, Nov 1998. doi: 10.1103/PhysRevB.58.12993. URL https://link.aps.org/doi/10.1103/PhysRevB.58.12993.

[33] Ines Safi. Time-dependent transport in arbitrary extended driven tunnel junctions, 2014.

[34] Neil W Ashcroft, N David Mermin, et al. *Solid state physics*, volume 2005. holt, rinehart and winston, new york London, 1976.

[35] John Bertrand Johnson. Thermal agitation of electricity in conductors. *Physical review*, 32(1):97, 1928.

[36] H. Nyquist. Thermal agitation of electric charge in conductors. *Phys. Rev.*, 32: 110–113, Jul 1928. doi: 10.1103/PhysRev.32.110. URL https://link.aps.org/doi/10.1103/PhysRev.32.110.

[37] Bernd Rosenow, Ivan P. Levkivskyi, and Bertrand I. Halperin. Current correlations from a mesoscopic anyon collider. *Phys. Rev. Lett.*, 116:156802, Apr 2016. doi: 10.1103/PhysRevLett.116.156802. URL https://link.aps.org/doi/10.1103/PhysRevLett.116.156802.

[38] Ya.M. Blanter and M. Büttiker. Shot noise in mesoscopic conductors. *Physics Reports*, 336(1-2):1166, Sep 2000. ISSN 0370-1573. doi: 10.1016/s0370-1573(99)00123-4. URL http://dx.doi.org/10.1016/S0370-1573(99)00123-4.

[39] David Tong. Lectures on the quantum hall effect, 2016.

[40] K. v. Klitzing, Gerhard Dorda, and Michael Pepper. New method for high-accuracy determination of the fine-structure constant based on quantized hall resistance. *Physical review letters*, 45(6):494, 1980.

[41] Steven M. Girvin. The quantum hall effect: Novel excitations and broken symmetries, 1999.

[42] R de Picciotto, M Reznikov, M Heiblum, V Umansky, G Bunin, and D Mahalu. Direct observation of a fractional charge. *Physica B: Condensed Matter*, 249-251: 395400, Jun 1998. ISSN 0921-4526. doi: 10.1016/s0921-4526(98)00139-2. URL http://dx.doi.org/10.1016/S0921-4526(98)00139-2.

[43] Picciotto R. Griffiths T. et al Reznikov, M. Observation of quasiparticle with one-fifth of an electrons charge. *Nature Communication*, 399:2526–2529, Jan 1999. doi: /10.1038/203846. URL https://doi.org/10.1038/203846.

[44] Aveek Bid, N. Ofek, M. Heiblum, V. Umansky, and D. Mahalu. Shot noise and charge at the 2/3 composite fractional quantum hall state. *Phys. Rev. Lett.*, 103: 236802, Dec 2009. doi: 10.1103/PhysRevLett.103.236802. URL https://link.aps.org/doi/10.1103/PhysRevLett.103.236802.

[45] R. Bisognin, H. Bartolomei, Manohar Kumar, Ines Safi, J-M Berroir, Erwann Bocquillon, Bernard Plaais, Antonella Cavanna, U. Gennser, Yong Jin, and Gwendal Fève. Microwave photons emitted by fractionally charged quasiparticles. *Nature Communications*, 10, 12 2019. doi: 10.1038/s41467-019-09758-x.

[46] C. de C. Chamon, D. E. Freed, S. A. Kivelson, S. L. Sondhi, and X. G. Wen. Two point-contact interferometer for quantum hall systems. *Phys. Rev. B*, 55: 2331–2343, Jan 1997. doi: 10.1103/PhysRevB.55.2331. URL https://link.aps.org/doi/10.1103/PhysRevB.55.2331.

[47] K. T. Law, D. E. Feldman, and Yuval Gefen. Electronic mach-zehnder interferometer as a tool to probe fractional statistics. *Phys. Rev. B*, 74:045319, Jul 2006. doi: 10.1103/PhysRevB.74.045319. URL https://link.aps.org/doi/10.1103/PhysRevB.74.045319.

[48] Bernd Rosenow, Ivan P. Levkivskyi, and Bertrand I. Halperin. Current correlations from a mesoscopic anyon collider. *Phys. Rev. Lett.*, 116:156802, Apr 2016. doi: 10.1103/PhysRevLett.116.156802. URL https://link.aps.org/doi/10.1103/PhysRevLett.116.156802.

[49] Julien Torrès. *Transport et bruit quantique dans les fils mésoscopiques*. Theses, Université de la Méditerranée - Aix-Marseille II, September 2001. URL https://tel.archives-ouvertes.fr/tel-00007395.

[50] J. K. Jain. Composite-fermion approach for the fractional quantum hall effect. *Phys. Rev. Lett.*, 63:199–202, Jul 1989. doi: 10.1103/PhysRevLett.63.199. URL https://link.aps.org/doi/10.1103/PhysRevLett.63.199.

[51] V. J. Goldman, B. Su, and J. K. Jain. Detection of composite fermions by magnetic focusing. *Phys. Rev. Lett.*, 72:2065–2068, Mar 1994. doi: 10.1103/PhysRevLett.72.2065. URL https://link.aps.org/doi/10.1103/PhysRevLett.72.2065.

[52] Fabien Lafont, Amir Rosenblatt, Moty Heiblum, and Vladimir Umansky. Counter-propagating charge transport in the quantum hall effect regime. *Science*, 363 (6422):5457, Jan 2019. ISSN 1095-9203. doi: 10.1126/science.aar3766. URL http://dx.doi.org/10.1126/science.aar3766.

[53] Aveek Bid, N. Ofek, H. Inoue, M. Heiblum, C. L. Kane, V. Umansky, and D. Mahalu. Observation of neutral modes in the fractional quantum hall regime. *Nature*, 466(7306):585590, Jul 2010. ISSN 1476-4687. doi: 10.1038/nature09277. URL http://dx.doi.org/10.1038/nature09277.

[54] C. L. Kane and Matthew P. A. Fisher. Transmission through barriers and resonant tunneling in an interacting one-dimensional electron gas. *Phys. Rev. B*, 46:15233–15262, Dec 1992. doi: 10.1103/PhysRevB.46.15233. URL https://link.aps.org/doi/10.1103/PhysRevB.46.15233.

[55] I. Safi and E. V. Sukhorukov. Determination of tunneling charge via current measurements. *Eur. Phys. Lett.*, 91(6):67008, 2010. URL http://stacks.iop.org/0295-5075/91/i=6/a=67008.

[56] I. Safi and E. V. Sukhorukov. Determination of tunneling charge via current measurements. *Eur. Phys. Lett.*, 91(6):67008, 2010. URL http://stacks.iop.org/0295-5075/91/i=6/a=67008.

[57] P. Fendley, A. W. W. Ludwig, and H. Saleur. 74:3005, 1995.

[58] M. Grayson, D. C. Tsui, L. N. Pfeiffer, K. W. West, and A. M. Chang. Continuum of chiral luttinger liquids at the fractional quantum hall edge. *Phys. Rev. Lett.*, 80: 1062–1065, Feb 1998. doi: 10.1103/PhysRevLett.80.1062. URL https://link.aps.org/doi/10.1103/PhysRevLett.80.1062.

[59] A. M. Chang, L. N. Pfeiffer, and K. W. West. Observation of chiral luttinger behavior in electron tunneling into fractional quantum hall edges. *Phys. Rev. Lett.*, 77:2538–2541, Sep 1996. doi: 10.1103/PhysRevLett.77.2538. URL https://link.aps.org/doi/10.1103/PhysRevLett.77.2538.

[60] Inès Safi. Fluctuation-dissipation relations for strongly correlated out-of-equilibrium circuits. *Phys. Rev. B*, 102:041113, Jul 2020. doi: 10.1103/PhysRevB.102.041113. URL https://link.aps.org/doi/10.1103/PhysRevB.102.041113.

[61] D. Rogovin and D. J. Scalapino. Fluctuation phenomena in tunnel junctions. *Annals of Physics*, 86(1):1–90, July 1974. doi: 10.1016/0003-4916(74)90430-8.

[62] Pierre Février and Julien Gabelli. Tunneling time probed by quantum shot noise. *Nature Communications*, 9:4940, Fev 2018. doi: 10.1038/s41467-018-07369-6. URL https://link.aps.org/doi/10.1103/PhysRev.129.647.

[63] R. Bisognin, H. Bartolomei, M. Kumar, I. Safi, J.-M. Berroir, E. Bocquillon, B. Plaçais, A. Cavanna, U. Gennser, Y. Jin, and G. Fève. Microwave photons emitted by fractionally charged quasiparticles. *Nature Communications*, 10(1), December 2019. doi: 10.1038/s41467-019-09758-x. URL https://hal.archives-ouvertes.fr/hal-03051650.

[64] Benjamin Roussel, Pascal Degiovanni, and Inès Safi. Perturbative fluctuation dissipation relation for nonequilibrium finite-frequency noise in quantum circuits. *Phys. Rev. B*, 93:045102, Jan 2016. doi: 10.1103/PhysRevB.93.045102. URL http://link.aps.org/doi/10.1103/PhysRevB.93.045102.

[65] W. Schottky. On spontaneous current fluctuations in various electrical conductors. *Annalen der Physik*, 362(23):541–567, 1918. doi: 10.1002/andp.19183622304. URL https://onlinelibrary.wiley.com/doi/abs/10.1002/andp.19183622304.

[66] C.L. Kane and Matthew P.A. Fisher. Nonequilibrium noise and fractional charge in the quantum hall effect. *Phys. Rev. Lett.*, 72:724–727, 1994. doi: 10.1103/PhysRevLett.72.724.

[67] P. K. Tien and J. P. Gordon. Multiphoton process observed in the interaction of microwave fields with the tunneling between superconductor films. *Phys. Rev.*, 129:647–651, Jan 1963. doi: 10.1103/PhysRev.129.647. URL https://link.aps.org/doi/10.1103/PhysRev.129.647.

[68] Xiao-Gang Wen. Edge transport properties of the fractional quantum hall states and weak-impurity scattering of a one-dimensional charge-density wave. *Phys. Rev. B*, 44:5708–5719, Sep 1991. doi: 10.1103/PhysRevB.44.5708. URL https://link.aps.org/doi/10.1103/PhysRevB.44.5708.

[69] Inès Safi. Driven quantum circuits and conductors: A unifying perturbative approach. *Phys. Rev. B*, 99:045101, Jan 2019. doi: 10.1103/PhysRevB.99.045101. URL https://link.aps.org/doi/10.1103/PhysRevB.99.045101.

[70] Maura Sassetti, Ulrich Weiss, and Bernhard Kramer. Photo-induced tunneling of a luttinger liquid. *Solid State Communications*, 97(7):605–609, 1996. ISSN 0038-1098. doi: https://doi.org/10.1016/0038-1098(95)00716-4. URL https://www.sciencedirect.com/science/article/pii/0038109895007164.

[71] Adeline Crépieux, Pierre Devillard, and Thierry Martin. Photoassisted current and shot noise in the fractional quantum hall effect. *Physical Review B*, 69(20), May 2004. ISSN 1550-235X. doi: 10.1103/physrevb.69.205302. URL http://dx.doi.org/10.1103/PhysRevB.69.205302.

[72] H. H. Lin and Matthew P. A. Fisher. Mode locking in quantum-hall-effect point contacts. *Phys. Rev. B*, 54:10593–10603, Oct 1996. doi: 10.1103/PhysRevB.54.10593. URL https://link.aps.org/doi/10.1103/PhysRevB.54.10593.

[73] S. Ol'khovskaya, J. Splettstoesser, M. Moskalets, and M. Büttiker. Shot noise of a mesoscopic two-particle collider. *Phys. Rev. Lett.*, 101:166802, Oct 2008. doi: 10.1103/PhysRevLett.101.166802. URL https://link.aps.org/doi/10.1103/PhysRevLett.101.166802.

[74] S. Juergens, J. Splettstoesser, and M. Moskalets. Single-particle interference versus two-particle collisions. *EPL (Europhysics Letters)*, 96(3):37011, Oct 2011. ISSN 1286-4854. doi: 10.1209/0295-5075/96/37011. URL http://dx.doi.org/10.1209/0295-5075/96/37011.

[75] Samuel Houle, Karl Thibault, Edouard Pinsolle, Christian Lupien, and Bertrand Reulet. Photon-assisted dynamical coulomb blockade in a tunnel junction. *Physical*

Review B, 100(4), Jul 2019. ISSN 2469-9969. doi: 10.1103/physrevb.100.045304. URL http://dx.doi.org/10.1103/PhysRevB.100.045304.

[76] Ines Safi, Cristina Bena, and Adeline Crépieux. Ac conductance and non-symmetrized noise at finite frequency in quantum wires and carbon nanotubes. *Phys. Rev. B*, 78, 11 2008. doi: 10.1103/PhysRevB.78.205422.

[77] Julie Dubois. *Vers une source mésoscopique à n-électrons basée sur des pulses de tensions Lorentziens*. Theses, Université Pierre et Marie Curie - Paris VI, October 2012. URL https://tel.archives-ouvertes.fr/tel-00828608.

[78] Francesca Battista, Federica Haupt, and Janine Splettstoesser. Energy and power fluctuations in ac-driven coherent conductors. *Phys. Rev. B*, 90:085418, Aug 2014. doi: 10.1103/PhysRevB.90.085418. URL https://link.aps.org/doi/10.1103/PhysRevB.90.085418.

[79] R. J. Schoelkopf, A. A. Kozhevnikov, D. E. Prober, and M. J. Rooks. Observation of "photon-assisted" shot noise in a phase-coherent conductor. *Phys. Rev. Lett.*, 80: 2437–2440, Mar 1998. doi: 10.1103/PhysRevLett.80.2437. URL https://link.aps.org/doi/10.1103/PhysRevLett.80.2437.

[80] A. A. Kozhevnikov, R. J. Schoelkopf, and D. E. Prober. Observation of photon-assisted noise in a diffusive normal metal–superconductor junction. *Phys. Rev. Lett.*, 84:3398–3401, Apr 2000. doi: 10.1103/PhysRevLett.84.3398. URL https://link.aps.org/doi/10.1103/PhysRevLett.84.3398.

[81] L.-H. Reydellet, P. Roche, D. C. Glattli, B. Etienne, and Y. Jin. Quantum partition noise of photon-created electron-hole pairs. *Phys. Rev. Lett.*, 90:176803, Apr 2003. doi: 10.1103/PhysRevLett.90.176803. URL https://link.aps.org/doi/10.1103/PhysRevLett.90.176803.

[82] J. Gabelli and B. Reulet. Dynamics of quantum noise in a tunnel junction under ac excitation. *Phys. Rev. Lett.*, 100:026601, Jan 2008. doi: 10.1103/PhysRevLett.100.026601. URL https://link.aps.org/doi/10.1103/PhysRevLett.100.026601.

[83] Matthieu Santin. *Dynamique quantique dans des conducteurs balistiques et cohérents : interrupteur quantique et transport photo-assisté*. PhD thesis, 2017. URL http://www.theses.fr/2017SACLS169. Thèse de doctorat dirigée par Glattli, Denis-Christian Physique Université Paris-Saclay (ComUE) 2017.

[84] Thibaut Jullien. *Mesoscopic few-electron voltage pulse source*. Theses, Université Paris Sud - Paris XI, April 2014. URL https://tel.archives-ouvertes.fr/tel-01158785.

[85] R. H. Morf, N. d'Ambrumenil, and S. Das Sarma. Excitation gaps in fractional quantum hall states: An exact diagonalization study. *Phys. Rev. B*, 66:075408, Aug 2002. doi: 10.1103/PhysRevB.66.075408. URL https://link.aps.org/doi/10.1103/PhysRevB.66.075408.

[86] I. Safi and E. V. Sukhorukov. Determination of tunneling charge via current measurements. *EPL (Europhysics Letters)*, 91(6):67008, Sep 2010. ISSN 1286-4854. doi: 10.1209/0295-5075/91/67008. URL http://dx.doi.org/10.1209/0295-5075/91/67008.

[87] A. H. MacDonald. Edge states in the fractional-quantum-hall-effect regime. *Phys. Rev. Lett.*, 64:220–223, Jan 1990. doi: 10.1103/PhysRevLett.64.220. URL https://link.aps.org/doi/10.1103/PhysRevLett.64.220.

[88] F. D. M. Haldane. Fractional quantization of the hall effect: A hierarchy of incompressible quantum fluid states. *Phys. Rev. Lett.*, 51:605–608, Aug 1983. doi: 10.1103/PhysRevLett.51.605. URL https://link.aps.org/doi/10.1103/PhysRevLett.51.605.

[89] B. I. Halperin. Statistics of quasiparticles and the hierarchy of fractional quantized hall states. *Phys. Rev. Lett.*, 52:1583–1586, Apr 1984. doi: 10.1103/PhysRevLett.52.1583. URL https://link.aps.org/doi/10.1103/PhysRevLett.52.1583.

[90] X. G. Wen. Gapless boundary excitations in the quantum hall states and in the chiral spin states. *Phys. Rev. B*, 43:11025–11036, May 1991. doi: 10.1103/PhysRevB.43.11025. URL https://link.aps.org/doi/10.1103/PhysRevB.43.11025.

[91] Xiao-Gang Wen. Theory of the Edge States in Fractional Quantum Hall Effects. *International Journal of Modern Physics B*, 6(10):1711–1762, January 1992. doi: 10.1142/S0217979292000840.

[92] Jinhong Park, Yuval Gefen, and H.-S. Sim. Topological dephasing in the $\nu = 2/3$ fractional quantum hall regime. *Phys. Rev. B*, 92:245437, Dec 2015. doi: 10.1103/PhysRevB.92.245437. URL https://link.aps.org/doi/10.1103/PhysRevB.92.245437.

[93] Ofek N. Inoue H. et al. Bid, A. Observation of neutral modes in the fractional quantum hall regime. *Nature*, 466:585590, Dec 2010. doi: 10.1038/nature09277. URL https://doi.org/10.1038/nature09277.

[94] Rajarshi Bhattacharyya, Mitali Banerjee, Moty Heiblum, Diana Mahalu, and Vladimir Umansky. Melting of interference in the fractional quantum hall effect: Appearance of neutral modes. *Phys. Rev. Lett.*, 122:246801, Jun 2019. doi:

10.1103/PhysRevLett.122.246801. URL https://link.aps.org/doi/10.1103/PhysRevLett.122.246801.

[95] O. Shtanko, K. Snizhko, and V. Cheianov. Nonequilibrium noise in transport across a tunneling contact between=23fractional quantum hall edges. *Physical Review B*, 89(12), Mar 2014. ISSN 1550-235X. doi: 10.1103/physrevb.89.125104. URL http://dx.doi.org/10.1103/PhysRevB.89.125104.

[96] Gurman I. Rosenblatt A. et al. Sabo, R. Edge reconstruction in fractional quantum hall states. *Nature Phys*, 13, Jan 2017. doi: 10.1038/nphys4010. URL https://doi.org/10.1038/nphys4010.

[97] Jianhui Wang, Yigal Meir, and Yuval Gefen. Edge reconstruction in the ν=2/3 fractional quantum hall state. *Phys. Rev. Lett.*, 111:246803, Dec 2013. doi: 10.1103/PhysRevLett.111.246803. URL https://link.aps.org/doi/10.1103/PhysRevLett.111.246803.

[98] Yigal Meir. Composite edge states in the $\nu = 2/3$ fractional quantum hall regime. *Phys. Rev. Lett.*, 72:2624–2627, Apr 1994. doi: 10.1103/PhysRevLett.72.2624. URL https://link.aps.org/doi/10.1103/PhysRevLett.72.2624.

[99] D. B. Chklovskii, B. I. Shklovskii, and L. I. Glazman. Electrostatics of edge channels. *Phys. Rev. B*, 46:4026–4034, Aug 1992. doi: 10.1103/PhysRevB.46.4026. URL https://link.aps.org/doi/10.1103/PhysRevB.46.4026.

[100] Casey Nosiglia, Jinhong Park, Bernd Rosenow, and Yuval Gefen. Incoherent transport on the $\nu = 2/3$ quantum hall edge. *Phys. Rev. B*, 98:115408, Sep 2018. doi: 10.1103/PhysRevB.98.115408. URL https://link.aps.org/doi/10.1103/PhysRevB.98.115408.

[101] C. L. Kane and Matthew P. A. Fisher. Contacts and edge-state equilibration in the fractional quantum hall effect. *Phys. Rev. B*, 52:17393–17405, Dec 1995. doi: 10.1103/PhysRevB.52.17393. URL https://link.aps.org/doi/10.1103/PhysRevB.52.17393.

[102] C. Chamon and E. Fradkin. How to observe distinct universal conductances in tunneling to quantum hall states: having the right contacts. *arXiv: Condensed Matter*, 1996.

[103] B. Trauzettel, P. Roche, D. C. Glattli, and H. Saleur. Effect of interactions on the noise of chiral luttinger liquid systems. *Phys. Rev. B*, 70:233301, Dec 2004. doi: 10.1103/PhysRevB.70.233301. URL https://link.aps.org/doi/10.1103/PhysRevB.70.233301.

[104] Flavio Ronetti, Luca Vannucci, Dario Ferraro, Thibaut Jonckheere, Jérôme Rech, Thierry Martin, and Maura Sassetti. Crystallization of levitons in the fractional quantum hall regime. *Phys. Rev. B*, 98:075401, Aug 2018. doi: 10.1103/PhysRevB.98.075401. URL https://link.aps.org/doi/10.1103/PhysRevB.98.075401.

[105] Satoshi Hiyamizu, Junji Saito, Kazuo Nanbu, and Tomonori Ishikawa. Improved electron mobility higher than 106cm2/vs in selectively doped GaAs/n-AlGaAs heterostructures grown by MBE. *Phys. Rev. Lett.*, 22:L609–L611, Oct 1983. doi: 10.1143/jjap.22.l609. URL https://doi.org/10.1143/jjap.22.l609.

[106] Frank Stern and Sankar Das Sarma. Electron energy levels in gaas-ga$_{1-x}$al$_x$As heterojunctions. *Phys. Rev. B*, 30:840–848, Jul 1984. doi: 10.1103/PhysRevB.30.840. URL https://link.aps.org/doi/10.1103/PhysRevB.30.840.

[107] Preden Roulleau, F. Portier, P. Roche, A. Cavanna, G. Faini, U. Gennser, and D. Mailly. Direct measurement of the coherence length of edge states in the integer quantum hall regime. *Physical Review Letters*, 100(12), Mar 2008. ISSN 1079-7114. doi: 10.1103/physrevlett.100.126802. URL http://dx.doi.org/10.1103/PhysRevLett.100.126802.

université PARIS-SACLAY | ÉCOLE DOCTORALE Physique en l'Île-de-France (PIF)

Titre: Vers une expérience de Hong-Ou-Mandel en vue d'explorer la statistique anyonique dans l'effet Hall fractionnaire

Mots clés: Physique mésoscopique, effet Hall quantique, statistique d'exclusion, bruit de partition

Résumé: Les particules élémentaires sont classées en deux familles selon leur statistique d'exclusion: les fermions et les bosons. Dans des systèmes mésoscopiques bidimensionnels soumis à un fort champ magnétique, un nouveau type de quasi-particules appelées "anyons" peut apparaître. Dans le régime d'effet Hall quantique fractionnaire (FQHE), les anyons sont un exemple de statistique intermédiaire entre les photons et les fermions. L'objectif à long terme de ce travail est de mesurer la statistique des anyons par des expériences de type Hong Ou Mandel (HOM) électronique dans le domaine temporel. Une telle expérience nécessiterait trois QPCs (Quantum Point Contact): deux pour réaliser les sources d'anyons et un troisième pour réaliser un "beam-splitter" électronique. La première étape est l'étude d'un système plus simple à un QPC afin de tester la faisabilité et la compréhension de mesures HOM dans l'effet Hall entier et factionnaire. Avec un unique QPC, les particules émises grâce à des pulses de tensions appliqués sur des contacts de part et d'autre du QPC peuvent être considérées comme des fermions, même dans le régime d'effet Hall factionnaire. Nous présentons les premières mesures d'interférences HOM fermioniques dans ce régime de FQHE. Nous observons une bonne supression du bruit ("HOM dip") comme attendu pour des corrélations fermioniques, mais limité à 65% au lieu des 100% attendus. Nos mesures pointent sur la nécessité d'améliorer l'expérience ainsi que notre compréhension avant d'aborder l'étude des corrélations anyoniques.

Title: Towards Hong-Ou-Mandel experiments to explore the anyonic statistics in the fractional Hall effect.

Keywords: Mesoscopic physics, quantum Hall effect, exclusion statistic, partition noise

Abstract: Elementary particles are usually classified into two categories depending on their exclusion statistics: bosons and fermions. In bidimensional mesoscopic conductors subject to a strong magnetic field, new kind of quasi-particles (called "anyons") can emerge. In the fractional quantum Hall effect (FQHE), anyons are an example of exchange statistics intermediate between bosons and fermions. The long term goal of this work is to perform "Hong Ou Mandel" (HOM) experiments for detecting anyonic statistics in time domain using a 3-QPC (Quantum Point Contact) sample (2 QPCs being used to generate single anyons and a central QPC as a beam splitter to perform 2-particle anyonic HOM correlation). Prior that, we explored a simpler system with a single QPC beam-splitter in order to test our ability to perform HOM measurements in the integer and fractional quantum Hall regime. With only one QPC beam-splitter, the particles emitted from voltage pulses applied on ohmic contacts on both sides of the QPC have to be considered like electrons (fermions) even in the FQHE. We present the first HOM noise measurements in the FQHE. We observe a large HOM dip at zero time delay, but not as high as the expected 100% deep of pure fermionic correlations. This points towards the need of improving the experimental setup and our understanding before addressing the study of anyonic correlations.

Université Paris-Saclay
Espace Technologique / Immeuble Discovery
Route de l'Orme aux Merisiers RD 128 / 91190 Saint-Aubin, France